

# **Predicting Free-Falling Droplet Drying Behaviours at High Temperatures**



**Nguyen Viet Tien**

*Submitted in accordance with the requirements for the degree of*

***Doctor of Philosophy***

University of Leeds

School of Chemical and Process Engineering

October, 2020



*The candidate confirms that the work submitted is his/her own and that appropriate credit has been given where reference has been made to the work of others.*

*This copy has been supplied on the understanding that it is copyright material and that no quotation from the thesis may be published without proper acknowledgement.*

*The right of Nguyen Viet Tien to be identified as the author of this work has been asserted by him in accordance with the Copyright, Designs and Patents Act 1988.*

*This thesis is dedicated to my family*

## **Acknowledgment**

First and foremost, I would like to express my special thanks to my supervisor, Professor Andrew Bayly, for his positive guidance, for giving me this opportunity, and with whom I had many interesting discussions during the Ph.D. I would like to thank Dr. Muzammil Ali for sharing his relevant expertise, valuable experiences, and for being always there when I needed his advice. I would like to show my appreciation to all members of Professor Andrew Bayly research's group for their help and feedback on my work. Thanks also to my friends, Peter and Monty, for proofreading the thesis. I would like to extend my gratitude to my external examiner, Professor Mark Simmons from the University of Birmingham for his outstanding attention to detail in marking my thesis, and also to my internal examiner, Dr. Xiaodong Jia for his constructive feedback. The thesis is in its best version after receiving all the valuable ideas, comments and questions raised in the viva.

Particularly helpful to me was the technical team at COMSOL Inc. that provided continuous supports and actively addressed all of my questions. I would like to acknowledge the scholarship and the financial support given to me by the School of Chemical and Process Engineering at the University of Leeds.

Finally, I must express my profound gratitude to my parents for their love, sacrifices, and endless support. I am truly motivated to complete this Ph.D. with integrity thanks to my father. I am also grateful to my siblings who provided me with emotional support throughout this journey. I would like to thank my girlfriend for her continuous support over the past years, and also acknowledge my friends from the 'Nghe academic hon' group.

There are many more names that I cannot fit into this page, but I could not have finished this without your help. It was such a memorable journey. Thank you.

## Abstract

Boiling within a falling droplet is a special and important phenomenon, which is poorly understood among the drying industry and is not well developed within the literature. Droplet drying at the boiling regime is explored and investigated in this research, of which the outcomes are of value to the spray drying community. The thesis presents a high-resolution model with innovative features, which predicts the behaviour of a free-falling droplet drying at high temperatures. The mathematical framework of the model includes coupling the conduction, convection and diffusion within the droplet to the phase change happening at the interface, whilst solving for the free-surface model simultaneously. The Finite Element Method (FEM) is used to solve this Multiphysics system, and the droplet moving interface is tracked by the Arbitrary Lagrangian-Eulerian (ALE) algorithm. The computed drying information, such as the droplet averaged temperature or weight profiles, agrees closely with the experimental data for a sucrose droplet. The detailed insights into the distribution of the temperature and moisture content within the droplet are achievable thanks to the 2D axis-symmetrical model. The description of the droplet internal flow field suggests the asymmetrical formation of vortices, which is impossible to predict using currently available models. The correlation of the species diffusion coefficient is a critical variable, as it determines the size of the vortices and the solid shell thickness. At the boiling point, bubble expansion drives the droplet shape and significantly decreases the droplet heat and mass transfer coefficients. As the bubble is offset from the droplet centre, it recentralises itself while growing due to the non-uniform pressure field within the droplet. The bubble behaviour is highly sensitive to the conditions set at boiling, and is mainly driven by the heat transfer, which is a function of the solute concentration.

# Table of Contents

<b>Acknowledgment</b> .....	<b>i</b>
<b>Abstract</b> .....	<b>ii</b>
<b>List of Tables</b> .....	<b>viii</b>
<b>List of Figures</b> .....	<b>ix</b>
<b>Nomenclature</b> .....	<b>xxvii</b>
<b>Abbreviations</b> .....	<b>xxxiii</b>
<b>Chapter 1 Thesis introduction and motivation</b> .....	<b>1</b>
1.1. Background of 'Spray Drying' .....	2
1.1.1. History .....	2
1.1.2. Motivation for modelling of single droplet drying at boiling point .....	3
1.2. Theory of 'Drying' .....	5
1.2.1. Droplet drying .....	5
1.2.2. Droplet boiling .....	7
1.3. Particle morphological evolution .....	8
1.4. Research gap and aims.....	9
1.5. Thesis's structure.....	12
1.6. Thesis's plan sketch .....	14
<b>Chapter 2 Progress and innovations in the literature and the drying industry</b> .....	<b>15</b>
2.1. Literature review .....	16
2.1.1. Introduction.....	16
2.1.2. Models on Single Droplet Drying (SDD) .....	16
2.1.3. Experimental techniques for Single Droplet Drying.....	25

2.1.4.	Particle morphologies and structural evolution....	29
2.1.5.	Systems for droplet drying modelling.....	33
2.1.6.	Comparison of the heat and mass transfer correlations .....	45
2.1.7.	Single droplet drying at boiling point.....	50
2.1.8.	Analogous problem - Fuel droplet evaporation ....	54
2.2.	Conclusions .....	56

### **Chapter 3 Fundamental theory and validation benchmarks .....57**

3.1.	History and principal theory of Finite Element Method (FEM).....	58
3.1.1.	Arbitrary Lagrangian-Eulerian interface tracking method .....	69
3.2.	Theory of 'Drag' and 'Lift' on an object .....	82
3.3.	Development of proportional-integral-derivative (PID) feedback loop for predicting the terminal falling velocity.....	83
3.3.1.	Problem formulation and setup .....	86
3.3.2.	Governing equations and boundary conditions....	87
3.4.	Study of flow past the fixed and falling cylinders.....	91
3.4.1.	Drag and lift validation .....	91
3.4.2.	Heat and mass transfer coefficients validation ..	114
3.5.	PID performance test on a freefalling liquid droplet.....	121
3.5.1.	Problem formulation .....	122
3.5.2.	Governing equations and boundary conditions..	123

3.5.3.	Results.....	124
3.6.	Conclusions .....	128
<b>Chapter 4</b>	<b>Benchmarks of bubble growth within a liquid medium.....</b>	<b>129</b>
4.1.	Solving Stefan problem using FEM .....	130
4.1.1.	Problem formulation.....	131
4.1.2.	Results.....	134
4.2.	Verification benchmarks of bubble growth in a liquid medium.....	137
4.2.1.	Verification of the pressure-driven growth of a bubble (inertia effect).....	138
4.2.2.	Verification of the temperature-driven growth of a bubble (thermal effect).....	142
4.3.	Conclusions .....	150
<b>Chapter 5</b>	<b>Investigation of droplet drying models using FEM.....</b>	<b>151</b>
5.1.	Considerations on the current PID feedback control scheme .....	152
5.1.1.	Gravity as a controlled variable .....	153
5.2.	Simulation and validation of a 1D drying model for a sucrose solution droplet.....	157
5.2.1.	Problem formulation.....	157
5.2.2.	Governing equations .....	158
5.2.3.	Material properties.....	162
5.2.4.	Results.....	169
5.3.	Simulation of a droplet drying model in a 2-dimensional coordinate.....	175

5.3.1.	A brief discussion on the incapability of solving the Navier-Stokes equation using 1D system ....	176
5.3.2.	Problem formulation .....	176
5.3.3.	Governing equations .....	178
5.3.4.	Boundary and initial conditions .....	180
5.3.5.	Material properties.....	181
5.3.6.	Numerical method.....	182
5.3.7.	Results and discussions .....	183
5.3.8.	Different diffusivity correlation models.....	206
5.4.	Simulation of a true-sized droplet drying within a spray dryer.....	210
5.4.1.	Problem formulation .....	210
5.4.2.	Results and discussions .....	211
5.5.	Important simulation aspects to achieve solution convergence and optimise efficiency ....	217
5.5.1.	Mesh structure.....	217
5.5.2.	Element Peclet and Reynolds numbers.....	218
5.5.3.	Variables scaling.....	220
5.5.4.	Time step of the solver .....	221
5.5.5.	'Smooth function' for numerical stability .....	221
5.6.	Conclusions .....	223

## **Chapter 6 Numerical probing of boiling droplet ..... 224**

6.1.	Discussion on the numerical stability and the time-stepping scheme for a bubble-droplet system .....	225
------	--	-----

6.2.	Drying droplet with a centred-bubble at boiling point in a 2D axis-symmetrical coordinate .....	228
6.2.1.	Governing equations .....	228
6.2.2.	Problem formulation .....	230
6.2.3.	Results and discussions .....	234
6.3.	Drying droplet with an offset-bubble at boiling point in a 2D axis-symmetrical coordinate .....	243
6.4.	Conclusions .....	251
<b>Chapter 7</b>	<b>Conclusions and future plan .....</b>	<b>252</b>
7.1.	Conclusions and considerations to improve the current model .....	253
7.2.	Suggestions for a more advanced simulation system and alternative methodology .....	256
<b>Appendix A</b>	<b>Drag coefficient, Newton-Raphson method and bubble-droplet system..</b>	<b>279</b>
A.1.	Iteration procedure for determining the drag coefficient of a flow past a cylinder .....	280
A.2.	Newton-Raphson method for solving the moving interface equations (transcendental equations) in Chapter 4 .....	280
A.3.	Bubble growth within a confined liquid with mass fluxes at the bubble-droplet and the droplet-air interfaces.....	282
<b>Appendix B</b>	<b>1D model for a boiling droplet using the solute-fixed coordinate.....</b>	<b>285</b>
B.1.	Matlab code for a 1D boiling droplet .....	286

## List of Tables

<b>Table 2-1.</b> Comparison between CDC and REA approaches (Fyhr and Kemp, 2007). .....	<b>20</b>
<b>Table 2-2.</b> Comparison between Ranz & Marshall and Kulmala heat and mass transfer correlations. ....	<b>49</b>
<b>Table 3-1.</b> Validation for computed $Cd$ against referential simulation values in the literature. ....	<b>95</b>
<b>Table 3-2.</b> Physical properties used in the simulation of the flow past a cylinder system. ....	<b>100</b>
<b>Table 3-3.</b> Comparison of the terminal falling velocity of a circular cylinder ( <b>300 <math>\mu\text{m}</math></b> in radius) with and without AMR .....	<b>102</b>
<b>Table 3-4.</b> Verification of terminal velocity against experimental correlation in the literature. ....	<b>103</b>
<b>Table 3-5.</b> Average drag and lift on the cylinder obtained from the simulation of the flow past a cylinder. ....	<b>103</b>
<b>Table 3-6.</b> The time step for the highest and lowest drag coefficients on both cylinders during the simulation. ....	<b>112</b>
<b>Table 4-1.</b> Physical properties of gas and liquid phases in the simulation. All the variables are evaluated at the temperature of the associated phase. ....	<b>133</b>
<b>Table 5-1.</b> Four experimental drying conditions for sucrose droplet with an initial moisture content of 60% (1.5 kg/kg) and 50% (1 kg/kg). The condition is adapted from Patel <i>et al.</i> (2008). ....	<b>158</b>
<b>Table 5-2.</b> Coefficient for water and sucrose activities in sucrose solution in equation (5-8). ....	<b>161</b>
<b>Table 5-3.</b> Physical properties of sucrose solution evaluated at the drying condition of the simulation. ....	<b>162</b>
<b>Table 5-4.</b> Coefficients for equation (5-26) including the water activity range at which the diffusion coefficients are valid. ....	<b>167</b>
<b>Table 5-5.</b> Sucrose solution physical properties used in the simulation of the 2D droplet drying model. ....	<b>182</b>

## List of Figures

<b>Figure 1-1.</b>	The evaporative flux plot (yellow line in the top plot) and the moisture (blue line in the bottom plot) and temperature (red line in the bottom plot) profile of the droplet at different drying stages. The droplet morphological evolution is represented at the bottom of the figure.....	<b>6</b>
<b>Figure 1-2.</b>	Temperature profile of a boiling droplet (Handscomb, Kraft and Bayly, 2009). The droplet morphology for each drying stage is provided. ....	<b>8</b>
<b>Figure 1-3.</b>	Overview of thesis goal. The background on the spray dryer and the morphological evolution route are presented together with the objectives of the research.....	<b>11</b>
<b>Figure 2-1.</b>	Buckle shape (left) and 'Puff' shape (right) particles at $T = 181^{\circ}\text{C}$ (Rogers <i>et al.</i> , 2012) .....	<b>19</b>
<b>Figure 2-2.</b>	Apparatus set-up of modified glass filament method (Xu, Lin and Chen, 2002). The droplet is hanging on the glass filament within a glass filament box (number 3), with the air is heated by the heaters (number 9).....	<b>25</b>
<b>Figure 2-3.</b>	(a)Contact levitation: Glass filament technique; (b) Non-contact: Acoustic wave technique (Sadek <i>et al.</i> , 2015) .....	<b>26</b>
<b>Figure 2-4.</b>	(left) Experimental configuration for electrodynamic balance (EDB); (right) Expandable view of EDB equipment setup. The schematic is taken from Davies <i>et al.</i> (2012).....	<b>27</b>
<b>Figure 2-5.</b>	Schematic of the mono-dispersed generator.....	<b>28</b>
<b>Figure 2-6.</b>	Droplet (circular domain) holds on a hydrophobic surface (grey squares) (Sadek <i>et al.</i> , 2015).....	<b>29</b>
<b>Figure 2-7.</b>	Different types of dried-particle morphologies (Nandiyanto and Okuyama, 2011a). The SEM images of each structure are presented with a representative sketch.....	<b>30</b>

- Figure 2-8.** SEM images of hollow (left) and spherical dense (right) particles. The length scales are **20  $\mu\text{m}$**  and **10  $\mu\text{m}$**  for the left and right images, respectively..... **31**
- Figure 2-9.** SEM images of multicomponents dried-particles (Akhavan Mahdavi *et al.*, 2016) (Nandiyanto and Okuyama, 2011b). The length scale is **10  $\mu\text{m}$** . Images of encapsulated particles (top and bottom left) and well-mixed particles (right) are illustrated..... **32**
- Figure 2-10.** SEM image of hairy dried-particles. (Van Hooijdonk *et al.*, 2013) ..... **33**
- Figure 2-11.** SEM image of porous dried-particles (Singh *et al.*, 2012)..... **33**
- Figure 2-12.** Drying mechanism of milk particle based on changing moisture and temperature (Kim, Chen and Pearce, 2009) ..... **34**
- Figure 2-13.** Increasing initial PEO polymer concentration affecting the final dried-particle (from left to right) (Sugiyama *et al.*, 2006)..... **39**
- Figure 2-14.** Final particle morphologies from different drying conditions. (a) High evaporation rate and highly porous shell; (b) High evaporation rate and very high volatiles solute (Rajagopalan, 2014)..... **42**
- Figure 2-15.** Experimental setup for Ranz and Marshall's heat and mass transfer correlations..... **47**
- Figure 2-16.** Kulmala's experimental setup with components number at the bottom. The droplet is produced through the microsyringe (number 9) and its temperature is measured by the thermocouple (number 8). The air is heated by the heater (number 6)..... **48**
- Figure 2-17.** Illustration of particle breakage using SEM images (Alamilla-Beltrán *et al.*, 2005) ..... **53**
- Figure 3-1.** Graphical representation of 'Strong form' (left) and 'Weak form' (right). The domain is divided into 5 modes (red points) and 4 elements. The heat flux gradient in the 'Strong form' is forced to be zero on all nodes, while the averaged heat flux gradient in the 'Weak form' is forced to zero. .... **61**

<b>Figure 3-2.</b> Heat flux gradient variation in the vicinity of the centre node .....	<b>62</b>
<b>Figure 3-3.</b> Linear weight function illustration.....	<b>63</b>
<b>Figure 3-4.</b> Graphical illustration of the inner product between the main function and the weight function at <i>node</i> = 3.....	<b>64</b>
<b>Figure 3-5.</b> Approximation of general function $f(x)$ using all 5 nodes. An approximation solution (dotted red line) is compared with an exact solution (blue line). The approximation solution converges to the exact solution as the number of nodes increase.....	<b>65</b>
<b>Figure 3-6.</b> Graphical plot of the piece-wise quadratic basis function. Different colours represent different basis functions for different nodes.....	<b>67</b>
<b>Figure 3-7.</b> Eulerian perspective of a ball rolling down the hill under gravity. The gravity always points downwards in the y-direction as the ball rolls down the slope. ....	<b>71</b>
<b>Figure 3-8.</b> Lagrangian perspective of a ball rolling down the hill under gravity. The ball velocity is pointing up the hill in the Lagrangian frame. The gravity changes its direction during the rolling instead of being fixed in the Eulerian frame. ....	<b>72</b>
<b>Figure 3-9.</b> Mesh distortion problem associated with the Lagrangian view. Movement direction of the nodes (red points) on an object (green domain) is showed on the left side, and the resultant mesh is on the right. The mesh does deform together with an object in the Lagrangian description of motion. ....	<b>73</b>
<b>Figure 3-10.</b> Loss of interface resolution problem associated with Eulerian view. The direction for every node (red points) on the object (green domain) is shown on the left, and the results movement is on the right. The mesh does not deform in Eulerian description of motion.....	<b>74</b>

- Figure 3-11.** Mesh structure and interface resolution in ALE mesh. Direction of mesh distortion is shown on the left and the resultant mesh is on the right. An object is represented as the green domain with the according nodes (red points). The mesh partly deforms with an object in the ALE algorithm. .... **76**
- Figure 3-12.** Domains and mapping function involved in the ALE method. All three domains and coordinates are accessible and mathematically convertible..... **76**
- Figure 3-13.** Convective velocity representation. At  $t = 0$ , both the mesh node and the object are in the same position. As time progresses, the mesh node moves due to the displacement of the object, but not at the same rate. This gives rise to the convective velocity variable. .... **78**
- Figure 3-14.** Illustration of fluid flow passing through a solid sphere .... **82**
- Figure 3-15.** Constraints for PID algorithms ..... **85**
- Figure 3-16.** Schematic of simulation setup for testing the PID algorithm. The domain includes the inlet (left), the outlet (right), two side walls not 'slip' condition and the cylinder with 'no-slip' condition at the interface. The air is introduced at the inlet and exits the domain through the outlet. The gravity is in horizontal direction. The domain length and height are 20000  $\mu\text{m}$  and 10000  $\mu\text{m}$ . ..... **86**
- Figure 3-17.** Terminal velocity of different cylinder sizes free falling air. The Reynolds number is provided for each terminal velocity value. The cylinder size ranges from **20  $\mu\text{m}$**  (grey line) to **300  $\mu\text{m}$**  (black line). The time interval is 20 ms..... **89**
- Figure 3-18.** Velocity contour of the wake in the flow past the cylinder (black circle) at different radii. The white number in each domain represents the radius of the cylinder in such domain, the velocity scale is colour-coded and the air flow is from right to left boundaries. .... **90**
- Figure 3-19.** Schematic setup for simulation of flow past the fixed cylinder. The solid domain (blue) is 600  $\mu\text{m}$  in diameter and the inlet velocity is set at 4.92 m/s..... **92**

- Figure 3-20.** Mesh details for the flow past a fixed cylinder of **300  $\mu\text{m}$**  in radius. The domain is divided into regions for better meshing. The mesh is denser around the cylinder and coarse at far-field..... **94**
- Figure 3-21.** 2D contour plot with velocity streamlines (black line) and vector field (black arrows). The vortex shedding is observed. The cylinder is represented by the white circle..... **94**
- Figure 3-22.** Simulation schematic for a falling cylinder of **300  $\mu\text{m}$**  in radius. A similar simulation setup to the case of the fixed cylinder (section 3.4.1.1), however, gravity is turned on in this case. .... **96**
- Figure 3-23.** Experimental data for the drag coefficient on a circular cylinder (Anderson Jr, 2010). The Reynolds number range covers from 0.1 to  $10^5$ . .... **98**
- Figure 3-24.** Comparison of drag coefficients on cross-flow circular cylinder between experimental data and empirical formulas from Wieselberg (1922), Cliff *et al.* (1978) and Munson *et al.* (1990). .... **100**
- Figure 3-25.** Example of meshing details during simulation of (a) non-adaptive mesh refinement and (b) Adaptive mesh refinement technique. The domain is divided into 6 small parts for a better meshing process. The refined mesh is concentrated around the cylinder and the wake area where the fluid flow happens. .... **101**
- Figure 3-26.** Velocity profile of a falling cylinder (**300  $\mu\text{m}$**  in radius) simulated with non-AMR (blue line) and AMR (red line) meshing technique. The studied time interval is 20 ms. .... **102**
- Figure 3-27.** Drag and lift profiles on the cylinder. The drag is plotted in the solid line and the lift in the dotted line. The period is **20 ms**. .... **104**
- Figure 3-28.** Vector field (red arrows) and streamlines (blue lines) plot of velocity around the cylinder (black circle). The angle of flow separation is at  $115^\circ$ . The air flows from left to right in the domain. .... **104**

- Figure 3-29.** The velocity in the wake region of the flow past the cylinder. The time interval ranges from 1 ms to 19 ms. The velocity vector field (black arrows) and streamlines (black line) are plotted together with the colour-coded plot of the velocity magnitude. .... **105**
- Figure 3-30.** Pressure field around the cylinder over time. The magnitude of pressure and the streamlines are colour-coded. The time interval is from 1ms to 19 ms ... **106**
- Figure 3-31.** Mesh configuration for fixed and falling cylinders. The domain is divided into 6 sections for a better meshing process. The mesh area near the flow inlet is coarse and the fine mesh is kept around the cylinder and along the wake where the complicated flow profiles appear..... **107**
- Figure 3-32.** The inlet velocity profile transitioning from controlled velocity to fixed velocity. The PID loop is applied to the inlet velocity at  $t < 20 \text{ ms}$  and a fixed inlet velocity of  $5.35 \text{ m/s}$  is applied at  $t > 20 \text{ ms}$ . .... **108**
- Figure 3-33.** Drag coefficients on a free-falling cylinder and fixed cylinder at two different velocity profiles at the inlet..... **109**
- Figure 3-34.** Lift coefficients on the free-falling cylinder and fixed cylinder at two different velocity profiles at the inlet..... **109**
- Figure 3-35.** Comparison between the local viscous stress and pressure along the upper half of the cylinder surface... **111**
- Figure 3-36.** 2D pressure plots and velocity streamlines (white lines) for the falling and fixed cylinders (white circles). The cylinder surface is shown in the yellow line and the angle of separation is provided for each plot..... **113**
- Figure 3-37.** Boundary conditions for flow past a fixed sphere simulation. The air flow is introduced by the inlet (lower boundary) and exit at the outlet (upper boundary). The wall (right boundary) is to slip condition. The channel is  $2000 \text{ }\mu\text{m}$  in height and  $500 \text{ }\mu\text{m}$  in width..... **115**

**Figure 3-38.** Mesh configurations during the simulation. The mesh refinement was adjusted based on the adaptive mesh refinement to have the optimal mesh. The initial mesh size was uniform everywhere in the domain. The mesh along the flow in the wake of the sphere is much more refined than the area in front of the sphere. .... 117

**Figure 3-39.** Mesh configurations during the simulation in the Nusselt number validation. The system starts with extremely fine mesh. The adaptive mesh refinement (AMR) algorithm relaxes the mesh in front of the sphere and keeps the refinement in the wake where the flow happens..... 118

**Figure 3-40.** Steady-state concentration (left) and velocity (right) fields around the sphere in the Sherwood number validation case. The concentration and velocity scales are provided in the colour-coded option. The axis of symmetry is plotted as a blue line. .... 119

**Figure 3-41.** Steady-state temperature (left) and velocity (right) fields around the sphere in the Nusselt number validation case. The temperature and velocity scales are provided in the colour-coded option. The axis of symmetry is plotted as a blue line. .... 120

**Figure 3-42.** Schematic setup of a droplet freefalling in air. The PID algorithm is adopted to ensure the droplet falls with terminal velocity. The air enters the channel from the inlet (lower boundary) and exits at the outlet (upper boundary). The wall is slip and the axis of symmetry is at  $r=0$  (red line)..... 122

**Figure 3-43.** Terminal velocity predicted by simulation versus analytical solution..... 124

**Figure 3-44.** Internal and external flow field near the droplet's interface. The velocity field is provided both internally and externally of the droplet. The vector arrow is colour-coded within the droplet and black in the air domain..... 125

- Figure 3-45.** 2D low field when the droplet viscosity is increased  $10^6$  folds. Colour-coded vector arrows are plotted within the droplet interior. The velocity scale is provided. The droplet surface is hidden for better visualisation of the vector field..... **126**
- Figure 3-46.** Drag on a solid sphere and liquid sphere of the same size. The drag force is averaged over the surface of the circular domain..... **127**
- Figure 4-1.** Domain and boundary conditions for Stefan's problem. The liquid temperature is maintained at  $100^\circ\text{C}$ , and the Air is heated up to  $150^\circ\text{C}$ . The interface is moving towards the water domain as phase change happens..... **132**
- Figure 4-2.** Mesh configuration for Stefan's problem – mapped structure. Quadrilateral mesh is chosen for this simulation. The square domain with the side of 0.1 m is used..... **132**
- Figure 4-3.** Initial temperature distribution within the Air (left) and Water (right) domains at  $t = 0\text{ s}$ . The moving interface is represented (middle line) and the temperature scale is provided in degree Celcius The water domain temperature is kept constant at  $100^\circ\text{C}$  and the left wall in the air domain is at  $150^\circ\text{C}$ ..... **134**
- Figure 4-4.** Interface position,  $x$  (m), along with the domain different numerical grid sizes. Three different grid size was provided. The difference between the simulation and analytical solution is small, which is visualised in the zoom-in plot..... **135**
- Figure 4-5.** Zoom-in section in Figure 4-4 for the mesh independence test. The grid size of 2.5 mm is different from the other 2 grid sizes. .... **136**
- Figure 4-6.** Temperature profile within the air and liquid domains. The temperature is plotted along the horizontal line, which starts from the wall in the air domain ( $T=150^\circ\text{C}$ ) towards the liquid domain ( $T=100^\circ\text{C}$ ). .... **136**
- Figure 4-7.** Mesh plot within the air and liquid domains. The mesh is deformed as the interface moves towards the liquid domain. The phase is colour-coded for the air (in blue) and the water (in red) domains. .... **137**

- Figure 4-8.** Mesh configuration for the pressure-driven bubble case (inertia-effect). The quadrilateral mesh is used for both domains, and the number of nodes on the droplet and bubble surfaces is 30 nodes. The number of nodes increases as the mesh is refined in the mesh independence test..... **139**
- Figure 4-9.** Mesh element and velocity field within the bubble during expansion at  $t = 30 \text{ ms}$  and  $t = 250 \text{ ms}$ . The arrow vector is plotted for the velocity field within the bubble, and is colour-coded for the magnitude of the velocity. .... **140**
- Figure 4-10.** Bubble radius against time at different grid sizes. The bubble oscillation profile is verified against the analytical solution from Rayleigh (1917). The mesh is refined at 3 different levels: Coarse (1792 elements, 30 surface nodes), Extra refine (5152 elements, 50 surface nodes) and Extreme refine (8980 elements, 70 surface nodes). .... **141**
- Figure 4-11.** Representation of the full geometry setup (in grey) and a computational domain (in blue). The blue domain is a portion of the whole domain with an angle of  $10^\circ$ . The simulation will be performed in the blue segment with symmetry boundary conditions to save computational resources..... **144**
- Figure 4-12.** Schematic of phase change across the two phases interface. The  $\Phi_g$  and  $\Phi_l$  are the gas and liquid phases.  $\Delta H_{lg}$  is the latent heat of evaporation. .... **144**
- Figure 4-13.** Bubble growth due to thermal effect (evaporation) over time at different grid sizes. The computed result is verified against the analytical solution from Scriven (1959). Four mesh configurations with two mesh structures are set up in the simulation. The grid size for swept mesh is extra coarse (3815 elements) and coarse (14350 elements). The grid size for tetrahedral mesh is fine (138768 elements) and extra fine (3971025 elements)..... **145**

- Figure 4-14.** Two types of possible mesh types for the symmetry 3D coordinates. In the free tetrahedral mesh (left), all the faces of the domain are meshed with tetrahedral mesh. In the swept mesh (right), the front side mesh is tetrahedral and being swept towards the backside, hence the mesh on the side faces is rectangular..... **146**
- Figure 4-15.** Temperature distribution at  $t = 0 \text{ s}$ . The bubble domain (blue) is maintained at  $100^\circ\text{C}$ , and the liquid domain (red) is at  $150^\circ\text{C}$ . The bubble radius is  $5 \mu\text{m}$  and the liquid domain is infinite. .... **147**
- Figure 4-16.** Thermal boundary layer thickness plot at the bubble surface. The temperature is plotted across the bubble interface for the visualisation of the thermal boundary layer. The layer thickness is  $\Delta d \approx 0.12 \mu\text{m}$ . .... **148**
- Figure 4-17.** Mesh plot of the gas (in red) and liquid (in blue) domains at  $t = 0 \text{ ns}$  and  $t = 20 \text{ ns}$ . The colour-coded phase is plotted for the bubble (red) and the liquid (blue) domains..... **148**
- Figure 4-18.** Flow vector field with colour-coded around the bubble ..... **149**
- Figure 5-1.** Gravity-controlled PID algorithm. The controlled variable is gravity (dotted black line) that is adjusted based on the droplet displacement (red line on the secondary axis). The total time interval is  $250 \text{ ms}$ . The PID loop reached equilibrium value after around  $190 \text{ ms}$ ..... **154**
- Figure 5-2.** (Left) 2D surface plot of velocity field and (Right) internal vector flow field with droplet with colour-coded ..... **155**
- Figure 5-3.** Flow field within the droplet during the PID control. The vortices size remains the same with the primary vortex occupying most of the droplet volume. .... **156**
- Figure 5-4.** Schematic setup of a 1D drying model. The droplet is presented by the blue dot and the interface is at the dotted blue line. The diameter of the droplet used in this study will be at  $2145 \mu\text{m}$  and  $2179 \mu\text{m}$ , with the air temperature at  $63^\circ\text{C}$  and  $95^\circ\text{C}$ , respectively. The external heat and mass transfer are estimated by dimensionless numbers..... **158**

- Figure 5-5.** Comparison of water activities correlations. The x-axis is the moisture content from **0** to **1**. The line of water activity equals **1** is plotted. The water activity is from **0** to **1**. The temperature dependence and fitting Margules correlation exceed 1 at low moisture content due to the lack of experimental data. .... **165**
- Figure 5-6.** Temperature-dependant water activity (Starzak and Peacock, 1997) against the solution moisture content. The temperature range is from 295K to 500K. The water activity exceeds 1 as the moisture content gets below 0.01. .... **166**
- Figure 5-7.** Comparison of different diffusivities models in log scale. The two internal developed correlations (green and blue lines) were obtained from the research group at the University of Leeds. The Price et al 2016 diffusivities are calculated from the water activities ( $a_w$ ) in equation (5-21) (yellow line) and in equation (5-23) (red line). .... **168**
- Figure 5-8.** Droplet temperature and weight loss over time at  $T_{air} = 950C$  and initial moisture content of **1.5 kg/kg – db**. .... **170**
- Figure 5-9.** Droplet temperature and weight loss over time at  $T_{air} = 950C$  and initial moisture content of **1 kg/kg – db**. .... **170**
- Figure 5-10.** Droplet temperature and weight loss over time at  $T_{air} = 630C$  and initial moisture content of **1.5 kg/kg – db**. .... **171**
- Figure 5-11.** Droplet temperature and weight loss over time at  $T_{air} = 630C$  and initial moisture content of **1 kg/kg – db**. .... **171**
- Figure 5-12.** Water activity at the droplet surface at different drying conditions (sucrose droplet with 60% and 50% initial moisture content). The drying time is 1000 s. The air temperature is 95°C and 63°C. .... **173**

- Figure 5-13.** The moisture concentration distribution along the droplet radius over time in the Eulerian coordinate. Ten nodes (black points) are plotted from the core to the droplet surface to keep track of the shrinking. The time period is 1000 s and with the time step of 50 s. The increase in time is indicated by the red arrow. .... 174
- Figure 5-14.** Schematic setup for falling sucrose droplet in 2D axis-symmetric system. The channel is **500  $\mu\text{m}$**  in width and **2000  $\mu\text{m}$**  in height. The inlet air is introduced at the bottom boundary at **1 m/s** and exit through the outlet at the upper boundary. The air temperature is at **95°C/63°C**. .... 177
- Figure 5-15.** Droplet mass profile of a **2179  $\mu\text{m}$  – 1.5 kg/kg – db** droplet. The computed results are compared against the 1D drying model developed in section 5.2. The drying interval is **1000 s** and the air temperature is at 95°C. 2D model was repeated with two mesh configurations for a mesh independence test. .... 184
- Figure 5-16.** The temperature profile of a **2145  $\mu\text{m}$  – 1 kg/kg – db** droplet against the Patel *et al.* (2008) data. The 'normal mesh' configuration (3392 elements) was used as the mesh independence is reached in Figure 5-15. Drying time is **1000 s** and the air temperature is at 95°C. .... 184
- Figure 5-17.** Comparison of the averaged mass transfer coefficient in the 1D and 2D drying model. The mass transfer coefficient is computed from the Sherwood number in the 1D model, and from the averaged flux along the droplet surface in the 2D model. The air temperature is at 95°C and the droplet initial moisture content is 1.5 kg/kg-db. .... 186
- Figure 5-18.** Droplet surface velocity magnitude at  **$t = 0.5\text{s}, 20\text{s}, 100\text{s}, 500\text{s}$**  and **1000s**. The plotting angle starts from the front of the droplet (0°) towards the back of the droplet (180°). .... 187
- Figure 5-19.** Three reference radii for calculating droplet sphericity. .... 188

- Figure 5-20.** Droplet sphericity plots. The definition of the three radii  $r_1, r_2$  and  $r_3$  can be found in Figure 5-19. The ratio between the three radii represents the shrinking rate at three different points on the droplet surface. The sphericity of the droplet will be based on how close the three ratios are to 1..... **188**
- Figure 5-21.** Temperature profile of a **2179  $\mu\text{m}$  – 1.5  $\text{kg}/\text{kg}$  – db** sucrose droplet in 1D (dotted green line) and 2D models (blue and dotted red lines). The 2D model was repeated with 2 mesh configurations for the mesh independence test. The subplot is the zoom-in of the wet-bulb section of the droplet temperature. The air temperature is set at  $95^\circ\text{C}$ . ..... **190**
- Figure 5-22.** Temperature profile of a **2145  $\mu\text{m}$  – 1  $\text{kg}/\text{kg}$  – db** sucrose droplet in 1D (dotted green line) and 2D models (black line). One mesh configuration was used as the mesh independence is reached in Figure 5-21. The subplot is the zoom-in of the wet-bulb section of the droplet temperature. The air temperature is set at  $95^\circ\text{C}$ . ..... **191**
- Figure 5-23.** Water activity on the droplet interface at  **$95^\circ\text{C}$  – 1.5 $\text{kg}/\text{kg}$  – db**. The water activity is plotted at three different locations along the droplet surface: bottom (blue), middle (red) and top (green) points. The averaged water activity is plotted in black line. .... **192**
- Figure 5-24.** Water activity on the droplet interface at  **$95^\circ\text{C}$  – 1 $\text{kg}/\text{kg}$  – db**. The water activity is plotted at three different locations along the droplet surface: bottom (blue), middle (red) and top (green) points. The averaged water activity is plotted in black line ..... **193**
- Figure 5-25.** Surface temperature difference to the maximum temperature along the droplet surface  **$T_{\text{max}} – T_{\text{surface}}$** . The time interval is from  $t = 0.5 \text{ s}$  to  $1000 \text{ s}$ . The temperature is plotted against the phase angle, from the droplet front ( $0^\circ$ ) to the back ( $180^\circ$ ) ..... **194**

- Figure 5-26.** Local flux along with the droplet interface versus time. The plotted timesteps are from  $t = 0.5 \text{ s}$  to  $t = 1000 \text{ s}$ . The flux is plot based on the angle to the droplet centre starting from the front of the droplet. Plots for all timesteps are colour-coded in the legend. .... 195
- Figure 5-27.** Moisture content along with the interface versus time. The time interval is from  $t = 0.5 \text{ s}$  to  $1000 \text{ s}$ . The moisture is plotted against the phase angle of the droplet, starting from the front ( $0^\circ$ ) to the back side ( $180^\circ$ ). The schematic for the phase angle can be found in Figure 5-26. .... 196
- Figure 5-28.** Illustration of plot types for visualisation of the droplet internal flow field. The streamlines and vector arrows are plotted for the velocity field, and colour-coded with the magnitude of the liquid viscosity. The stress on the surface is shown in the Line plot (red means high and black means low stress). .... 198
- Figure 5-29.** Droplet internal flow field with stress plot at the surface. The internal velocity field is plotted using streamlines and vector arrows, the surface stress is plotted using a line plot. The flow field is plotted from  $t = 0.5 \text{ s}$  to  $1000 \text{ s}$ . .... 199
- Figure 5-30.** Internal velocity field comparison between the pure water droplet to the drying sucrose droplet ..... 202
- Figure 5-31.** Moisture content of the sucrose droplet during drying. The air temperature is at  $95^\circ\text{C}$  and the initial moisture content is  $1.5 \text{ kg/kg}$ . The surface plot of the water concentration is colour-coded and the streamline of the velocity field is plotted in white lines. The drying time is  $1000 \text{ s}$ . .... 204
- Figure 5-32.** Temperature distribution within the sucrose droplet during drying. The droplet and air temperature are at  $25^\circ\text{C}$  and  $95^\circ\text{C}$ , and the initial moisture content is  $1.5 \text{ kg/kg}$ . The colour-coded temperature scale for the first  $5 \text{ s}$  (upper 3 plots) is provided separately for better visualisation of the temperature field in the early drying stage. The temperature scale for the lower 3 plots is also provided The drying time is  $1000 \text{ s}$ . .... 205

- Figure 5-33.** Comparison plot between two diffusion coefficients. **Dws\_1:** Price *et al.* (2016) diffusivities **Dws\_2:** internally-developed diffusivities Max and Min points: diffusion coefficients ( $m^2/s$ ) ..... **208**
- Figure 5-34.** Mass profile of a **2179  $\mu m$  – 1.5 kg/kg – db** droplet with different diffusivity models. The air temperature is set at 95°C and the drying time is 1000 s. The mass of the droplet from using the Price *et al.* (2016) diffusivity is compared with the results in section 5.3.2. .... **209**
- Figure 5-35.** Mass profile of a **2179  $\mu m$  – 1.5 kg/kg – db** droplet with different diffusivity models. The air temperature is set 95°C and the drying time is 1000 s. The droplet temperature from using the Price *et al.* (2016) diffusivity is compared with the results in section 5.3.2. . **209**
- Figure 5-36.** Schematic of a falling 50  $\mu m$  droplet at 25°C, 1.5 kg/kg initial moisture content. The air temperature is at 95°C and the relative humidity is 2.5%. The terminal falling velocity of the droplet is controlled by the PID algorithm developed in Chapter 3. The domain is 450  $\mu m$  in width and 1000  $\mu m$  in height. ‘Slip’ condition at the side wall..... **211**
- Figure 5-37.** Droplet temperature (in black) and mass (in red) against time. The drying time is around 5s. The computed temperature is taken at the centre of the droplet and the moisture content is averaged over the droplet domain ..... **212**
- Figure 5-38.** Surface plot of sucrose content within a 50  $\mu m$  droplet falling in air with initial temperature and moisture content to be 25.33°C and 1.5 kg/kg. The air temperature is 95°C. The sucrose content plot is colour-coded and the streamline (black lines) is plotted for the velocity field within the droplet. .... **214**
- Figure 5-39.** Velocity profile within 50  $\mu m$  droplet falling in air with initial temperature and moisture content to be 25.33°C and 1.5 kg/kg. The air temperature is 95°C. The velocity plot is colour-coded The maximum velocity is **1.2e – 4m/s**..... **215**

- Figure 5-40.** Temperature distribution within a 50  $\mu\text{m}$  droplet falling in air with initial temperature and moisture content to be 25.33°C and 1.5 kg/kg. The air temperature is 95°C. The temperature surface plot is colour-coded and the streamline (black lines) is plotted for the velocity field within the droplet..... **215**
- Figure 5-41.** Terminal falling velocity (black line) and averaged surface velocity (blue line) of a 50  $\mu\text{m}$  droplet falling in air with initial temperature and moisture content of 25.33°C and 1.5 kg/kg. The air temperature is at 95°C. The droplet falling velocity is controlled by the PID algorithm developed in Chapter 3..... **216**
- Figure 5-42.** Different mesh structure with/without boundary layers ..... **218**
- Figure 5-43.** Plot of the 'Smooth' function used to decrease the high gradient changes across the interface in the simulation initially. All the initially variables are ramped up smoothly using this function in a period of **150 ms**, instead of setting the initial value at  **$t = 0 \text{ ms}$** ..... **222**
- Figure 6-1.** CFL condition visualisation. The cases of comparison are  **$CFL < 1$**  and  **$CFL > 1$**  ..... **226**
- Figure 6-2.** Number of nodes required at the interface to have a good representation of the surface curvature..... **227**
- Figure 6-3.** Schematic setup of the bubble-droplet system. The droplet and the bubble are **50  $\mu\text{m}$**  and **5  $\mu\text{m}$**  in radius, respectively. The droplet initial temperature and moisture content are 25°C and 1.5 kg/kg-db, respectively. The bubble contains air only at the boiling point ( **$t = 70 \text{ ms}$** )..... **232**
- Figure 6-4.** Droplet temperature and weight profiles over time in stage 1. No bubble is included, and the droplet dries until its averaged temperature reaches the air temperature. The 'boiling point' (blue dot) is marked at  **$t = 70 \text{ ms}$** , from which the bubble domain is added to continue the droplet drying in stage 2. At boiling point (70 ms), the droplet temperature is at 104°C and its averaged moisture content is at 0.48. The bubble will take these values as an initial condition in the stage 2 study. .... **235**

- Figure 6-5.** The initial condition of stage 2 (boiling). The average droplet temperature is at 104°C and the moisture content is at 0.48 (refer to Figure 6-4). ..... **236**
- Figure 6-6.** Mesh plot of the bubble-droplet system over time. The phase is colour-coded (blue for gas phase and red for liquid phase). ..... **236**
- Figure 6-7.** Concentration and temperature 2D plot in stage 2 (boiling). The concentration profile (upper plot) and the temperature profile (lower plot) are plotted at  $t = 70\text{ ms}, 110\text{ ms}$  and  $150\text{ ms}$ . The scale for the surface are provided for concentration and temperature surface plots. .... **237**
- Figure 6-8.** Droplet temperature (red line) and moisture content (black line) in stage 2 (boiling) of the drying. The stage 2 study starts at  $t = 0.07\text{ s}$  (from the dotted blue line). The simulation stops at  $t = 173\text{ ms}$ . ..... **238**
- Figure 6-9.** The averaged heat (red line) and mass transfer (black line) coefficients at the droplet interface in Stage 2. The bubble domain is added at  $t = 70\text{ ms}$ . The heat and mass transfer coefficients for Stage 1 (no bubble) were included (dotted red and black lines) to see the effect of the bubble on the droplet drying. .... **240**
- Figure 6-10.** Droplet (black line) and bubble (blue line) radii over time in Stage 2 (boiling) study. The droplet radius is plotted for the whole drying period and the bubble radius is plotted from  $t = 70\text{ ms}$ . ..... **242**
- Figure 6-11.** Schematic of the offset-bubble at the boiling point of the drying droplet. The bubble centre is  $0.25\text{ }\mu\text{m}$  vertically above the droplet centre at the boiling point ( $t = 70\text{ ms}, T \approx 104\text{ }^\circ\text{C}$ ). The droplet initial radius and moisture content are  $50\text{ }\mu\text{m}$  and 1.5 kg/kg-db. The initial bubble radius is  $5\text{ }\mu\text{m}$ . ..... **244**
- Figure 6-12.** Droplet averaged temperature and moisture content in the offset-bubble case. The time interval is 112 ms. The offset-bubble starts to grow at the boiling point (blue circle). The droplet temperature and moisture content from the centred-bubble case are also plotted (dotted green lines). ..... **245**

- Figure 6-13.** Averaged heat and mass transfer coefficients at the droplet surface in the offset-bubble case. The two stages are divided at  $t = 70 \text{ ms}$  (boiling point). The heat and mass transfer coefficients in the centred-bubble case are plotted in the dotted green lines. The heat and mass transfer coefficients profile without the presence of the bubble are plotted (faded colour lines) ..... **246**
- Figure 6-14.** The droplet and bubble radius over time of the offset-bubble case. The droplet radius is plotted for the whole time interval (112 ms) and the bubble radius is plotted from  $t = 70 \text{ ms}$ . The droplet and centred-bubble radius profiles are in dotted green lines..... **247**
- Figure 6-15.** The temperature variation along the droplet and the bubble surfaces. The angle (measured in degree) starts from the bottom point ( $0^\circ$ ) and ends at the top of the surface ( $180^\circ$ ). The temperature of the droplet surface (colour lines) and the bubble surface (dotted lines) are plotted at the same time step. .... **248**
- Figure 6-16.** Temperature surface plot of the droplet and bubble domains. The bubble surface is represented by the half-white circle. The droplet and bubble temperatures at the boiling point are  $104^\circ\text{C}$  and  $100^\circ\text{C}$  respectively..... **249**
- Figure 6-17.** Pressure variation plot along the droplet surface for the timesteps at  $t = 75 \text{ ms}, 90 \text{ ms}$  and  $100 \text{ ms}$ . The pressure is plotted against the angle (as represented above the plot) starting from the bottom to the top of the droplet surface. The offset-bubble (solid colour lines) and the centred-bubble (dotted colour lines) cases are compared..... **250**

# Nomenclature

---

$\bar{X}$	Moisture content	
$X_e$	Equilibrium moisture	
$X_{cr}$	Critical moisture	
$\psi$	Surface relative humidity	
$E_A$	Activation energy	$J/mol$
$T_s$	Surface temperature	$K, ^\circ C$
$q$	Heat flux	$W/m^2$
$T$	Temperature	$K, ^\circ C$
$x$	x-coordinate	$\mu m, m$
$w_i(x)$	Weight function	
$c_i$	Coefficients	
$\phi_i$	Trial function	
$\mathbf{x}$	Referential domain	
$\mathbf{X}$	Material domain	
$x$	Spatial domain	
$v(t)$	Material velocity	$m/s$

$\mathbf{w}(t)$	Mesh velocity	$m/s$
$\mathbf{c}(t)$	Convective velocity	$m/s$
$\sigma_{total}$	Total stress	$Pa$
$\rho$	Density	$kg/m^3$
$\mathbf{U}$	Velocity field	$m/s$
$p$	Pressure	$Pa$
$\mu$	Dynamic viscosity	$Pa * s$
$\mathbf{F}$	Volume force	$N$
$u_{ctrl}$	Control velocity	$m/s$
$k_p$	Proportional gain	$s^{-1}$
$k_I$	Integral gain	
$k_d$	Derivative gain	
$x_{set}$	Setpoint for PID system	$\mu m, m$
$u_{terminal}$	Terminal falling velocity	$m/s$
$v_{terminal}$		
$C_d$	Drag coefficient	
$\rho_s$	Solid density	$kg/m^3$
$\rho_l$	Liquid density	$kg/m^3$

$L$	Lift coefficient	
$F_D$	Drag force	$N$
$F_L$	Lift force	$N$
$A_{projected}$	Projected area	$m^2$
$g$	Gravitational constant	$m/s^2$
$n$	Normal vector	
$F_{stress}$	Total stress	$Pa$
$\mathbf{u}_i$	Fluid velocity on $i^{th}$ side	$m/s$
$\tau_i$	Stress tensor of $i^{th}$ domain	$Pa$
$C_p$	Specific heat capacity	$J/K$
$q$	Conduction heat flux	$W/m^2$
$q_r$	Radiation heat flux	$W/m^2$
$\alpha_p$	Coefficient of thermal expansion	
$f_{st}$	Force per unit area	$Pa$
$M_f$	Mass flux across the interface	$\frac{kg}{m^2 * s}$

$k_g$	Thermal conductivity of gas	$W$
$C_{pg}$	Heat capacity of gas	$\frac{W}{m * K}$
$\alpha_g$	Thermal diffusivity of the gas phase	$m^2/s$
$\gamma$	Growth constant	
$h_{lg}, H_{evap}$	Latent heat of evaporation	$J/kg$
$T_{sat}$	Saturation temperature	$K, ^\circ C$
$T_w$	Wall temperature	$K, ^\circ C$
$t$	Time	$s$
$\sigma$	Surface tension	$N/m$
$c_{ig}$	Concentration of $i^{th}$ species in the gas phase	$\frac{mol}{m^3}$
$c_{il}$	Concentration of $i^{th}$ species in the liquid phase	$\frac{mol}{m^3}$
$u_g$	Velocity field in the gas phase	$m/s$
$u_l$	Velocity field in a droplet	$m/s$

$D_{va}$	Diffusion of vapour in the air	$m^2/s$
$D_{ws}$	Relative diffusivity of water to sucrose	$m^2/s$
$\omega_i$	Mass fraction of $i^{th}$ species in the concentrated solution	
$\mathbf{j}_i$	Mass flux of $i^{th}$ species relative to the mass-average velocity	$kg/m^2$
$\mathbf{u}$	Mass-averaged velocity of the mixture	
$a_w$	Water activity	
$m_{evap}$	Evaporation mass flux	$kg/m^2$
$P_{sat}$	Saturation pressure	$Pa$
$c_{sat}$	Saturation concentration	$\frac{mol}{m^3}$
R	Gas constant	$\frac{J}{mol.K}$
$q_{b-d interface}$	Heat flux at the bubble-droplet interface	$W/m^2$

---

---

**Subscripts**

---

wa	water phase
sat	saturation
ws	water-sucrose
va	vapour-air
ctrl	PID control
D	drag
L	lift
ig	of $i^{th}$ species in gas phase
il	of $i^{th}$ species in liquid phase
evap	evaporation
w	wall

---

**Dimensionless numbers**

---

Nu	Nusselt number
Re	Reynolds number
Pr	Prandtl number
Sh	Sherwood number
Sc	Schmidt number
Pe	Peclet number

---

## Abbreviations

ALE	Arbitrary Lagrangian-Eulerian
AMR	Adaptive Mesh Refinement
CDD	Characteristic Drying Curve
CFD	Computational Fluid Dynamics
CFL	Courant-Friedrichs-Lewyor
CNN	Convolutional Neural Network
CNT	Carbon Nanotube
DMC	Dimethyl-Carbonate
FEM	Finite Element Method
ODE	Ordinary Differential Equation
PDE	Partial Differential Equation
PEO	Poly(Ethylene Oxide)
PID	Proportional-Integral-Derivative
REA	Reaction Engineering Approach
SDD	Single Droplet Drying
SEM	Scanning Electron Microscopy
THD	Tetrahydrofuran
VOAG	Vibrating Orifice Aerosol Generator

# Chapter 1

**Thesis introduction and motivation**

## **1.1. Background of 'Spray Drying'**

### **1.1.1. History**

Drying is a critical unit operation in the manufacturing process of solid materials in which the moisture is removed from a liquid medium by means of heat. The drying of a wide variety of feedstock is required in the industry due to the inconvenience of packaging products with a high moisture content which can be easily segregated during transportation. Within the drying industry, spray drying is a well-known single-step process for the production of particulate products from solutions, suspensions or emulsions taking advantage of hot drying gas. The spray drying mechanism employs the removal of moisture from billions of droplets which are produced from the liquid feedstock by the atomiser before coming into contact with the hot gas stream. The low product temperature and a short droplet-gas contact time allow excellent handling of heat-sensitive products. Moreover, spray drying is a fully automated, fast and continuous process, thus it is convenient to redesign to any desirable scale. It has found broad applications in the chemical, food, ceramics or pharmaceutical industries. The first spray dryer is believed to have been constructed around the 1860s in the United States (Chequer *et al.*, 2013) (Mujumdar, 1995). Spray drying gradually became a favourable method in the food industry, and milk powder is still produced using this method nowadays. Due to the high demand for light and compact food products during wars in the early 20<sup>th</sup> century, spray drying became popular and proved to be a versatile process for the production of clean and fine powder (Mujumdar and Hall, 2006). The spray dryer offers extensive advantages such as a flexible design depending on various process requirements, the ability to handle any required capacity and effective control of the end product's morphology.

### **1.1.2. Motivation for modelling of single droplet drying at boiling point**

The demand for flexible product fabrication is increasing in the drying industry. A scientific understanding of the spray drying process is critical in manufacturing a product that meets the industry requirements. Therefore, detailed insights and research into the drying mechanism within the spray dryer are required in order to have better control over the process. The research can be done via both modelling and experimental methods. The modelling approach is less desirable for a large-scale spray dryer as it involves numerous factors, which cannot be simplified in the model and could affect the drying outcomes. Hence, the experimental approach is more suitable to study the large-scale spray dryer. On the industrial-scale spray dryer, the challenges are the high operation cost and replication of experimental runs. The small-scale spray dryers, such as the pilot or laboratory scale, are less time-consuming, more energy-efficient, and flexible to repeat series of tests (Woo, Mujumdar and Daud, 2010) (Kieviet *et al.*, 1997). However, the physical similarity to other scales, the powder properties, and the drying model accuracy is compromised (Zbicinski, 2017) (Raffin *et al.*, 2006) (Poozesh and Bilgili, 2019), hence causing discrepancies in product quality across different scales. For example, a better powder flowability was reported for a large scale spray dryer compared to the lab-scale (Al-Khattawi *et al.*, 2018) (Langrish, 2009). In terms of the modelling approach, the non-monodisperse nozzle used in the spray dryer produces a wide distribution of droplet sizes, ranging from a few hundreds of microns to a few millimetres. Meanwhile, the drying model is usually developed based on a narrow droplet size range, hence it will not be accurate, practical, or representative for the real drying within all types of spray dryers (Thybo *et al.*, 2008) (Langrish and Fletcher, 2003).

*Single droplet drying (SDD)* is a method in which an isolated droplet is brought into contact with a hot air stream. The droplet can be isolated by a number of methods: intrusively by suspending it from a thin filament or non-intrusively by levitation using an external field (Maevski, Levy and Borde, 2010). Although the droplet does not experience droplet-droplet interactions, droplet-particle collision or droplet-wall collision as in the spray dryer, the SDD can monitor the droplet drying kinetics and its morphological evolution under a controlled drying environment. As a result, it can provide valuable information into the convective drying of droplets within the spray dryer (Boel *et al.*, 2020). However, the size of the droplet is limited to what can be re-created under laboratory conditions. In practice, droplets that hang on a filament are limited to a minimum diameter of 1 mm, a few orders of magnitude greater than the actual size of droplets exiting an atomiser within a spray dryer.

It is motivating to have a robust numerical model that can provide deeper knowledge of the drying mechanism of the droplet, such as the local moisture distribution or temperature profile that is inaccessible by the current SDD technique. In fact, the modelling approach is capable of investigating the drying of micron-sized droplets, which is not possible using the SDD approach. Researchers in the past decades have devoted extensive efforts to develop numerous models for a variety of drying conditions. Many approaches were conducted from the empirical or semi-empirical models. Previously developed models were able to capture the global drying information in a radially symmetric coordinate, such as the average droplet temperature or the total mass profile, without providing much detail on the final morphology of the dried-particle (Woo *et al.*, 2008). In recent years, researchers have considered modelling the formation of the solid layer at the droplet surface in attempting to predict the final morphology outcomes. Most of the work has, however, focused on the temperature range

below the boiling point of the droplet solution, whilst experimental data has shown completely different dynamics leading to different morphological route for a droplet drying above the boiling point (Grosshans *et al.*, 2016). Many experiments were carried out to study the effect of the vapor bubble on the drying droplet (Frost, 1988) (Kuznetsov, Piskunov and Strizhak, 2016). Although progress has been made in terms of understanding the bubble evolution within a solvent (Gopireddy and Gutheil, 2013), there is still a lack of a model that completely couples and resolves the fluid flow, heat transfer, and phase change dynamics at the bubble surface (Xi *et al.*, 2017). The reported behaviours in the literature include droplet inflation, surface cracking, or reduction in crust thickness (Boel *et al.*, 2020). The physics of the bubble is complicated especially when coupled with drying phenomena at the droplet surface. Therefore, this thesis focuses on developing a numerical model for droplet drying beyond *the boiling point*. The research aims to improve the accuracy and validity of the currently available drying models, gain further insight into the droplet interior that is limited, and extend the numerical framework to capture the boiling effect on the final dried-particle morphology.

## **1.2. Theory of ‘Drying’**

### **1.2.1. Droplet drying**

The drying of a droplet is fundamentally based on the heat and mass exchange at the interface. The droplet is heated up due to the *heat flux* gained from the hot air stream, and once it exceeds the energy barrier, evaporation happens in which the vapor mass flux from the droplet’s surface is released into the air. The balance between the two fluxes governs the whole drying process which can be visualised in Figure 1-1,

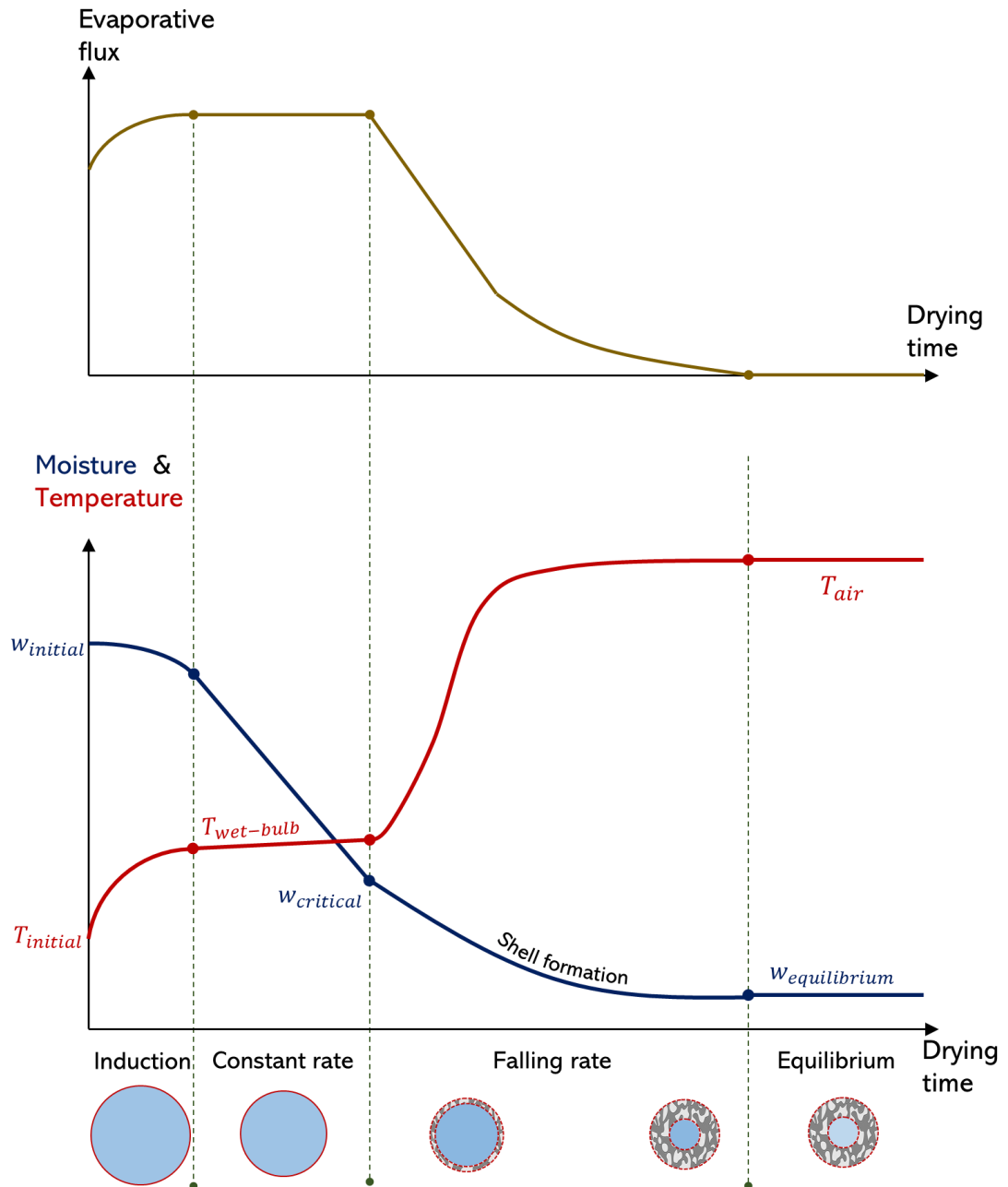


**Figure 1-1.** The evaporative flux plot (yellow line in the top plot) and the moisture (blue line in the bottom plot) and temperature (red line in the bottom plot) profile of the droplet at different drying stages. The droplet morphological evolution is represented at the bottom of the figure.

Initially, the droplet gains heat from the hot air flow, and the temperature increases, which is represented by the 'induction' period (Figure 1-1). A portion of the heat received is used to change the liquid into the gas phase, according to the enthalpy of

vaporisation. The evaporation rate gradually increases and levels out at the saturated state, in which the droplet moisture content is above the 'critical moisture content' and the amount of vapour generated is maximum. The 'critical moisture content' is defined as the transition from the constant rate to the falling rate period. The droplet is in the '*constant rate*' period, where the heat transfer to the droplet and the heat loss by evaporation is equal, causing droplet temperature to remain approximately constant. Meanwhile, the solute accumulates towards the surface, due to the diffusion and convection effects, that creates resistance to the heat and mass transfer. The shell formed reduces the vapour pressure at the surface. The mechanical characteristics and the porosity of the shell depending on the type of solutes and the drying conditions. As drying progresses, the amount of water supplied to the surface is insufficient to maintain the saturation condition due to internal resistance, and the droplet enters the '*falling rate*' period. The vapour flux lessens over time as the solute concentration increases at the surface. The droplet temperature increases with a steeper gradient closing the gap with the air temperature. Subsequently, the vapour flux smoothly drops to zero as the droplet enters the 'equilibrium' stage. The droplet has now reached the air temperature with zero evaporating flux. The described stages are typical for drying below the boiling point (Amador and Juan, 2016).

### **1.2.2. Droplet boiling**

As the droplet temperature exceeds the boiling point, the internal pressure within the droplet is higher than that of the surrounding air (Chinè and Monno, 2011) (Vachaparambil and Einarsrud, 2020). At this point, the dissolved air pocket in the solution, which is caused by the spraying process from the atomiser, increases in size and forms a vapor-air bubble at the droplet core or moisture-rich region. The bubble growth is driven by either the fluid dynamics or the thermodynamic process (Taqieddin, Allshouse and Alshawabkeh,

2018). The vapor bubble is expected to affect the internal moisture content and temperature profiles (Legros, 2015). The heat flux from the air is now used for the generation of vapor both into the air and the bubble interior (Pandey and Basu, 2019) (Nešić and Vodnik, 1991). The temperature profile is illustrated in Figure 1-2.

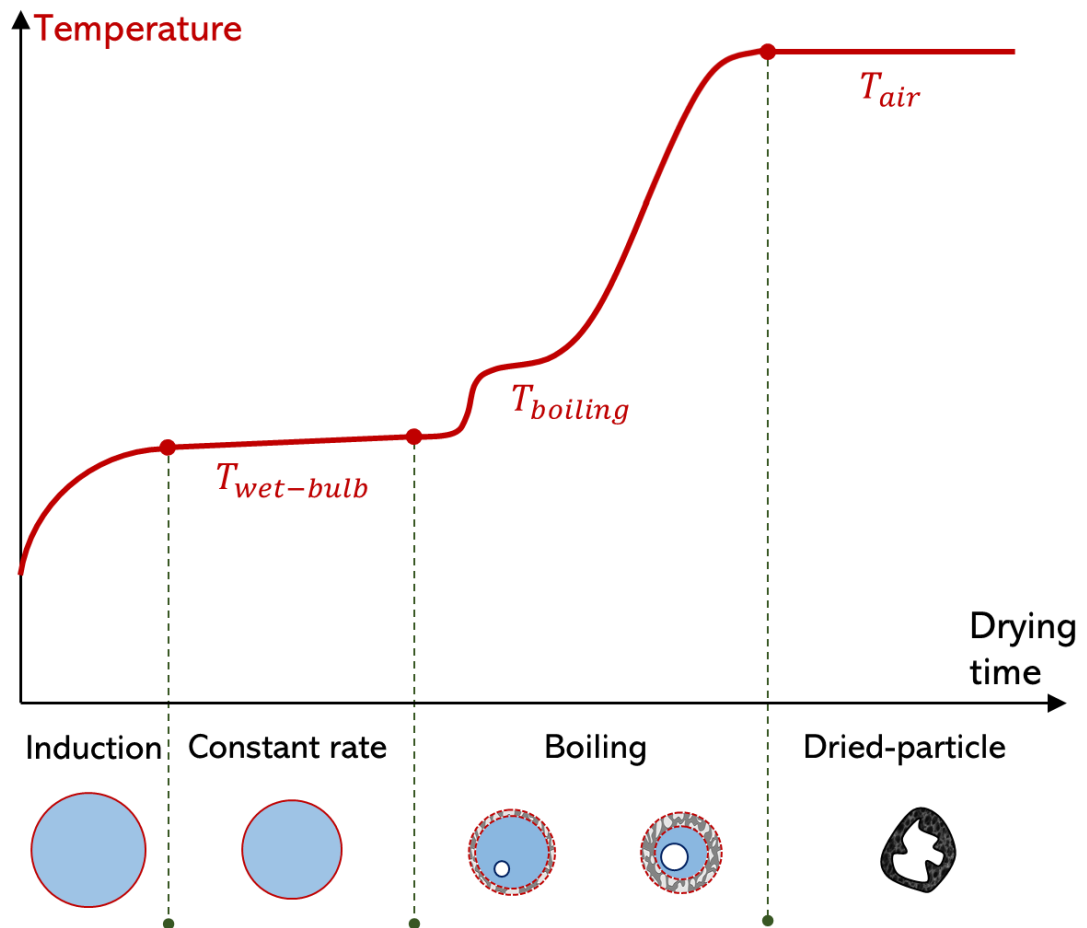


**Figure 1-2.** Temperature profile of a boiling droplet (Handscomb, Kraft and Bayly, 2009). The droplet morphology for each drying stage is provided.

### 1.3. Particle morphological evolution

Different particle morphologies were observed in drying a droplet that contains solid (Charlesworth and Marshall, 1960). The particle morphology outcome is influenced by various factors such as the drying conditions and the droplet initial moisture content. In a

multicomponent solution, the shell is formed at the droplet's surface during drying due to an increase in solute concentration at the interface. The shell structure and its mechanical properties depend on the type of solution being dried, the air temperature and the drying rate (Bayly, 2015). The nature of the shell or the skin formed determines the droplet inflation and deflation cycles during drying (Tran *et al.*, 2017) (Adhikari *et al.*, 2009). The physics of the skin rupture is critically dependant on its mechanical strength. There are generally two morphological outcomes in the skin forming system: dense or hollow particles. Dense particles result from a core shrinkage which can probably shatter if dried at high temperature (Alharbi, 2019). Hollow particles, on the other hand, do not shrink much during drying and tend to inflate due to bubble nucleation (Mezhericher, Levy and Borde, 2008) if the temperature exceeds the boiling point (Jeffreys and Mumford, 1986).

#### **1.4. Research gap and aims**

Current models and studies focus on the drying range below boiling, in which the main interests are to capture the relevant kinetic information (Schutyser, Perdana and Boom, 2012) (Fyhr and Kemp, 2007). Challenges remain for complex dynamic systems such as boiling phenomena within the droplet. The bubble 'growth and collapse' cycles disturb both the global and local drying rate, as well as the outcomes of the particle morphologies. Numerical probing of the drying at a high-temperature range is particularly scarce, and a well-developed knowledge of the bubble dynamics is not available in the literature (Epstein and Plesset, 1951) (Robinson and Judd, 2004). The limitation is also rooted in the availability of computational tools to accurately resolve a highly non-linear set of partial differential equations, and a mathematical method to track the very fast-moving bubble interface. Hence, this thesis focuses on developing a mathematical model that provides a detailed prediction

of different particle morphology routes beyond the boiling point. The 2D asymmetrical model will be implemented to capture real physics within the droplet during drying.

In summary, the solute concentration accumulates at the droplet surface, as drying progresses, to form a viscous layer that can be treated as a solid shell. The deformation of this layer, which is mainly driven by the bubble growth behaviour within a droplet, is critical to the dried-particle shape. According to the literature, as the vapour builds up within the droplet, the expansion of the dissolved air bubble can cause a crack in the shell (Grosshans *et al.*, 2016). This leads to convective vapor releases into the environment and the hole is healed and sealed when the pressure within the bubble equals the external air pressure. The cycles repeat until the crust is thick and strong enough to withstand the bubble growth (Pandey and Basu, 2019) (Roesle and Kulacki, 2010). The material properties of the shell determine the physical process followed during the bubble growth, for example, a sugary droplet will form a viscous layer (Gopireddy and Gutheil, 2013) instead of a solid shell, as is found during the drying of a colloid droplet. This will lead to droplet inflation or surface wrinkle instead of cracking which results in different particle morphologies (Adhikari *et al.*, 2009). There are two challenging aspects of integrating the bubble domain into the droplet: the conditions and the boundary conditions (how the bubble grows) at boiling. Thermodynamically, the condition for the bubble nucleation varies in different solutions, as different molecules accommodate different nucleation sites depending on their size and molecular shapes (Lubetkin, 2003). The aim is to couple all of the discussed physics into one model to predict and understand the morphological evolution of the droplet. An overview on the research question and approach is illustrated in Figure 1-3,

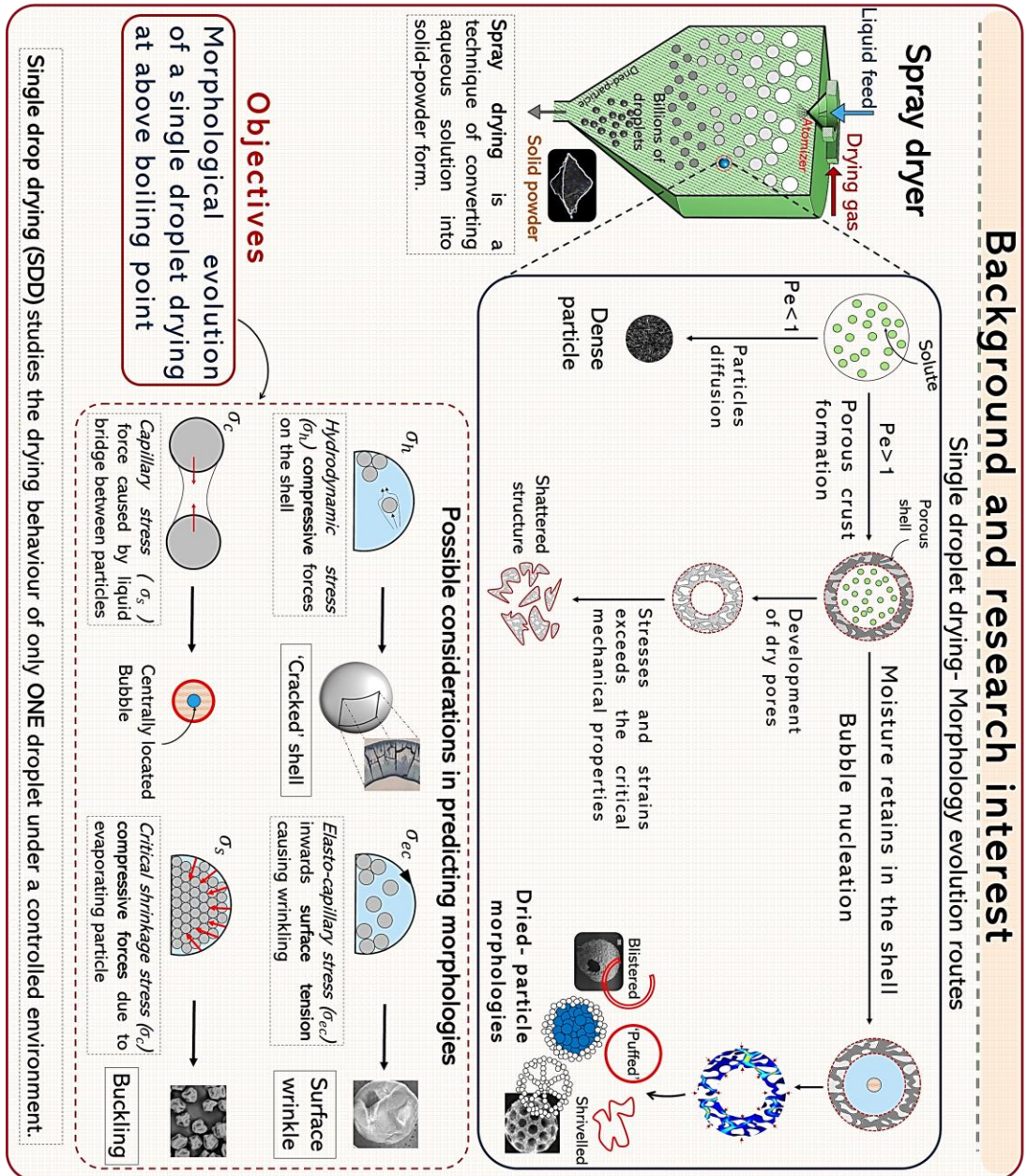


**Figure 1-3.** Overview of thesis goal. The background on the spray dryer and the morphological evolution route are presented together with the objectives of the research.

## 1.5. Thesis's structure

Following the introduction to the research interest in *Chapter 1*, the overall picture of the thesis is outlined in the following:

*Chapter 2* presents a detailed literature review on a single droplet drying. This section addresses different approaches for droplet drying modelling, model validation, the limitation of the current correlations used for estimating the heat and mass transfer coefficients, the influence of the drying condition on the final dried-particle morphologies, and finally the types of solution available for spray drying.

*Chapter 3* focuses on the principal theory behind the numerical method (FEM) in the thesis. The simulation is built for the case of a falling sphere, which is analogous to the droplet drying system. The verification and validation of this system are performed and compared against the benchmarks. The governing equations, boundary conditions implemented in the simulation, are justified to start building up the droplet drying model.

*Chapter 4* analyses the moving interface due to phase change phenomena (Stefan problem), and the bubble behaviour within a confined layer of liquid. An analytical solution of the transcendental equation from the Stefan problem is solved using the Newton-Raphson method, and compared against the simulation result. The governing equation for the bubble growth due to pressure is also derived from first principles. The computed results are validated against the analytical solution of the bubble growth, and the method of integrating the bubble into the drying droplet model is discussed.

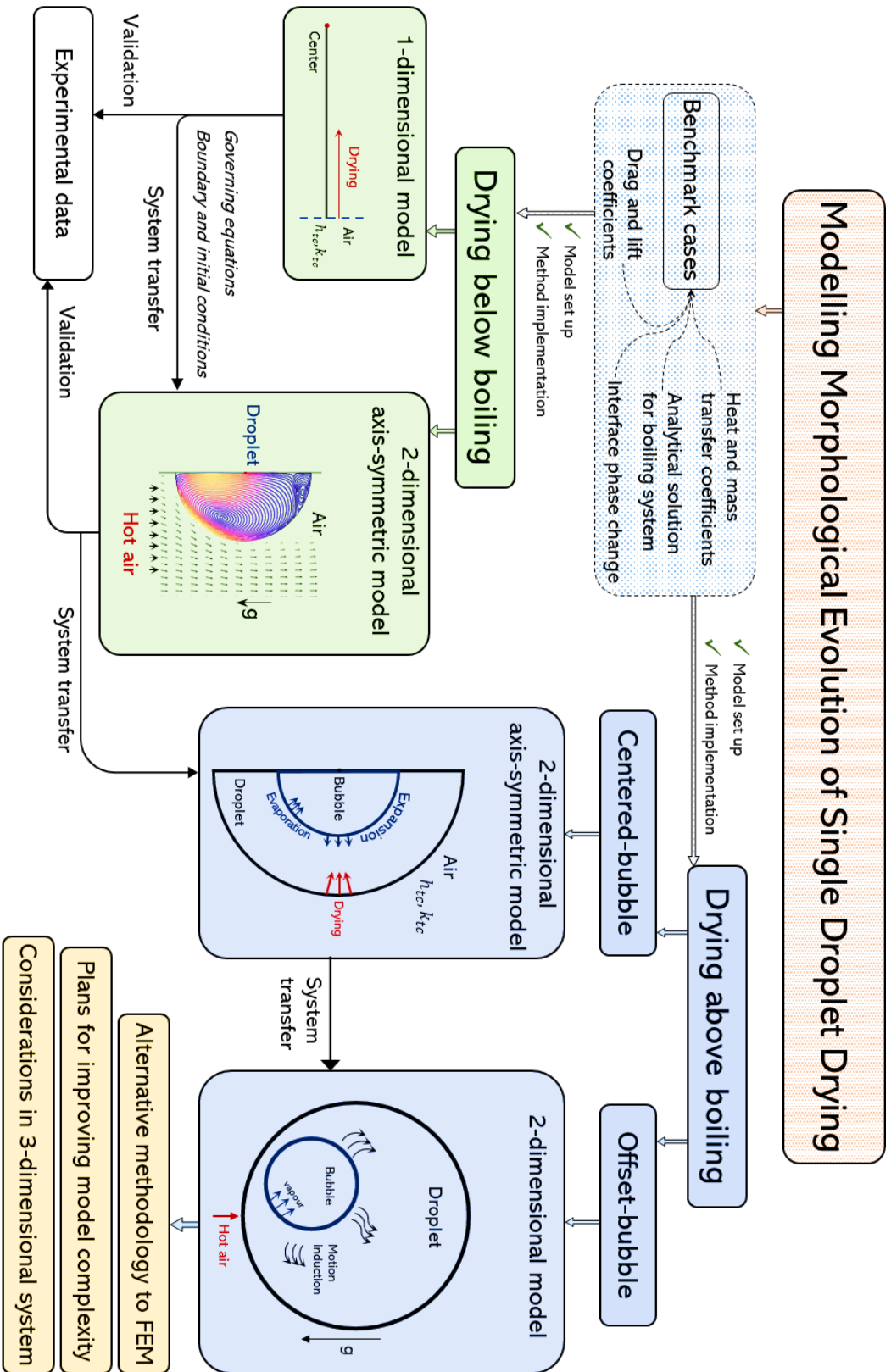
*Chapter 5* reports the drying model developed in 1-dimensional, 2-dimensional, and 2-dimensional axis-symmetrical coordinates. The drying model is developed upon adapting the simulation scheme setup in Chapter 3. The computational results are compared against

the experimental data from the literature (Patel *et al.*, 2008). Detailed insights into the internal drying of the droplet are achievable thanks to the high-resolution drying model. The asymmetrical distribution of temperature, moisture content and the formation of the vortices are presented. In addition to the above, the sensitivity analysis of different diffusion coefficients and droplet sizes is carried out.

*Chapter 6* demonstrates the main challenge of the thesis: the integration of the growing bubble into the drying droplet. Different positions of the bubble at the boiling point are considered in different simulation scenarios. The accuracy and practicality of each case are reviewed. The influence of the bubble dynamics on the droplet drying rate, heat and mass transfer coefficients, and the sensitivity of the bubble kinetics to its initial condition at the boiling point are examined.

*Chapter 7* sums up and concludes the thesis's key findings. The provisional plan for advancing into a more complicated simulation scheme is provided. An alternative approach of using the convolutional neural network (CNN) instead of the finite element method (FEM) in the computational fluid dynamics (CFD) problems is recommended. The benefit of coupling the CNN to the FEM method is discussed.

### 1.6. Thesis's plan sketch



# Chapter 2

## **Progress and innovations in the literature and the drying industry**

This chapter provides an overview of the drying industry, particularly in the single droplet drying area. Key aspects of a single droplet drying model are reviewed in detail, in order to justify its applicability to a more advanced drying model. Analogous systems to droplet drying at high temperatures is also reported.

## **2.1. Literature review**

### **2.1.1. Introduction**

Spray drying is a widely used industrial operation in numerous manufacturing sectors such as biochemical, pharmaceutical, dairy and food products. The product specifications, which depend mainly on particle morphologies, vary across sectors hence demanding different operating conditions and processing strategies. Methods for quick and effective prediction of particle morphologies are required to replace the time-consuming and high-cost experimental approaches. Currently, spray dryer models are based on simplified assumptions of single droplet drying, where a system of billion drops is reduced down to one. This resulted in a convenient Single Droplet Drying (SDD) method that can provide valuable information in terms of mass, moisture and temperature profiles through the spray drying process. There have been many attempts to study different types of droplet solution, such as colloidal, multicomponent or polymeric, with different modelling approaches. This literature review will summarise all the main modelling approaches, emphasise important results, define critical problems and recommended improvements for future work.

### **2.1.2. Models on Single Droplet Drying (SDD)**

#### **2.1.2.1. Characteristic drying curve (CDC)**

The characteristic drying curve (CDC) is a semi-empirical and fast-computational approach with a set of simplified equations. The drying rate is divided into two stages: i) constant rate and ii) falling rate. The first stage is treated as unhindered evaporation of a pure liquid droplet. The vapour boundary layer is the main resistance to mass transfer,

$$\hat{N}_v = k_c(C_{v,s} - C_{v,b}) \quad (2-1)$$

Where  $k_c$  is the mass transfer coefficient,  $C_{v,s}$  and  $C_{v,b}$  are the vapour concentrations at the surface and bulk gas respectively. The unhindered mass transfer rate equation can be derived by the integration from Fick's Law and it can also be expressed in terms of humidity. The mass transport of the falling rate period is related to the constant rate period through moisture function,

$$N_v = f(\phi) \times \hat{N}_v \quad (2-2)$$

Where  $N_v$  is the mass flux in the falling rate period,  $\hat{N}_v$  is the mass flux of constant rate period and  $f(\phi)$  is the function of characteristic moisture content defined by,

$$\phi = \frac{\bar{X} - X_e}{X_{cr} - X_e} \quad (2-3)$$

Where  $\bar{X}$  is the moisture content,  $X_e$  is the equilibrium moisture and  $X_{cr}$  is the critical moisture at which the particle's surface is no longer saturated. The function,  $f(\phi)$ , is unique for each material and independent of gas temperature. Consequently, the drying of the same material at different conditions should be only a mathematical transformation of its unique drying curve. There are also disadvantages associated with this approach. The critical moisture content is always taken as a constant whereas it may vary according to different operating conditions, initial droplet moisture and size. The model is not capable of providing reliable results when performing at different conditions of the same experiment. The characteristic drying curve (CDC) is however still preferable and applicable, since it is fast and simple yet capturing essential information of the drying process.

#### **2.1.2.2. Reaction engineering approach (REA)**

The reaction engineering approach (REA) introduces an energy barrier that moisture needs to overcome for evaporation to happen. This approach works well for small particles or a thin layer of liquid. Similarly to the CDC model, the characteristic material property is

the relationship between activation energy and moisture content. The drying rate can then be expressed as,

$$\frac{dm}{dt} = -h_m A (\rho_{v,s} - \rho_{v,b}) \quad (2-4)$$

Where  $\rho_{v,s}$  and  $\rho_{v,b}$  are vapour concentration at the surface and bulk respectively.  $A$  is droplet surface area and  $h_m$  is the external mass transfer coefficient. The surface vapour concentration is proportional to the saturated vapour concentration,  $\rho_{v,sat}$ , by a factor,  $\psi$ ,

$$\rho_{v,s} = \psi \times \rho_{v,sat}(T_s) \quad (2-5)$$

Where  $\psi$  is the surface relative humidity and  $\rho_{v,sat}$  is a function of surface temperature,  $T_s$ . The activation energy,  $E_A$ , is,

$$E_A = \exp\left(-\frac{\Delta E_v}{RT_d}\right) \quad (2-6)$$

Where  $\Delta E_v$  is apparent activation energy which accounted for the difficulties of evaporation at low temperatures due to adhesion. The activation energy can be obtained experimentally for each type of material. REA approach utilises an empirical correlation between partial vapour concentration and surface temperature. There is no need to define the critical moisture content,  $X_{cr}$ , since this approach suggested a smooth change from constant rate to falling rate period. An agglomeration and wall deposition of particles is determined empirically since the model does not calculate surface concentration. REA is a highly useful method for predicting drying behaviour at different operating conditions.

### **Modelling attempts:**

Rogers *et al.* (2012) studied a single droplet drying using REA and monodisperse technique. The work suggested there should be an increasing number of 'puffed' particles with increasing air temperature. According to the result, nearly half of the particles are puffed at 181°C and the rest is buckled in shape, as shown in

Figure 2-1. The size of the buckled particle depends on how fast the skin formed and shell permeability.

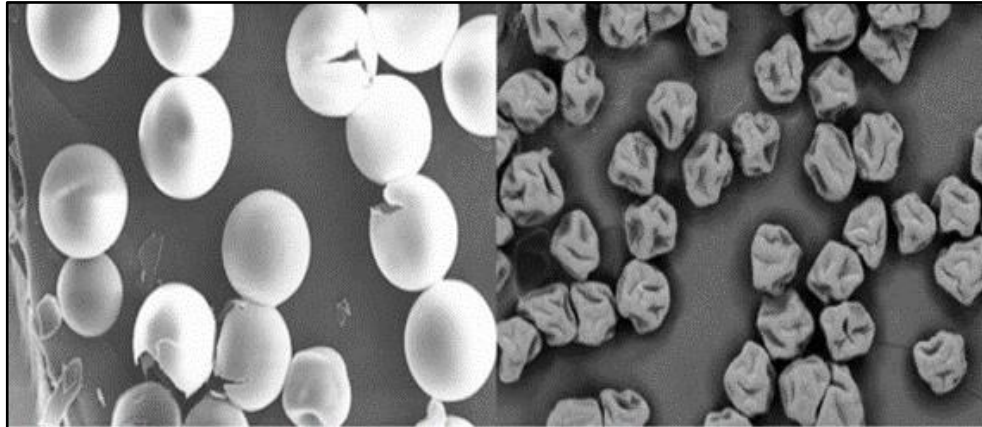


**Figure 2-1.** Buckle shape (left) and 'Puff' shape (right) particles at  $T = 181^{\circ}\text{C}$  (Rogers *et al.*, 2012).

Haque *et al.* (2016) developed a model targeting the drying behaviour of multi-solutes droplets. A droplet containing protein and sugar is hung on a tip of a glass filament and dried at a low-temperature range ( $65^{\circ}\text{C}$  and  $80^{\circ}\text{C}$ ). An extended version, which is the composite-REA model, took into account the effect of multiple solutes. As mentioned before, a huge advantage of REA is the minimum number of experiment attempts needed to generate model parameters, which is economical and time-saving. A set of normal reaction engineering equations were constructed to describe the moisture and temperature time-dependent profiles. A composite approach was then implemented. A system's activation energy,  $E_A$ , is expressed through the sums of the product of each solute's activation energy and mass fraction. The model provided accurate results for moisture content and temperature change against experimental data. The similarities and differences between the two approaches are represented in Table 2-1.

	CDC (Fyhr and Kemp, 2007)	REA
Similarities	<ul style="list-style-type: none"> <li>• Utilise empirical correlations.</li> <li>• Perform well for small particles.</li> <li>• Droplet surface area is needed.</li> <li>• Characteristic properties of each material are required.</li> <li>• Can be used in CFD modelling.</li> </ul>	
Differences	<ul style="list-style-type: none"> <li>• Require information on web-bulb temperature and critical moisture content</li> <li>• No smooth transition from constant rate to falling rate period.</li> <li>• Drying behaviour of material is defined by the function of characteristic moisture content, <math>f(\phi)</math>.</li> </ul>	<ul style="list-style-type: none"> <li>• Model the difficulties in evaporation through the energy barrier.</li> <li>• Natural transition from free water to bound water stage.</li> <li>• External mass transfer coefficient and surface temperature are needed.</li> <li>• Apparent activation energy is the characteristic properties of materials.</li> </ul>

**Table 2-1.** Comparison between CDC and REA approaches (Fyhr and Kemp, 2007).

### 2.1.2.3. Diffusion models

The diffusion drying model utilises the diffusion phenomenon of species aiming to describe the physics of droplet drying. Together with the diffusion being accounted for in the model, particles containing suspended or dissolved solid will form a skin after a constant rate period and the drying rate will depend on the internal

moisture diffusing to the surface. Specifically for a droplet containing sugary substances, the solid crust can reach a glass-transition point and exhibits viscoelastic behaviour. The crust will then shrink and recede until a constant radius (Tsapis *et al.*, 2005).

#### 2.1.2.3.1. Dry shell-Solid porous crust

This type of diffusion model proposes that solute forms hard skin during evaporation. The droplet radius remains constant after shell formation until complete drying. The moisture diffuses through the interface between the wet core and porous crust. All the solute will be diffused towards the skin increasing its thickness.

#### **Modelling attempts:**

Dalmaz (2007) developed a model that considered both heat and mass transfer during the drying process together with skin formation. The governing equations for mass and heat transfer were formulated considering the receding interface of the droplet. Ranz & Marshall (1952) heat and mass transfer correlations were used for calculating convective heat and mass transfer coefficient. Colloidal silica droplets and skimmed milk droplets were tested for model validation. The mathematical model agreed with the measured experimental data.

#### 2.1.2.3.2. Wet shell- Expandable crust

The wet-shell is considered a pliable and pressure-responsive structure. The solvent vaporisation within the wet core will happen if the moisture temperature reaches the boiling point. This may lead to expanding droplets or 'puffing' behaviour (Handscomb *et al.*, 2009). A single centrally located bubble is formed through two factors: low internal pressure or high droplet temperature. The low internal pressure is created by the capillary force withdrawing water towards the porous crust, which encourages bubble formation. This explains the hollow shape of the final particle. If the ambient

temperature is high, the bubble can be nucleated homogeneously and the droplet can be inflated and shriveled. The wet shell model is more complicated than the dry shell model, and many of the observed morphologies can be related using the wet shell model.

### **Modelling attempts:**

Werner *et al.* (2008) disagreed with the assumption of constant crust radius throughout the drying process, or the so-called receding interface model. The author argued that the contraction only stops when there is a balance between the collapsing pressure caused by moisture loss and the mechanical stress on the skin layer. Experimental evidence showed that even when a solvent saturation concentration is exceeded, the solution is still viscous and flowable. Werner *et al.* (2008) specifically used the model to describe the 'collapsed shell' and 'dense skin-porous crumb' shapes. The effective diffusion model is used for early shrinkage until the crust starting to form and grows toward the centre at the critical temperature. Then the receding interface model is applied at the second stage, where the droplet outer radius is fixed. The change of coordinates from solid-fixed to spatial is utilised in order to give the solution for 'collapsed shell' and 'dense skin-porous crumb' morphologies. The collapsed shell and dense skin-porous crumb shape were mathematically calculated by reversing the radii direction so the origin is from the surface to the centre, the difference lies in the changing crust thickness. The hollow in the middle of 'dense skin-porous crumb' was also assumed to fill with air to get rid of the collapsing effect when the water vapour condenses. The results showed that the two extended models provided a better fit to experimental data than the previous shrinkage-diffusion model.

### **Conclusions:**

In diffusion models, the drying process is described by a set of differential equations with suitable boundary conditions. As there is a moving interface in shrinking or inflating cases, those equations are time-consuming and very hard to solve due to the moving interface and changing boundary conditions. The final droplet morphologies also strongly depend on the physical properties of the crust formed. However, the diffusion model can solve for the internal moisture gradient, leading to the ability to predict agglomeration and wall depositions inside the drying chamber.

#### **2.1.2.4. Heat and mass transfer correlations study**

There were a number of reported papers focusing on understanding the heat and mass transfer between the droplet surface and the bulk gas phase. Early important work is from Ranz & Marshall (1952). They developed the following correlations by evaporating pure liquid droplets with a restricted range of Reynolds number from 0 to 200,

$$Nu = 2 + 0.6 Re^{\frac{1}{2}} Pr^{\frac{1}{3}} \quad (2-7)$$

$$Sh = 2 + 0.6 Re^{\frac{1}{2}} Sc^{\frac{1}{3}} \quad (2-8)$$

Where  $Nu$  is Nusselt number,  $Re$  is Reynolds number,  $Pr$  is Prandtl number,  $Sh$  is Sherwood number and  $Sc$  is Schmidt number. The experimental technique used to derive this correlation was the glass filament technique. The evaporation rate was determined by how much water is needed to keep the droplet size constant and the droplet diameter was measured from a projection microscope. This method potentially shows errors in measurements due to a small size droplet and the heat conduction through the filament. Moreover, the feed of new liquid to maintain a droplet size can be a disturbance to the concentration profile, and this is indeed not feasible in the crust formation case. Due to a restriction to low Reynolds number, Ranz & Marshall (1952) correlation cannot be

used in the high-temperature environment without corrections. Beard & Pruppacher (1971) and Rasmussen *et al.* (1985) proposed the following modified version,

$$Nu = 1.56 + 0.616 Re^{\frac{1}{2}} Pr^{\frac{1}{3}} \quad (2-9)$$

$$Sh = 1.56 + 0.616 Re^{\frac{1}{2}} Sc^{\frac{1}{3}} \quad (2-10)$$

Harpole (2015) predicted that the water vapour concentration at the surface is higher at high temperature. This results in a 'blowing' effect and variable fluid properties. The Nusselt number accounted for the 'blowing effect' was corrected as,

$$Nu^* = Nu^+(1 + aB)^{-0.7} \quad (2-11)$$

Where  $Nu^*$  is Nusselt number at high temperature ( $T \geq 400^\circ C$ ),  $Nu^+$  is the no-blowing Nusselt number,  $a$  is the weighting factor and  $B$  is the blowing parameter.

Xu *et al.* (2002) proposed a modified glass filament technique, which is believed to be more accurate, cost-effective and able to generate high-quality monitoring results of droplet drying. The aim is to efficiently measure the droplet weight, size and temperature in order to obtain quantitatively the information on heat and mass transfer. A brief schematic of the experimental apparatus is shown in Figure 2-2,

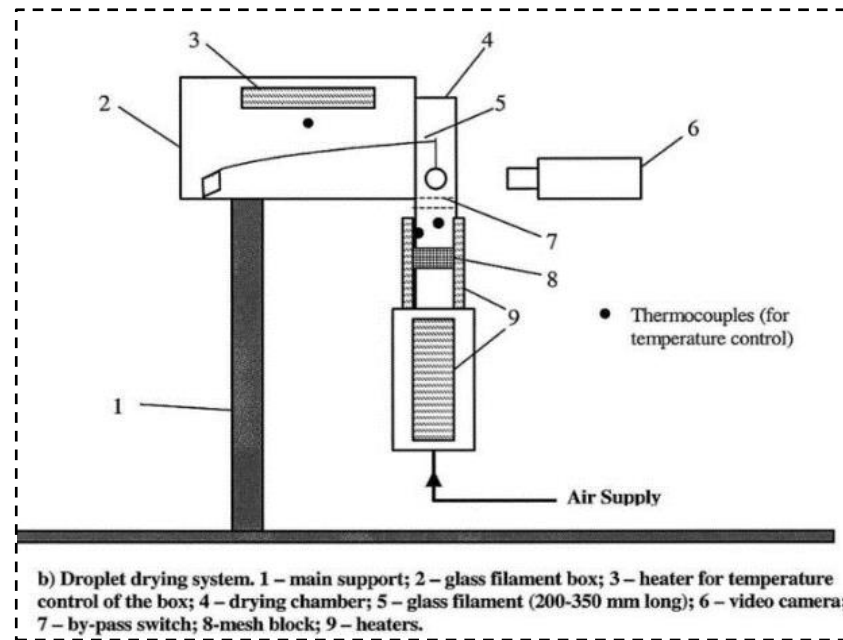


**Figure 2-2.** Apparatus set-up of modified glass filament method taken from Xu *et al.* (2002). The droplet is hanging on the glass filament within a glass filament box (number 3), with the air is heated by the heaters (number 9).

Comparing to Ranz & Marshall's experiment, several improvements have been implemented. A standard Ranz & Marshall's experiment was performed again by Xu *et al.* (2002) with the vapour flux to be 10 times greater than in the original experiment. The following heat and mass transfer correlations were obtained using film theories,

$$Nu = 2.04 + 0.62 Re^{\frac{1}{2}} Pr^{\frac{1}{3}} \quad (2-12)$$

$$Sh = 1.63 + 0.54 Re^{\frac{1}{2}} Sc^{\frac{1}{3}} \quad (2-13)$$

### 2.1.3. Experimental techniques for Single Droplet Drying

#### 2.1.3.1. Current experimental techniques

Based on different requirements on the accuracy and output information, various experimental techniques are chosen for different purposes. Currently, three widely used experimental methods that can maintain droplet spherical shape within an

acceptable degree are the contact or non-contact levitation, free-falling and hydrophobic surface contact (sessile) (Sadek *et al.*, 2015) (Fu, Woo and Chen, 2012) (Baldelli *et al.*, 2016) (Perdana *et al.*, 2013).

### 2.1.3.2. Contact or non-contact levitation method

There are two basic methods in this category: thin glass filament and acoustic-aerodynamic fields. In the glass filament technique (contact levitation) shown in Figure 2-3 **(a)**, a droplet of 1 mm in diameter is dispensed at the tip of the filament and placed in a heated air stream from the nozzle. The high-speed camera then captures the change in particle diameter and two thermocouples can measure the droplet temperature. Any deflection of glass filament from its original position can be converted to the mass loss through the calibration curve. Figure 2-3 **(b)** is a non-contact acoustic field levitation, a droplet experiences an upward soundwave generated by ultrasound. The fundamental idea is to hover the droplet in the mid-air by introducing an equal and stable opposing force to gravity. The main disadvantage lies in the evaporation rate being affected by the heat conduction through the filament or being disturbed by the sound wave. A long capturing time and stabilisation of droplets are also challenging factors.

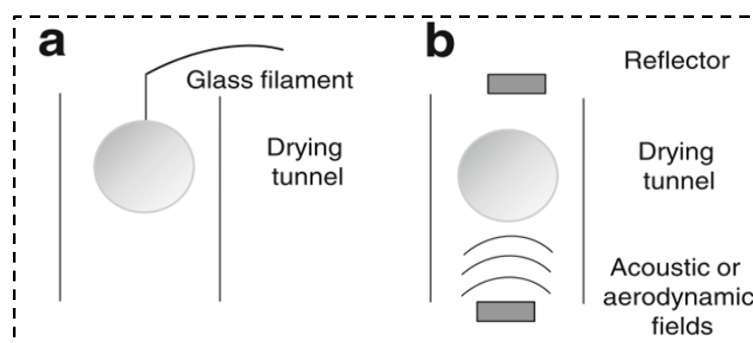


**Figure 2-3.** (a) Contact levitation: Glass filament technique; (b) Non-contact: Acoustic wave technique (Sadek *et al.*, 2015).

### 2.1.3.3. Electrodynamic balance (EDB)

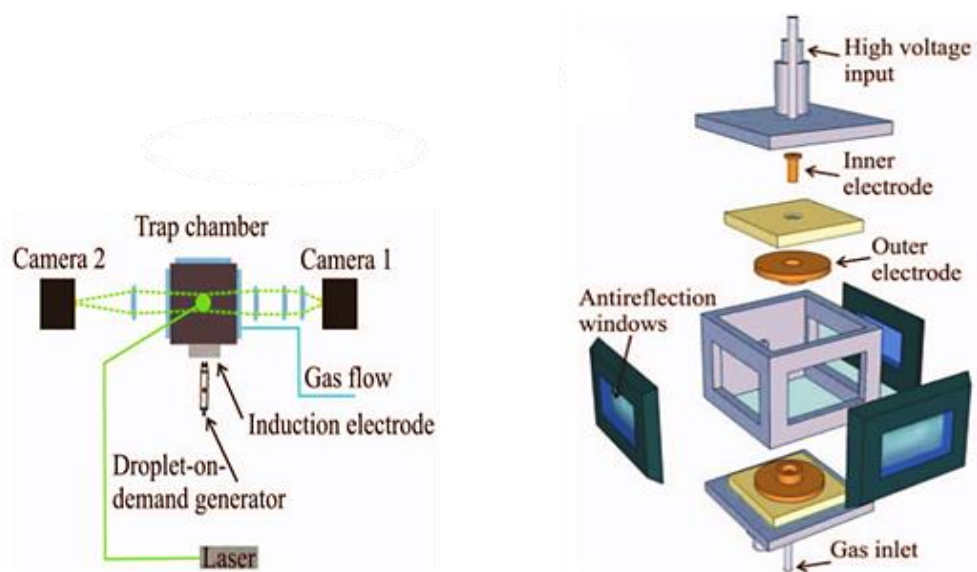


**Figure 2-4.** (left) Experimental configuration for electrodynamic balance (EDB); (right) Expandable view of EDB equipment setup. The schematic is taken from Davies *et al.* (2012).

Electrodynamic balance (EDB) is another SDD technique that can trap a droplet inside a chamber without contact. Figure 2-4 (right) consists of two concentric cylindrical electrodes to which AC voltage is applied to create a potential well. A voltage pulse induces pressure to the voltage-activated dispenser to create a droplet with the controlled volume on demand, as shown in Figure 2-4 (left). The droplet then travels horizontally from the outer wall to get charged up before entering the chamber. The gravity force exerted on the droplet is cancelled by a DC voltage across the vertical electrode. A heated gas flow then enters the chamber through a gas inlet. A droplet vibration can be controlled and stabilised through an oscillating electric field created by an AC current. The laser light is used to measure the droplet size over time. Its scattering angle is plotted against the light intensity and a droplet radius can be calculated consequently. The advantage of this technique is the ability to maintain a spherical shape of a droplet during the experiment. A disadvantage, however, is the operation restriction of

the low-temperature range which cannot exceed the droplet boiling point.

#### 2.1.3.4. Free falling droplet

The mono-dispersed generator (Figure 2-5) creates a single or chain of droplets free falling through a drying tunnel. A stream of separate identical droplets is formed by a micro-syringe from the generator, and injected into a downward air flow. This method accurately represents the drying history of a droplet in the drying chamber. It can create the same drying condition for each droplet leading to a consistent final particle shape. However, it is challenging to monitor drying kinetics and observe the droplet shape development inside the tunnel.

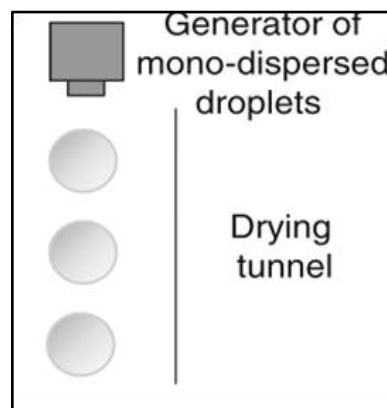


**Figure 2-5.** Schematic of the mono-dispersed generator.

#### 2.1.3.5. Sessile droplet

This method is developed due to the demand for rapid and inexpensive measurements while maintaining the key parameters of the drying process. A droplet is deposited on a hydrophobic plate to minimise the contact angle thus reducing the effect of heat conduction from the plate (refer to Figure 2-6).

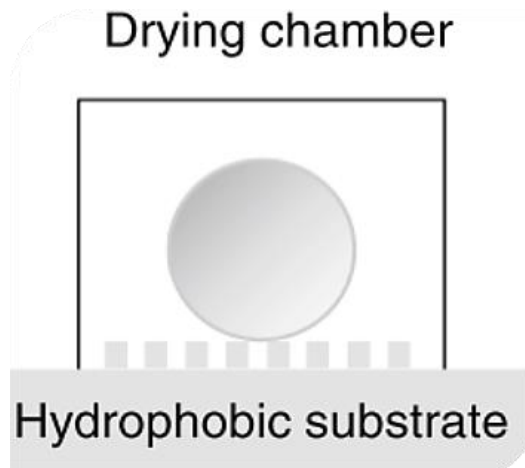


**Figure 2-6.** Droplet (circular domain) holds on a hydrophobic surface (grey squares) (Sadek *et al.*, 2015).

The droplet size and residence time can be varied flexibly so the close resemblance of an industrial droplet is achievable. The technique requires a high-quality optical device to capture the droplet structure transformation. The main drawback is the difference in velocity profiles, and the difference in the air temperature near the plate contact point compared to that at the top of the droplet. Since this is not a free space, a reverse-flow or turbulence area might occur near a contact point.

#### **2.1.4. Particle morphologies and structural evolution**

Numerous particle morphologies can be developed from different drying conditions, solvents and solutes. This has drawn a tremendous amount of attention lately since different particle microstructures result in completely different product performances, such as density, flowability, powder mixing, stickiness or conductivity. Therefore, an effective strategy to tailor the final dried-particle morphologies in spray drying is highly important and requires huge modelling and experimental efforts (Nandiyanto and Okuyama, 2011a). There are currently a number of methods for controlling particle shapes such as mechanical milling, freeze-drying, precipitation or spray drying. Spray drying is considered to

be the most favourable method for producing high purity powder, uniform morphologies and achievable nanostructured powder. Figure 2-7 lists all the possible particle morphologies formed from the spray drying technology.

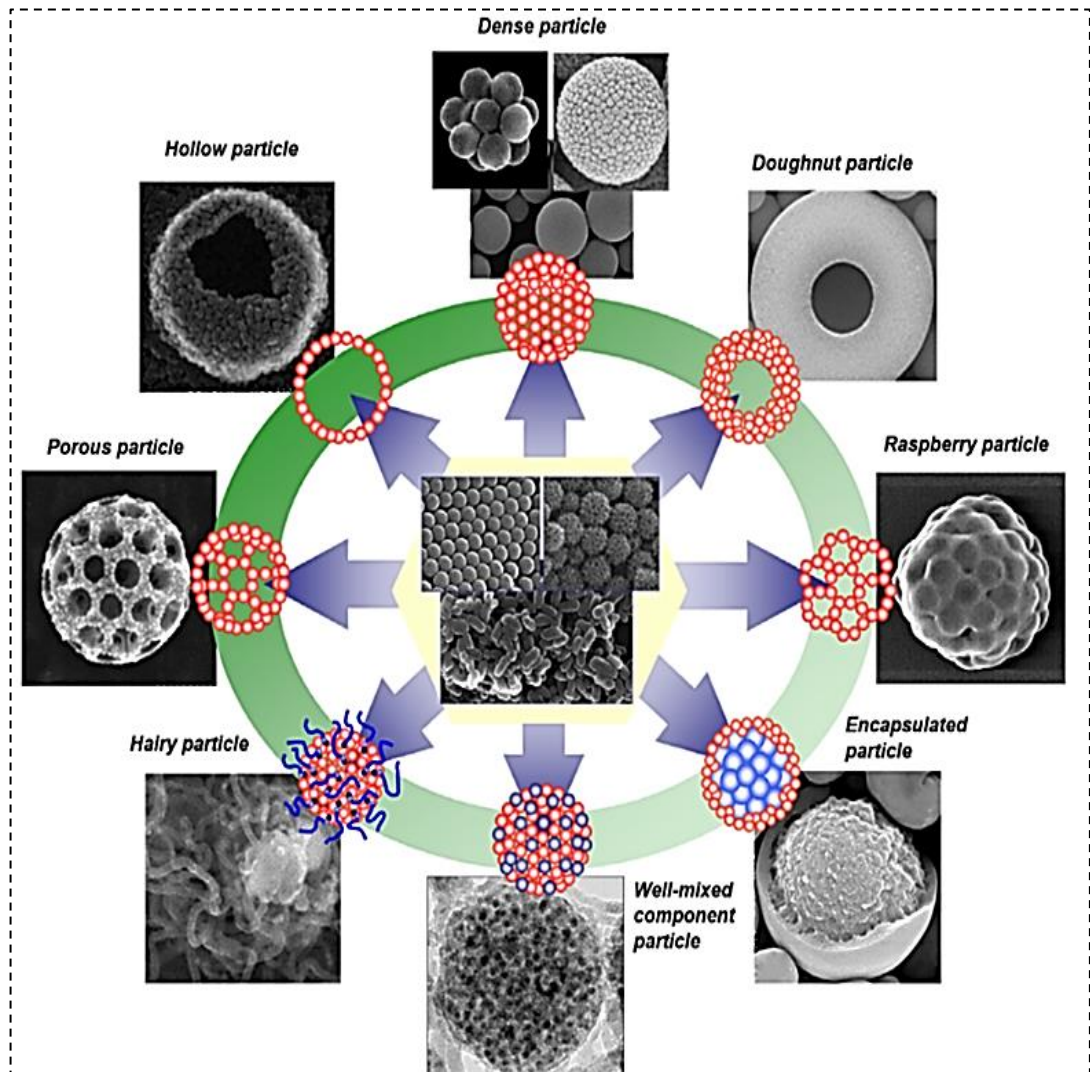


**Figure 2-7.** Different types of dried-particle morphologies (Nandiyanto and Okuyama, 2011a). The SEM images of each structure are presented with a representative sketch.

#### 2.1.4.1. Dense, hollow and doughnut particles

Particle microstructures are mainly determined by two diffusion phenomena: the outwards evaporative solute flux and the inwards diffusive solute flux towards the centre. They are combined under dimensionless Peclet number formulated as,  $Pe = \frac{\kappa}{D}$ , where  $\kappa$  is

evaporation rate and  $\mathcal{D}$  is the inwards diffusion rate. If the evaporation rate dominates ( $Pe > 1$ ) during the drying, all the solute particles tend to move to the interface and form a solid crust given enough heat and initial concentration. The droplet shell is then buckled leading to a rigid hollow or doughnut form.

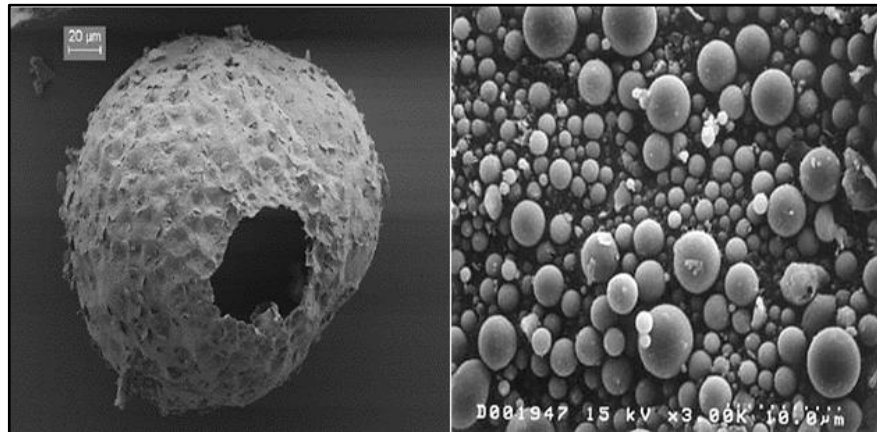


**Figure 2-8.** SEM images of hollow (left) and spherical dense (right) particles. The length scales are **20  $\mu\text{m}$**  and **10  $\mu\text{m}$**  for the left and right images, respectively.

The remaining moisture vaporises through a porous medium (refer to Figure 2-8). In the case of  $Pe < 1$ , an even distribution of solute within the droplet resulting in dense particles with a smaller radius (right image in Figure 2-8). These structures can be manipulated by varying operating parameters such as the ambient temperature, moisture or solute solubility.

#### **2.1.4.2. Composite particles- Multicomponent system**

##### 2.1.4.2.1. Mixed or encapsulated particle

A *well-mixed particle* is formed when each component/species sizes and their mass fractions are identical, leading to similar movements within the droplet. Components within this type of droplet have the same chance of buoying towards the surface. A capillary force is then induced by the moisture evaporation through the porous shell, that compresses the solute into close-packed arrays. For *encapsulated particles*, when the size of one component dominates

the mixture, it experiences a larger buoying force due to greater density, but less Brownian motions due to its large size. Hence, a larger component moves slowly inside while small particles arrange themselves easily outside resulting in an encapsulated structure (Figure 2-9). Apart from component sizes, the surface charge is also an important factor to consider (Nandiyanto and Okuyama, 2011a).

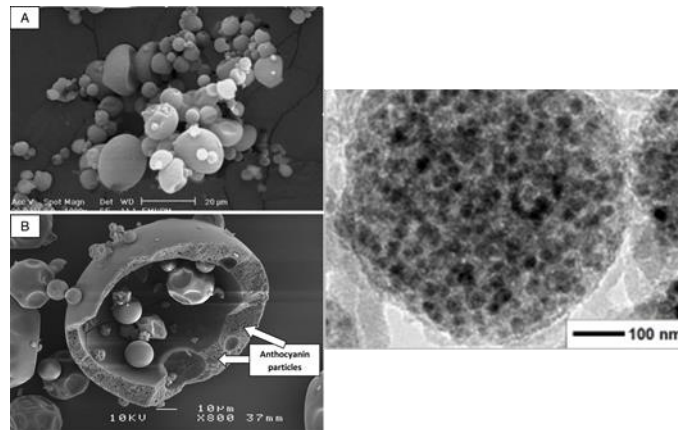


**Figure 2-9.** SEM images of multicomponent dried-particles (Akhavan Mahdavi *et al.*, 2016) (Nandiyanto and Okuyama, 2011b). The length scale is **10  $\mu\text{m}$** . Images of encapsulated particles (top and bottom left) and well-mixed particles (right) are illustrated.

#### 2.1.4.2.2. Hairy particles

This is a different version of a well-mixed shape with a carbon nanotube (CNT) catalyst added initially. The mechanism proposed by Van Hooijdonk *et al.* (2013) explained that this is mainly based on the catalytic decomposition of the organic component and the growth on the surface of the CNT tube, as shown in Figure 2-10. The higher concentration of catalyst added, the more hairy-like structure obtained.



**Figure 2-10.** SEM image of hairy dried-particles (Van Hooijdonk *et al.*, 2013).

#### 2.1.4.2.3. Porous particle

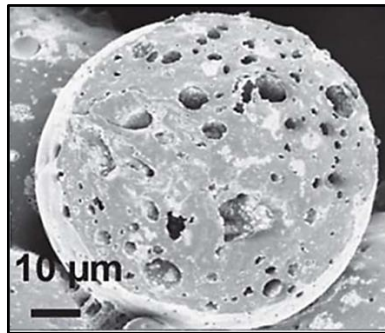


**Figure 2-11.** SEM image of porous dried-particle (Singh *et al.*, 2012).

Initially, inorganic and organic materials are mixed in a ratio and conditions such that the drying route follows and forms an encapsulated particle as described previously (Chou *et al.*, 2014). A mixture normally consists of large organic particles and smaller inorganic components. An organic compound is removed later through evaporation creating pores. The pore size can be controlled through the size of organic particles. A major advantage of porous particles, as shown in Figure 2-11, is that they can be re-formed into other shapes like packed-bed and fibre (Singh *et al.*, 2012).

#### **2.1.5. Systems for droplet drying modelling**

The choice of modelling approaches based on the droplet's solution types and drying conditions. A simple approach sometimes cannot provide enough insights, and a complex model would be redundant

for the non-complicated drying system. Different types of solutes within a droplet can lead to different skin formation and physical properties. A droplet containing solids can form dense solid or hollow particles whereas a sugary droplet can form a glassy crust which can eventually lead to 'inflated' or 'puff' particles. This section describes mathematical models used in each of the four droplet systems: colloidal, crystallisation, multi-component and polymeric system.

### 2.1.5.1. Colloidal system

A colloidal system is a droplet consisted of suspended solid that disperse within a solvent. The solid can have different diffusion behaviours within a droplet according to different operating conditions. The diffusion-limit model, which only considers the diffusive transfer of heat and mass between the droplet and ambient air while neglecting the internal convection, is typically applied in the colloidal system. Moreover the dry shell route (refer to section 2.1.2.3.1) is normally considered due to the formation of rigid porous skin during drying. A large number of published works have utilised this system to validate the measured data against the model.

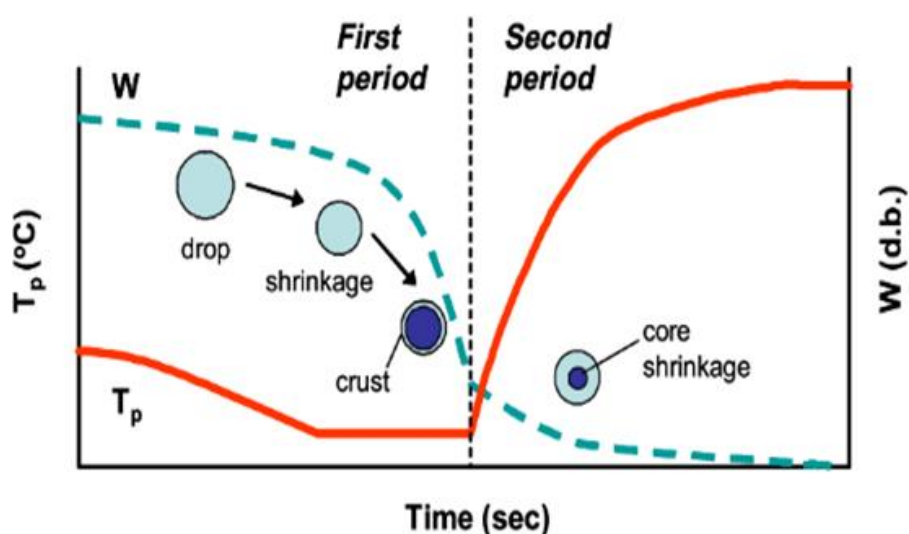


**Figure 2-12.** Drying mechanism of milk particle based on changing moisture and temperature (Kim, Chen and Pearce, 2009).

The effects of varying drying operating conditions on a milk droplet's surface composition were studied by Kim *et al.* (2009). Kim suggested that the drying process needed to be fast and at low heat in order to be efficient and cause no damage to the final powder product. The drying history of milk particles is modified from previous models and shown in Figure 2-12. The drying process is divided into two periods: the shell-forming and core shrinkage. The result showed that the initial solid concentration significantly affects the surface's composition. It was explained that the large solid content will prohibit the redistribution of milk components causing a high gradient in concentration. Kim proposed that due to different diffusivities, the fat molecule and protein will both end up cover more at the surface compared to lactose (Kim, Chen and Pearce, 2009). This explains the high-fat concentration coverage on the final dried-milk powder. This work is useful for studying a surface's composition of a droplet with different initial suspended solid size and diffusivity. Huang (2011) developed and tested a model that can provide reliable data on the internal composition profiles, skin formation, final structure and density. The author discovered a further shrinkage can happen and the crust may collapse after the skin formation stage. The temperature gradient within the droplet is negligible due to greater heat conduction inside compared to surface heat convection. The diffusion equations and boundary conditions were transformed into dimensionless so that the Peclet number becomes a control parameter. The shell-forming mechanism hence was determined based on the Peclet number. A model from Tran (2015) considered the spatial distribution of solute and shell porosity while neglecting the aggregation effect. The physical model was developed where the particles shrink at early stages, until the point where the solute concentration at the droplet surface is enough to form the crust. Then the drying rate happens via the evaporation of water through the non-uniform crust. Farid

(2003) developed a new model for modelling single droplet drying focusing on internal temperature distribution. The dimensionless Biot number, which is defined as a ratio of heat resistance within and at the surface of a body, was used. The discussion is that the uniform temperature distribution assumption due to a small Biot number is not valid even for a very small droplet (<200 micrometre). However, it is acceptable at the early drying stage since the thermal conductivity of the droplet is high. As the droplet continues to dry and forms a shell, the crust's thermal conductivity decreases by one order of magnitude causing the Biot number to increase significantly. The shrinkage time can be derived by integrating a differential equation of changing the droplet radius. Overall, Farid (2003) showed an interesting approach to single drop modelling with improvements on assumptions for the temperature field from previous models. However, there is still a lack of predictions for final particle structures. Miglani and Basu (2015) studied morphologies transition of nanoparticle laden droplets utilizing the acoustic levitation method. The aim was to investigate how the functional properties, such as droplet size or initial solute concentration, can alter the 'buckling' behaviour. The particle used in the experiment was the nanosilica solution with an average diameter of 24 nm suspended in de-ionised water. The buckling rate and its response to heating rate were described using energy balance and experimental data. Miglani and Basu (2015) showed that the shell thickness is a critical factor that determine the amount of stress required for shell deformation. Zhang and Zhang (2016) proposed a simpler diffusion-control model utilizing a quasi steady-state assumption. In this model, a perturbation method was implemented to solve the complex Navier-Stokes heat and mass transfer equations. It breaks down the solution into smaller parameters. A droplet size formula following Fick's law was expressed in terms of radius-dependent pressure. Wu *et al.* (2016)

also considered the temperature gradient within the droplet, which was previously ignored by Huang (2011), causing by heat conduction between the interface and the surrounding air, and the heat taken out by water vapour. The model produced good results against experimental data at low Stefan number. The authors suggested an adoption of 'higher-order finite element' method for modelling droplet at high Stefan number as the time for evaporation would increase.

### **Comments:**

Modelling approach for colloidal systems mainly focuses on understanding the skin forming mechanisms through dimensionless ratios such as the Lewis number or the Peclet number, initial solute concentration and droplet size. Most of the reported papers developed the heat and mass transfer equations in various approaches, since it is the critical factor determining the crust formation. Moreover, the mechanical properties of the droplet shell were analyzed through information on the surface's composition, concentration gradient at the interface. There is no mathematical tool to solve the system efficiently as it often includes partial differential equations (PDEs). Therefore, it is desirable to have a better numerical method and modelling approach to solve the complex set of PDEs. Although the drying process was studied broadly, no papers proposed a decent model for predicting the final morphologies. In order for the drying model to capture the particle morphologies, the local drying variable, such as the internal concentration profile, internal diffusion or shell composition should be focused on. This requires a high level of model complexity which needs to be solved in higher-order coordinate systems, such as the 2-dimensional or 3-dimensional coordinates.

### **2.1.5.2. Crystallisation**

A number of reported studies were done on the crystallisation system. In this type of droplet solution, a solid crust is formed through solute crystallisation during drying. Baldelli *et al.* (2016) studied the effect of crystallisation on Sodium Nitrate droplets using a droplet chain method in which monodispersed droplets are produced using a piezo-ceramic dispenser. Previous models published by Vehring (2008) and Boraey and Vehring (2014) required constant evaporation rate to work and provided partial knowledge on particle formation in liquid-diffusion and slow diffusion cases. A number of parameters were considered: the mass fraction of solute, particle density, shell thickness, evaporation rate, the Peclet number, saturation stage and surface enrichment which is the ratio between the surface's concentration and the average concentration. The crystallisation does not start at the saturation, but rather at the supersaturation state. The result showed that Sodium nitrate droplet began to crystallise at 83 *wt%* to 98 *wt%*. A significant decrease in density can indicate the crystallisation process. The crystals continued to nucleate, grows and forms a porous shell. This emphasises the importance of the crystallisation step in determining the final properties of dried particles. The study provided a detailed explanation on the crystallisation mechanism. However, there were lack of insights on the structure of porous shell and a numerical model to describe the drying process.

### **2.1.5.3. Polymeric solution droplet**

The droplet contains a polymer solute and water/polymeric solvent is discussed in this section. The system is described to be dependent on the initial concentration and the dimensionless Peclet number. The polymer solute exhibits special properties in which its concentration increases during drying up until the glass transition point and forms a glass-like skin which is permeable and pliable.

Ozawa *et al.* (2005) investigated the drying of a thin film of polymer solution pinned on a flat solid surface. It was argued that the assumption of Newtonian fluid inside the droplet is only true for the early-stage drying and it breaks down when solute concentration dominates. Therefore the change in viscosity and evaporation rate were two main concerns. The shape evolution is described by the change in height and liquid velocity within the droplet. The model predicts the ring shape, in which a droplet has a dip in the centre, in the case of high initial solute concentration and low evaporation. Low initial solute concentration and high evaporation rate resulted in a flat shape called the 'dot' type. Although the experimental technique did not represent a perfect spherical droplet, the paper's result showed how important the polymer concentration is to the final shape. Sugiyama (2006) aimed to study the effect of different molecular weights of dissolved particles on final morphologies. The droplet shell is formed by the compressive capillary stress induced by the receding interface. This paper investigated how changing the molecular weight of dissolved poly(ethylene oxide) (PEO) can affect the buckling rate and final particle morphology. The result illustrated different dried particle shapes according to a different molecular weight of PEO. The higher the PEO molecular weight, the more crumple the particle will be, as shown in Figure 2-13.

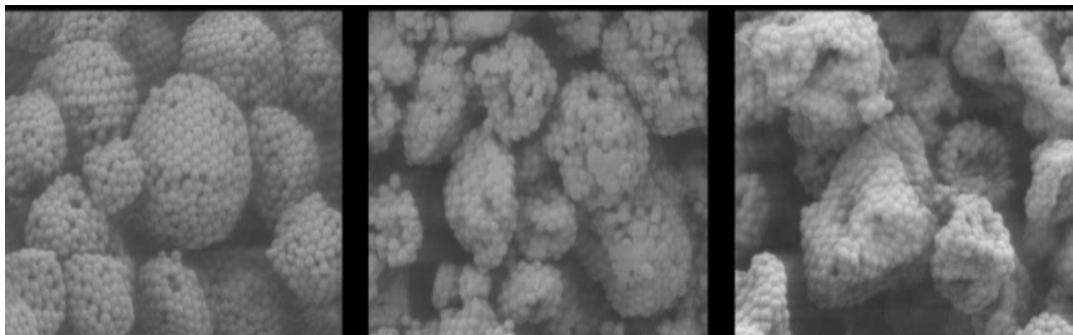


**Figure 2-13.** Increasing initial PEO polymer concentration affecting the final dried-particle (from left to right) (Sugiyama *et al.*, 2006).

In addition to the particle buckling, Sugiyama (2006) also qualitatively observed new behaviours: rippling, violent explosion and jumping. This provides vital information on the mechanical response of the viscoelastic polymer droplet. Baldwin *et al.* (2011) studied the drying of sessile Poly(ethylene oxide) droplet on a flat surface under various experimental conditions to see how the Peclet number affects the droplet morphologies. The skin formation of the PEO droplet was predicted by a four-stage process: pinned drying, receding contact line, boot-strap building, late-stage drying. A droplet is pinned in the first stage with a constant radius but decreasing height and volume. Subsequently, once the surface concentration is saturated, the solid semi-crystalline spherulites formed and trapped water. The outer layer is then solidified given enough drying time. This stage is critical to final structures since the speed of crust solidification determines the 'flat rough puddle' or 'unstable pillar'. The study on skin formation and properties of final dried particle can be applied in single drop drying of polymeric system. A process parameters such as the relative humidity, pressure, contact angle and temperature were varied in order to change the Peclet number. However, the transition between the two morphologies was not investigated and is recommended in the future work. The two papers from Baldwin *et al.* (2011) and Sugiyama *et al.* (2006) illustrated important variables, such as the effects of initial concentration, polymer's molecular weight and the diffusive flux, and its effects on the final morphologies. This emphasises the importance of solute physical properties. Gopireddy & Gutheil (2012) studied the drying of a bi-component polymer droplet: evaporating liquid and dissolved solid particles. The model developed in this paper is applied for a polymeric system which included the modification to the solid formation model and the activity coefficient. The heat and mass transfer equations of Abramzon & Sirignano (1989) model were used with modifications

accounting for the crust formation. The drying process was explained following the paper from Nešić & Vodnik (1991) consisting of four stages: initial heating and evaporation, quasi-equilibrium evaporation, crust formation and growth, boiling and particle drying. The crust formation in the polymeric system is formed by the molecular entanglement with an increasing concentration until solid. The rate of evaporation used the droplet radius variable, instead of the volume-equivalent radius. A temperature gradient was found by solving the heat conduction equation at the droplet centre and surface. The model showed a good understanding of how droplet dries over time with good agreements of parameters such as the temperature, the evaporation rate, and the solute mass distribution. However, the model was based purely on equations constructed previously without taking into account the polymer properties. Hence, there was a lack of thermal conductivity and diffusion through the skin investigation and the results did not show any importance of polymeric crust behaviours.

Rajagopalan (2014) investigated the generation of blended micro-particles from a solution containing two immiscible polymers. A vibrating orifice aerosol generator (VOAG) was used as a monodisperse equipment to generate polymer droplets. A model was developed taking into account the convection phenomenon inside the droplet. If the evaporation time is shorter than polymer diffusion time, a homogeneous blend of polymers is achievable due to no phase separation. At a low solid concentration, the polymer shell is formed along the drying process and collapses eventually due to low solid concentration leading to the final solid with a hollow surface and indentations. However, a thicker crust is formed with higher initial polymer content, hence the droplet wall will stop collapsing given a strong holding force. A system with high polymer volatility (THF) and a highly porous shell resulted in an inflated-like balloon shape as shown in Figure 2-14 (a). The evaporating

polymer, DMC, has significantly higher volatility than the blended polymer solution, hence as soon as the crust is formed, the remaining DMC penetrated through the skin leaving pores on the droplet surface shown in Figure 2-14 (b). The only case where the spherical particle was formed (refer to Figure 2-14 (c)) is when the solvent evaporates slowly with relatively high initial polymer concentration, the skin is thickened to prevent collapsing, even though all the particle obtained were brittle. This would result in a rough surface and creates flakes falling off the skin.

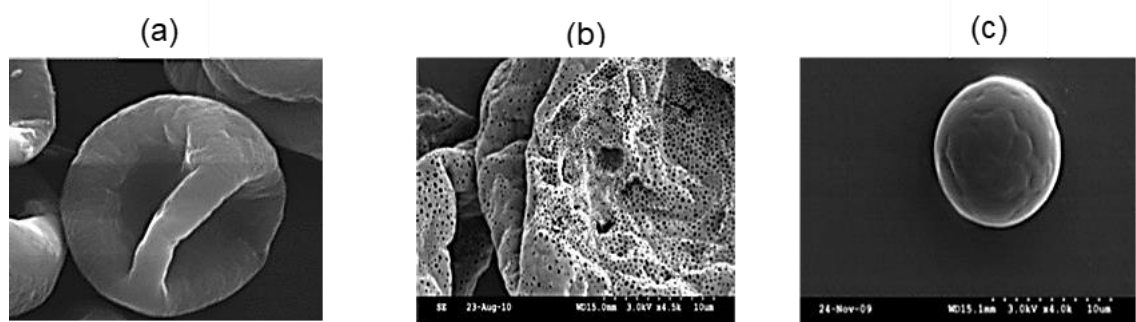


**Figure 2-14.** Final particle morphologies from different drying conditions. (a) High evaporation rate and highly porous shell; (b) High evaporation rate and very high volatiles solute (Rajagopalan, 2014).

The author illustrated the limitations of applying the previous model to the polymer system. A droplet contains polymer does not have a critical saturation concentration for precipitation. Moreover, the polymer solute will undergo degradation at high temperatures and the droplet surface might not reach the solvent boiling point due to a high evaporation rate, which leads to the effect of particle convection that needed to be considered. Kaneda *et al.* (2008) also studied the internal flow and receding surface of polymer droplets. The Marangoni effect, which is the mass transfer effect along a liquid interface due to the gradient in the surface tension, that was neglected previously is included in this paper. The surface used for depositing a droplet is lyophobic. The evaporation rate and initial

solute concentration are the two main factors. The results showed that the evaporation rate is independent of the initial solute concentration, but decreases at the droplet pinning. The convection effect and variation in the solvent's viscosity are also important.

### **Comments:**

A low number of published studies targeted the modelling on single droplet drying containing dissolved polymer components. The experiments were mainly on the evaporation of droplets on a flat or hydrophobic surface which is not fully applicable to droplets in a spray dryer. Most of the currently available models were developed taking into account the receding interface. Since the polymer shell performs viscoelastic properties, the skin can collapse or be penetrated by another higher volatility component. Moreover, the entanglement or solid-like behaviour of polymeric solute will lead to different porosity. Most of the works yielded similar results that the evaporation flux is independent of initial polymer concentration and the shell-forming time is critical to final morphology.

#### **2.1.5.4. Multicomponent droplet without solid content**

The multi-component droplet contains more than one solute in the solution. Hence, there exists a competition between the heat and mass transport, volatility, spatial distribution between solutes. This section reviews reported studies that considered a single droplet type which consists of more than two dissolved or suspended components. Newbold and Amundson (1973) aimed to have a better approach to describe the multicomponent droplet evaporation in stagnant gas near its boiling point. The goal was to understand a flux of heat and mass transferring between the droplet and ambient air. This can be used later to describe the change of droplet radius, concentration and temperature from differential equations. A pseudo-steady state approach was suggested to provide the analytical solution over the transient equations which cannot be

solved for the exact solution. The model was tested against the two-component and three-component droplets. Prakash & Sirignano (1980) studied the droplet evaporation in a convective heat gas stream. The droplet contains three hydrocarbons which are n-hexane, n-decane and n-hexadecane. In this model, a quasi-steady state was employed for both gas and liquid phases. The governing equations in the gas phase and liquid phase were coupled at the liquid-gas interface to predict the evaporation rate. Results exhibited the temperature difference between the surface and interior is more significant for a heavy and less volatile droplet. The model suggested the importance of temperature distribution and further researches are needed for the drying mechanism. Renksizbulut *et al.* (1983) studied the heat and mass transfer between the multicomponent droplet and the superheated steam passing through in a Reynolds number range of 10 to 100. At a high-temperature gas flow, the evaporation of the solvent affects the flow field near the surface leading to a change in drag force and heat transfer. A mass, momentum and energy equations for both liquid and gas were performed. Although Renksizbulut *et al.* (1983) obtained an equation for pressure distribution which was useful in terms of predicting dried structure, a final particle shape was not analysed further. Trueman *et al.* (2012) studied the film formation phenomenon during droplet drying known as the stratification effect. The shell is said to not always vertically homogeneous throughout the process and different solute has a different preferential position. The condition for skin formation depends upon the Peclet number which can be altered by changing the particle's radius. The governing parameters were the ratio of two Peclet numbers,  $Pe_1 Pe_2$ , for two solutes, and the square root of their multiplication,  $\sqrt{Pe_1 Pe_2}$ . These represent the concentration gradient vertically along the film forming and how each type of particles distributed within droplet. Strotos *et al.* (2011) derived a numerical

model for blended fuel-droplet containing n-heptane and n-decane at various concentrations. The evaporation rate is derived from Fick's law considering a vapour concentration's gradient as a driving force. The main difference compared to previous models is the interface property, which was used as a boundary condition. The obtainable information from the model is the gas flow field, temperature, droplet receding interface, droplet shape and the final composition.

**Comments:**

The main concerns in models for the multicomponent system are the non-homogeneous composition within the shell, along with the radius and the vapour region near the droplet interface being affected by the hot gas flow. The direction of upcoming gas to different sides of the droplet was believed to be an important factor that creates the asymmetrical internal flow field. The dimensionless Peclet number representing the motions of solutes is still highly useful for studying droplet's structure development. There was also an attempt using the reaction engineering method couple with a composite approach to take into account all the components. In conclusion, all models for the multicomponent system are critical for future study of skin formation behaviour and final morphologies.

**2.1.6. Comparison of the heat and mass transfer correlations**

Heat and mass transfer correlations are a critical factor to explain and understand the process of droplet drying. Many correlations have been developed using different experimental techniques, test substances and drying conditions. This section will compare in detail from an experimental approach to the correlation derivation of the two popular correlations from Ranz & Marshall (1952) and Kulmala *et al.* (1995).

In Ranz and Marshall's experiment as shown in Figure 2-15, the drying of a water droplet suspended on a glass filament was performed. The heated air enters through the nozzle placed directly below the suspended drop. There are two ways of determining the evaporation rate: a rate of changing droplet's diameter suspended on a thermos-element, or the rate of the feed water to keep a constant droplet size hanging on a filament. The rotational velocity of a droplet is less than one percent of the air velocity and hence negligible. The drop diameter is within the range of  $\pm 0.03$  cm. The droplet temperature is measured by emerging a thermos-element junction inside the droplet. In order to prevent heat loss through conduction in a filament, the thermo-element is removed during evaporation. Instead, the temperature profile is determined priorly by operating at similar conditions keeping droplet diameter constant. A diffusivity of vapour in the air is used in this correlation. This is valid for the free convection case but needs modification in the forced convection case. The experiment covered Reynolds number range from 0 to 200 and air temperature up to 220°C. Ranz and Marshall's heat and mass transfer correlations are expressed as,

$$Nu = 2 + 0.6 Re^{\frac{1}{2}} Pr^{\frac{1}{3}} \quad (2-14)$$

$$Sh = 2 + 0.6 Re^{\frac{1}{2}} Sc^{\frac{1}{3}} \quad (2-15)$$

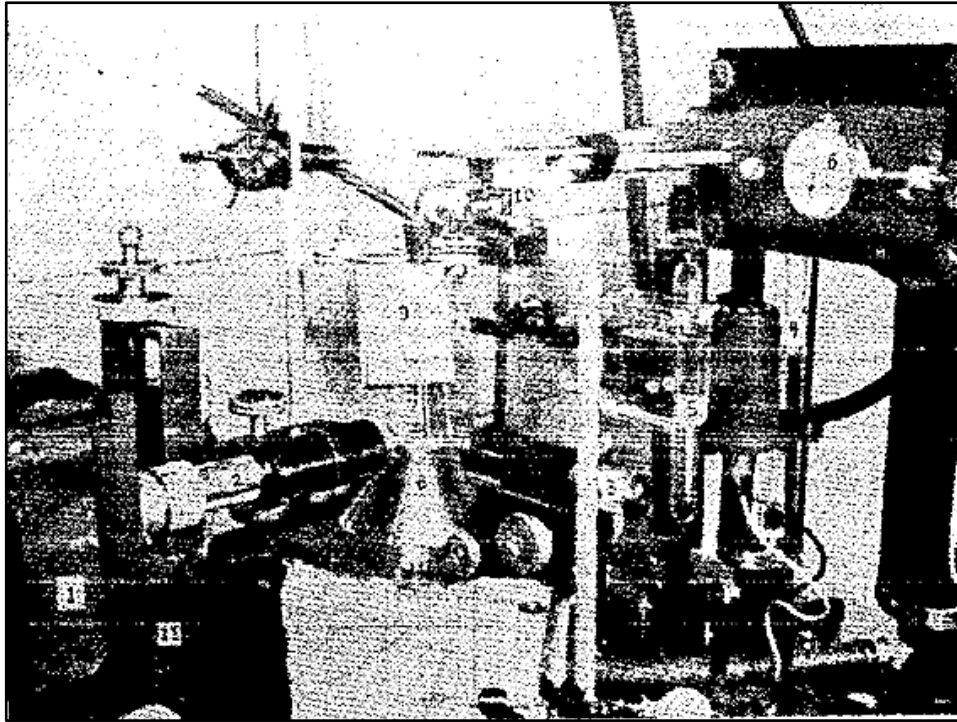


**Figure 2-15.** Experimental setup for Ranz and Marshall's heat and mass transfer correlations.

In the Kulmala experiment, the droplet is injected from a microsyringe and hung on a capillary as in Figure 2-16 . The air is compressed, filtered and heated before flowing through the droplet from below. The thermos-elements were mounted to measure both the droplet and the surrounding temperature. The droplet size is kept constant after 10-20 minutes and the evaporation rate is obtained from the rate of water supplied. This method is discussed to be less accurate than for the evaporation rate calculated from changing droplet size. The surface of the droplet is not assumed to be spherical but ellipsoidal. The short axis is taken as the droplet diameter and the long axis ranging from the capillary tip to the bottom of the droplet.

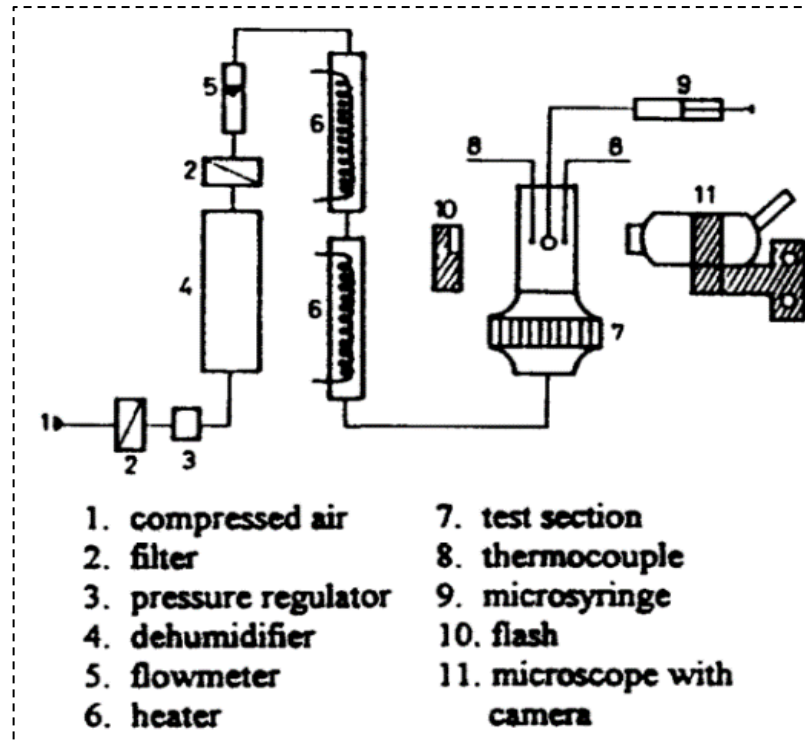


**Figure 2-16.** Kulmala's experimental setup with components number at the bottom. The droplet is produced through the microsyringe (number 9) and its temperature is measured by the thermocouple (number 8). The air is heated by the heater (number 6).

The Kulmala heat and mass transfer coefficients are in the form of,

$$Nu = 1.738 + 0.479 Re^{\frac{1}{2}} Pr^{\frac{1}{3}} \quad (2-16)$$

$$Sh = 1.738 + 0.479 Re^{\frac{1}{2}} Sc^{\frac{1}{3}} \quad (2-17)$$

**Table 2-2** below compares different variables between the two correlations.

Variables	Ranz & Marshall (Ranz and Marshall, 1952)	Kulmala (Kulmala, Schwarz and Smolík, 1994)
Temperature range	298 to 493K	314 to 449K

Reynolds number range	0 to 200	30 to 180
Droplet diameter	0.6 to 1.1 mm	0.7 to 2.3mm
Diffusivity	Diffusivity of vapor in air	Binary diffusivity
Any assumption during correlation derivation	-	Temperature deviation is estimated by the hyperbolic temperature profile indicating estimation.
Accuracy against experimental data	Correlations based on changing droplet diameter	Correlation calculated on constant droplet diameter.
Derivation approach	Derive analogously from the heat transfer equation, which includes heat deviation from conduction along capillary and radiation.	Sherwood number is derived directly from the diffusive mass flux equation based on ordinary molecular diffusion.
Air condition	Forced convection means finite air velocity	Free convection means diffusion only
Difference in other variables used	$p_f$ is the average of (total pressure - vapour partial pressure) along the transfer path	-

**Table 2-2.** Comparison between Ranz & Marshall and Kulmala heat and mass transfer correlations.

This information in Table 2-2 is useful for determining the suitable heat and mass transfer correlations for a different system with

different initial conditions. This also indicates that in order to model a drying process accurately, the validity of the heat and mass transfer correlations always needs to be revised. The comparison showed a high sensitivity of the correlation to the drying conditions which means that for high-temperature drying, a correction factor might be needed.

### **2.1.7. Single droplet drying at boiling point**

The bubble dynamics has been the subject of heavy investigation for many years. It is an important and interesting topic that has drawn a lot of attention lately. Rayleigh (1917) is believed to be the one who laid the foundation knowledge on the bubble oscillation within the liquid medium. The work purely focuses on the effect of pressure on driving the bubble growth. The force balance is evaluated at the bubble surface to derive the PDE for the bubble dynamics, called the 'Rayleigh-Plesset' (RP) equation.

$$R \frac{d^2 R}{dt^2} + \frac{3}{2} \left( \frac{dR}{dt} \right)^2 + \frac{4\vartheta_L}{R} \frac{dR}{dt} + \frac{2\sigma}{\rho_l R} + (P_\infty - P_b) = 0 \quad (2-18)$$

Where  $R$  is the bubble radius,  $\sigma$  is the surface tension,  $\vartheta_L$  is the kinematic viscosity,  $P_b$  and  $P_\infty$  are the pressure within the bubble and at infinity, respectively,  $\rho_l$  is the density of a liquid. The pressure-driven bubble growth is referred to as the 'inertia effect' in order to distinguish it from the 'thermal effect', in which the bubble grows due to the heat flux from the surrounding. As the Rayleigh-Plesset (RP) equation assumes no mass flux at the bubble interface, Prosperetti (1982b) derived from first principles and extended the RP equation that includes the mass flux at the bubble. It should be noted that the work from Rayleigh Plesset and Prosperetti considers only a single bubble in an infinite liquid domain. However, their work is critical since the problem of interest in this thesis is the bubble growth within the droplet. The same principle can be followed to derive an extended version for the

bubble growth within a confined layer of liquid. Scriven (1959) investigated the dynamics of phase change which is applicable to study the bubble growth by the 'thermal effect'. There are two verifications tests related to the phase change phenomenon called the 'Stefan problem' and the 'Sucking problem' (Sato and Ničeno, 2013). The two problems basically consist of two phases sharing an interface in the middle. The interface will move due to evaporation with the temperature constrained on the interface to be the saturation temperature. The analytical solution of the Stefan problem will be discussed in Chapter 4. Ruckenstein looked at the bubble growth within the superheated liquid (Ruckenstein and Davis, 1971). The focus of the paper is on the effect of the motion of the bubble on the bubble growth rate. The result has shown to be similar to that of the Plesset or Scriven equations if turning off the translation motion effect in the limiting cases. The motion of the bubble, hence, has been shown to be important to the rate of bubble growth. This is considerable to the boiling droplet phenomenon as the bubble motion would be under the effect of the convection within the drying droplet in reality. Payvar (1987) studies the mass transfer effect to the bubble growth on a rapid decompression of the liquid. The theoretical model considers the gas bubble domain within a liquid and dissolved gas domain. The continuity, mass and momentum equations are used to relate the pressure within the bubble to the instantaneous pressure in the liquid phase. Osamu Miyatake *et al.* (1997) attempted to describe the bubble growth in a pure or binary solution with the non-volatile solute. The bubble acceleration effect was taken into account when deriving the equation. Osamu argues that for a bubble growth within a binary solution, the growth rate is not only determined by the superheated temperature, liquid pressure but also the mass fraction of solute. The solute concentration has been shown to have a significant impact on the bubble growth rate if the pressure at far-field is

constant. An improved model for bubble kinetics within a pure liquid was also proposed with the correction of the non-linear relationship between the vapour pressure and temperature. Feng *et al.* (1997) examined the bubble behaviour in a compressible liquid which results in non-linear bubble dynamics. The bubble shape deformation was taken into account as most of the previous work always assumes a perfectly spherical bubble. The aim is to have another Rayleigh-Plesset version for the non-spherical bubble. Pai *et al.* (2002) studied the bubble growth in a viscous polymer solution, which is relevant to this thesis work as the droplet would get more viscous during drying. The growth of the bubble takes into account both the momentum and the heat and mass transfer effects. The governing equation of the bubble is derived from the first principles in a radially symmetric coordinate. The heat transfer is not a controlling factor for the bubble growth in a viscous liquid. Preston *et al.* (2007) proposed an alternative set of ODEs equations to solve for the heat and mass transfer effect on the bubble dynamics. The idea of this reduced-order model is to transform a complex set of PDEs for the bubble growth into ODEs which can be solved numerically. All the variables in the reduced-model are transformed into dimensionless form. In general, the model relates the temperature and the concentration gradient at the bubble surface to the volume-averaged temperature and concentration, respectively. The model has been shown to match with the solution from PDEs at  $Pe < 10$ .

Alamilla-Beltrán *et al.* (2005) investigated the particle morphological changes along the vertical spray dryer using scanning electron and light microscopy. A sample at different heights is withdrawn in order to analyze for moisture content and particle structure development. At an intermediate drying temperature, no particle breakage was observed compared to operating at high

temperatures. An example of particle breakage is shown in Figure 2-17.

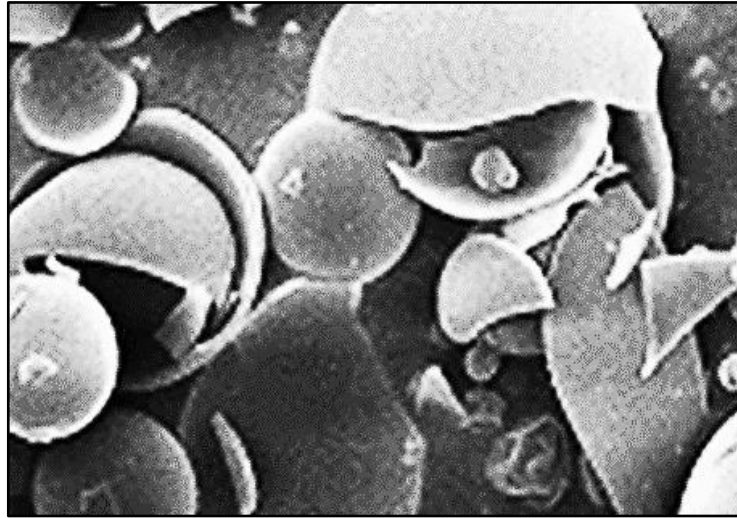


**Figure 2-17.** Illustration of particle breakage using SEM images (Alamilla-Beltrán *et al.*, 2005).

A thick, compact and irregular crust was formed at a low temperature while the smooth-surface particles were observed at high temperatures with broken pieces. The low evaporation rate gives enough time for the solid to distribute within the droplet whereas, at a high-temperature condition, the species within the droplet rushed to form the solid skin in a short timescale leading to constant particle diameter and smooth surface eventually. The broken materials were created due to an intensive thermal condition. Alamilla-Beltrán *et al.* (2005) provided a clear explanation and description of the skin forming process. This work is crucial for the understanding of particle shape at different conditions and moisture contents at high temperatures. Renksizbulut and Yuen (1983) studied the suspended water, methanol and n-heptane droplet drying at a high-temperature environment. Although there were a number of previous heat transfer correlations formulated at the high-temperature range, the effect of flow blowing and variable properties were not yet considered according to the paper. In the work presented, the droplet's heat transfer is measured with the

upcoming gas stream's temperatures up to 800°C. By validating the existed correlations data against the experimental data, an improved correlation was constructed. All three components within the droplet show a good fit following a new correlation. Hecht & King (2000) considered two models for droplet drying including the internal bubble. The first model is a simple model for calculating the evaporation rate and temperature profile. The drying rate is based on the average droplet moisture content and the temperature is based on the energy balance equation. The second model assumes a centrally located bubble with a given initial size and temperature. The energy balance equation was modified to include the evaporation towards the bubble. The bubble size can be calculated through two variables: bubble volume or bubble pressure. The changing bubble volume is calculated based on the ideal gas and the sphere volume equations. The changing bubble pressure is also obtained through the ideal gas equation and the ambient pressure term. This pressure difference is then converted to the expansion or shrinkage velocity hence obtaining a new bubble size.

### **2.1.8. Analogous problem - Fuel droplet evaporation**

Drying a droplet at high temperatures can generate a very high evaporating flux. This is similar to drying a droplet with a highly volatile component. Hence, a fuel droplet is considered in this section to investigate and examine the similarity and its applicability. Godsave (1953) studied the evaporation and combustion of fuel droplets in the spray injection systems. The high mass transfer phenomenon can affect the heat transfer process during drying. Sazhin (2006) suggested that the fuel droplet evaporation process should be split into two steps: (1) fuel molecules detach into the vicinity gas medium and (2) the diffusion of fuel vapour to the gas phase. The fuel vapour is assumed to be always saturated so only the diffusion process is considered. This is called a hydrodynamic model of droplet evaporation. Sazhin (2006)

aimed to improve this model by taking into account the convection of gas and fuel vapour away from the droplet's surface. The net gas flux towards the droplet was assumed to be zero, therefore, the diffusion of ambient gas towards the droplet equals the convection of gas away from the surface. The mass diffusion of the liquid phase was then described by the diffusion equation for each individual component/species. All the convection effects and recirculation inside the droplet were neglected. The model from Sazhin (2006) is highly practical in describing the high evaporation flux from drying a fuel droplet. Kotake & Okazaki (1969) also contributed to the study of the evaporation and combustion of fuel droplets. Droplets of benzene, methyl alcohol, ethyl alcohol and n-octane were the system of interest. The author compared the two assumptions for the evaporation process: quasi-steady state and unsteady evaporation. The result also showed that the droplet surface temperature increases rapidly at the beginning in a short amount of time and reaches the asymptotic value close to the liquid boiling point.

## 2.2. Conclusions

The literature review for spray drying, single droplet drying and boiling are conducted in detail. Although there is numerous work on droplet drying, the boiling model is scarce. The most relevant area to the boiling droplet is the development of the governing equation for the bubble growth within an infinite liquid medium and the analytical solution for the phase change problem from Scriven (1959). In terms of morphological development, the currently available models focus mainly on the global drying rate without any information on the droplet internal domain. The high-resolution model developed within the next chapters is able to capture specifically the temperature and moisture distribution within the droplet, hence contributing to the goal of predicting the morphological development of the dried-particle. It should be mentioned that there has not been any published drying model that considers the physics of a droplet falling while drying. In the single droplet drying experiment, the droplet is hung within a hot gas stream with a constant velocity. This does not represent accurately the velocity field that the droplet experiences within the spray dryer. Theoretically, the terminal falling velocity is reached shortly after the droplet leaves the atomiser. The droplet falling velocity will then change as the drying progresses, since the droplet radius decreases leading to different drag and lift on its surface. Therefore, the Reynolds number of this system will be highly dynamical considering the changes in the terminal falling velocity during drying. An innovative simulation scheme has been developed in this thesis (Chapter 3), that can model accurately both the droplet drying and the falling physics, while keeping the droplet from leaving the domain through the PID algorithm which will be discussed in the next Chapter 3.

# Chapter 3

## Fundamental theory and validation benchmarks

This chapter focuses on the principal theory of the methodology, which is the Finite Element Method (FEM), the verification and validation studies of the simulation scheme against the benchmarks, and the justification of the mathematical model that will be used for developing the droplet drying model further. The first part introduces the history and theoretical framework of the FEM followed by the development of the PID feedback loop that can simulate the falling droplet with terminal velocity. The third section is the benchmark study of the *flow past the cylinder* system. Finally, the modification of the boundary conditions of the flow past the cylinder is applied to analogously represent the liquid droplet falling in the air.

### **3.1. History and principal theory of Finite Element Method (FEM)**

The finite element method (FEM) was not invented by any individuals, but by a group of enthusiastic engineers and researchers over many decades in the 1950s. The two papers from *Schellback (1851)* and *Courant (1943)* are referred to be the earliest attempt in terms of mathematical development. The use of FEM to solve engineering problems began around the 1950s in the field of civil and aerospace engineering. There are four individuals with huge contributions to this field namely *John H. Argyris, Ray W. Clough, M. J. Turner and O. C. Zienkeiwicz*. It depends on one's point of view to decide when was the first application of FEM, but the paper from Turner (1956) is often mentioned as the first published paper in the FEM community. This paper was written when Prof R W Clough worked at Boeing in his summer job under the supervision of Mr. M J Turner. Many papers were published after that from Turner, Clough (1956), Argyris (1957) and Aziz (1972). Mr. O. C. Zienkeiwicz also published a book specifically for FEM named 'The Finite Element Method: Its Basis and Fundamentals'.

The **finite element method (FEM)** is a numerical technique that provides an approximation solution for the partial differential equations (PDEs). The partial differential equation is a type of equation in which the dependent variable is a function of multivariable and their partial derivatives. They are encountered frequently in mathematics and structural engineering which is challenging to solve for an exact solution. The PDEs can be divided into parabolic, elliptic, and hyperbolic classes. The two common ways of solving such PDEs are finite-difference and variational methods. The latter method is essentially the backbone and the philosophy of FEM. The main idea is based on the 'Principle of energy minimisation', which describes how nature works as every energy

states always seek maximum entropy or in other words, minimum internal energy at equilibrium. The concept of entropy is based on probability, or how likely the system evolves into other states of energy. A glass of water at 80°C will be more likely to cool down at room temperature than being heated up, even though the latter chance is not exactly zero statistically. For example, given a boundary condition on any interface, there are countless morphologies probabilities an object could deform into yet exactly one configuration is observed in reality. The state which is observed by the 'naked' eye, experiment, or predicted by FEM is called the minimum energy state. The way FEM interestingly utilises this idea to solve the PDEs is explained in detail next.

As multiple phases are involved in many engineering problems, the difference in physical parameters across the interface introduces the discontinuities in the solution, at which the derivative of variables is discontinuous. In practice, the derivative of some physical variables is not always trivial to evaluate and can even cause numerical issues at higher differential orders. Therefore, it is often estimated, or avoided to be solved directly due to a lack of mathematical frameworks to work with.

The problem of solving the temperature profile across two walls made from two materials is a good representative example to highlight the practical application of FEM. In order to evaluate the heat flux across the interface, the temperature needs to be differentiated twice which is numerically challenging. The first derivative of temperature across the interface is a discontinuous function, which results in an even more solution 'jump' at the second derivative. This is undesirable as most of the PDEs require continuous solution throughout the domain.

Hence, a concept of '**Weak form**' is introduced, as opposed to the 'Strong form' which is referred to as the exact solution of the PDE.

The purpose is to guess the exact solution in an ‘average sense’ to overcome any problematic discontinuous functions. Technically, the weak form turns the differential equation into an integral equation without altering its context, which is also an obvious approach at the first attempt. This will help, at least, reducing the derivative order or getting rid of it eventually. Considering the 1D rod with a simple 1D heat equation at steady state,

$$q = -\frac{dT}{dx} \quad (3-1)$$

$$\frac{dq}{dx} = \frac{d^2T}{dx^2} = 0 \quad (3-2)$$

Equation (3-1) indicates as long as there is still a non-zero heat flux gradient anywhere in the domain, it will automatically ‘spread out’ to the nearby spatial domain to achieve an equilibrium state. An alternative way to think about this is that the temperature will distribute within a domain at a steady state in a way that there will be no more change in temperature profile anywhere along with time, which obeys the principle of minimum energy. The fact that the change of heat flux **must** be zero is advantageous, as the only main task now is to minimise the error associated with estimating the heat flux gradient. The zero error indicates the exact solution is obtained.

The equation (3-1) and (3-2) can be integrated by hand to get to the exact solution, however, this is a good example to explain the fundamental concept behind FEM without being distracted by the mathematics complication. The equation can get challenging, or virtually impossible, to solve once the heat flux varies in  $y$ ,  $z$  directions and also with time. The derivative would be then in the form of divergence and gradient operators instead. In returning to the problem, the equation (3-2) is turned into the ‘weak form’ as follows,

$$\int_0^{\Omega} \frac{dq}{dx} dx = 0 \quad (3-3)$$

This new equation now requires the **average heat flux gradient** in the domain to be zero instead of forcing the **heat flux gradient** to be exactly zero everywhere in the domain, which explains the use of the terminology ‘weak’ (seen in Figure 3-1).

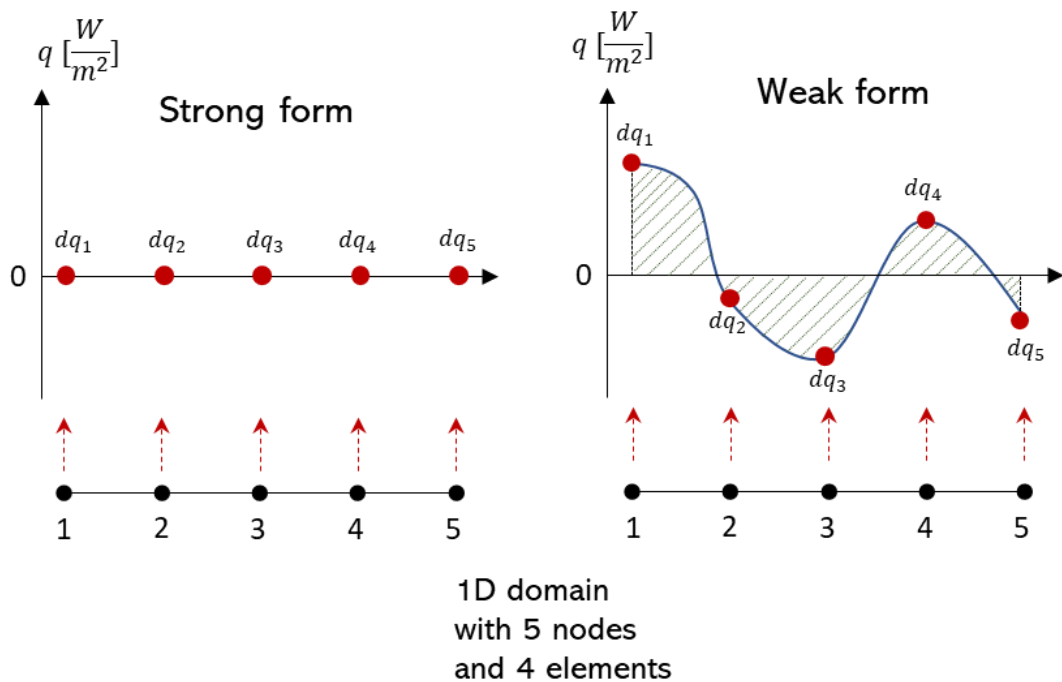


**Figure 3-1.** Graphical representation of ‘Strong form’ (left) and ‘Weak form’ (right). The domain is divided into 5 nodes (red points) and 4 elements. The heat flux gradient in the ‘Strong form’ is forced to be zero on all nodes, while the **averaged** heat flux gradient in the ‘Weak form’ is forced to zero.

The heat flux gradient in Figure 3-1(left) is exactly zero throughout the domain, while it is not the case in Figure 3-1(right), the total area under the curve is zero. Now, the constraint is relaxed. However, its usefulness can be argued that the change of heat flux at some nodes can be far off from its true solution, which is not good, and as long as the shaded area in Figure 3-1(right) is zero, the ‘weak form’ equation still holds. In other words, there is a

chance that the solution obtained satisfies the governing equation and can be unrealistic at the same time, and this is true especially in the case of an insufficient number of elements. If we reduce the integral limit of equation (3-3) to an extremely small range, for example,

$$\dots, \int_{1.99}^{2.01} \frac{dq}{dx} dx = 0, \dots, \int_{3.99}^{4.01} \frac{dq}{dx} dx = 0, \dots \quad (3-4)$$

Since the element is narrow down, the condition of zero heat flux gradient is likely to achieve which is shown in Figure 3-2,

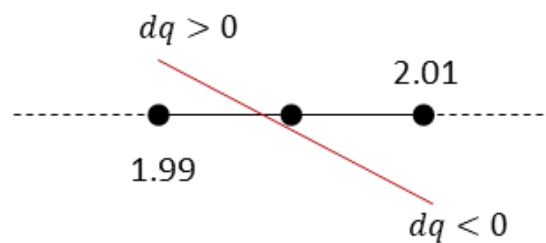


**Figure 3-2.** Heat flux gradient variation in the vicinity of the centre node.

As in Figure 3-2, the change of heat flux at the middle node is brought to near-zero value thanks to small elements around it. The heat flux gradient at the centre node and its vicinity are unlikely to be far off from zero as it must satisfy the 'Weak form' solution. The approximation approaches the exact solution as the integration limit approaches the infinitesimal range. So we now have many small 'chunks' along the 1D rod that must satisfy its unique integral.

At this stage, all the integrations need to be collected and connected to form a final solution. This is where the 'weight functions', or 'test functions', are introduced to conveniently collect and project all the integration onto the whole domain in an ordered manner. There are a variety of ways to choose the weight functions, such as the *Dirac delta function* in the collocation method or the *residual functions* in the method of least squares. However, it is normally chosen as a linear combination of polynomials functions which are effortless to

differentiate (seen in equation (3-5)). The purpose of this will be more clear later.

$$\bar{w} = \sum_{i=0}^n c_i w_i(x) = c_0 w_0(x) + c_1 w_1(x) + \dots + c_i w_i(x) + \dots + c_n w_n(x) \quad (3-5)$$

The weight function is introduced into the weak form as,

$$\int_0^{\Omega} \frac{dq(x)}{dx} w_i(x) dx = 0 \quad (3-6)$$

The term  $\frac{dq(x)}{dx}$  is called the 'residuals' meaning how far off from zero is the prediction. The shape of the weight function is plotted in Figure 3-3.

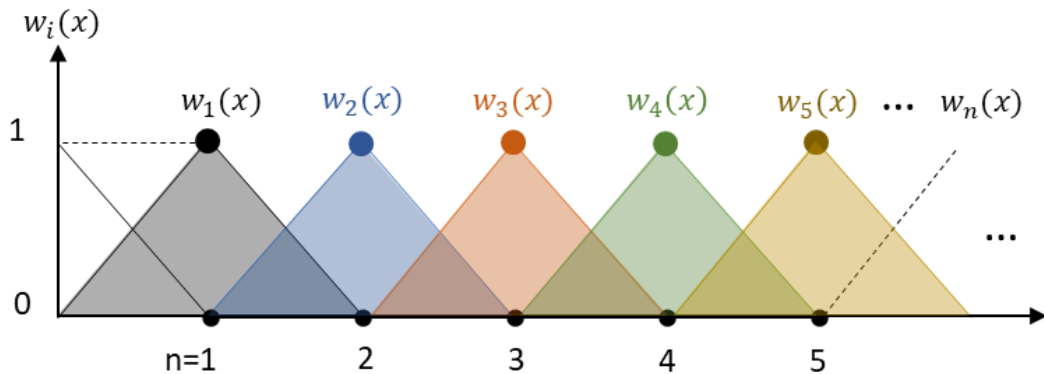


**Figure 3-3.** Linear weight function illustration.

Technically, the weight function is very flexible due to its combination of polynomials. It can be chosen so that for every  $x$  position along with the domain, the weight value at that node at  $x$  is 1 and smoothing out to 0 to neighboring nodes (as seen in Figure 3-3). Mathematically, the product  $\frac{dq(x)}{dx} w_i(x)$  is equivalent to,

$$\frac{dq(x)}{dx} c_0 w_0(x) + \frac{dq(x)}{dx} c_1 w_1(x) + \dots + \frac{dq(x)}{dx} c_n w_n(x) \quad (3-7)$$

The inner product of  $\left(\frac{dq(x)}{dx}\right)$  and  $w_i(x)$  can be thought of as the orthogonal projection of the residuals onto each term of the weight function. Therefore, instead of having to manually collect all the integrals at every node, the weight function restricts the contribution of the integral onto a small range centering around node  $x$ , thus achieving the same effect. The graphical representation of this procedure is shown in Figure 3-4, where a general function,  $f(x)$ , is projected onto the weight function, for example, at *node 3*,

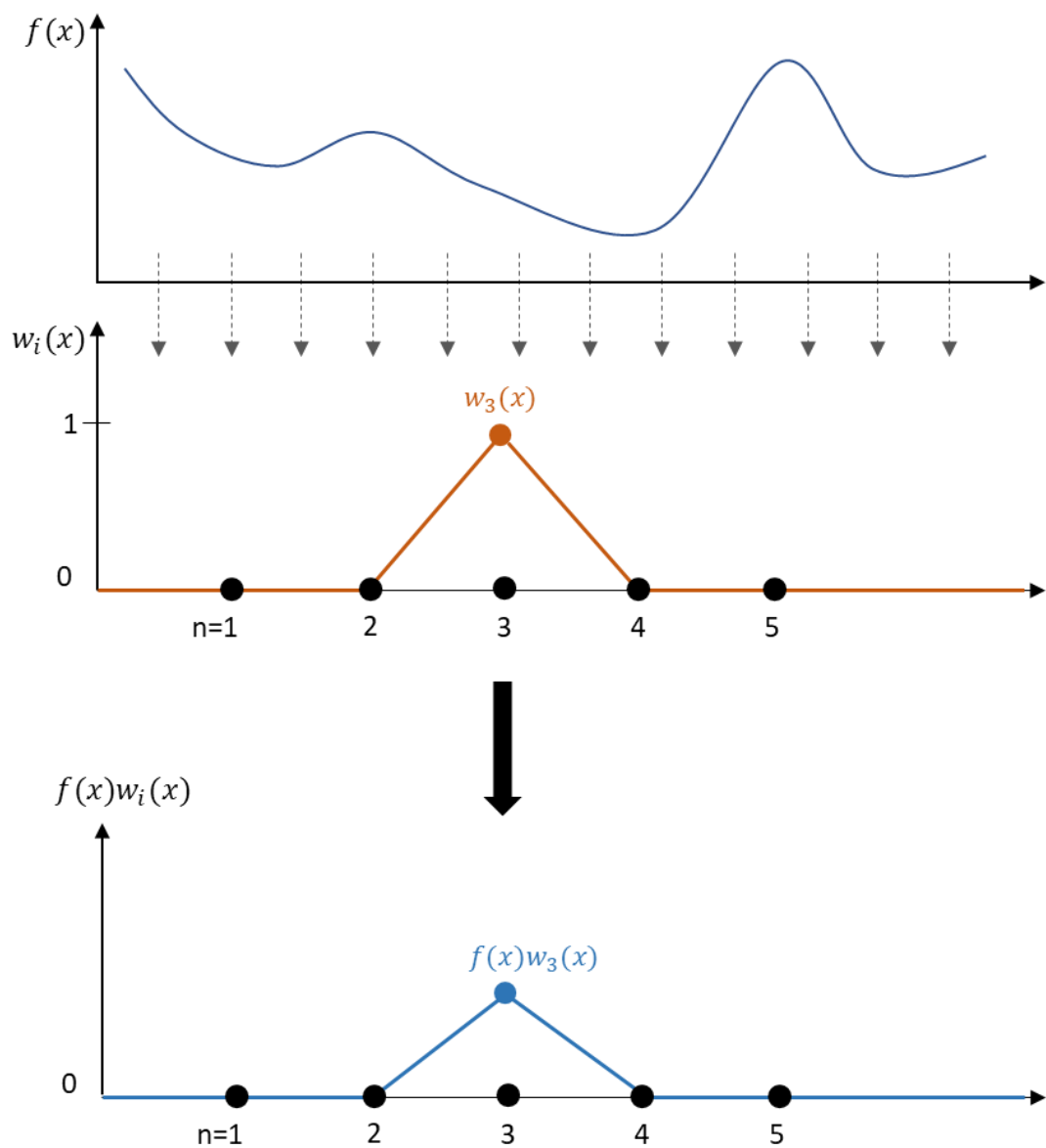


**Figure 3-4.** Graphical illustration of the inner product between the main function and the weight function at *node* = 3.

Figure 3-5 shows the approximation of function  $f(x)$  using 5 nodes on the interval  $\{0, \Omega\}$ .

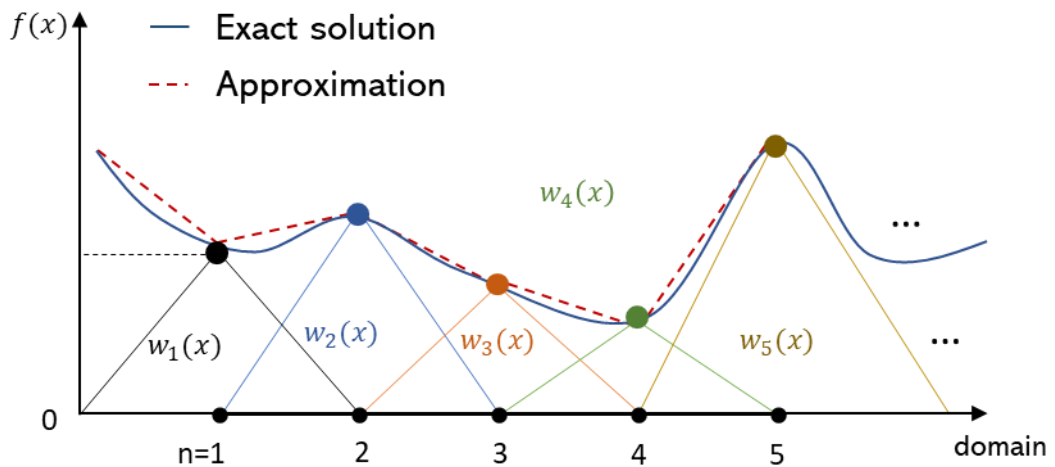


**Figure 3-5.** Approximation of general function  $f(x)$  using all 5 nodes. An approximation solution (dotted red line) is compared with an exact solution (blue line). The approximation solution converges to the exact solution as the number of nodes increase.

To sum up, the temperature profile along the 1D rod is the topic of interest and the principle of minimum energy requires the change of heat flux to be zero along the rod. The condition on the zero heat flux gradient is relaxed by asking for an *average heat flux gradient* to be zero instead of the exact heat flux gradient at any point, which is called '**Weak formulation**'. This approach is not accurate if the distance between nodes is too large. Hence, the rod is divided into many smaller parts and the 'Weak form' condition is applied to each individual part. The weight function is introduced to collectively connect the weak form of all pieces. The difference between the *approximated heat flux gradient* and *zero heat flux gradient* is termed 'residuals' and the main task is to minimise this difference. Moreover, the equation (3-6) is equivalent to,

$$\int_0^{\Omega} \frac{dq(x)}{dx} w_i(x) dx = \int_0^{\Omega} T'' w_i(x) dx = 0 \quad (3-8)$$

After carrying out the integration by parts,

$$\int_0^{\Omega} T''(x) w_i(x) dx = T'(x) w_i(x) - \int_0^{\Omega} T'(x) w_i'(x) dx \quad (3-9)$$

Conveniently, the temperature is now required to be only once-differentiable instead of twice-differentiable, as the derivative is shifted to the weight function. This is the reason why the weight function should be a combination of polynomials so that the whole equation (3-9) still holds at this point.

The method for approximating the temperature at each node to obtain the heat flux gradient for the formation of the 'weak formulation' is discussed next. The temperature is physically a continuous variable as it can take any number of significant figures and also can be evaluated at any point along with the domain at any time. Hence it needs to be transformed into a discretisable function, which is analogous to the 'weight function' concept. The temperature is approximated by a 'trial function' as follows,

$$\bar{T} = \sum_1^n T_i \phi_i(x) \quad (3-10)$$

Where  $u_i$  are unknown coefficients and  $\phi_i(x)$  is the 'basis function', or 'shape function' or 'interpolation function'.

All the main equations and main variables are now in the form of summation functions ready to be discretised. The question now lies in how to choose the basis function within the trial function. Galerkin method is the original FEM technique in which the basis function is chosen as the weight function to ensure differentiability. This simplest form of basis function is informally named as 'a hat function' and expressed in equation (3-11) and (3-12),

$$N_i(x) = \begin{cases} \frac{x - x_{i-1}}{h_i} & \text{for } x_{i-1} < x < x_i \\ \frac{x_{i+1} - x}{h_{i+1}} & \text{for } x_i < x < x_{i+1} \\ \dots & \dots \end{cases} \quad (3-11)$$

And its derivatives,

$$N'_i(x) = \begin{cases} \frac{1}{h_i} & \text{for } x_{i-1} < x < x_i \\ \frac{-1}{h_{i+1}} & \text{for } x_i < x < x_{i+1} \\ \dots & \dots \end{cases} \quad (3-12)$$

This function is technically known as a *piece-wise linear basis function*, of which the illustration can be referred to as the weight function in Figure 3-3. A more complicated form such as the *piece-wise quadratic basis function* is shown in Figure 3-6,

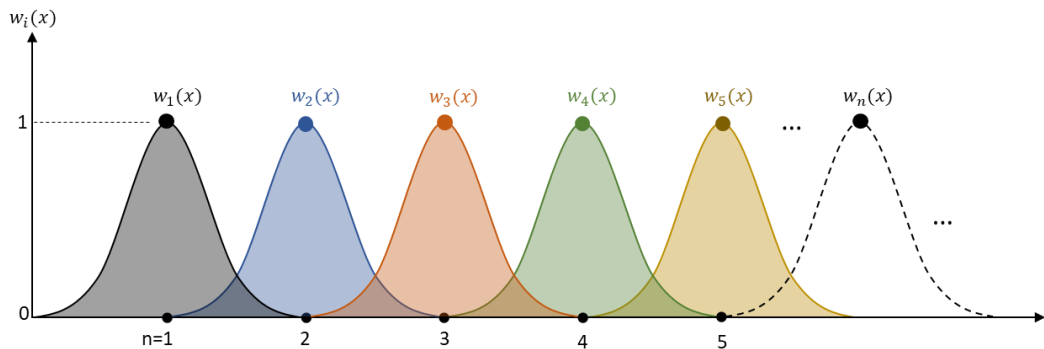


**Figure 3-6.** Graphical plot of the piece-wise quadratic basis function. Different colours represent different basis functions for different nodes.

Any components in the weak form can be transformed to the trial function's format which is the sum of polynomials,

$$\int_0^{\Omega} T'' w_i(x) dx = \int_0^{\Omega} \left[ \sum_1^n T_i \phi_i(x) \sum_1^n c_i w_i(x) \right] dx = 0 \quad (3-13)$$

Or

$$\int_0^{\Omega} T'' w_i(x) dx = \sum_1^n T'_i \phi_i(x) \sum_1^n c_i w_i(x) - \dots$$

$$\dots \int_0^{\Omega} T'(x) \sum_1^n c_i w'_i(x) dx = 0$$
(3-14)

Rearranging equation (3-14) into a matrix form gives,

$$\mathbf{AT} = \mathbf{b}$$
(3-15)

Where  $T$  is the vector of unknown variable  $T = [T_1, T_2, \dots, T_n]$ ,  $A$  is the stiffness matrix ( $n \times n$ ) containing all the unknown coefficients of  $T_i$  in row  $j$ , and  $\mathbf{b}$  is the heat source value vector which is 0 in this case.

We have now transformed the 'Strong form' into the 'Weak form', and into a discretisable form using the summation scheme (seen in equation (3-5)). This equation will be solved by a designated solver, either by Direct or Iterative solvers. The process repeats until the residual, in which the approximated heat flux gradient is close to zero within a given tolerance.

A finite element method is a powerful tool in solving an engineering problem involving irregular geometry with discontinuities at interfaces. The computational result is accurate and reliable given small enough elements. Many physics problems also involve a moving interface in which a controlled domain changes its size with time. An extra mathematical tool is needed to track this movement of the boundary condition, and hence the computed solutions are kept accurate. The next section discussed the interface tracking method used in this thesis and its theory.

### **3.1.1. Arbitrary Lagrangian-Eulerian interface tracking method**

The chosen interface tracking method is the Arbitrary Lagrangian-Eulerian (ALE) method. This is a powerful method to track the moving interface in computational fluid mechanics. This method is explained in the following sections including the fundamental principle, the limitations and the motivation behind developing such method, and also its implementation into the simulation.

#### **3.1.1.1. Principal theory**

The theoretical concepts underlying the formation of the arbitrary Lagrangian-Eulerian method is reviewed in this section, which will explain the motivation behind the method. In any set of governing equations, all the dependent variables can be a function of the spatial coordinates and time. The time evolution of the physics involved can be described using a coordinate system, or so-called the '*kinematics description*'. The choice of an appropriate coordination scheme, which is formally named the '*frame of reference*', determines the practicality for solving the problem accurately and efficiently. First, there are two basic viewing perspectives to an object or particles in motion: the Lagrangian and the Eulerian views, which were developed by the two great mathematicians *Leonhard Euler(1707)* and *Joseph-Louis Lagrange (1736)*. While Leonhard Euler made a huge contribution to Mathematics including geometry, trigonometry, and calculus, Joseph-Louis Lagrange is famous for his work in variational calculus and his well-known *Lagrangian multiplier* method in mechanics. Their work is both important and critical in the development of the continuum mechanics field.

In the Lagrangian perspective, the frame of reference moves together with an object. This type of frame is called the '*Material frame*'. An analogous example of this is the speedometer attached

to a car to measure its instantaneous velocity. In this type of description, all the mesh nodes and elements will move with the physical object. This is particularly helpful in structural mechanics and modeling of the material with history-dependent properties. The deformation of solid over time can be conveniently calculated, without the need of updating the spatial position at every time step. However, when the material is exceedingly distorted, such as the vortices in turbulent flow, the accuracy is completely lost due to inverted mesh. The 'remeshing' procedure is often needed in the Lagrangian system.

In contrast, the Eulerian perspective holds a fixed frame of reference and an object moves with respect to the frame, or the computational grid. Therefore it allows for a strong deformation without the need of reconstructing the mesh. The frame used in this approach is called the 'Spatial frame' or 'Laboratory frame'. This can be thought of as a fixed speed camera taking the velocity of many cars passing through a fixed area on the road.

The following example illustrates the distinct characteristics between the two coordinate systems and how they can be converted interchangeably. This is highly useful to understand the basis of the ALE method. Consider a ball made up of two different materials with different densities represented by the blue and the orange domains (seen in Figure 3-7 and Figure 3-8), rolling down a slope under the effect of gravity. The gravitational force on each domain will, therefore, be of different magnitude due to the different mass on each half. The position of the ball is taken at  $t = 0 \text{ s}$ ,  $t = 1 \text{ s}$  and  $t = 2 \text{ s}$ .

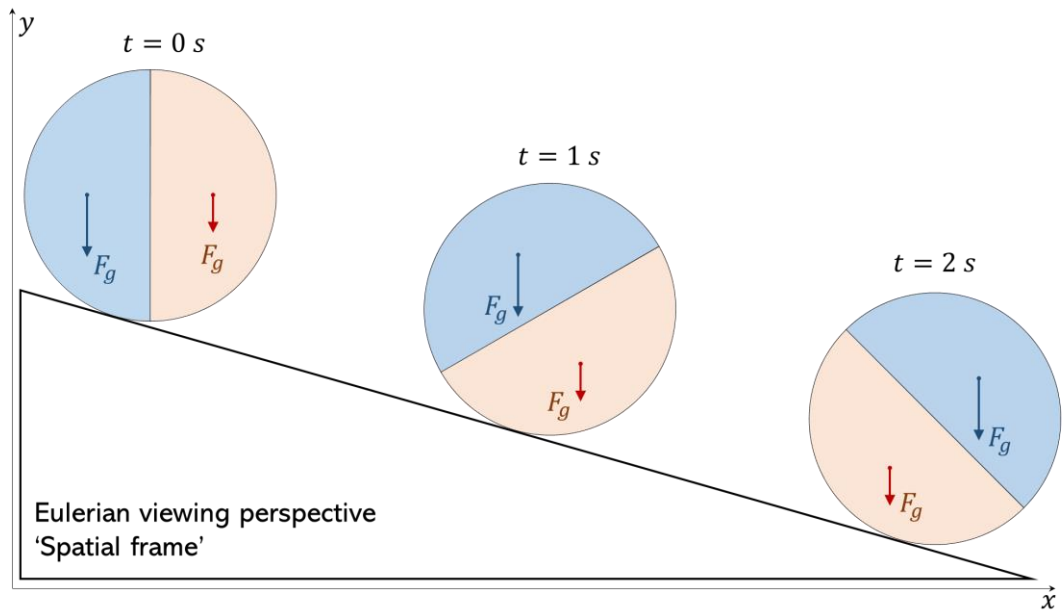


**Figure 3-7.** Eulerian perspective of a ball rolling down the hill under gravity. The gravity always points downwards in the  $y$ -direction as the ball rolls down the slope.

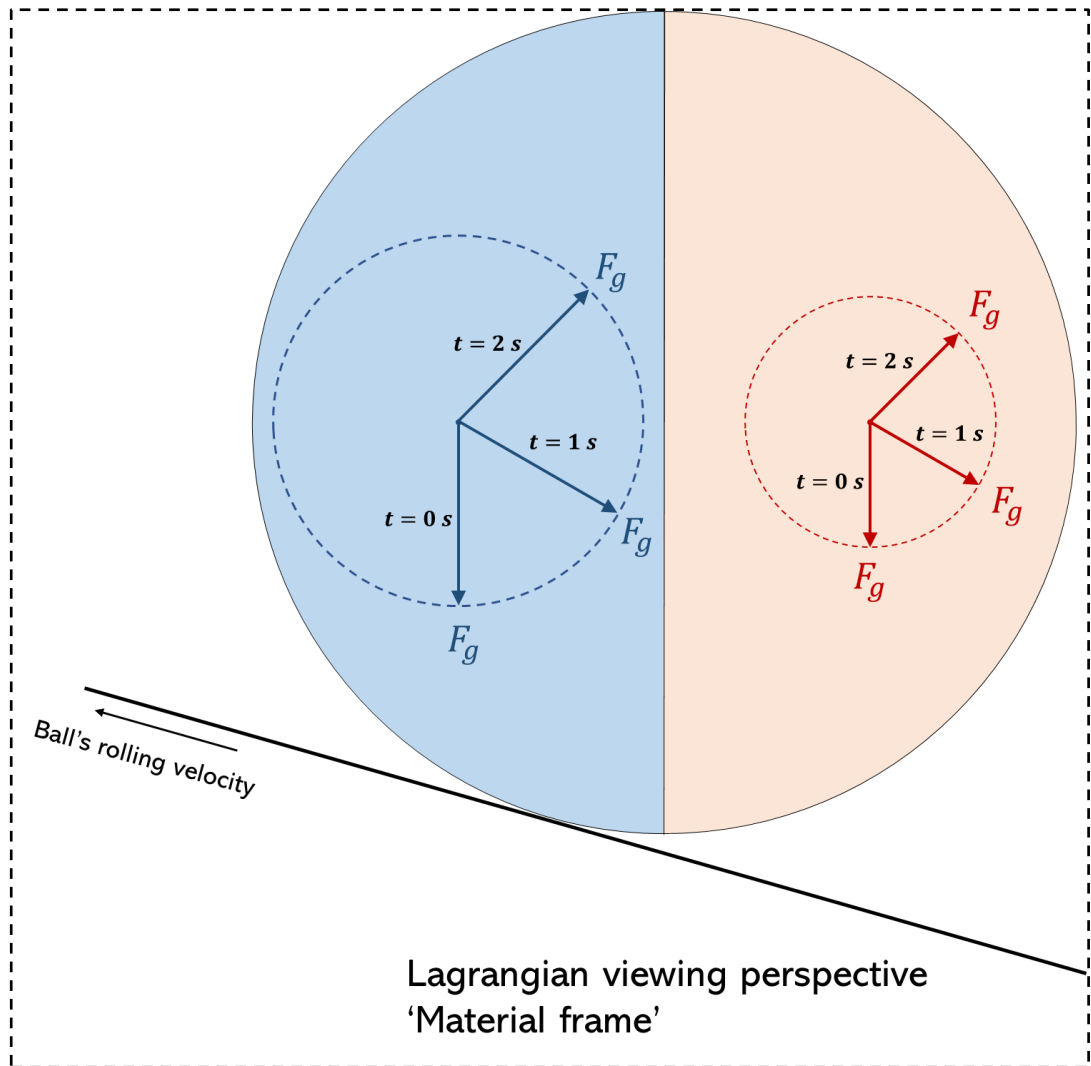


**Figure 3-8.** Lagrangian perspective of a ball rolling down the hill under gravity. The ball velocity is pointing up the hill in the Lagrangian frame. The gravity changes its direction during the rolling instead of being fixed in the Eulerian frame.

The position and direction of the gravitation force are what distinguishes the Eulerian and Lagrangian coordinate systems. In the Eulerian view (Figure 3-7), the gravitational force is always vertically downwards despite the state of the ball. This is because the gravity is calculated with respect to a fixed coordinate ( $x,y$ ). So the  $x$ -component of  $F_g$  changes over time while the  $y$ -component is fixed. The picture is different in the Lagrangian view, which is shown in Figure 3-8. In this system, the rolling action will not be observed because the viewing frame is attached to the ball, so it is always

stationary. The slope will move relatively upwards as time progresses.

In this material frame, the changing external force, such as gravity, acting on a fixed ball is varied. Hence, instead of observing the rotational motion of the ball, the circular locus of the gravitational forces on two halves of the ball is seen (dotted lines in Figure 3-8). The x and y components of  $F_g$  are now fixed while its direction changes over time. The angle of rotation of gravity in Figure 3-8 can be related to the distance travelled by the ball in Figure 3-7 accordingly.

Generally, due to the nature of the Lagrangian coordinate system, the free surface or the fluid-structure interface can be tracked accurately. However, the mesh associated with the Lagrangian method cannot afford a strong distortion, as seen in Figure 3-9.

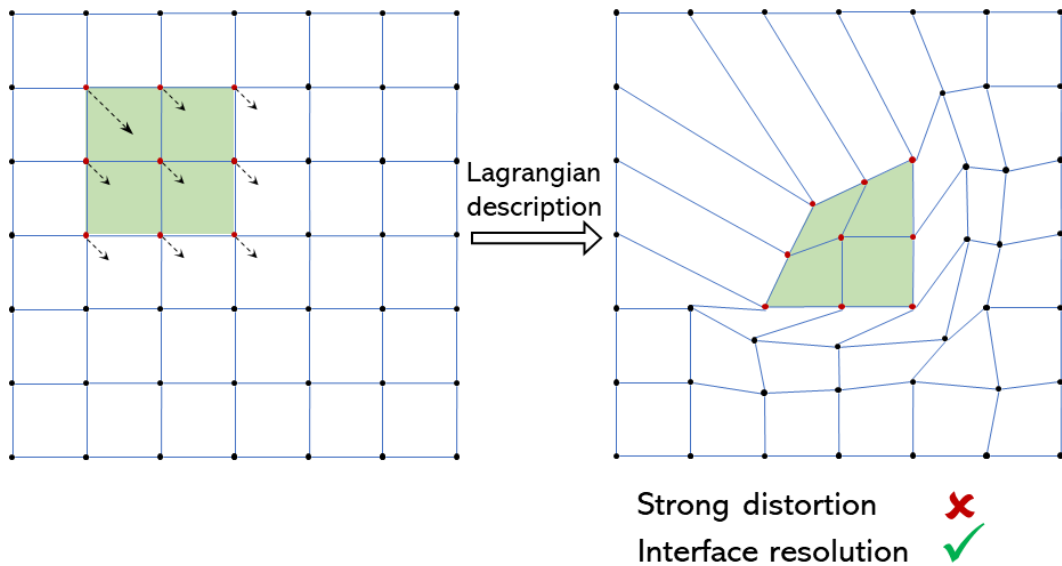


**Figure 3-9.** Mesh distortion problem associated with the Lagrangian view. Movement direction of the nodes (red points) on an object (green domain) is showed on the left side, and the resultant mesh is on the right. The mesh **does** deform together with an object in the Lagrangian description of motion.

As all the red nodes must move together with the green object, a slight deformation on the top left corner of the square results in a heavy mesh skewness. Any heavier deformation will cause inverted elements and terminate the FEM solving procedure, hence requiring frequent 'remeshing' operations. The general velocity description of the green square in Lagrangian and Eulerian system are expressed as follows,

$$v_{Lagrangian} = v(t) \quad (3-16)$$

$$v_{Eulerian} = v(x, y, t) \quad (3-17)$$

On the other hand, as the spatial coordinate  $(x, y, z)$  is required at each time step in the Eulerian method, a precise interface tracking is essential for the next time step to be reliable, which is computationally demanding. An illustration of the Eulerian mesh is in Figure 3-10.

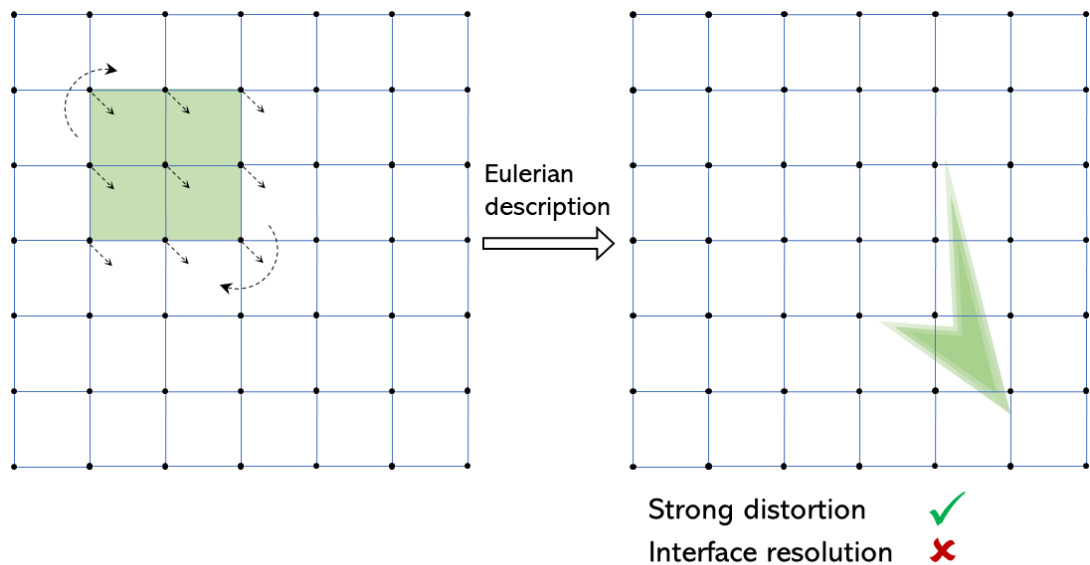


**Figure 3-10.** Loss of interface resolution problem associated with Eulerian view. The direction for every node (red points) on the object (green domain) is shown on the left, and the results movement is on the right. The mesh **does not** deform in Eulerian description of motion.

Extreme distortion of the green square can now be described using the Eulerian system without a meshing problem, however at the cost of the interface resolution. In order to have a highly resolved interface, it requires a small time step and higher-order interpolation function to achieve. The Lagrangian method favors the problems in mechanics while the Eulerian's coordinate is mostly used in fluids flow equations. The limitations of each approach had been discussed. Therefore, the problem involving the fluid-structure interaction will be a challenge to model using only one viewing perspective.

The arbitrary Lagrangian-Eulerian (ALE) method was developed aiming to combine the best features of Lagrangian's and Eulerian's methods, while trying to minimise their weaknesses. A first obvious approach to combine the two systems is to have a mesh moving in an 'average' manner between the Lagrangian and Eulerian motion, so the detail of the interface is clearly retrieved and a large distortion is still bearable (seen in Figure 3-11). The motion of ALE mesh can be defined arbitrarily so that the mesh rezoning capability is conserved.

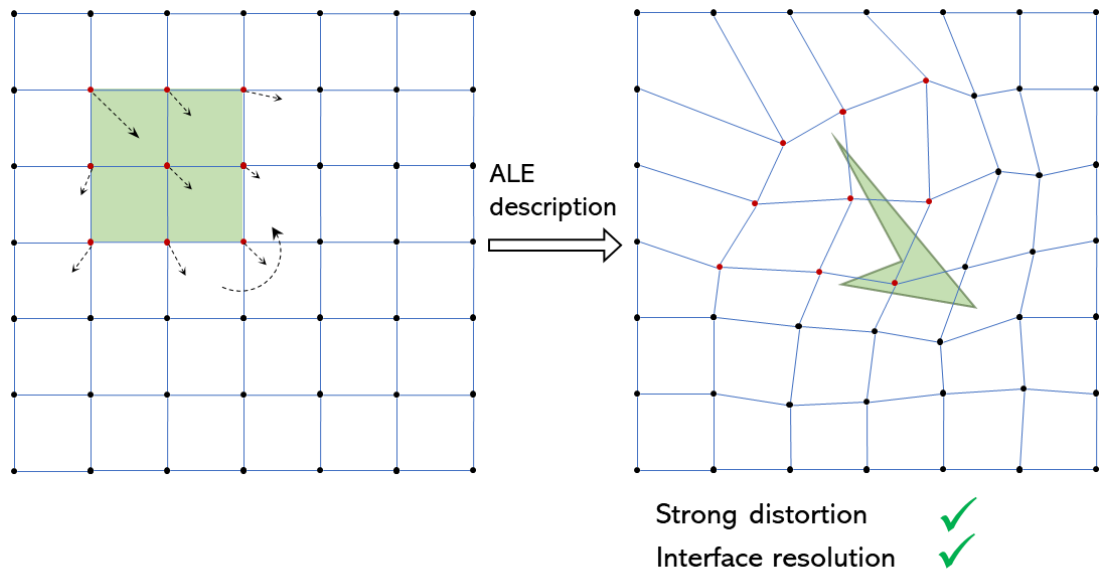


**Figure 3-11.** Mesh structure and interface resolution in ALE mesh. Direction of mesh distortion is shown on the left and the resultant mesh is on the right. An object is represented as the green domain with the according nodes (red points). The mesh partly deforms with an object in the ALE algorithm.

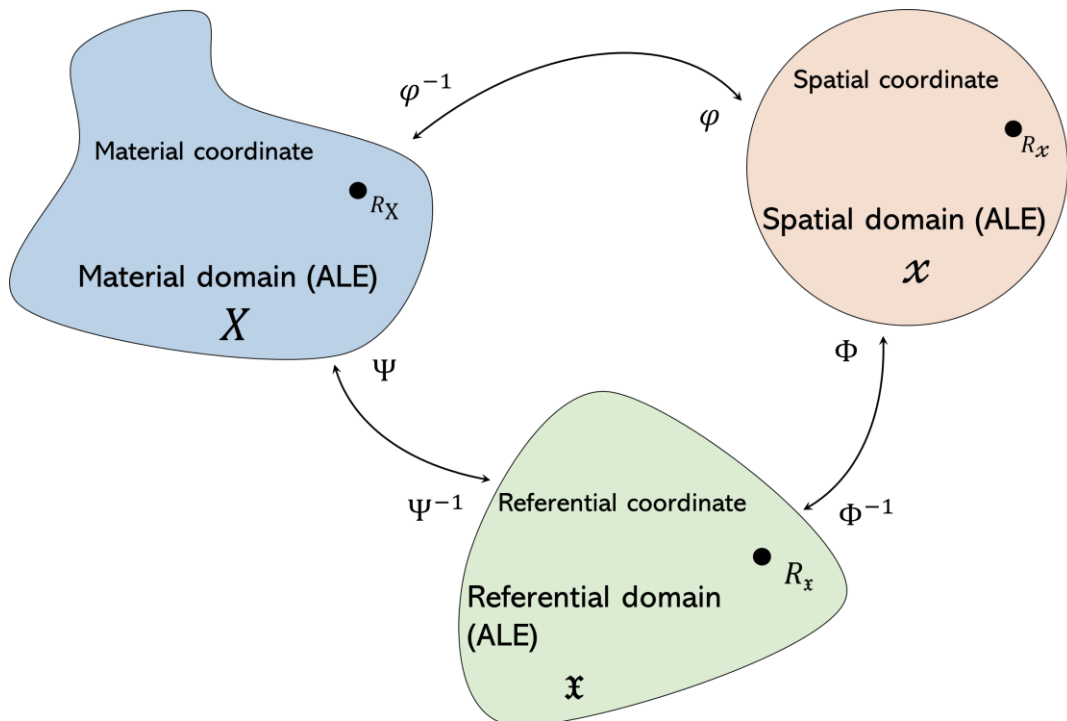


**Figure 3-12.** Domains and mapping function involved in the ALE method. All three domains and coordinates are accessible and mathematically convertible.

Neither the material frame nor spatial frame is taken as reference in the ALE method, but a third domain named 'referential domain'. One-to-one mapping functions are needed to map the 'spatial frame',  $x$ , and the 'material frame',  $X$ , to the 'referential frame',  $\mathfrak{x}$ . This mapping procedure is illustrated in Figure 3-12. The mapping functions used to convert the 'referential domain',  $\mathfrak{x}$ , to the 'material domain',  $X$ , and the 'referential domain',  $\mathfrak{x}$ , to the 'spatial domain',  $x$ , and the 'material domain',  $X$ , to the 'spatial domain',  $x$ , are symbolised as  $\Psi$ ,  $\Phi$ , and  $\varphi$  respectively. Their inverse functions for inverse mapping are also in the same order. It should be noted that the mesh in the referential domain is now moving arbitrarily at a different velocity relative to the material object that gives rise to the concept of convective effects. The relative velocity between 3 domains are defined as,

$$v(t) = \left. \frac{\partial x}{\partial t} \right|_{\mathfrak{x}} - \text{material velocity} \quad (3-18)$$

$$w(t) = \left. \frac{\partial X}{\partial t} \right|_{\mathfrak{x}} - \text{mesh velocity} \quad (3-19)$$

$$c(t) = v(t) - w(t) = \left. \frac{\partial \mathfrak{x}}{\partial t} \right|_x - \text{convective velocity} \quad (3-20)$$

It is instinctively easy to interpret these mapping functions. Imagine if we stand on the spatial domain, the referential domain will move at the mesh velocity,  $w(t)$ , and if we stand on the material domain, the referential domain will move at the convective velocity,  $v(t)$ . The convective velocity,  $c(t)$  is an object velocity relative to the mesh seen from the spatial domain. Figure 3-13 shows a graphical representation of all relative velocity,

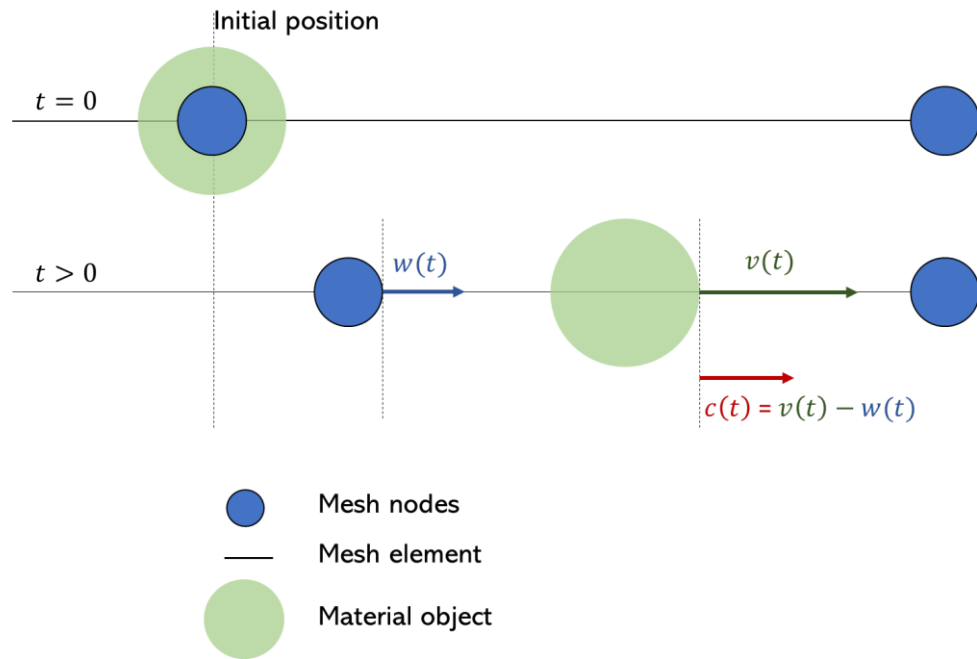


**Figure 3-13.** Convective velocity representation. At  $t = 0$ , both the mesh node and the object are in the same position. As time progresses, the mesh node moves due to the displacement of the object, but not at the same rate. This gives rise to the convective velocity variable.

In the fluid-structure interaction problem, the material displacement is solved within the solid domain using the Lagrangian coordinate, while the flow governing equation using the Eulerian coordinate is solved within the fluid domain. More specifically, the structural mechanics equation determines the mechanical displacement of the spatial coordinate to the material coordinate, meanwhile, the fluid flow equation determines the flow motion using spatial coordinate. Hence to couple the two governing equations in two domains, the boundary condition is applied at the fluid-structure interface, such that the movement of the spatial frame (Eulerian system) must match the mechanical displacement of the spatial frame obtained from the solid mechanics (Lagrangian system). However, the deformation vector from the solid domain does not need to be transferred exactly to the fluid. This is because the orientation of the nodes and elements in the fluid domain is not critical since all

the solution is solved from the fixed frame of Eulerian coordinate. Moreover, an exact translation of the solid deformation might cause an inverted mesh near the fluid-structure interface. Therefore, it is instead adapted and smoothed out over the liquid domain using smoothing techniques. The smoothing options are very important affecting how the interface deformation can be easily interpreted. It should be noticed that even the ALE is best suited for fluid-solid interaction or any problem that utilises both the Lagrangian-Eulerian systems, it is also relevant and applicable to the fluid-only system with the phase change that occurs at the interface. The interface displacement due to the material exchange can act similarly to the displacement from solving solid mechanics. Next, the smoothing techniques are discussed and finalizing to choose which technique is the most suitable for the droplet drying system.

### 3.1.1.2. Smoothing techniques

The domain mesh will deform together with the movement of the fluid-fluid or fluid-structure interfaces. In order to ensure a consistent deformation, the interface displacement is propagated throughout the domain by solving the Laplace, Winslow, Hyperelastic, or Yeoh's smoothing partial differentiation equations. The expression of these PDEs are shown below with  $x$  and  $y$  is the spatial coordinates,  $X$  and  $Y$  is the reference coordinates.

- Laplace smoothing equations

$$\frac{\partial^2}{\partial X^2} \frac{\partial x}{\partial t} + \frac{\partial^2}{\partial Y^2} \frac{\partial x}{\partial t} = 0 \quad (3-21)$$

$$\frac{\partial^2}{\partial X^2} \frac{\partial y}{\partial t} + \frac{\partial^2}{\partial Y^2} \frac{\partial y}{\partial t} = 0 \quad (3-22)$$

- Winslow smoothing equations

$$\frac{\partial^2 X}{dx^2} + \frac{\partial^2 X}{dy^2} = 0 \quad (3-23)$$

$$\frac{\partial^2 Y}{dx^2} + \frac{\partial^2 Y}{dy^2} = 0 \quad (3-24)$$

- Hyperelastic smoothing equations

This smoothing technique is inspired by Neo-Hookean materials where it solves the mesh deformation by minimizing the energy equation,

$$W = \int \frac{\mu}{2}(I_1 - 3) + \frac{\kappa}{2}(J - 1)^2 dV \quad (3-25)$$

Where  $\mu$  and  $\kappa$  are artificial shear and bulk moduli. The invariants  $J$  and  $I_1$  are given as,

$$J = \det(\nabla_X x) \quad (3-26)$$

$$I_1 = J^{-\frac{2}{3}} \text{tr}((\nabla_X x)^T \nabla_X x) \quad (3-27)$$

- Yeoh smoothing equation

The Yeoh technique is based on the hyperelastic material. It is a general version of the Hyperelastic technique which contains the three-term Yeoh hyperelastic model,

$$W = \frac{1}{2} \int C_1(I_1 - 3) + C_2(I_1 - 3)^2 + C_3(I_1 - 3)^3 + \kappa(J - 1)^2 dV \quad (3-28)$$

Where  $C_1$  and  $C_2$  and  $C_3$  are artificial material properties.  $C_1$  and  $C_3$  are set to 1 and 0, while the  $C_2$  value controls the stiffening of the deformation.

In general, Laplace smoothing method requires the least computational power due to its linearity and independence between coordinate directions. The inversion of the mesh elements is likely to be encountered using this method, and therefore is only suitable for small linear deformations. The other three non-linear smoothing techniques, on the other hand, couple all the coordinate directions together which is more expensive to solve. Mathematically, the solution to these highly non-linear equations requires positive volume everywhere and hence avoiding the inverted elements. The Winslow method is best to solve for a stretched mesh because it allows the furthest stretching. The Hyperelastic and Yeoh methods share the same theoretical property for compression mesh. The Yeoh method is more advanced in terms of distributing evenly the large deformation across the domain by increasing the stiffness of the distorted elements. However, it is more likely to cause a divergence solution because of the strong non-linearity set of equations. As the droplet drying system is likely to encounter stretched mesh and linear surface deformation, the Laplace or Winslow smoothing techniques are most suited due to the low computational time and effort.

In summary, the finite element method (FEM) with the Arbitrary Lagrangian-Eulerian (ALE) interface tracking method are used to model the droplet drying system. All the governing equations are turned into weak forms, discretised using linear or higher-order shape functions, and assembled into a final matrix. The whole matrix was then solved by a specific solver adopting the Backward Differentiation Formula (BDF) used as the time-stepping scheme. The deformation of the mesh at the fluid-solid interface is propagated to all other elements. The mesh deformation within the fluid domain is smoothed out using the smoothing functions (Laplace or Winslow algorithms).

### 3.2. Theory of 'Drag' and 'Lift' on an object

An introduction to the theory of drag and lift is presented here as background knowledge for the next section in the validation benchmarks. When a flow passes an object, such as a sphere, it exerts a force onto the surface. The force can be decomposed into the 'Lift' and 'Drag' components that are perpendicular and parallel to the flow direction, respectively. When the flow approaches the sphere, the velocity field changes as the fluid curves around the sphere, as shown in Figure 3-14. The vortex shedding might develop in the wake at a high Reynolds number (Kaneko *et al.*, 2014).

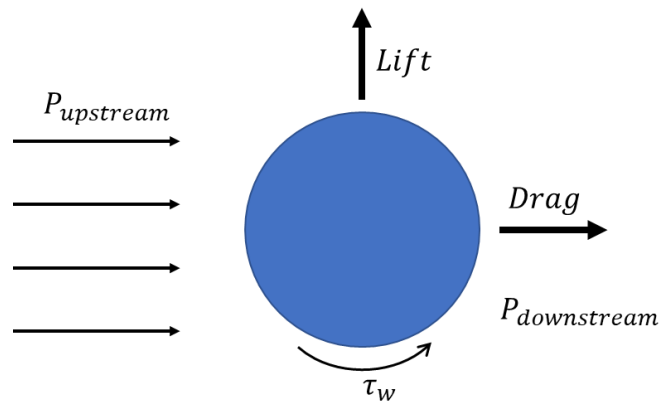


**Figure 3-14.** Illustration of fluid flow passing through a solid sphere.

Mathematically, the relative velocity is more important in this system rather than the individual velocity profile of the sphere or the fluid. Therefore, it is often more convenient to have a frame of reference on the sphere while the fluid is flowing past it. The drag and lift forces arise due to the pressure and viscous stresses acting on the surface of a sphere. The pressure acts perpendicular to the surface and will be higher on the upstream due to the nature of the flow, hence creating an overall force acting in the flow direction. The viscous stress acts tangentially along the solid surface as the flow curves around to past the sphere. The *drag* resulted from the pressure and viscous stresses are called the 'form drag' and the 'friction drag', respectively. The parallel component (x-component

in this case) of total forces forms the '*drag*' and the perpendicular component (y-component) forms the '*lift*' on the body. The drag and lift depend heavily on the morphology of an object and Reynolds number, and it is normally referred to under the form of the drag and lift coefficients. The two coefficients are formulated by dividing the correspondent forces by the projected area of the body onto the plane perpendicular to the flow's direction, and the reference stress,

$$C_D = \frac{2F_D}{\rho U^2 A_{projected}} \quad (3-29)$$

$$C_L = \frac{2F_L}{\rho U^2 A_{projected}} \quad (3-30)$$

Where  $F_D$  and  $F_L$  are the drag and lift force on the body,  $A_{projected}$  is the projected area of the body to the perpendicular plane to the flow,  $U$  is the relative velocity between fluid and a considered body,  $\rho$  is the fluid density.

### **3.3. Development of proportional-integral-derivative (PID) feedback loop for predicting the terminal falling velocity**

The lack of investigation on the physics of a falling droplet mentioned in the conclusion section (section 2.2) on page 56 is mentioned again to clarify the purpose of this section. In the experimental studies of the single droplet drying, the droplet is hung on a filament subjecting to a constant velocity of a hot gas stream. Although this is a stable and controllable environment, the experiment does not represent fully the drying condition the droplets encountered within the spray dryer. Theoretically, the droplet would reach its terminal velocity after leaving the atomiser. This terminal falling velocity would changes as drying progresses due to the change in the droplet size. Overall, the droplet would fall

with a dynamic terminal velocity which is challenging and not practical to recreate under the laboratory environment. This area is left untouched and the published work that considered this physics is extremely scarce despite the importance of the phenomenon. Therefore, this thesis develops an innovative simulation scheme that can capture the droplet drying while falling with a changing terminal velocity in the air. This section discusses the development of the feedback algorithm which is designed to control the terminal falling velocity of a droplet. The chosen feedback algorithm is the proportional-integral-derivative (PID) loop that is commonly used in chemical process control. One of the reasons for the implementation of PID is due to the mesh deforming nature of the ALE method. Particularly, the ALE method ensures an accurate interface capturing with its mesh being deformed together with the interface. Despite the advantage over other interface tracking methods, it poses a problem of not being able to have zero volume or the mesh cannot be 'torn', which means the ALE method is only applicable to a 'moving' interface' without breaking up or inverting any element's facet. This is challenging in terms of modeling a falling cylinder or droplet in an infinite air channel, since the periodic boundary condition cannot be applied. The only viable solution is to design a domain that is long enough to accommodate the whole drying process. This will likely cause the channel to be unrealistically long and require huge computational resources to solve for unnecessary domain elements. Therefore, a *proportional-integral-derivative* (PID) control algorithm is needed to prevent the object from leaving its original position while still preserving the physics of falling.

The PID control algorithm includes the variables to be controlled and the condition to which the controlled variables will be adjusted to satisfy such conditions. Many variables can be controlled to achieve this terminal falling velocity goal, for example, the inlet velocity, gravity or the outlet pressure. Since the constraint is to have no

displacement of the droplet from its initial position, the condition can be set on the following variable,

$$\Delta x = 0 \quad (3-31)$$

$$\Delta v = 0 \quad (3-32)$$

$$\sigma_{total} = 0 \quad (3-33)$$

Where  $x$  is an object's displacement,  $v$  is the object's velocity and  $\sigma_{total}$  is the total stress acting on the surface of the falling object in the direction of the airflow. All three constraints can be visualised in Figure 3-15.

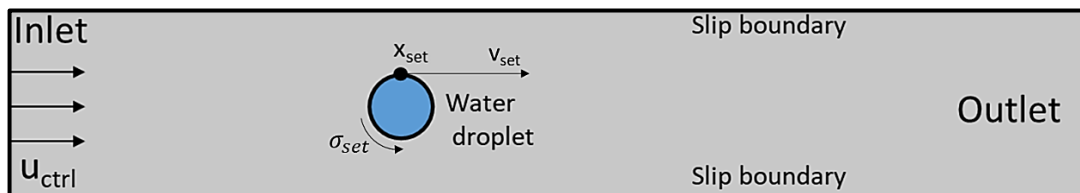


**Figure 3-15.** Constraints for PID algorithms.

The constraint on an object's displacement is well suited in this context since it is directly linked to the goal (zero droplet displacement) set by PID. However, given the fact that the falling object will surely slip from its original position in the first few time steps when the control variable is varying and trying to approach its equilibrium value, the control variable might keep adjusting unnecessarily to push the droplet back to the initial position, rather than keeping the new equilibrium position. The PID algorithm is set up using the displacement constraint first, and in case the PID performance is not adequate, the two other constraints will be considered. The inlet air velocity is, hence, chosen as a controlled variable in this study.

### 3.3.1. Problem formulation and setup

The simulation setup involves a falling circular cylinder in the air at room temperature (25°C) and atmospheric pressure (1 atm), as shown in Figure 3-16,

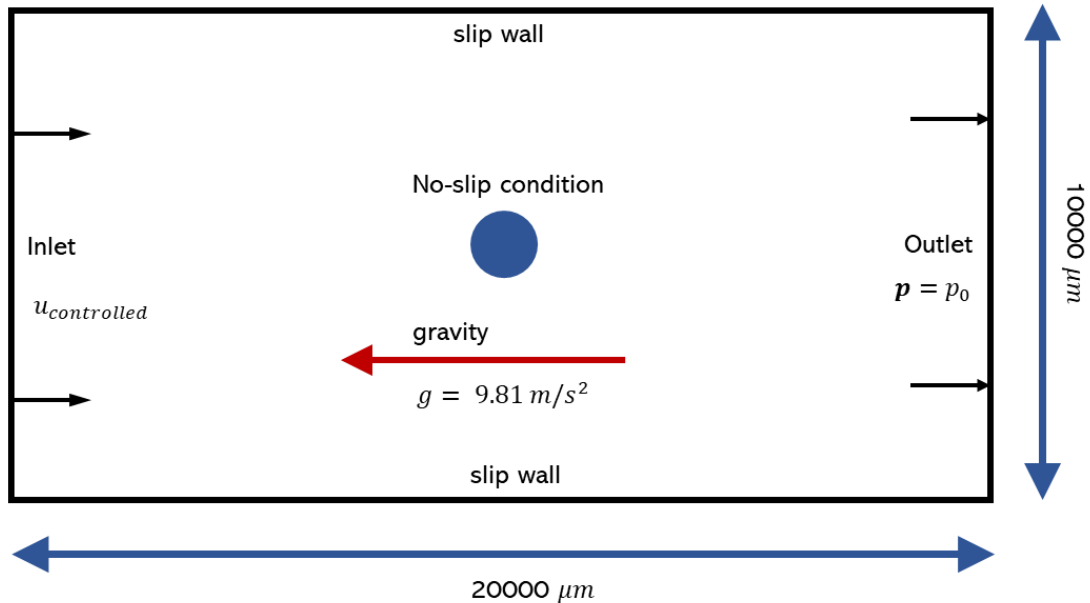


**Figure 3-16.** Schematic of simulation setup for testing the PID algorithm.

The domain includes the inlet (left), the outlet (right), with the 'slip' condition at two side walls and the 'no-slip' condition at the cylinder interface. The air is introduced at the inlet and exits the domain through the outlet. The gravity is in a horizontal direction. The domain length and height are  $20000 \mu\text{m}$  and  $10000 \mu\text{m}$ .

The gravity set in the x-direction is opposite to the direction of the inlet velocity. The wall is set to the 'slip' condition to have no flow profile at the two side walls, and the 'no-slip' condition is applied to the cylinder surface. The cylinder radius is varied from  $20 \mu\text{m}$  to  $300 \mu\text{m}$  and the air channel is  $20,000 \mu\text{m}$  in length and  $10,000 \mu\text{m}$  in height. The cylinder density is chosen to be  $1000 \text{ kg/m}^3$  which is similar to the water droplet. The reason to choose this density is to have a more convenient transition from falling of the solid cylinder to the falling of a water droplet in a later stage. The Reynolds

number in this study will cover the range in which both the stable wake and the vortex shedding in the wake are observed.

### 3.3.2. Governing equations and boundary conditions

The main governing equation solved for in the model is the general Navier-Stokes equation in the form of,

$$\frac{\partial \rho}{\partial t} + \rho \nabla \cdot \mathbf{u} = 0 \quad - \text{Incompressible flow} \quad (3-34)$$

$$\rho \frac{\partial \mathbf{u}}{\partial t} + \rho (\mathbf{u} \cdot \nabla) \mathbf{u} = \nabla \cdot \left[ -p\mathbf{I} + \mu(\nabla \mathbf{u} + (\nabla \mathbf{u})^T) - \frac{2}{3}\mu(\nabla \cdot \mathbf{u}) \right] + \mathbf{F} \quad (3-35)$$

Where  $\rho$  is the density,  $\mathbf{u}$  is the velocity field,  $p$  is the pressure,  $\mu$  is the dynamic viscosity and  $\mathbf{F}$  is the volume force which is gravity in this setup. The 'no-slip' and 'slip' conditions are expressed as,

$$\mathbf{u} \cdot \mathbf{n} = 0 \quad - \text{Slip condition} \quad (3-36)$$

$$\mathbf{u} = 0 \quad - \text{No slip condition} \quad (3-37)$$

The boundary conditions at the inlet and outlet are,

$$\mathbf{u} = (u_{ctrl}, 0) \quad - \text{horizontal inlet flow} \quad (3-38)$$

$$p_{outlet} = 101325 \text{ Pa} \quad (3-39)$$

And the PID algorithm is,

$$u_{ctrl} = \mathbf{k}_p(x - x_{set}) + \mathbf{k}_I \int_0^t (x - x_{set}) dt + \mathbf{k}_D \frac{\partial}{\partial t} (x - x_{set}) \quad (3-40)$$

Here, the  $u_{ctrl}$  (m/s) is the control velocity at the inlet,  $k_p$  ( $s^{-1}$ ) is the proportional gain,  $k_I$  ( $s^{-2}$ ) is the integral gain,  $k_D$  is the derivative gain and  $x$  is the displacement in the x-direction of the point originally at  $(x_{set}, r_{drop})$  coordinate (referred to  $x_{set}$  in Figure 3-15). Initially, the  $k_I$  and  $k_D$  are set to 0. The theoretical terminal falling velocity of a sphere is calculated to have a rough estimation of tuning the  $k_p$  gain. The idea is to consider the worst case scenario

where the sphere slips a large distance from its initial position at the first few timesteps. And from that large distance slip,  $k_p$  can be tuned to prevent this scenario from happening. The force balance for the derivation of the falling velocity is expressed as,

$$F_{weight} = F_{drag} + F_{buoyance} \quad (3-41)$$

Where  $F_{weight}$ ,  $F_{drag}$  and  $F_{buoyance}$  are respectively the gravitational force, the drag force on the cylinder and the buoyancy force. Considering the cylinder dimension, the formula for these forces are,

$$F_{weight} = mg = \rho_{cylinder} A_{cross-sectional} Lg \quad (3-42)$$

$$F_{buoyance} = \rho_{fluid} A_{cross-sectional} Lg \quad (3-43)$$

$$F_{drag} = \frac{1}{2} C_d \rho_{fluid} v_{terminal}^2 A_{projected} \quad (3-44)$$

Rearranging equation (3-41), (3-42), (3-43) and (3-44) gives,

$$v_{terminal} = \sqrt{\frac{2A_{cross-sectional}Lg}{A_{projected}C_d} \left( \frac{\rho_{cylinder} - \rho_{fluid}}{\rho_{fluid}} \right)} \quad (3-45)$$

This terminal velocity is derived from the force balance between 3 forces acting on a spherical object: gravity, drag and buoyancy forces. There was a numerical study on the settling velocity of the cylindrical particles from Gabitto and Tsouris (2008), which can be referred to have insights into the terminal velocity of a solid object. The drag coefficient,  $C_d$ , is taken generally as 0.47 for a sphere, the solid density,  $\rho_s$ , is  $1000 \text{ kg/m}^3$  and the air density is  $1.25 \text{ kg/m}^3$ . In this preliminary study, the surface tension was not considered and the simulated terminal velocity is expected to be different from the theoretical terminal velocity value. It is worth mentioning that the calculated value of the terminal velocity only serves as an initial rough guess on the  $k_p$  gain and this will not affect the validity of the

results. The initial  $k_p$  was set to  $1 \times 10^6 \text{ s}^{-1}$  and tuned down down to  $0.5 \times 10^6 \text{ s}^{-1}$  accordingly to how fast the falling sphere becomes stable, which is indicated by how fast the control velocity,  $u_{ctrl}$ , converges or starts to oscillate around a fixed value. The control velocity profiles for each case are plotted in Figure 3-17.

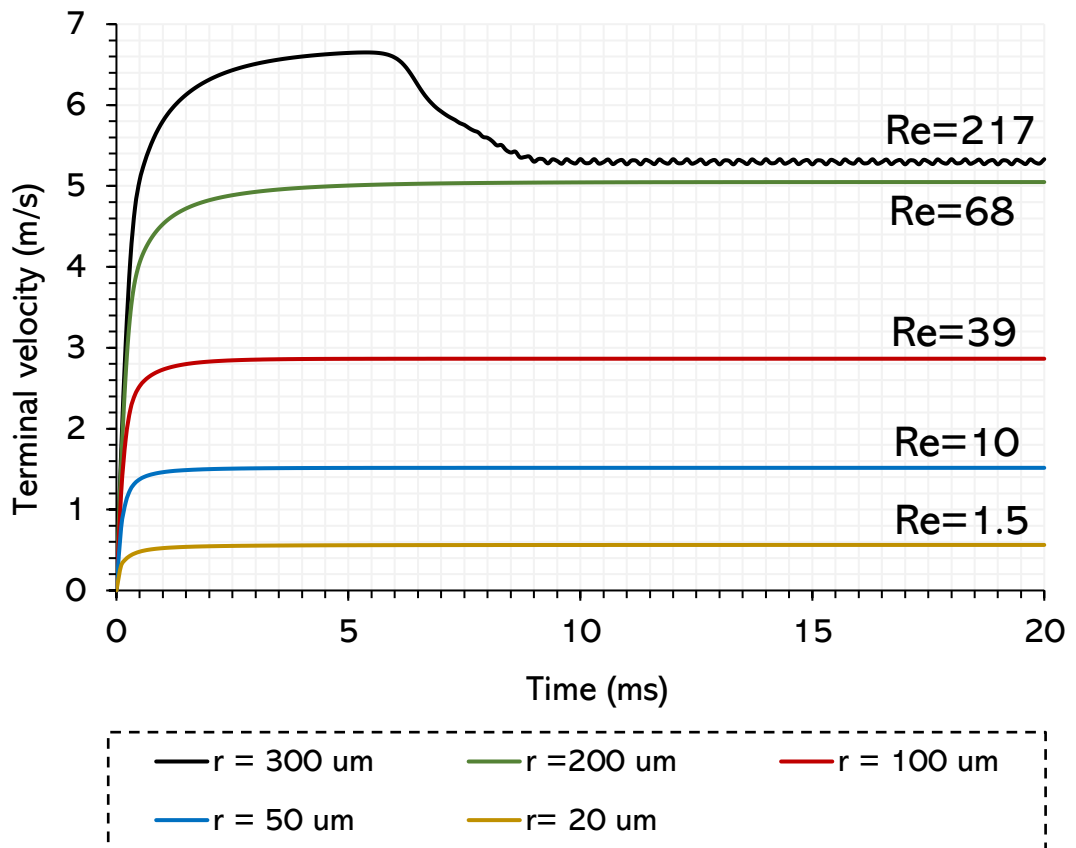


**Figure 3-17.** Terminal velocity of different cylinder sizes free falling air.

The Reynolds number is provided for each terminal velocity value.

The cylinder size ranges from **20  $\mu\text{m}$**  (grey line) to **300  $\mu\text{m}$**  (black line). The time interval is 20 ms.

At the radius of 300  $\mu\text{m}$ , the formation of Karmen vortex (M. Horowitz, 1989) street in the wake is shown through the oscillation in the controlled velocity due to the fluctuation of the stress on the surface (refer to Re=217 line in Figure 3-17). The PID control loop has reached a terminal velocity after around 8 ms. The wake profiles for each cylinder radius are plotted together at  $t = 15 \text{ ms}$  in Figure 3-18.

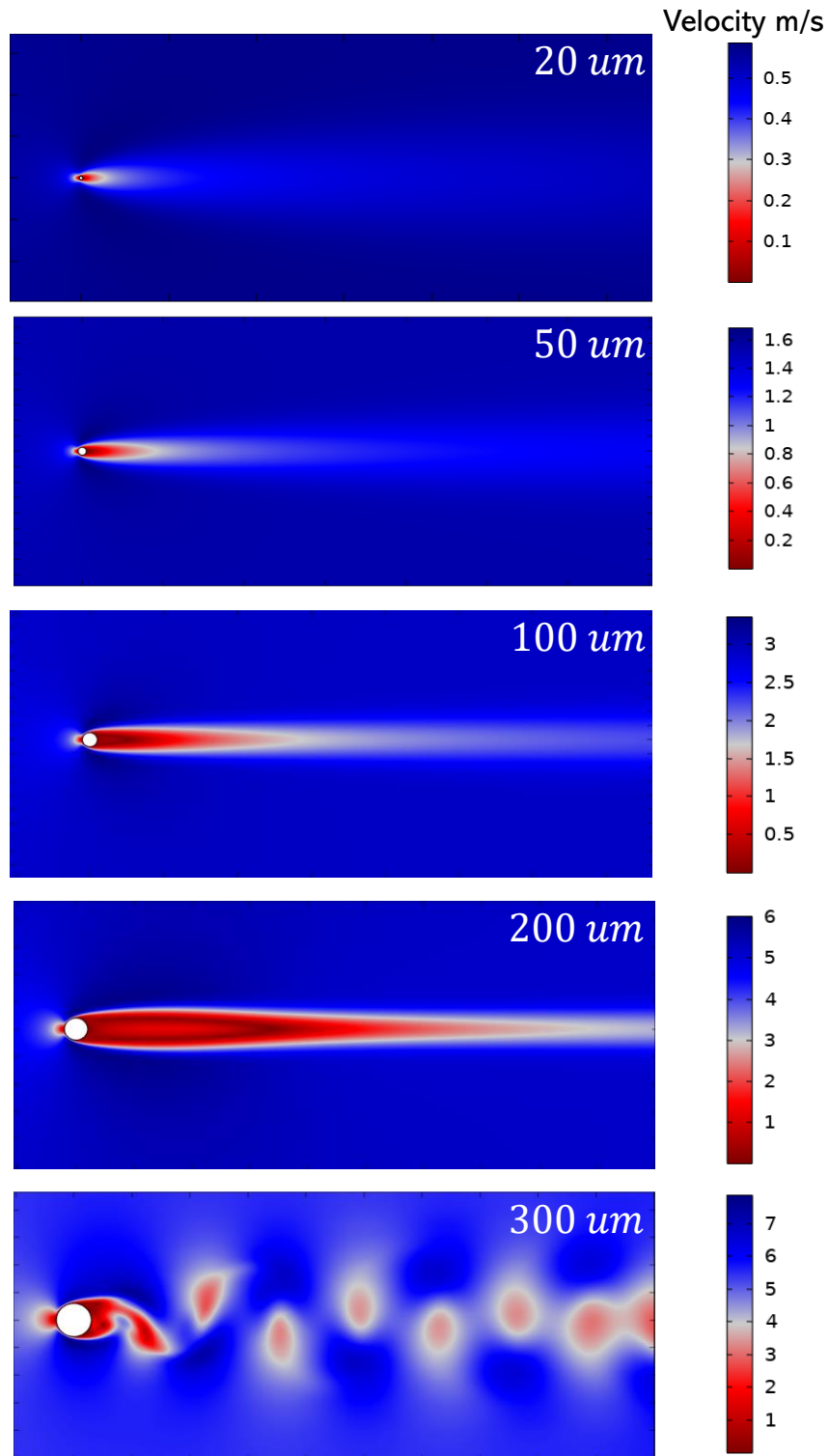


**Figure 3-18.** Velocity contour of the wake in the flow past the cylinder (black circle) at different radii. The white number in each domain represents the radius of the cylinder in such domain, the velocity scale is colour-coded and the air flow is from right to left boundaries.

### **3.4. Study of flow past the fixed and falling cylinders**

This section investigates the flow past a cylinder and spherical object, and performs validation and verification benchmarks on the chosen system. The purpose is to study the performance and the accuracy of the FEM method, and to investigate the governing equations to gain a degree of confidence that the framework can be used to study the droplet drying system later.

#### **3.4.1. Drag and lift validation**

##### **3.4.1.1. Fixed cylinder**

A numerical study of flow past a cylinder was performed. This aims to study the wake profile of a cylinder, and test the capability of a developed PID control algorithm on maintaining the stability of the system. Providing the main system of interest is a falling spherical droplet, this study helps to gain an understanding of the flow around a circular domain without the need of large computational resources of setting up a full 3D sphere. The experimental flow patterns through a body with different shapes can be found in the literature (van Dyke and White, 1982). According to the published work, the flow is completely symmetric and fully attached to the cylinder at  $Re < 1$ . At  $1 < Re < 5$ , the wake profile is stretched along the flow direction but the symmetry of the flow is still maintained. The flow starts to separate from the cylinder surface at  $Re > 5$  and forms small eddies behind the cylinder. The eddies size increases steadily along with increasing Reynolds number up to the limit of  $Re \approx 40$ . The Karmen vortex street appears and induces an oscillation on the cylinder body. In this study, Reynolds number of the system is purposely chosen to be around **200**, in order to test the PID control loop on damping the cylinder oscillation.

First, a fixed cylinder is considered and the drag coefficient on the cylinder body is validated against the literature data. It also justifies the validity of the critical Reynolds number at which a flow separation or Karmen vortex street appears. A fixed circular cylinder is set within an air channel with an inlet, outlet, and two side walls shown in Figure 3-19. The diameter of a cylinder is  $600 \mu\text{m}$ , the width and height of the channel are  $20 \text{ mm}$  by  $10 \text{ mm}$ . An inlet velocity is set at  $4.92 \text{ m/s}$  to have a Reynolds number of 200. The outlet is set at atmospheric pressure and a 'slip' condition is set at the two side walls. This implies no viscous effect on the two side walls so no boundary layers can develop.

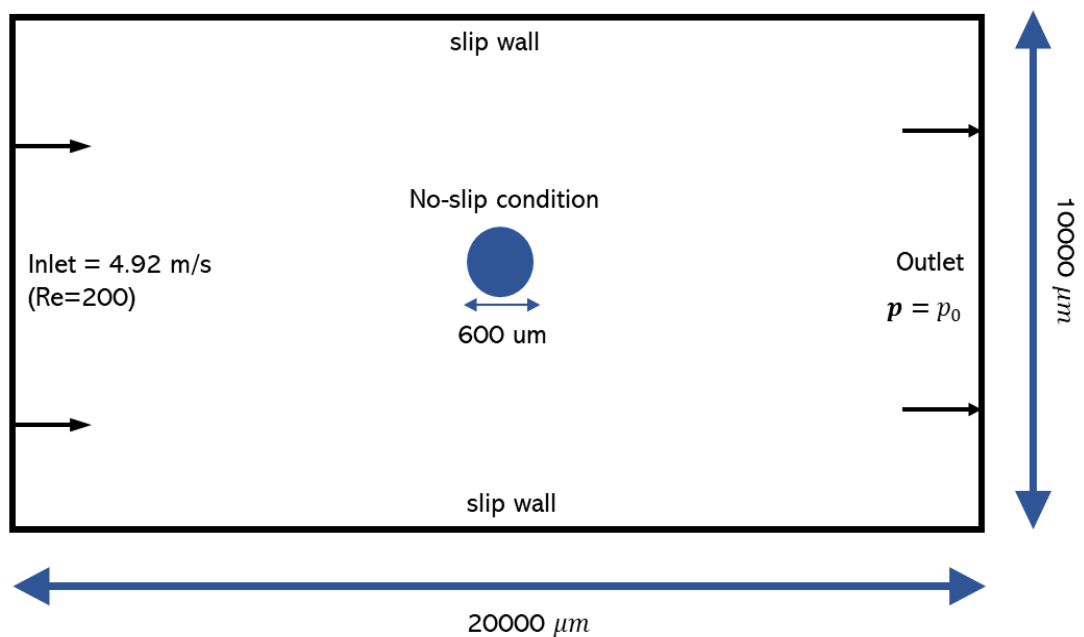


**Figure 3-19.** Schematic setup for simulation of flow past the fixed cylinder. The solid domain (blue) is  $600 \mu\text{m}$  in diameter and the inlet velocity is set at  $4.92 \text{ m/s}$ .

#### 3.4.1.1.1. Governing equations

The governing equation is the incompressible Navier-Stokes equation for the isothermal system (refer to equations (3-34) and (3-35)).

#### 3.4.1.1.2. Boundary conditions

The slip condition is applied to the side walls to prevent the development of boundary layers (refer to equation (3-36)). A no-slip condition is applied to the cylinder interface (refer to equation (3-37)).

All the material properties will be evaluated at the set reference temperature ( $T_{ref}$ ) and pressure ( $p_{ref}$ ), and the flow is incompressible. The whole set of differential equations is solved using the Finite Element Method (FEM) and the time-stepping scheme is the Backward Differentiation Formula (BDF). The mesh element is a free triangular shape with boundary layers added to the cylinder surface. As shown in Figure 3-20, the mesh is denser around the cylinder interface for resolving the high gradients of the velocity and pressure fields. Extra three layers are added to separate the domain into 6 sections for a more efficient meshing process. The mesh consists of 2,650 elements and 719 boundaries. The cylinder domain is empty and no interior mesh is produced. This method is preferred over the option of having to assign a solid material to the cylinder. Not having a domain assigned to the cylinder space consequently prevents the rotation of the cylinder due to the non-symmetrical meshing even though the cylinder is placed exactly in the middle of a rectangular domain.

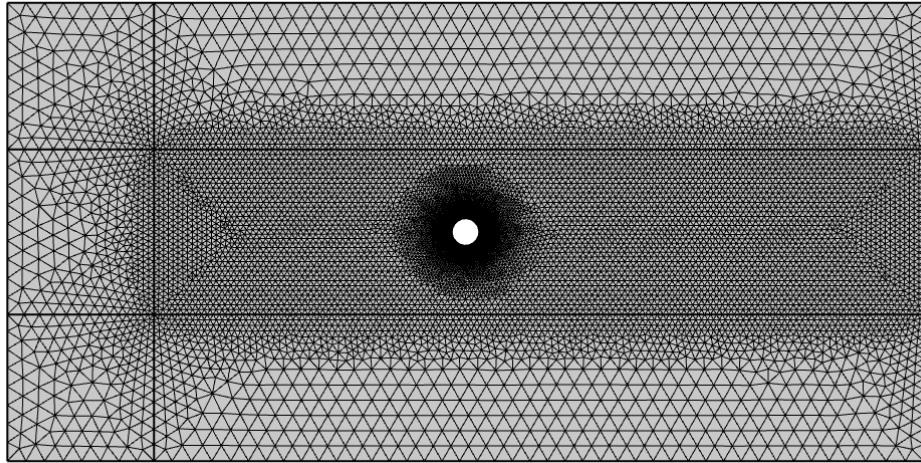


**Figure 3-20.** Mesh details for the flow past a fixed cylinder of  $300 \mu\text{m}$  in radius. The domain is divided into regions for better meshing. The mesh is denser around the cylinder and coarse at far-field.

The Karmen vortex street is expected within the flow field behind the cylinder shown in Figure 3-21. This phenomenon is also observed in the simulation work in the literature (Rajani, Kandasamy and Majumdar, 2009)

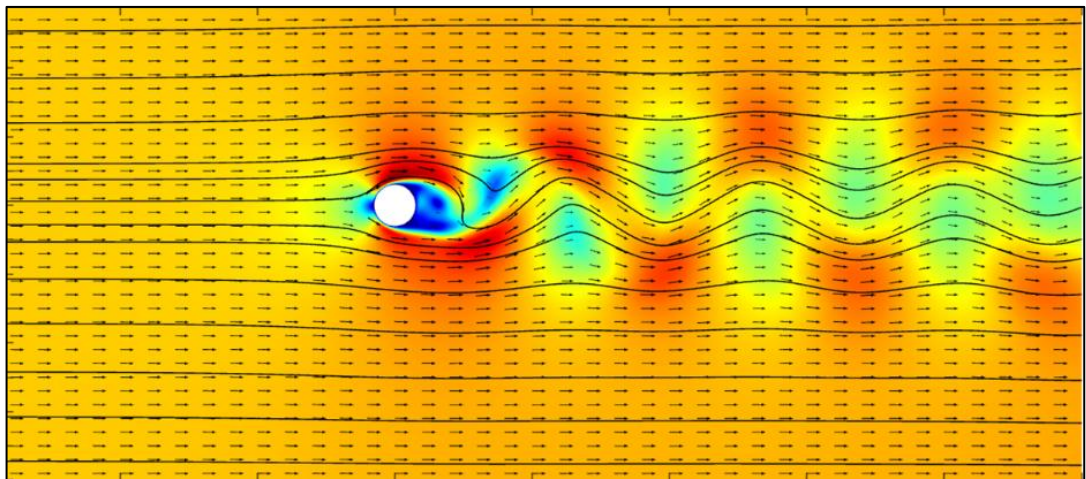


**Figure 3-21.** 2D contour plot with velocity streamlines (black line) and vector field (black arrows). The vortex shedding is observed. The cylinder is represented by the white circle.

Reference	Drag coefficients
Computed value (at $Re \approx 200$ )	<b>1.3308</b>
Park and Choi (1998)	1.32
J. R. Meneghini and F. Saltara (2001)	1.33
Ploumhans <i>et al.</i> (2002)	1.37
Williamson (1996)	1.33

**Table 3-1.** Validation for computed  $C_d$  against referential simulation values in the literature.

The computed drag coefficient is validated, with an averaged difference of 1.54%, against the referential values in the literature. The system of droplet drying undoubtedly involves more physics than the current study, this validation however confirms the feasibility and capability of the finite element method and the current mesh configuration to solve the well-posed problem with high accuracy. Moreover, it provides a good benchmark case to develop further.

#### **3.4.1.2. Falling cylinder at terminal velocity**

Next, a falling cylinder with terminal velocity is studied and compared with the previous fixed cylinder case. The exact system is recreated except the cylinder is now falling under gravity, as presented in Figure 3-22.

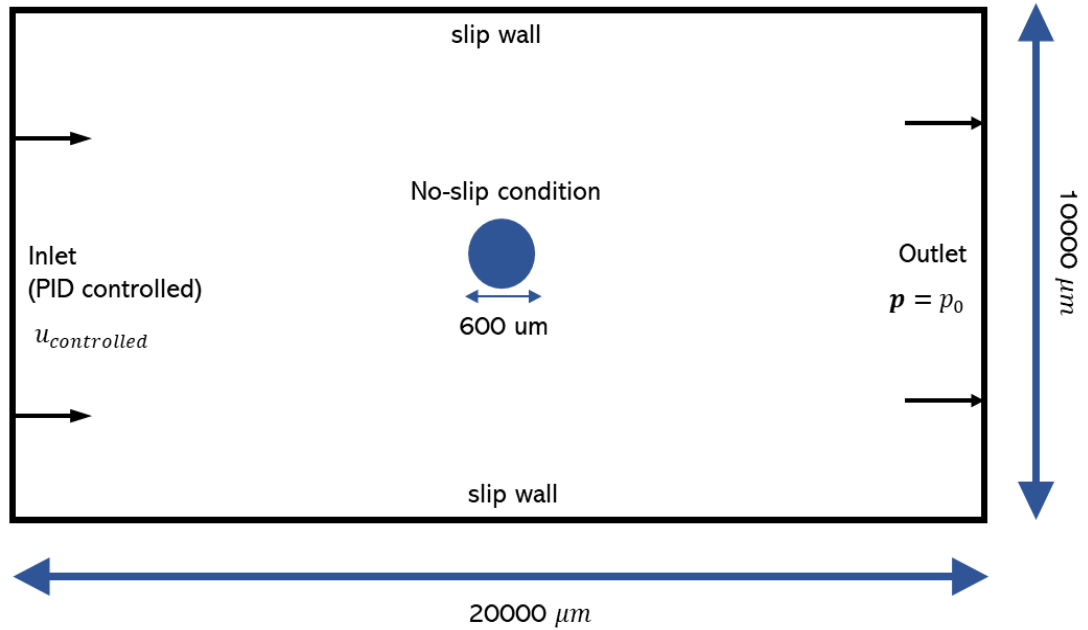


**Figure 3-22.** Simulation schematic for a falling cylinder of **300 μm** in radius. A similar simulation setup to the case of the fixed cylinder (section 3.4.1.1), however, gravity is turned on in this case.

#### 3.4.1.2.1. Governing equations

The same governing equation for fluid flow in the ‘fixed cylinder’ case is applied. Since the droplet is falling through the air along the gravity direction, and no shrinking is involved, the falling velocity of the cylinder can be calculated by solving the ordinary differential equation from the force balance,

$$F_{stress} + mg = ma = m \frac{dv}{dt} \quad (3-46)$$

$$v = \frac{du}{dt} \quad (3-47)$$

Where  $m$  is the mass of the cylinder,  $g$  is the gravitational force,  $u$  is the cylinder displacement,  $v$  is the falling velocity of the cylinder,  $a$  is the acceleration rate and  $F_{stress}$  is the total stress exerted on the cylinder’s surface by the fluid. The total stress at the interface is expressed in the incompressible and compressible flow,

$$F_{stress} = n \left( -pI + \left( \mu(\nabla u + (\nabla u)^T) - \frac{2}{3}\mu(\nabla \cdot u)I \right) \right) \quad (3-48)$$

– Compressible flow

$$F_{stress} = n(-pI + \mu(\nabla u + (\nabla u)^T)) \quad (3-49)$$

– Incompressible flow

Here, the PID algorithm is developed to control the inlet velocity in order to have the cylinder falling at terminal velocity. The aim is to keep the droplet in the stationary frame respective to the flowing fluid. The inlet velocity will be adjusted depending on the displacement of the cylinder.

#### 3.4.1.2.2. Boundary conditions

The movement of the interface between immiscible fluids are resolved by a set of equations that relates the fluid flow and the mesh velocity,

$$u_1 = u_2 + \left( \frac{1}{\rho_1} - \frac{1}{\rho_2} \right) M_f n_i \quad (3-50)$$

$$n_i \cdot \tau_2 = n_i \cdot \tau_1 + f_{st} \quad (3-51)$$

$$u_{mesh} = \left( u_1 \cdot n_i - \frac{M_f}{\rho_1} \right) n_i \quad (3-52)$$

Where  $\mathbf{u}_1, \mathbf{u}_2$  are the fluid velocities on the two sides of the interface,  $\mathbf{u}_{mesh}$  is the mesh velocity at the interface,  $\mathbf{n}_i$  is the normal vector of the interface (pointing from the higher-numbered domain to lower-numbered domain),  $\tau_1$  and  $\tau_2$  are the total stress tensor of the two domains 1 and 2 respectively,  $f_{st}$  is force per unit area due to the surface tension (tangential component),  $M_f$  is the mass flux across the interface.

Hence, all the nodes and edges around the cylinder's interface are given the mesh velocity,  $\mathbf{u}_{mesh}$ , which is calculated as above. There is no mass transfer across the interface so the velocity on both sides of the cylinder equals in this case:  $\mathbf{u}_1 = \mathbf{u}_2 = \mathbf{u}_{mesh}$ . The stress balances are evaluated on the cylinder surface to obtain the total stress  $F_{stress}$  and the falling velocity is calculated as a result. It is important to compare the controlled velocity and the theoretical terminal velocity for the validity of the PID. As seen from the equation (3-45), all the variables can be easily evaluated at the current system condition except the drag coefficient -  $C_d$ . There are many published empirical formulas for estimating the drag coefficient at specific ranges of Reynolds numbers (Imron *et al.*, 2018). The literature review in the area of the drag coefficient can be found in the paper from Goossens (2019). The drag on the cylinder decreases non-linearly with decreasing Reynolds number due to complicated vortices patterns formed behind an object, which is shown in the well-known graph in Figure 3-23.

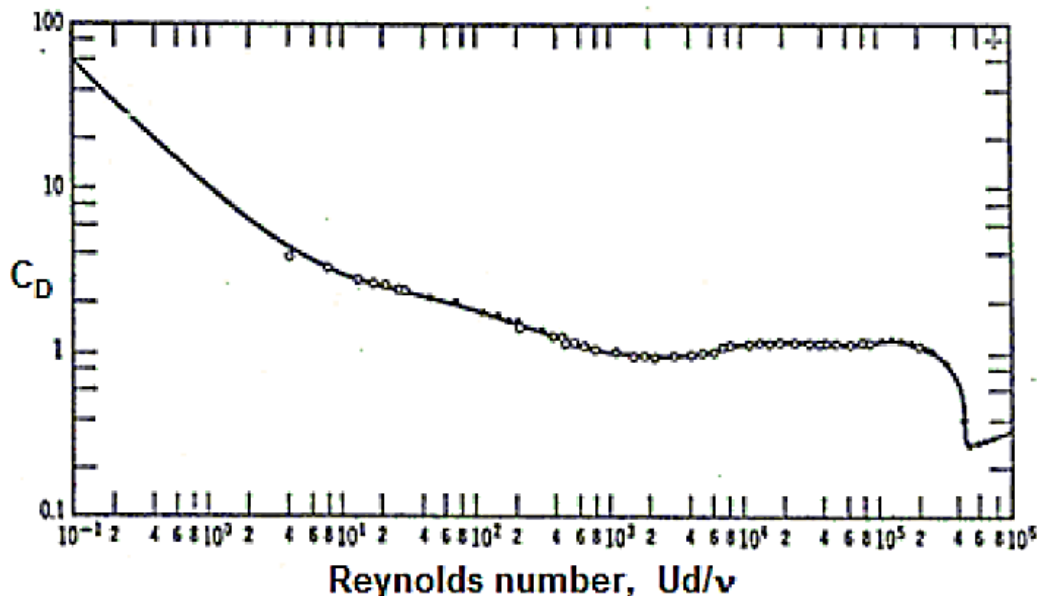


**Figure 3-23.** Experimental data for the drag coefficient on a circular cylinder (Anderson Jr, 2010). The Reynolds number range covers from 0.1 to  $10^5$ .

The drag decreases steadily until the range of  $2000 < Re < 20000$  and drops significantly in an area called the 'drag crisis'. The turbulence flow behind an object reduces the pressure difference between the upstream and downstream through vortices. Due to this non-linearity relationship, it is often challenging to calculate the drag coefficient analytically. A numerical study (Guo, Lin and Nie, 2011) for the empirical correlation of the drag coefficient on the cylinder was carried out, however it only covers the range up to  $Re = 100$ . The flow around the cylinder using numerical methods was also studied and validated from Baracu and Boşneagu (2019). There are many formulae for drag coefficients on a cylinder and the three following are often used according to the review paper (Baracu and Boşneagu, 2019).

$$C_D = \frac{8\pi}{Re(2.002 - \log(Re))} \quad (\text{small } Re \text{ only}) \quad (3-53)$$

(Wieselberg, 1922)

$$C_D = 9.689Re^{-0.78}(1 + 0.0838Re^{0.82}) \quad (40 < Re < 400) \quad (3-54)$$

(Clift *et al.*, 1978)

$$C_D = \frac{5.93}{\sqrt{Re}} + 1.17 \quad (Re < 30,000) \quad (3-55)$$

(Munson *et al.*, 1990)

The correlations from Clift *et al.* (1978), Munson *et al.* (1990) and Wieselberg (1922) were plotted by Boşneagu (2019) against the experimental data for comparison in Figure 3-24,

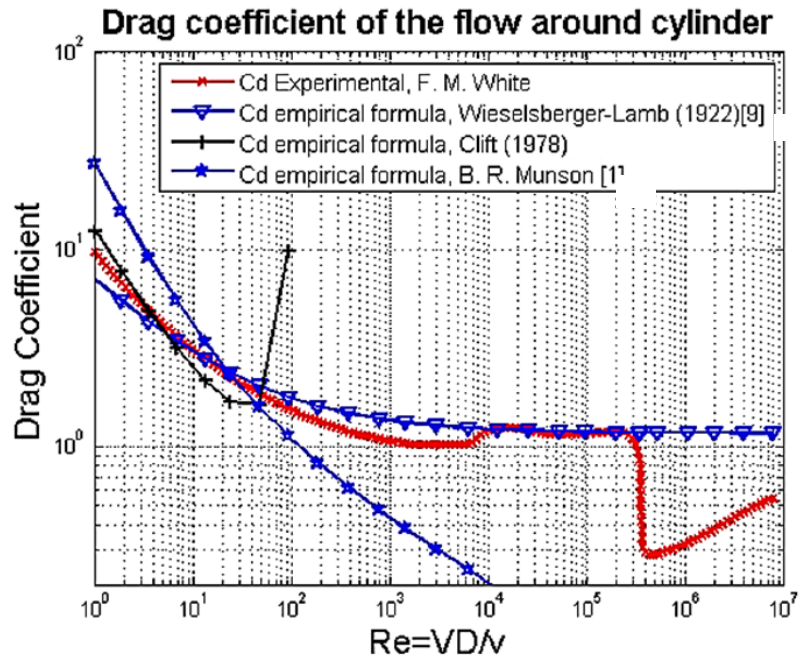


**Figure 3-24.** Comparison of drag coefficients on cross-flow circular cylinder between experimental data and empirical formulas from Wieselberg (1922), Clift *et al.* (1978) and Munson *et al.* (1990).

A summary of the physical properties of materials use in the study are in Table 3-2.

Physical properties	Value (units)
Air density	1.225 (m/s)
Air dynamic viscosity	$1.81e^{-5}$ [kg/(m.s)]
Solid density	1000 (kg/m <sup>3</sup> )

**Table 3-2.** Physical properties used in the simulation of the flow past a cylinder system

The drag coefficient cannot be determined explicitly since it is a function of the Reynolds number which is needed for a terminal velocity equation. Hence, it requires an iteration procedure to obtain the converged values of both the drag coefficient and Reynolds number. The correlation used to calculate the drag coefficient is chosen to be from Munson *et al.* (1990) due to its wide range of Re validity. It should be noticed that this correlation is valid only if the

boundary layers flow on the cylinder is laminar, which means the Reynolds number range of below 30,000 for a smooth cylinder. The iterations for the drag coefficient correlation from Clift *et al.* (1978) and Munson *et al.* (1990) formula can be found in section A.1 in Appendix A. Since the drag coefficient in the previous validation of flow past a fixed sphere was done at  $Re = 200$ , it is necessary to keep the consistency to this simulation. The simulation will also run with and without adaptive-mesh-refinement (AMR) to test the mesh independence of the results. The mesh details in the two cases are illustrated in Figure 3-25. A similar simulation study to the current system was also carried out from M. Horowitz (1989). A cylinder with the same dimensions to the previous case is set up. All the governing equations and boundary conditions applied are the same as previous, as shown previously in Figure 3-22.

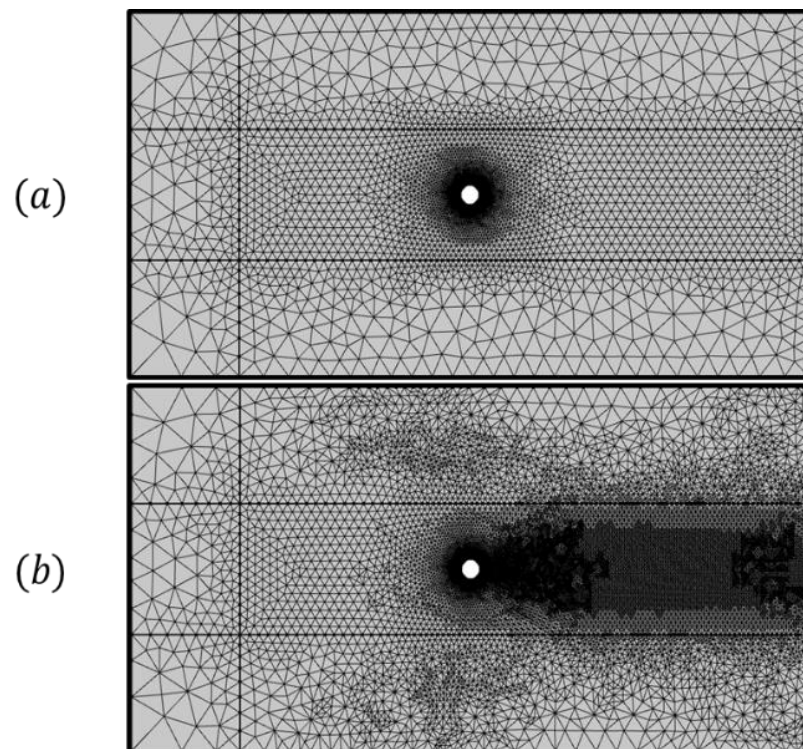


**Figure 3-25.** Example of meshing details during simulation of (a) non-adaptive mesh refinement and (b) Adaptive mesh refinement technique. The domain is divided into 6 small parts for a better meshing process. The refined mesh is concentrated around the cylinder and the wake area where the fluid flow happens.

In the ARM algorithm, the triangular element will be divided into two smaller elements whenever the numerical error exceeds the tolerance criteria. The non-AMR and AMR meshes have 12859 elements and 36116 elements with a simulation time of 12 minutes and 52 minutes, respectively. The falling velocity of the two cases is plotted in Figure 3-26.

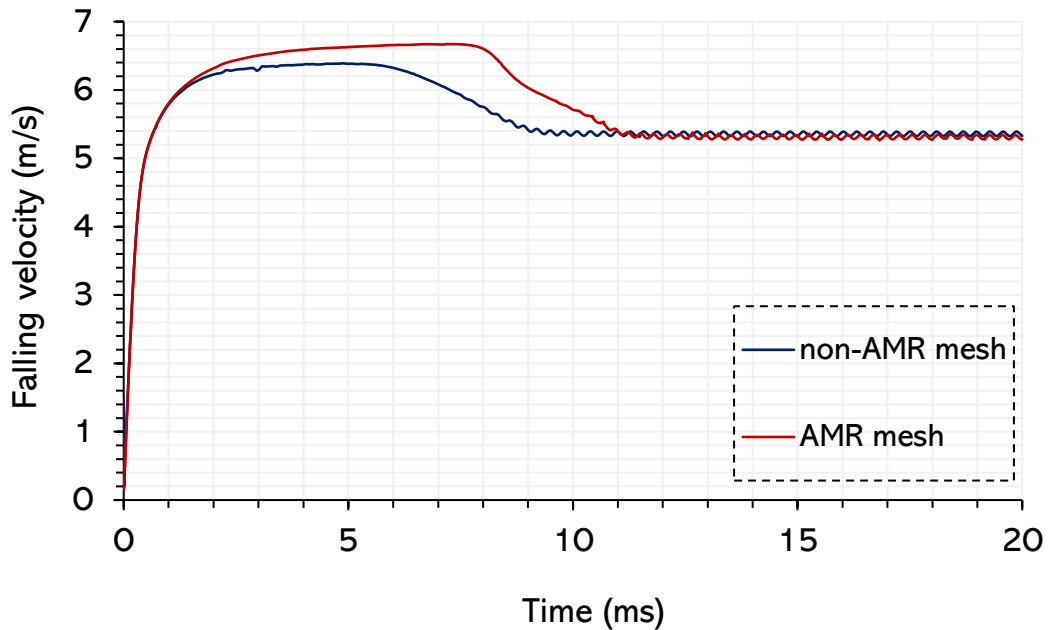


**Figure 3-26.** Velocity profile of a falling cylinder ( $300\ \mu\text{m}$  in radius) simulated with non-AMR (blue line) and AMR (red line) meshing technique. The studied time interval is 20 ms.

The two velocity plots show different profiles in which an AMR-mesh cylinder takes longer to reach a steady state. However, both cases yield a similar terminal velocity of a circular cylinder as in Table 3-3.

	Non-ARM mesh	AMR mesh	Difference (%)	Reynolds number
Terminal velocity (m/s)	5.3578	5.3108	0.8771	216

**Table 3-3.** Comparison of the terminal falling velocity of a circular cylinder ( $300\ \mu\text{m}$  in radius) with and without AMR.

Given a small increase in accuracy and a huge spike in computational time, the AMR algorithm has been shown to not be effective in this scenario. This result is compared against the terminal falling velocity obtained previously by iteration (refer to Appendix A).

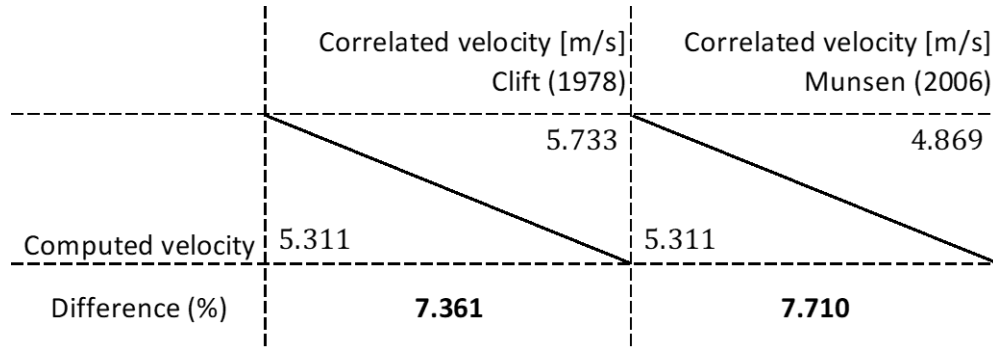


**Table 3-4.** Verification of terminal velocity against experimental correlation in the literature.

The Reynolds number of the computed system is 216 (refer to Table 3-3). Theoretically, the literature value of the drag coefficient on this falling cylinder is expected to be around **1.41** (according to Figure 3-24). The computed drag and lift coefficients are plotted in Figure 3-27 and averaged in Table 3-5. The simulation agrees closely with the correlation obtained from the literature, with an error of  $\pm 3.5\%$ .

	Average drag coefficient	Average lift coefficient
Re=216	1.36 (compared to the <b>1.41</b> value from the literature)	$\approx 0$

**Table 3-5.** Average drag and lift on the cylinder obtained from the simulation of the flow past a cylinder.

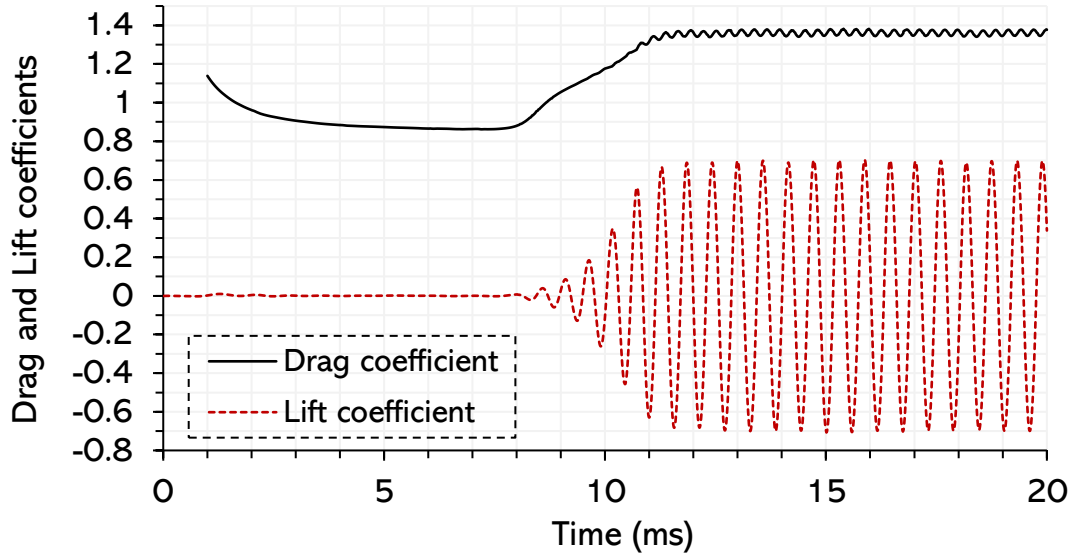


**Figure 3-27.** Drag and lift profiles on the cylinder. The drag is plotted in the solid line and the lift in the dotted line. The period is **20 ms**.

The behavior of the wake is also traced. The angle of separation is shown in Figure 3-28 at  $t = 0.5 \text{ ms}$ .

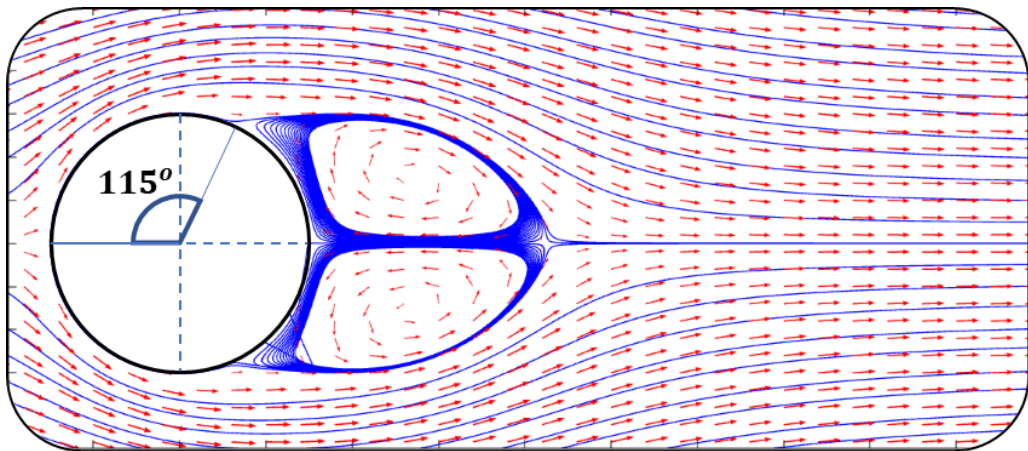


**Figure 3-28.** Vector field (red arrows) and streamlines (blue lines) plot of velocity around the cylinder (black circle). The angle of flow separation is at  $115^\circ$ . The air flows from left to right in the domain.

The adverse pressure gradient area forms at around  $t = 0.5 \text{ ms}$  and at an angle of  $115^\circ$  starting from the stagnation point on the cylinder (Figure 3-28). The vortices begin to appear in an elliptical region as shown in the wake (blue lines). The velocity is zero at the stagnation point and it is easily noticeable that the flow is attached fully to the

surface up until the separation point. The length of the arrow vectors is proportional to its magnitude and the streamlines are plotted around the cylinder. According to Bernoulli's principle, velocity is inversely proportional to pressure which explains the detachment from the surface as the velocity gets significantly small reaching the midpoints. This is due to the reduction in pressure gradient and the viscous effect of the flow so that the air can no longer travel along with the cylinder's interface. The velocity on a streamline around the vortex region keeps a consistent magnitude as well as direction. The velocity profile is plotted with streamlines around the cylinder in Figure 3-29. The vortex shedding starts to develop at 8 ms and reach steady state at after 11 ms.

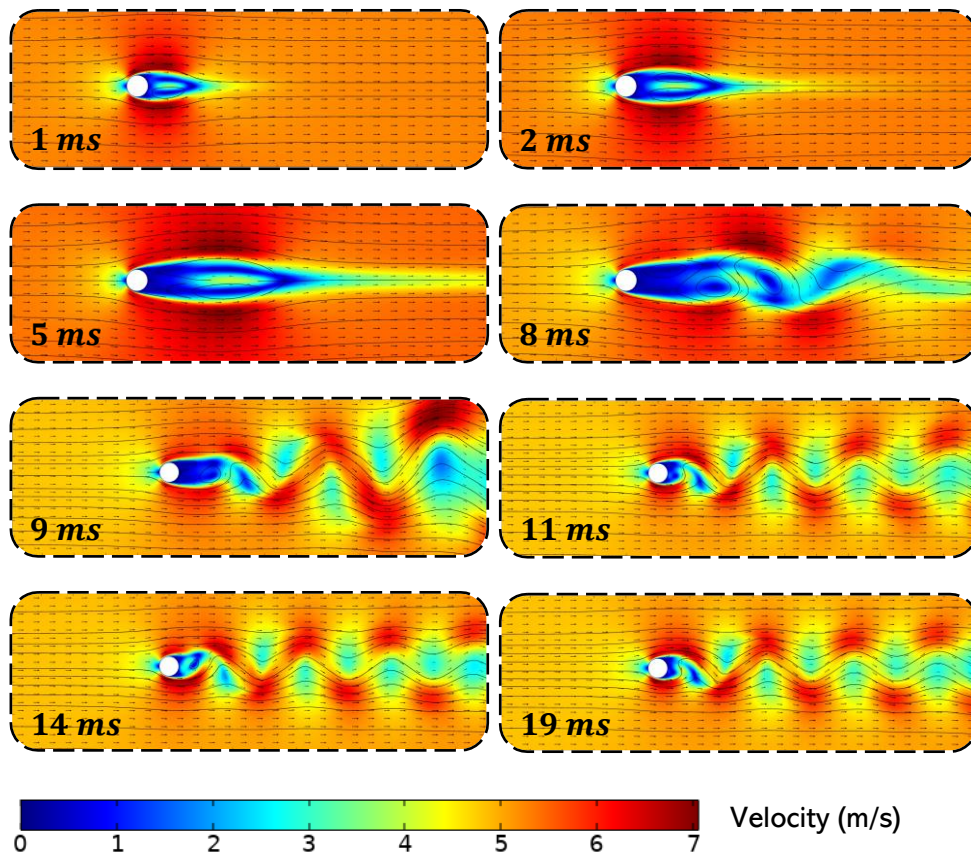


**Figure 3-29.** The velocity in the wake region of the flow past the cylinder. The time interval ranges from 1 ms to 19 ms. The velocity vector field (black arrows) and streamlines (black line) are plotted together with the colour-coded plot of the velocity magnitude.

The pressure field around the cylinder is also plotted in Figure 3-30. The pressure is highest at the stagnation point at the cylinder's front and remains high along the surface up until the separation point.

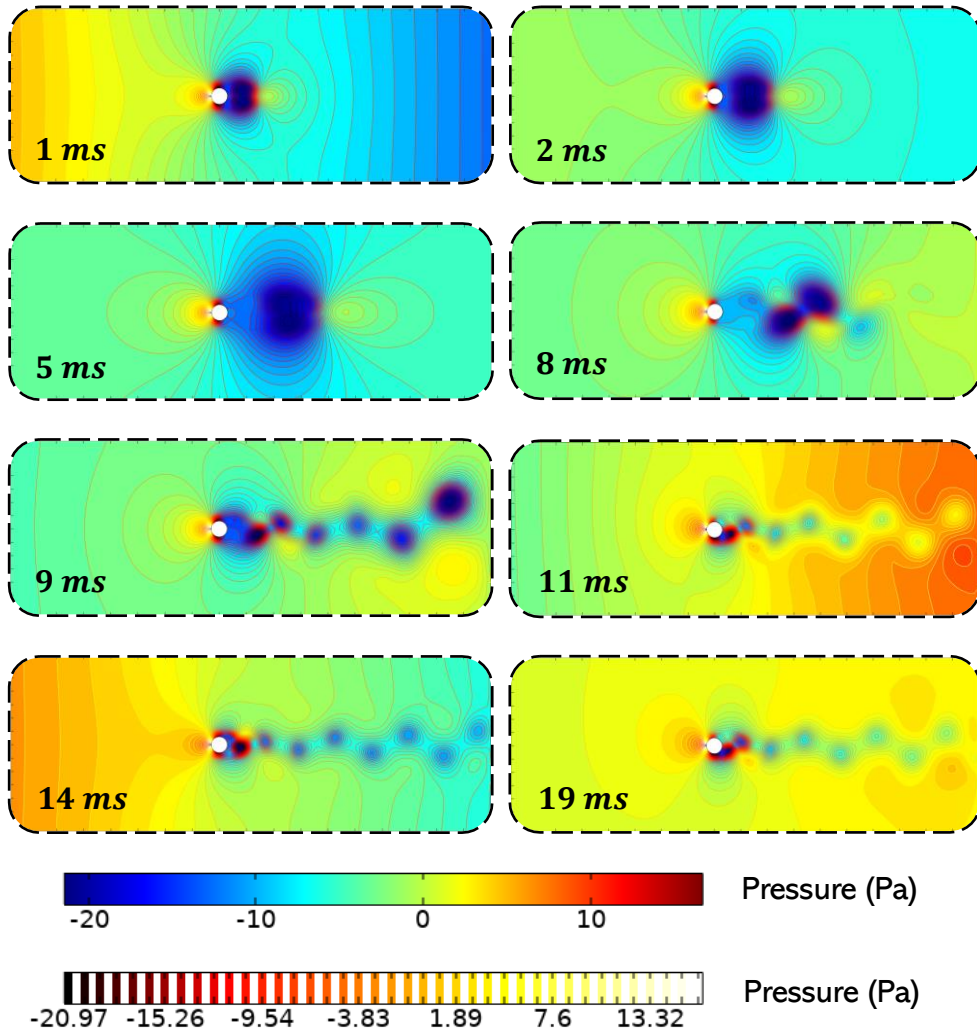


**Figure 3-30.** Pressure field around the cylinder over time. The magnitude of pressure and the streamlines are colour-coded. The time interval is from 1ms to 19 ms.

### 3.4.1.3. Comparison of the flow past fixed and falling cylinders

An extra domain with a fixed cylinder is added below the falling cylinder's domain in the following simulation, as shown in Figure 3-31. The inlet velocity for both domains will be the PID controlled velocity based on the falling rate of a free-fall cylinder. All wall

conditions are set to slip-wall and the outlet is at atmospheric pressure. This study will exhibit a difference in the velocity field, the drag and lift coefficients between the fixed and falling cylinders. The simulation domain is split into 6 smaller sections for a better meshing process and to reduce the computational efforts.

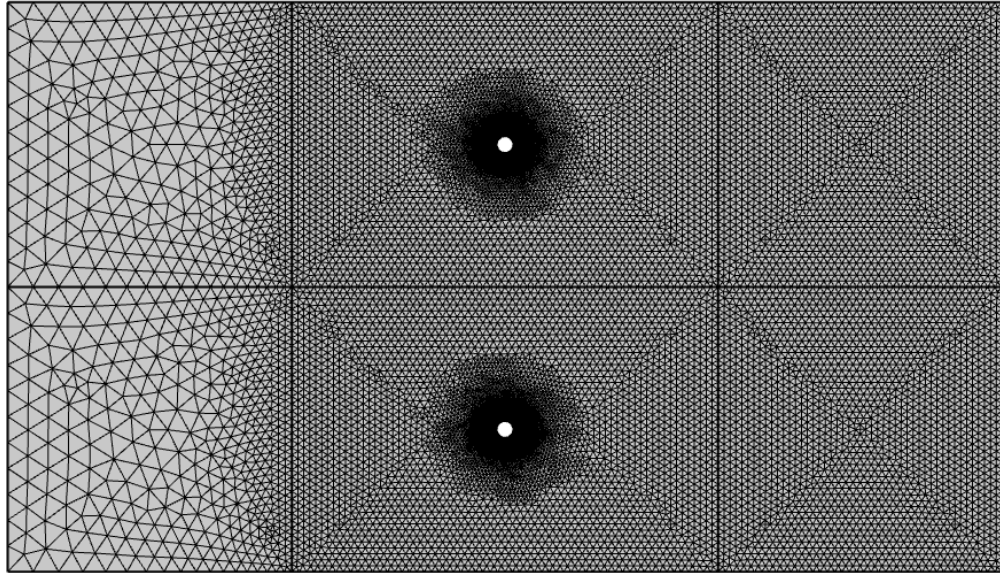


**Figure 3-31.** Mesh configuration for fixed and falling cylinders. The domain is divided into 6 sections for a better meshing process. The mesh area near the flow inlet is coarse and the fine mesh is kept around the cylinder and along the wake where the complicated flow profiles appear.

It is interesting to study the difference of the drag coefficients on the cylinders, in which the inlet velocity is set both to PID controlled and a fixed value. This will be done in the current simulation set up. First, the inlet velocity to both domains is controlled by the PID algorithm, which is based on the falling cylinder, and then set to a fixed velocity once the PID reached a steady-state value.

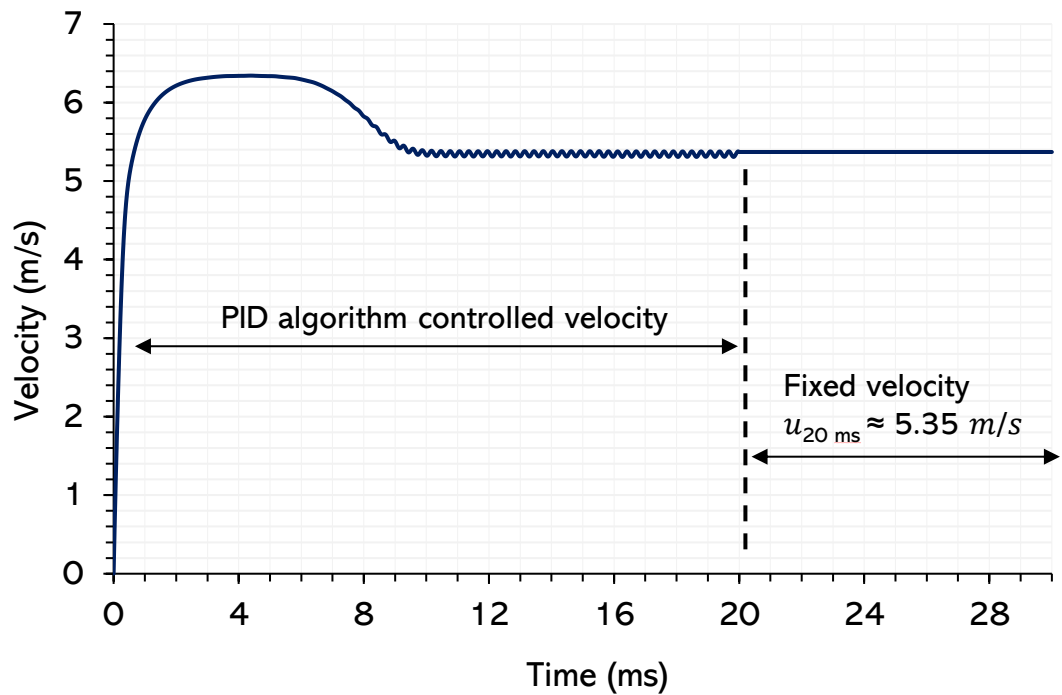


**Figure 3-32.** The inlet velocity profile transitioning from controlled velocity to fixed velocity. The PID loop is applied to the inlet velocity at  $t < 20 \text{ ms}$  and a fixed inlet velocity of  $5.35 \text{ m/s}$  is applied at  $t > 20 \text{ ms}$ .

The drag and lift coefficients on both cylinders are shown in Figure 3-33 and Figure 3-34. The data up to  $t = 2 \text{ ms}$  was not plotted due to the spike in value, which will prevent the oscillation scale from being observable.

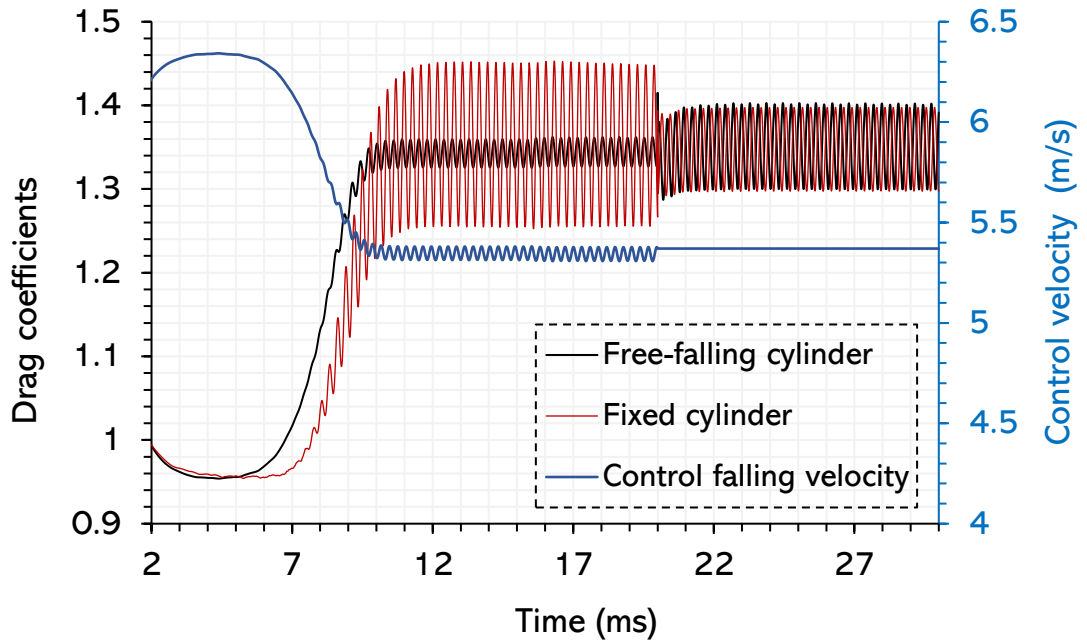


**Figure 3-33.** Drag coefficients on a free-falling cylinder and fixed cylinder at two different velocity profiles at the inlet.

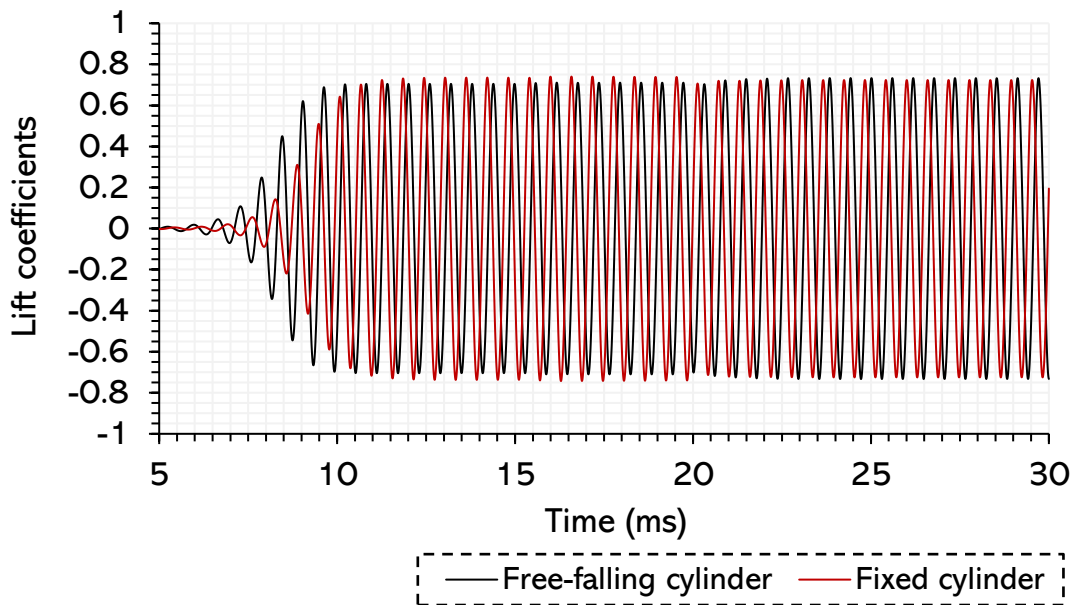


**Figure 3-34.** Lift coefficients on the free-falling cylinder and fixed cylinder at two different velocity profiles at the inlet.

This PID system, which is the same as the PID developed in section 3.3, is designed to react to the displacement of the cylinder and only includes the proportional parameter hence the oscillation of drag coefficients in Figure 3-33. At  $t < 20 \text{ ms}$ , the peak value of the drag coefficient on the fixed cylinder is 1.3795 compared to the value of

1.3805 for the falling cylinder, and at  $t > 20 \text{ ms}$ , the peak values are 1.3804 and 1.3785 for the fixed and falling cylinders respectively. It is noticed that the drag coefficient on the fixed cylinder is now more than that of the falling cylinder after  $t = 20 \text{ ms}$ , which is the opposite to when  $t < 20 \text{ ms}$ . The two drag coefficients are very similar once the coming air flow is fixed to the mean value calculated from its previous oscillation period. This indicates an apparent effect of the inlet velocity on the drag force. Despite the distinct difference when comparing the drag coefficients on the two cylinders before and after  $t = 20 \text{ ms}$ , the magnitude of the drag coefficient on the two cylinders is not much different from each other. The results of the drag coefficients study imply that a freefalling object system can be replaced and represented by fixing an object's position providing the incoming air velocity is equal to the object's velocity in the freefalling case. This is a useful study outcome as the freefalling object is less convenient to investigate both numerically and experimentally, comparing to the fixed object. It is important to interpret the purpose of setting up different velocity scenarios between  $t < 20 \text{ ms}$  and  $t > 20 \text{ ms}$  (Figure 3-33). In the SDD experiment, a fixed airflow is introduced towards a fixed droplet on a filament to study the drying kinetics of a freefalling droplet within the spray dryer. Hence, it is preferred to confirm the accuracy of the SDD experiment on mimicking the falling droplet by a fixed droplet system, which is proven to be valid by this study outcome. In the first PID controlled-velocity scenario at  $t < 20 \text{ ms}$ , the interpretation is that the falling velocity of the falling object is projected onto a fixed object showing how good the PID loop in controlling the drag oscillation. In the second fixed-velocity scenario ( $t > 20 \text{ ms}$ ), the fixed inlet flow at  $t > 20 \text{ ms}$  and the similar drag coefficients on two cylinders justifies the practicality of having a fixed airflow in the SDD experiment.

The following section is the investigation of the cause of the difference in the drag coefficients on the two cylinders. The drag force on a body comprises of two components: pressure force and viscous stress. Since Reynolds number is at a laminar flow range, the pressure on the cylinder surface is expected to dominate the effect. Figure 3-35 plots the pressure and viscous stress of airflow on the upper half of the cylinder surface at  $t = 15\text{ ms}, 19\text{ ms}, 21\text{ ms}, 25\text{ ms}$  and  $30\text{ ms}$ .

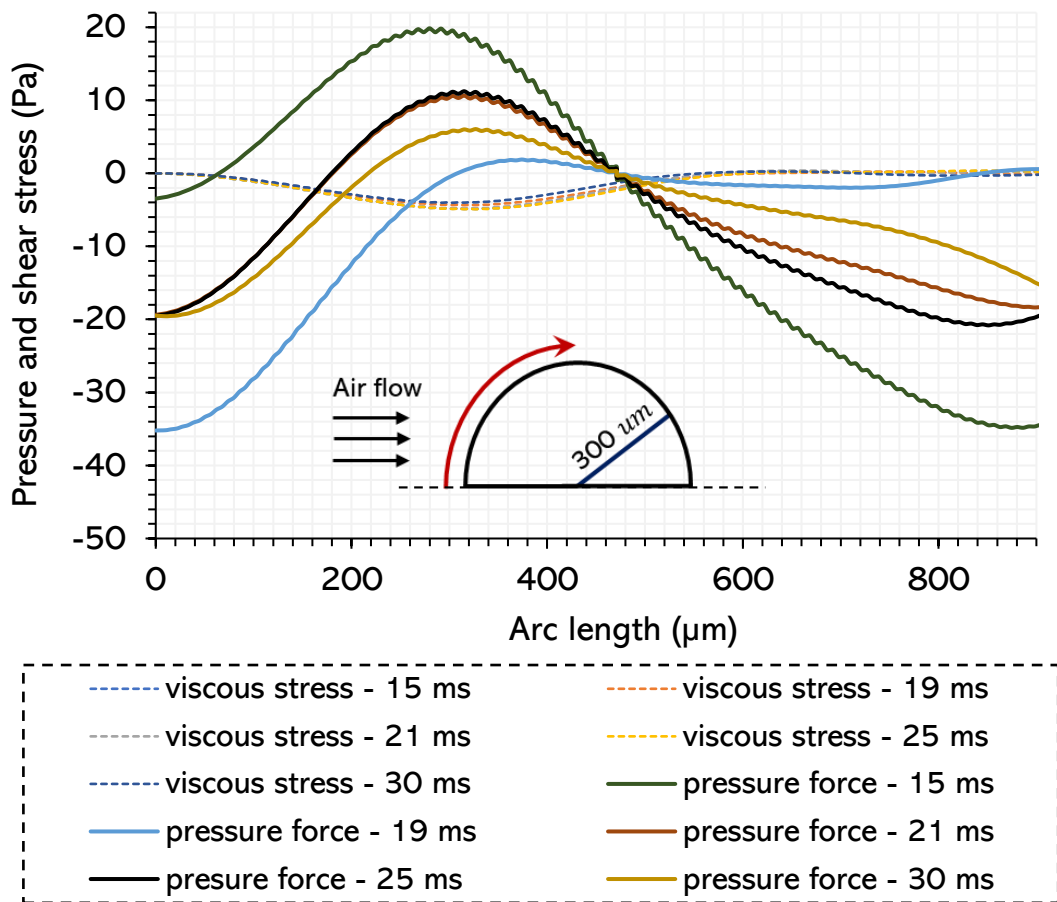


**Figure 3-35.** Comparison between the local viscous stress and pressure along the upper half of the cylinder surface.

The graph was purposely plotted at a time right before and after the velocity transitioning time to illustrate the difference in local stress on the cylinder surface. Figure 3-35 showed an insignificant contribution of the viscous stress (dotted lines) to the total stress comparing to the pressure force (solid lines). The shear stress also

does not vary much during the falling of the cylinder, with its absolute peak value at around 6 Pa happened close to the separation point. Therefore, the pressure is predicted as the main contribution to the drag force on the cylinder. However, the drag on an object at this range of Reynolds number also depends on the pressure profile in the wake. When the flow starts to detach from the cylinder surface, it creates a low-pressure area in the wake which contributes to the total drag due to the pressure gradient. The angle of separation is therefore critical since it determines the size of the low-pressure zone. The position of the eddies after each vortex shedding also affects the size of this zone. It is necessary to investigate the velocity and pressure profile at a specific point in time, when the drag coefficient reaches the highest and lowest for both the free-fall and fixed cylinders. Table 3-6 presents the sample points for this study.

		Time	
		Fixed cylinder	Free fall cylinder
Drag coefficient	Highest	$t = 14.84 \text{ ms}$	$t = 14.78 \text{ ms}$
	Lowest	$t = 14.70 \text{ ms}$	$t = 14.63 \text{ ms}$

**Table 3-6.** The time step for the highest and lowest drag coefficients on both cylinders during the simulation.

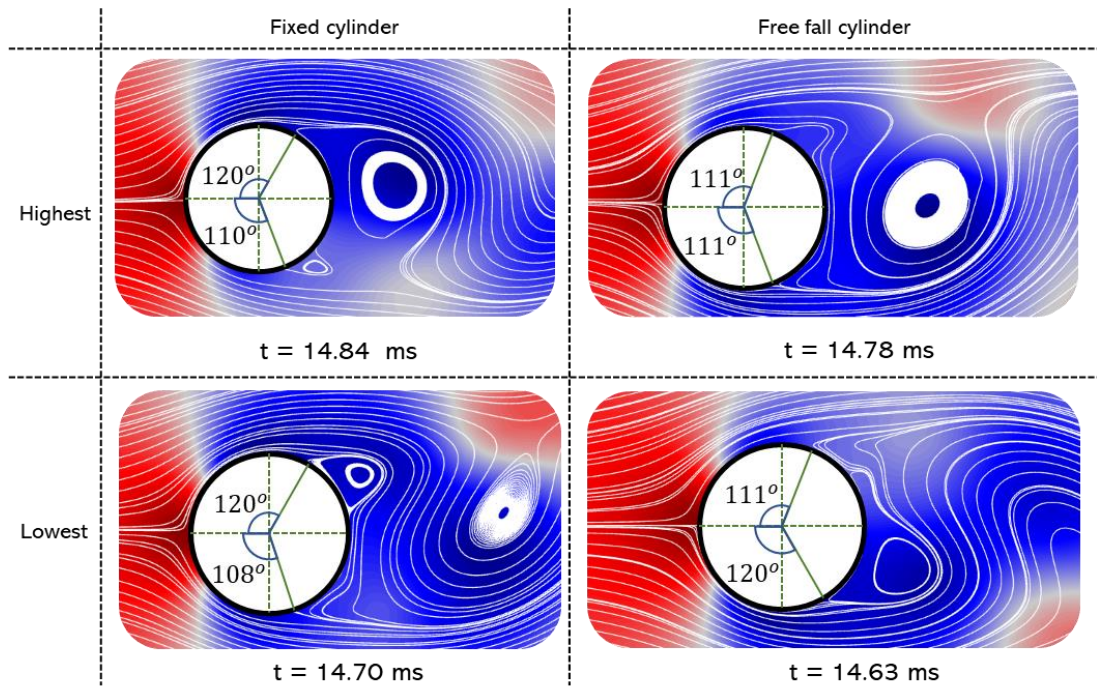


**Figure 3-36.** 2D pressure plots and velocity streamlines (white lines) for the falling and fixed cylinders (white circles). The cylinder surface is shown in the yellow line and the angle of separation is provided for each plot.

Next, the velocity streamlines and pressure contours are plotted in Figure 3-36. The angle of separation is shown to not correlate with the drag coefficients and cannot be used as an indicator for predicting such variables. This is mainly due to the complicated vortex shedding process once the flow detached from the surface. It is however noticeable that the highest drag always happens with large eddies and when the vortices are in the middle of the shedding process. Similarly, the drag is minimal when the wake is near completion of shedding. This can be explained by examining and comparing the measure of flow detachment in the wake area in the highest and lowest drag cases. The flow is significantly detached from the cylinder's surface when a large vortex is formed in the wake, which also the case of the highest drag. On the other hand, the small vortex in the *low drag* case implies a lower degree of flow detachment meaning a lower pressure droplet in the wake. The

insignificant difference between the two cylinders in the drag and lift coefficients test cases confirmed the validity of representing the falling droplet within the spray dryer with a droplet hanging technique. However, in the case of the liquid droplet, the effect on the internal flow and temperature distribution might be non-negligible which will be discussed later.

### 3.4.2. Heat and mass transfer coefficients validation

The simulation system, which is similar to the previous section, is set up in the 2D axis-symmetric plane. In this study, the validation tests for the heat and mass transfer coefficients of the flow past the sphere were carried out. The correlation (Ranz & Marshall, 1952) used to validate the heat and mass transfer coefficients are expressed as,

$$Nu = \frac{h_{Nu}D}{k} = 2 + 0.6 Re^{\frac{1}{2}} Pr^{\frac{1}{3}} \quad (3-56)$$

$$Sh = \frac{h_{Sh}D}{D_{va}} = 2 + 0.6 Re^{\frac{1}{2}} Sc^{\frac{1}{3}} \quad (3-57)$$

Where Nu is the Nusselt number, Sh is the Sherwood number, Re is Reynolds number, Sc is the Schmidt number and Pr is the Prandtl number, all of which are dimensionless. The sketch of the system setup is shown in Figure 3-37. The sphere radius is 50  $\mu m$  and the channel dimension is 2000  $\mu m$  in height and 500  $\mu m$  in width. The air is incompressible and the wall is at 'slip' condition (refer to equation (3-37)).

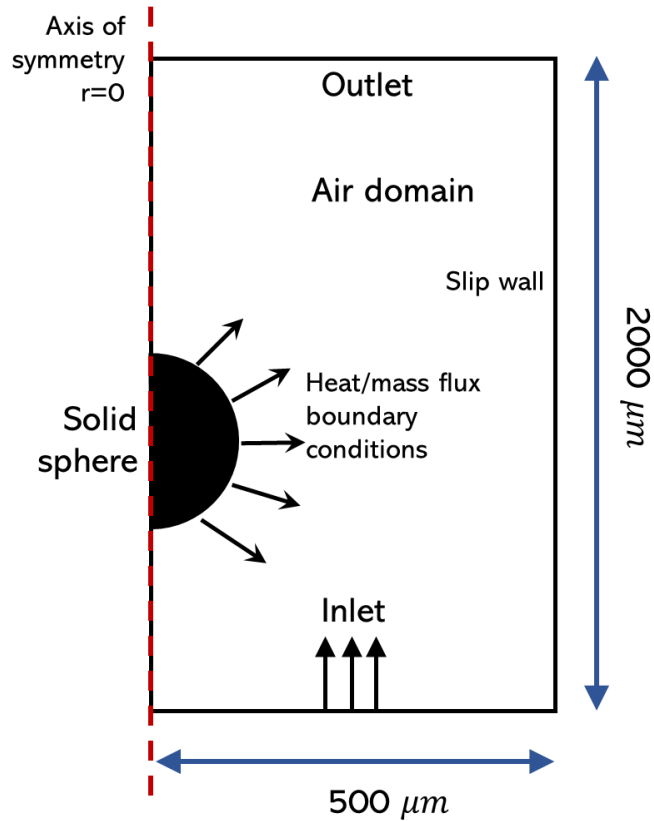


**Figure 3-37.** Boundary conditions for flow past a fixed sphere simulation.

The air flow is introduced by the inlet (lower boundary) and exit at the outlet (upper boundary). The wall (right boundary) is to slip condition. The channel is **2000 μm** in height and **500 μm** in width.

### 3.4.2.1. Governing physics and equations

#### 3.4.2.1.1. Fluid flow

The governing equation is the general form of the isothermal Navier Stokes equation (refer to equation (3-34)).

#### 3.4.2.1.2. Moisture transport in air

The diffusion of vapor in the air is governed by the equation,

$$\frac{\partial c_i}{\partial t} + \nabla \cdot (-D_{va} \nabla c_i) + \mathbf{u} \cdot \nabla c_i = 0 \quad (3-58)$$

Where  $c_i$  is the concentration of  $i^{th}$  species,  $\mathbf{u}$  is the velocity field,  $D_{va}$  is the diffusion of vapour in the air.

#### 3.4.2.1.3. Heat transfer in fluid

$$\rho C_p \left( \frac{\partial T}{\partial t} + \mathbf{u} \cdot \nabla T \right) = \nabla \cdot (k \nabla T) - (\nabla p \mathbf{u}) + \mathbf{u} \nabla \tau + Q \quad (3-59)$$

Where  $T$  is the temperature,  $p$  is the pressure,  $C_p$  is the specific heat capacity,  $\mathbf{u}$  is the velocity,  $\tau$  is the viscous stress tensor,  $Q$  is a source term.

#### 3.4.2.1.4. Boundary conditions

In this study, the heat and mass fluxes are applied at the surface to compute the heat and mass transfer coefficients. The aim is to test the accuracy of the simulation setup against the analytical solution. The outcome of this study will provide confidence in the chosen governing equations, boundary conditions and the FEM method. Consequently, it ensures the drying model, which will be developed at a later stage, is based on a valid mathematical framework.

A 'no-slip' condition (refer to equation (3-37)) is set at the sphere's interface. The inlet velocity boundary (refer to Figure 3-7) is set to be 0.237 m/s which is the analytical solution of the terminal velocity for a falling sphere. There are two viable options for choosing the boundary condition at the sphere interface: the Dirichlet boundary condition, in which a value is specified, and the Neuman boundary condition, in which the flux is applied. Since the flux is the quantity of interest used to calculate the heat or mass transfer coefficient, a Neuman condition is employed for a more convenient calculation. It should be noted that the Dirichlet boundary condition will also give the same answer to the Neuman condition in the same simulation setup, assuming the mesh independence is reached.

##### 3.4.2.1.4.1. Sherwood validation case

A constant mass flux of  $1 \text{ mol}/(\text{m}^2\text{s})$  is applied at the sphere's surface in the Sherwood cases. The initial concentration of species in the air is  $0 \text{ mol}/(\text{m}^2\text{s})$ . The air density is  $1.25 \text{ kg}/\text{m}^3$ . The mesh

configuration obtained during simulation based on the adaptive mesh refinement (AMR) is shown in Figure 3-38.

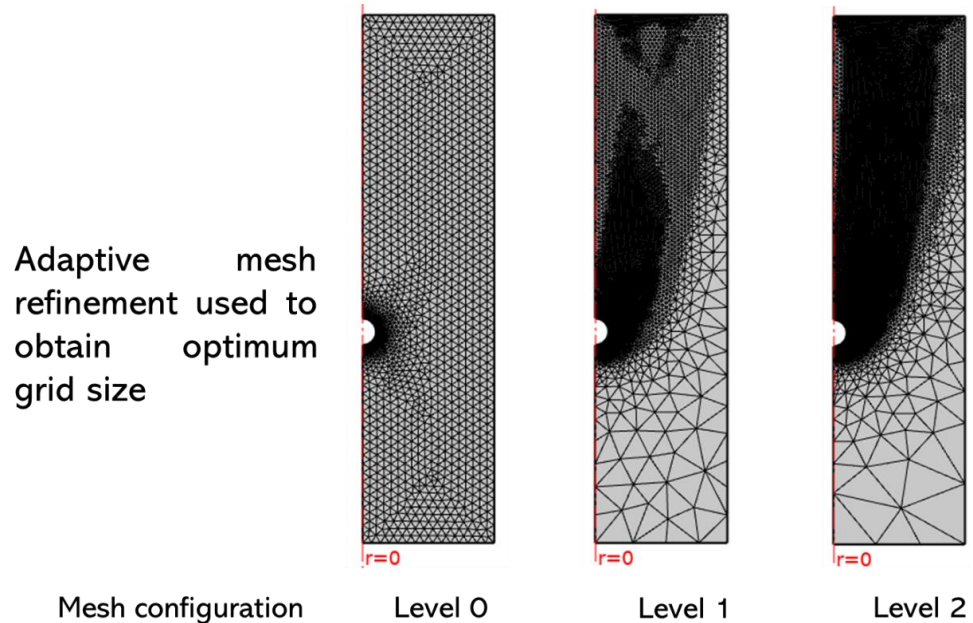


**Figure 3-38.** Mesh configurations during the simulation. The mesh refinement was adjusted based on the adaptive mesh refinement to have the optimal mesh. The initial mesh size was uniform everywhere in the domain. The mesh along the flow in the wake of the sphere is much more refined than the area in front of the sphere.

#### 3.4.2.1.4.2. *Nusselt validation case*

A constant heat flux of  $10000 \text{ W/m}^2$  is applied at the sphere interface. The inlet air velocity is set at  $0.237 \text{ m/s}$ . The initial air temperature is at  $293.15 \text{ K}$  and the air density is at  $1.25 \text{ kg/m}^3$ . The adjustment of the mesh refinement based on the adaptive mesh refinement algorithm is shown in Figure 3-39.

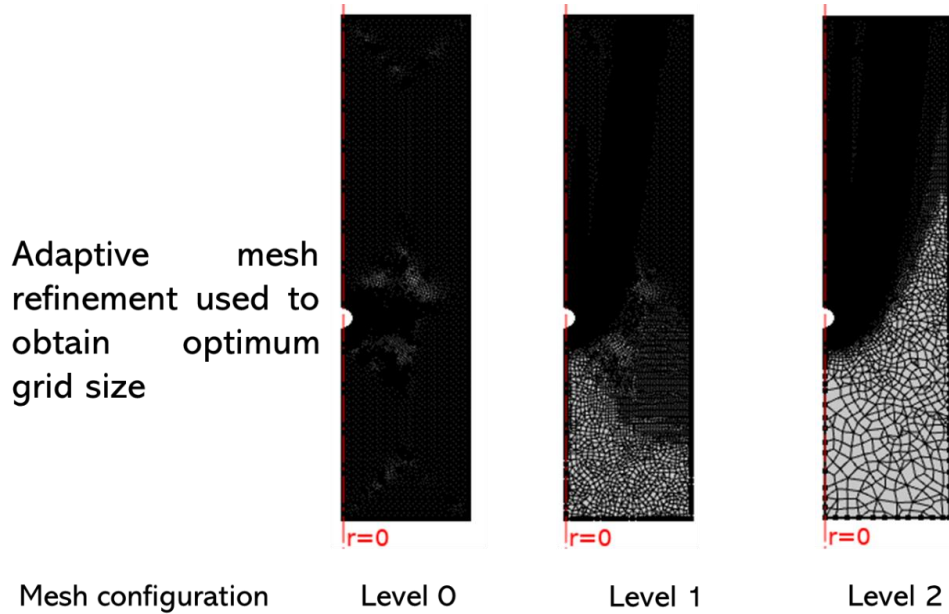


**Figure 3-39.** Mesh configurations during the simulation in the Nusselt number validation. The system starts with extremely fine mesh. The adaptive mesh refinement (AMR) algorithm relaxes the mesh in front of the sphere and keeps the refinement in the wake where the flow happens.

#### 3.4.2.2. Sherwood number validation

The adaptive mesh refinement algorithm is adopted for a more efficient meshing process. For the inlet flow at  $0.237 \text{ m/s}$ , the Reynolds and Schmidt numbers are shown in the following equations. The difference between the correlated and simulated mass transfer coefficient values is 10%. Theoretically, the error is expected to decrease at a much-refined mesh and a higher order of interpolation function.

$$Re = \frac{\rho U D}{\mu} = \frac{1.225 * 0.237 * 2 * 50e^{-6}}{1.814e^{-5}} = 1.604 \quad (3-60)$$

$$Sc = \frac{\mu}{\rho D} = \frac{1.81e^{-5}}{1.225 * 2.65e^{-5}} = 0.568 \quad (3-61)$$

$$Sh_{correlation} = 2 + 0.6 Re^{\frac{1}{2}} Sc^{\frac{1}{3}} = 2.576 \quad (3-62)$$

$$\bar{h}_{Sh-correlation} = \frac{Sh * D_{va}}{D} = 0.67 \text{ (ms}^{-1}\text{)} \quad (3-63)$$

$$\bar{h}_{Sh-simulation} = \frac{J_o}{(c_{surface} - c_{bulk})} = 0.602 \text{ (ms}^{-1}\text{)} \quad (3-64)$$

The velocity profile at a steady state is shown in Figure 3-40.

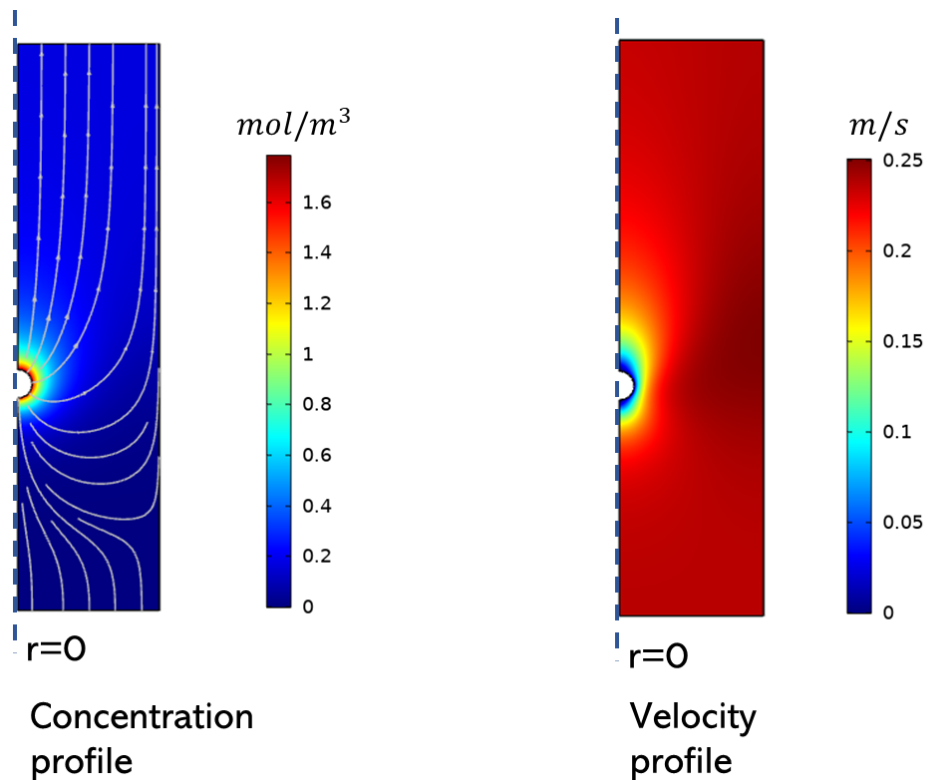


**Figure 3-40.** Steady-state concentration (left) and velocity (right) fields around the sphere in the Sherwood number validation case. The concentration and velocity scales are provided in the colour-coded option. The axis of symmetry is plotted as a blue line.

### 3.4.2.3. Nusselt number validation

The thermal conductivity of air around the sphere surface will be averaged at the sphere surface due to the non-uniform temperature profile. All the related dimensionless numbers are calculated.

$$Re = \frac{\rho UD}{\mu} = \frac{1.225 * 0.237 * 2 * 50e^{-6}}{1.814e^{-5}} = 1.604 \quad (3-65)$$

$$Pr = \frac{C_p \mu}{k} = \frac{1005.397 * 1.814e^{-5}}{0.0257} = 0.704 \quad (3-66)$$

$$h_{Nu-correlation} = \frac{Nu * k}{D} = 627.36 \text{ (Wm}^{-2}\text{K}^{-1}) \quad (3-67)$$

$$h_{Nu-simulation} = \frac{q_0}{(T - T_{ambient})} = 672.65 \text{ (Wm}^{-2}\text{K}^{-1}) \quad (3-68)$$

The velocity contour plot at steady state is provided in Figure 3-41.

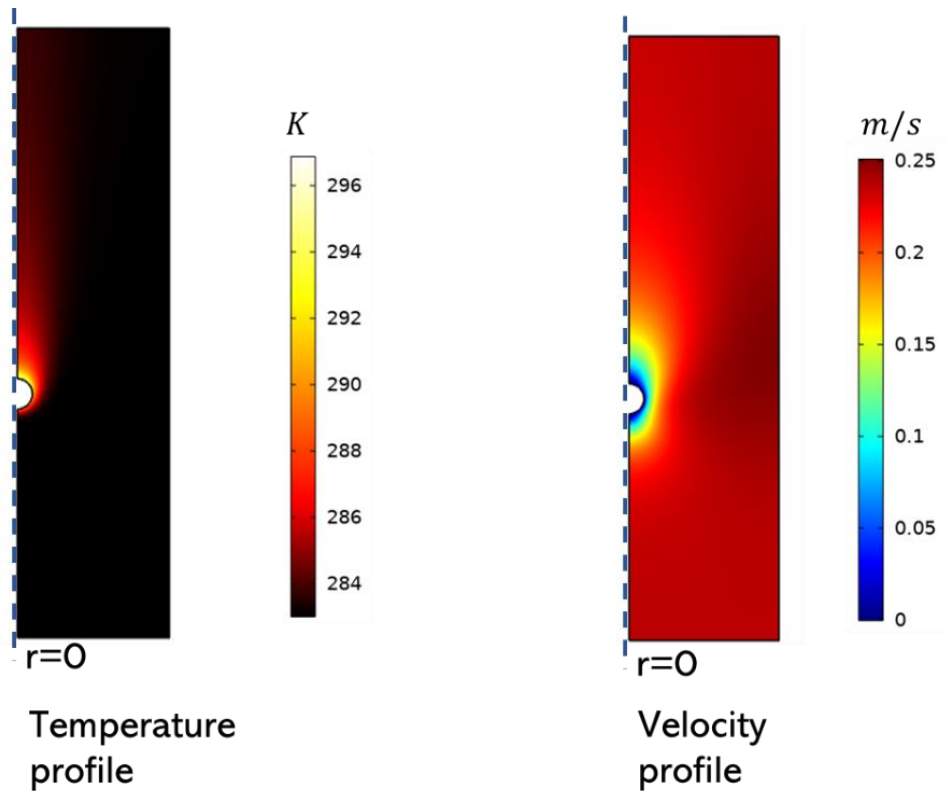


**Figure 3-41.** Steady-state temperature (left) and velocity (right) fields around the sphere in the Nusselt number validation case. The temperature and velocity scales are provided in the colour-coded option. The axis of symmetry is plotted as a blue line.

The difference between the correlated and simulated heat transfer coefficients value is 6.71%. In summary, the percentage error in the heat and mass transfer coefficients are within an acceptable range, providing that the experimental data used in this validation tests are less accurate at a low Reynolds number range. This is due to less experimental data is collected at this range, hence making the correlation less accurate. In summary, the verification and validation benchmarks are performed for the flow past a cylinder case. The FEM method, the ALE algorithm with the chosen governing equations, boundary conditions are proven to be sufficient for developing into the droplet drying system.

### **3.5. PID performance test on a freefalling liquid droplet**

In this study, a 50  $\mu\text{m}$  droplet is set up to freefall in the air at a terminal velocity which is controlled by a previously developed PID algorithm. No heat and mass transfer were considered in this simulation. The purpose of this investigation is to test the PID effectiveness in controlling a falling liquid object regarding the surface boundary condition at an object's interface. The simulation setup is adapted from the previous validation test with the sphere domain being replaced by the liquid water domain. The boundary condition is changed from 'no-slip' in the solid case to the 'water-air' surface tension in this water droplet case (refer to equation (3-71)). The outcome of this study will demonstrate the robustness of the PID loop which implies that it can be used to control the falling velocity of a drying droplet with high accuracy. It should be mentioned that the air velocity and the droplet size can be controlled independently in a single droplet drying experiment. However, it is the free-falling droplet system that is of interest in this section. Hence, the terminal falling velocity is associated with the droplet

size which means that the Reynolds number is unique and cannot be controlled freely in this study.

### 3.5.1. Problem formulation

The system describes a  $50\ \mu\text{m}$  spherical droplet free-falling in the air. The upcoming air velocity is controlled by the PID. The wall is set to 'slip' for symmetry condition (seen in Figure 3-42). The parameters for the PID control loop are taken from the falling cylinder case.

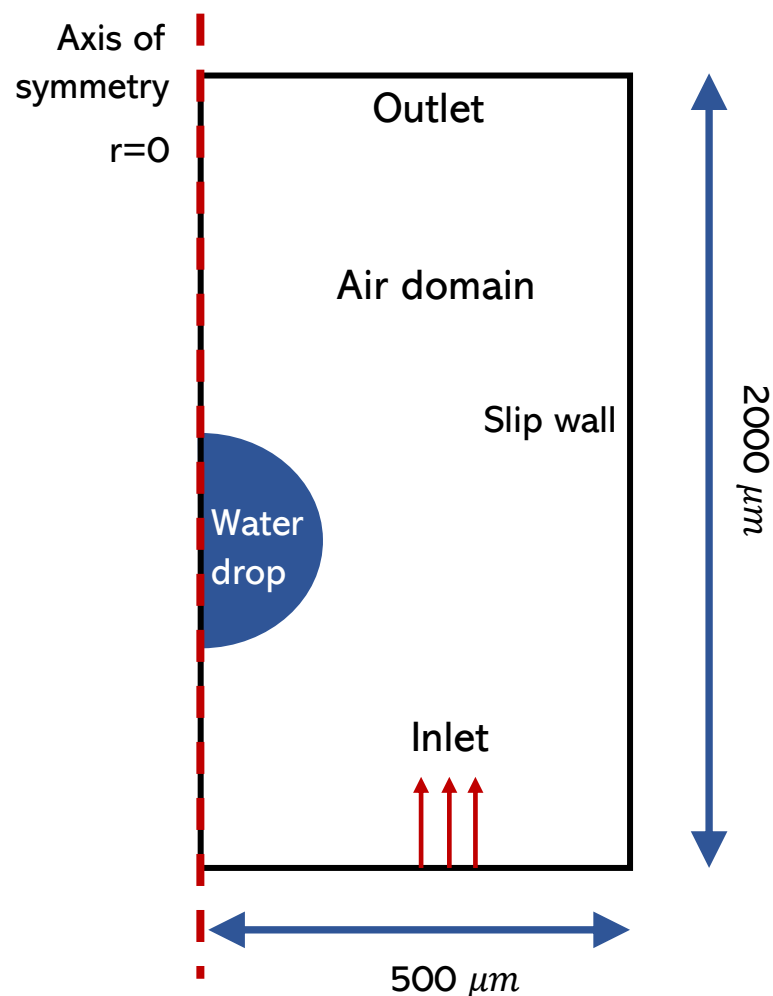


**Figure 3-42.** Schematic setup of a droplet freefalling in air. The PID algorithm is adopted to ensure the droplet falls with terminal velocity. The air enters the channel from the inlet (lower boundary) and exits at the outlet (upper boundary). The wall is slip and the axis of symmetry is at  $r = 0$  (red line).

### 3.5.2. Governing equations and boundary conditions

The governing equations are the same as the falling cylinder case (refer to section 3.4.2.1). The difference lies in the liquid-air interface condition which is expressed as follows,

$$\mathbf{u}_1 = \mathbf{u}_2 + \left( \frac{1}{\rho_1} - \frac{1}{\rho_2} \right) M_f \mathbf{n}_i \quad (3-69)$$

$$\mathbf{n}_i \cdot \boldsymbol{\tau}_2 = \mathbf{n}_i \cdot \boldsymbol{\tau}_1 + \mathbf{f}_{st} \quad (3-70)$$

$$\mathbf{f}_{st} = \sigma (\nabla_s \cdot \mathbf{n}_i) \mathbf{n}_i - \nabla_s \sigma \quad (3-71)$$

$$\mathbf{u}_{mesh} = \left( \mathbf{u}_1 \cdot \mathbf{n}_i - \frac{M_f}{\rho_1} \right) \mathbf{n}_i \quad (3-72)$$

Where  $\mathbf{u}_1, \mathbf{u}_2$  are the fluid velocities on the two sides of the interface,  $\mathbf{u}_{mesh}$  is the mesh velocity at the interface,  $\mathbf{n}_i$  is the normal vector of the interface (pointing from the higher-numbered domain to lower-numbered domain),  $\boldsymbol{\tau}_1$  and  $\boldsymbol{\tau}_2$  are the total stress tensor of the two domains 1 and 2 respectively,  $\mathbf{f}_{st}$  is force per unit area due to the surface tension (tangential component),  $\nabla_s$  is the surface gradient operator,  $\sigma$  is the surface tension at the fluid interface,  $M_f$  is the mass flux across the interface.

The mass flux is set to  $0 \text{ kg}/(\text{m}^2\text{s})$  at the moment for the simplification of the study. It is expected to be more dynamically complicated when the droplet starts to dry and shrink, resulting in a changing terminal velocity. The analytical solution for this system is one of the most important works in the particle hydrodynamics field and was obtained separately by Hadamard and Rybczynski in the same year (Hadamard, 1911) (Rybczynski, 1911). They proposed a general form of force exerted on the fluid sphere passing through another viscous solution with constant surface tension at the interface as,

$$F = 6\pi R_d \mu_d \mathbf{U} \frac{2\mu_d + 3\mu_a}{3(\mu_d + \mu_a)} \quad (3-73)$$

Where  $F$  is the force exerted on the droplet by ambient fluid,  $R_d$  is the droplet radius,  $\mu_d$  and  $\mu_a$  are the dynamic viscosity of droplet and surrounding air and  $\mathbf{U}$  is the terminal velocity of the droplet. The boundary condition at the droplet's surface is set to be the water-air surface tension.

### 3.5.3. Results

The analytical solution from the equation (3-73) is  $0.003 \text{ m/s}$ . The terminal falling velocity of a  $5 \text{ }\mu\text{m}$  droplet through the air is calculated to be  $0.0017 \text{ m/s}$ .

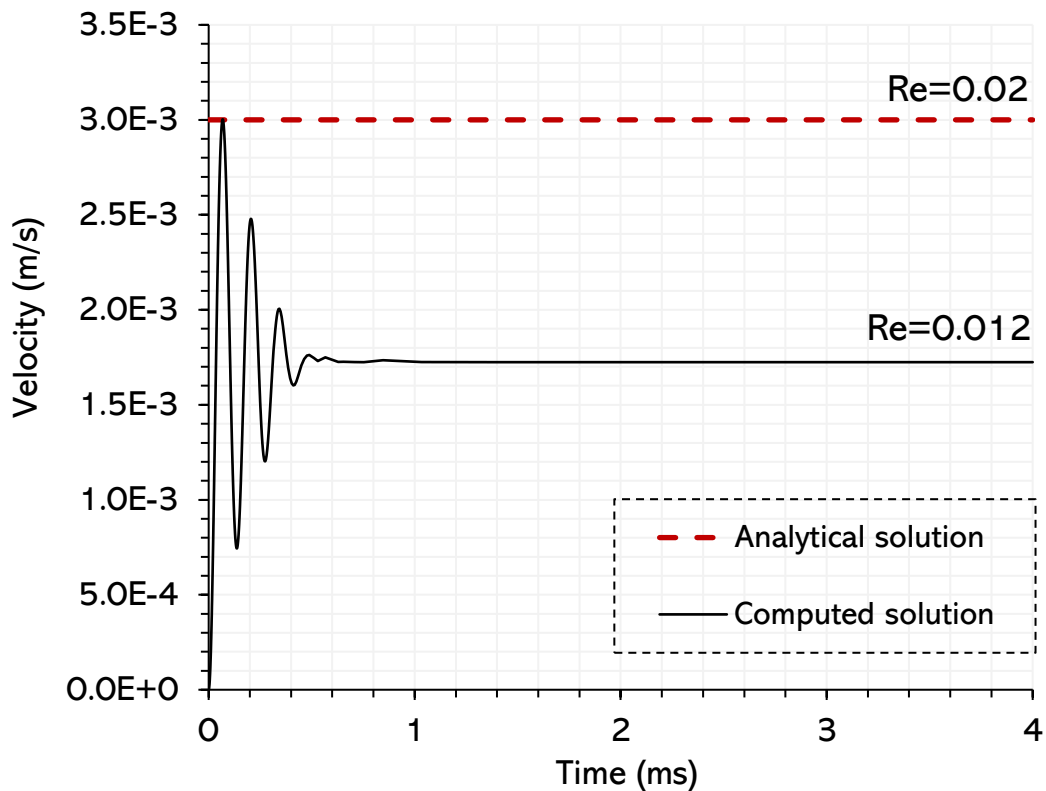


**Figure 3-43.** Terminal velocity predicted by simulation versus analytical solution.

According to Zapryanov and Tabakova (2013), the terminal velocity prediction by Hadamard-Rybczynski for a droplet in the creeping

flow is up to 50% higher than that of a rigid sphere with the same physical parameters. This can be explained by a different surface condition in both cases, however, the experimental drag on droplets agrees more with Stoke's formula, which is closer to a solid sphere, than the Hadamard-Rybczynski's solution. The influence of internal circulation on the drag force was taken as one of the factors for this discrepancy. The flow field within the droplet can be visualised in Figure 3-44.

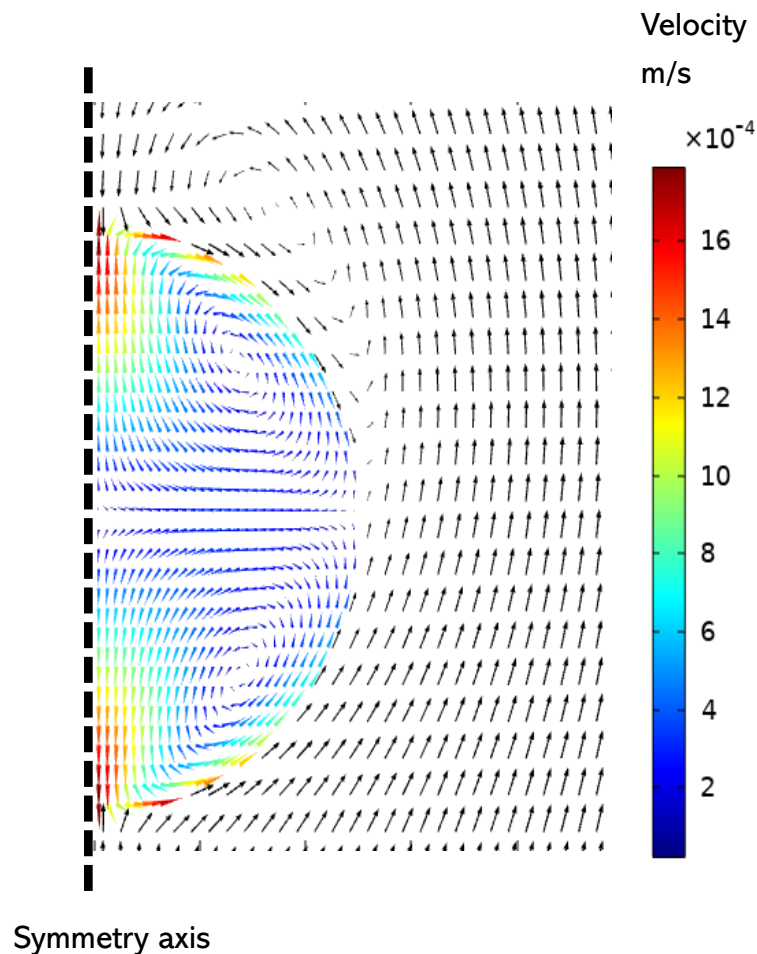


**Figure 3-44.** Internal and external flow field near the droplet's interface.

The velocity field is provided both internally and externally of the droplet. The vector arrow is colour-coded within the droplet and black in the air domain.

In order to test if this argument is true, the droplet dynamic viscosity can be altered to mimic the rigid sphere condition to some

degree. The simulation tests again with the droplet's viscosity increased from  $0.001 \text{ Pa}\cdot\text{s}$  to  $1000 \text{ Pa}\cdot\text{s}$ . The terminal velocity, in this case, resulted in  $0.00167 \text{ m/s}$  and the internal circulation is significantly prohibited due to an extremely high viscosity fluid, as in Figure 3-45.

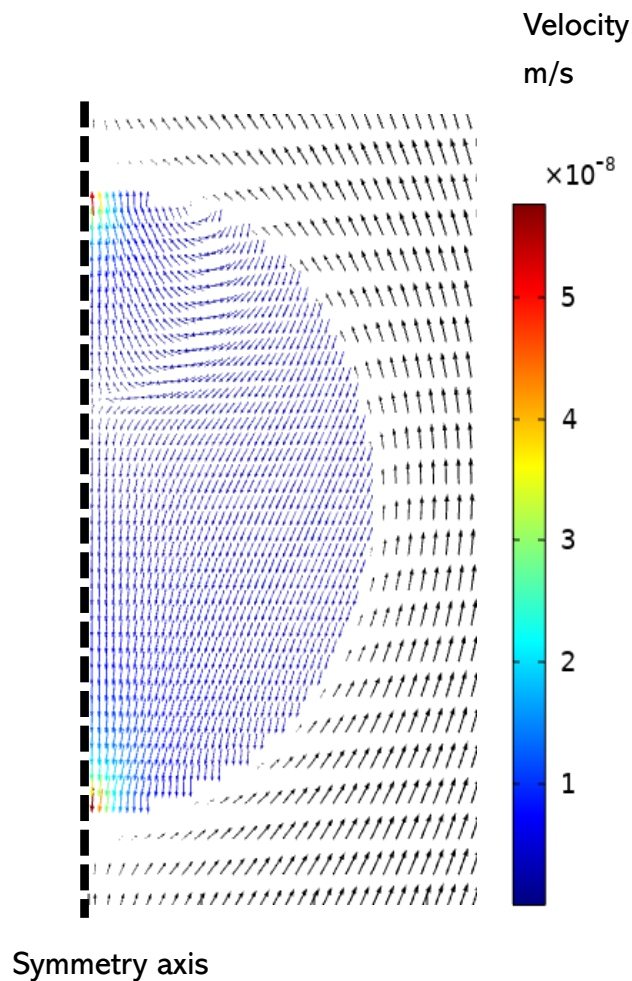


**Figure 3-45.** 2D low field when the droplet viscosity is increased  $10^6$  folds. Colour-coded vector arrows are plotted within the droplet interior. The velocity scale is provided. The droplet surface is hidden for better visualisation of the vector field.

The velocity magnitude within the droplet is reduced by a thousand times compared to the case in Figure 3-46. This confirms a considerable influence of the internal flow on the terminal falling velocity of the droplet. Next, a falling sphere with the same size and

density as the droplet is simulated (black line in Figure 3-46). This test run is to justify the previous claim on the over-prediction of Hadamard-Rybczynski's solution to the Stoke's flow. The terminal velocity for a sphere is computed to be  $0.0025 \text{ m/s}$ , which is 20% less than the analytical solution from Hadamard-Rybczynski. The total drag on a water droplet and sphere in both cases are plotted together in Figure 3-46. The difference in the surface drag suggests the spherical droplet of water would fall at a different speed compared to the solid sphere with a 'no-slip' boundary condition on the surface.

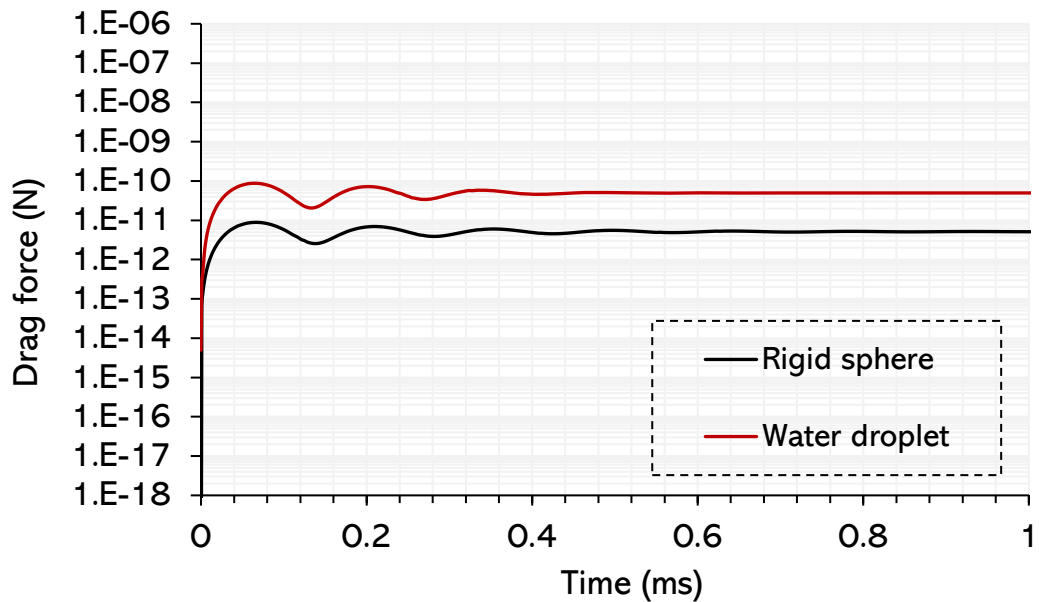


**Figure 3-46.** Drag on a solid sphere and liquid sphere of the same size. The drag force is averaged over the surface of the circular domain.

### **3.6. Conclusions**

In conclusion, The PID loop was tuned to model an object falling with terminal velocity in a 2-dimensional system. It has proven to be highly efficient to numerically compute the terminal velocity. The FEM method has been shown to validate all benchmark studies and be ready to implement into the droplet drying modelling system. The governing equations and boundary conditions used in Chapter 3 will be adapted, and the assumption of incompressible flow will be revisited in Chapter 5. The average droplet size within the spray dryer is reported to be in the range of  $5 \mu m$  to  $500 \mu m$ , so the droplet within this range will be chosen in the following chapters. It is expected that the droplet within this size range will fall without the vortex shedding in the wake, which will be shown in the study in Chapter 5.

# Chapter 4

## **Benchmarks of bubble growth within a liquid medium**

In Chapter 4, a mathematical framework is developed to model the bubble dynamics within a liquid medium which will be used to model the droplet boiling. The aim is to set up a simulated system for the phase change phenomena, and verify it against the available benchmark studies. The first section is the verification of the simulation outcome (using the FEM method), which is based on the Stefan problems, against the analytical solution. The following section investigates the bubble growth due to the inertia (pressure) and the thermal (temperature) effects. The computed result from the pressure-driven bubble growth will be verified against the analytical solution developed by Rayleigh (1917), who laid the foundation for the vapor bubble research field. Rayleigh (1917) work focuses on modelling the pressure-driven bubble growth in an infinite liquid domain. Prosperetti (1982a) then generalised the Rayleigh-Plesset equation taking into account the mass exchange at the bubble's interface. Scriven (1959) contributed to the field by deriving an analytical solution for the bubble growth due to phase change at the bubble interface. The analytical solution from Scriven (1959) will therefore be used to compare against the simulation of the thermal-driven bubble growth. The outcome of Chapter 4 provides the verified choice of governing equations and boundary conditions for modelling the bubble growth within the droplet.

#### 4.1. Solving Stefan problem using FEM

The Stefan problem is a very well-known test case for phase-change dynamics (Irfan and Muradoglu, 2017). The problem involves two phases in a 2D geometry in which the phase change happens at the interface. The gas phase is heated and the liquid phase is constrained to the saturation temperature. The evaporation is driven by the heat flux between two phases, which must be sufficient to maintain the interface at the saturation temperature. The interface position is analytically expressed in equation (4-1).

$$x_{interface} = 2\gamma\sqrt{\alpha_g t} \quad (4-1)$$

$$\alpha_g = \frac{k_g}{\rho_g C_{pg}} \quad (4-2)$$

Where  $x_{interface}$  is the interface horizontal position within the domain, and  $\alpha_g$  the thermal diffusivity of the gas phase,  $k_g$  is the thermal conductivity of gas,  $\rho_g$  is the gas density,  $C_{pg}$  is the gas heat capacity at constant pressure.  $\gamma$  is the growth constant which is also derived analytically.

$$\gamma e^\gamma \operatorname{erf}(\gamma) = \frac{C_{pg}(T_w - T_{sat})}{h_{lg}\sqrt{\pi}} \quad (4-3)$$

Where  $h_{lg}$  is the latent heat of evaporation and the error function (erf) of  $\gamma$  is in the form of,

$$\operatorname{erf}(\gamma) = \frac{2}{\sqrt{\pi}} \int_0^\gamma e^{-h^2} dh \quad (4-4)$$

The growth constant,  $\gamma$ , can be obtained using iteration or Newton-Raphson methods. The analytical temperature profile across the domain is also a function of the growth constant.

$$T(x, t) = T_w + \left( \frac{T_{sat} - T_w}{\text{erf}(\gamma)} \right) \text{erf} \left( \frac{x}{2\sqrt{\alpha_g t}} \right) \quad (4-5)$$

Where  $x$  is the horizontal position along with the domain. The initial temperature profile is calculated analytically from equation (4-5) and later plotted in Figure 4-3.

#### **4.1.1. Problem formulation**

A cavity containing a liquid and gas phase has a temperature difference between the two outer walls. The heat transfer will be solved separately within the two domains sharing a moving interface. The liquid phase temperature is initially at saturation temperature, 100°C, and stays constant throughout the simulation. The gas phase is superheated by the wall on the left at 150°C. The evaporating front is the vertical lines located at  $x = 0.01 \text{ m}$  where the temperature is constrained at 100°C. The temperature gradient is established as the heat conducts through the gas domain, and the interface starts to move in the direction that ensures the temperature is always constrained to the saturation temperature. The fluid flow and gravity will not be considered in this test which can be referred to as the 'stagnant fluid problem' with no natural convection. The simulation schematic is shown in Figure 4-1.

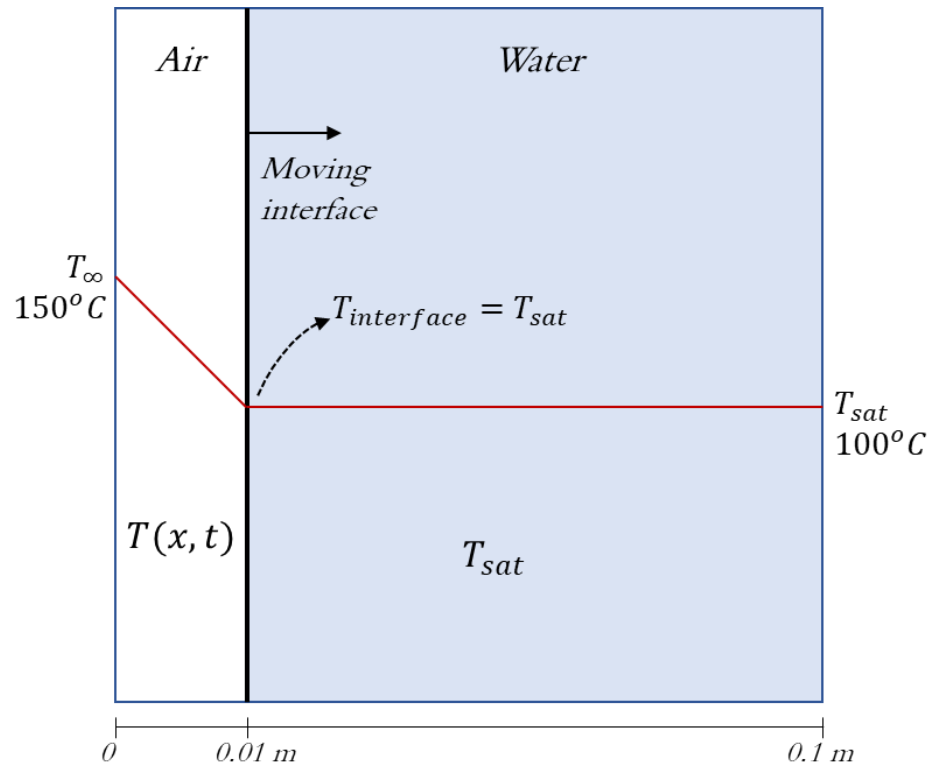


**Figure 4-1.** Domain and boundary conditions for Stefan's problem. The liquid temperature is maintained at  $100^\circ\text{C}$ , and the Air is heated up to  $150^\circ\text{C}$ . The interface is moving towards the water domain as phase change happens.

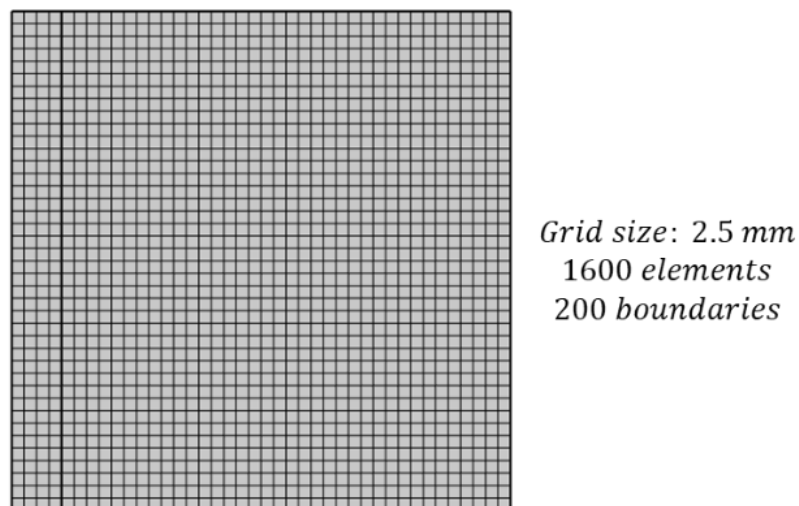


**Figure 4-2.** Mesh configuration for Stefan's problem – mapped structure. Quadrilateral mesh is chosen for this simulation. The square domain with the side of 0.1 m is used.

The domain was meshed with the mapped structure, shown in Figure 4-2. The mesh independence test was also done with 3 different quadrilateral element sizes: 10 mm, 5 mm, and 2.5 mm. Table 4-1 reviews the material properties for phases used in this study.

Parameters	Gas	Liquid
Density , $\rho$ [kg/m <sup>3</sup> ]	1.25	1000
Dynamic viscosity , $\mu$ [Pa.s]	$2.39e^{-5}$	$2.82e^{-4}$
Thermal conductivity , $k$ [W/(m.K)]	0.0353	0.6794
Heat capacity , $C_p$ [J/(kg.K)]	1017.72	4218.21
Latent heat of vaporisation, $h_{lg}$ [J/kg]	$2.45e^6$	
Saturation temperature, $T_{sat}$ [K]	373.15	
Superheated temperature [K]	423.15	

**Table 4-1.** Physical properties of gas and liquid phases in the simulation.

All the variables are evaluated at the temperature of the associated phase.

As equation (4-3) is the transcendental equation, the Newton-Raphson technique can be applied to find the solution (refer to appendix A.2). The growth constant,  $\gamma$ , for this system is calculated to be 0.10147. The interface is already at  $x = 0.01$  m initially. This indicates the simulation will not start at  $t = 0$ , but at the time it takes for the interface to move from  $x = 0$  m to  $x = 0.01$  m. Hence, the initial distribution of temperature within the gas phase, in Figure 4-3, is known, and should be obtainable analytically.

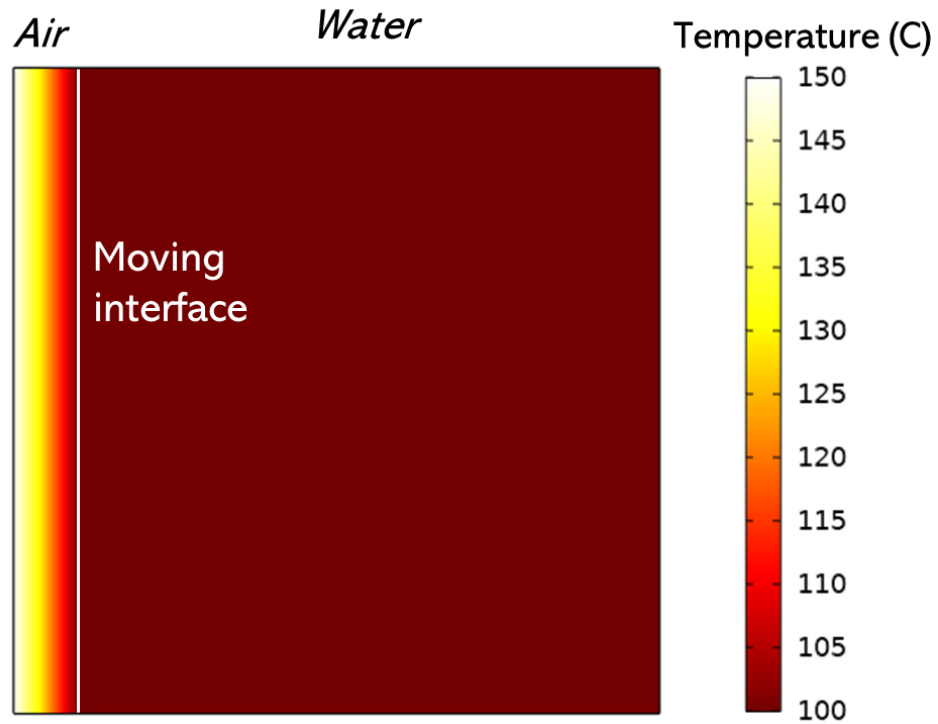


**Figure 4-3.** Initial temperature distribution within the Air (left) and Water (right) domains at  $t = 0s$ . The moving interface is represented (middle line) and the temperature scale is provided in degree Celcius. The water domain temperature is kept constant at  $100^{\circ}C$  and the left wall in the air domain is at  $150^{\circ}C$ .

#### 4.1.2. Results

The interface's position and the temperature variation from left to right at  $t = 2000s$  are given in Figure 4-4 and Figure 4-6, respectively.

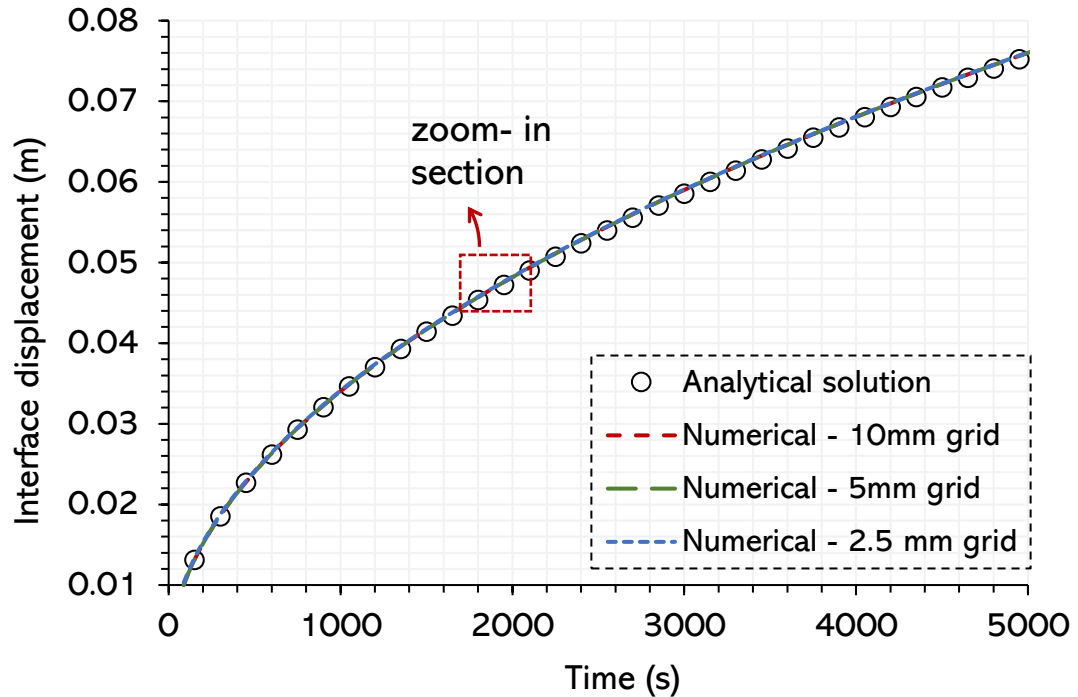


**Figure 4-4.** Interface position,  $x(m)$ , along with the domain different numerical grid sizes. Three different grid size was provided. The difference between the simulation and analytical solution is small, which is visualised in the zoom-in plot.

The three mesh configurations show a high level of numerical accuracy. Their difference cannot be seen clearly from the scale in Figure 4-4. The zoom-in section at  $t = 2000 s$  are plotted separately on Figure 4-5 to check for the discrepancy. Meanwhile decreasing the grid size from  $10 mm$  and  $5mm$  does not improve the prediction of the interface position, the smallest grid size of  $2.5 mm$  improves the result by 1.2% (as shown in Figure 4-5). Since this is a negligible increment in the accuracy, it can be concluded that the mesh independence is reached.

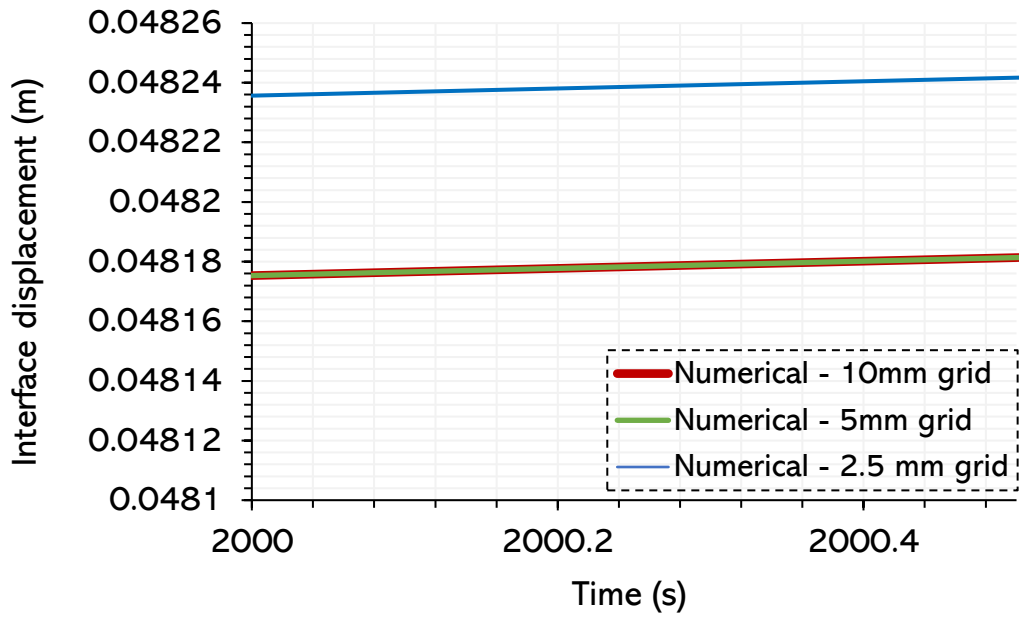


**Figure 4-5.** Zoom-in section in Figure 4-4 for the mesh independence test. The grid size of 2.5 mm is different from the other 2 grid sizes.

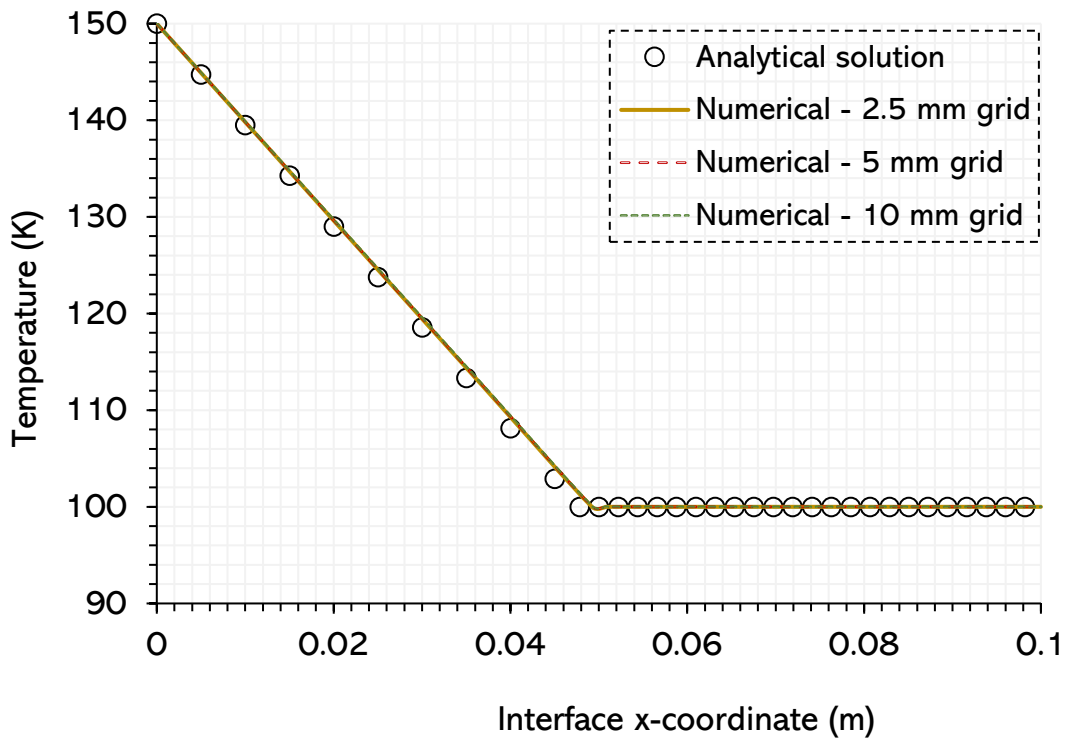


**Figure 4-6.** Temperature profile within the air and liquid domains. The temperature is plotted along the horizontal line, which starts from the wall in the air domain ( $T=150^{\circ}\text{C}$ ) towards the liquid domain ( $T=100^{\circ}\text{C}$ ).

The numerical temperature profile matches the analytical solution as shown in Figure 4-6. The three different mesh refinement options have a negligible error at an order of  $\pm 0.01^{\circ}\text{C}$ . The mesh deformation shown in Figure 4-7 is important to consider for the result's reliability.

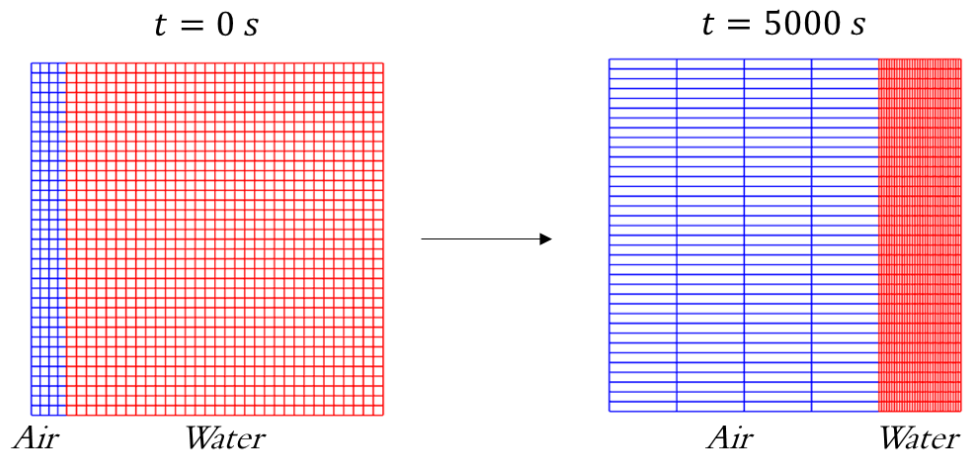


**Figure 4-7.** Mesh plot within the air and liquid domains. The mesh is deformed as the interface moves towards the liquid domain. The phase is colour-coded for the air (in blue) and the water (in red) domains.

The mesh is stretched as the interface moves towards the liquid side. The mesh refinement technique was not used. The quality of the mesh is kept at highest throughout the simulation since all nodes are deformed in the x-direction only and all element is well-maintained at the rectangular shape. This is the advantage of mapped mesh, however, since the geometry is simple in this particular case, it does not guarantee the same behaviour in the case of the droplet with the curvature surface geometry.

## 4.2. Verification benchmarks of bubble growth in a liquid medium

The verification benchmarks analysis in this section is to investigate the accuracy and reliability of the bubble growth within a liquid

domain case. A successful validation against analytical solutions can improve the credibility of the simulation and confidence when integrating the boiling into the drying model.

#### **4.2.1. Verification of the pressure-driven growth of a bubble (inertia effect)**

This section studies the pressure effects on the bubble expansion within an infinite liquid and a droplet with the mass exchange at interfaces. An analytical solution is derived by Rayleigh-Plesset (1917) for the case of bubble growth due to the inertia effect.

$$R \frac{d^2R}{dt^2} + \frac{3}{2} \left( \frac{dR}{dt} \right)^2 + \frac{4\vartheta_L}{R} \frac{dR}{dt} + \frac{2\sigma}{\rho_l R} + (P_\infty - P_b) = 0 \quad (4-6)$$

Where  $R(t)$  is the bubble radius as a function of time,  $\vartheta_L$  is the kinematic viscosity of the surrounding fluid,  $\sigma$  is the surface tension,  $P_\infty$  and  $P_b$  are the pressure at infinity and within the bubble. This equation implies the bubble can grow out of zero volume which is a challenge to model. It is therefore less complicated to assume a certain initial bubble radius starting at reference size and temperature. The temperature of the bubble interior is set to the same as the surrounding liquid to study specifically this inertia effect, since the temperature gradient might cause a significant difference in vapour pressure causing and make the inertia effect less distinguishable. The behaviour of the gas within the bubble is polytropic at which the pressure can be expressed as,

$$P_b = P_{b0} \left( \frac{R_0}{R} \right)^{3k} \quad (4-7)$$

Where  $p_b$  and  $p_{b0}$  are the bubble pressure at time  $t$  and  $t_0$ ,  $R$  and  $R_0$  are the bubble radius at time  $t$  and  $t_0$  and  $k$  is a constant which will be set as 1 to describe the ideal gas behaviour. The final form of the analytical equation used in this study reads,

$$R \frac{d^2 R}{dt^2} + \frac{3}{2} \left( \frac{dR}{dt} \right)^2 + \frac{4\vartheta_L}{R} \frac{dR}{dt} + \frac{2\sigma}{\rho_l R} + P_\infty - P_{b0} \left( \frac{R_0}{R} \right)^3 = 0 \quad (4-8)$$

The extra radius-ratio term is introduced to get rid of the zero-volume problem and should make the bubble expansion well behaved and more realistic. This will be tested against the simulation setup in the next section.

#### 4.2.1.1. Problem formulation

The air bubble of 5 mm in radius is placed within an infinite liquid circular domain at 5000 mm in radius. The bubble's interior is slightly over-pressured initially by  $\Delta p = 1 Pa$ . The temperature for both phases is 298.15 K, and the surface tension between air-water is at a constant of 0.07 N/m. The quadrilateral mesh was used as the expansion is only radial symmetric. The number of nodes distributed on the bubble and the liquid surfaces is of the same value to conform better to the mesh deformation, as in Figure 4-8.

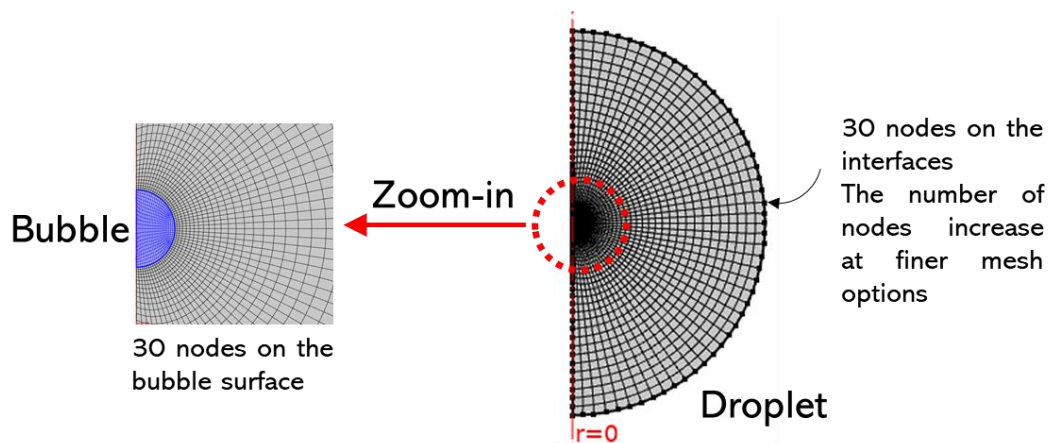


**Figure 4-8.** Mesh configuration for the pressure-driven bubble case (inertia-effect). The quadrilateral mesh is used for both domains, and the number of nodes on the droplet and bubble surfaces is 30 nodes. The number of nodes increases as the mesh is refined in the mesh independence test.

A circular-shaped liquid domain has a better meshing process without screwing elements at the corner. The water and air physical

properties are taken at room temperature and the whole system is solved with a fully compressible Navier-Stokes equation.

#### 4.2.1.2. Results

The velocity field within the bubble during expansion is shown in Figure 4-9.

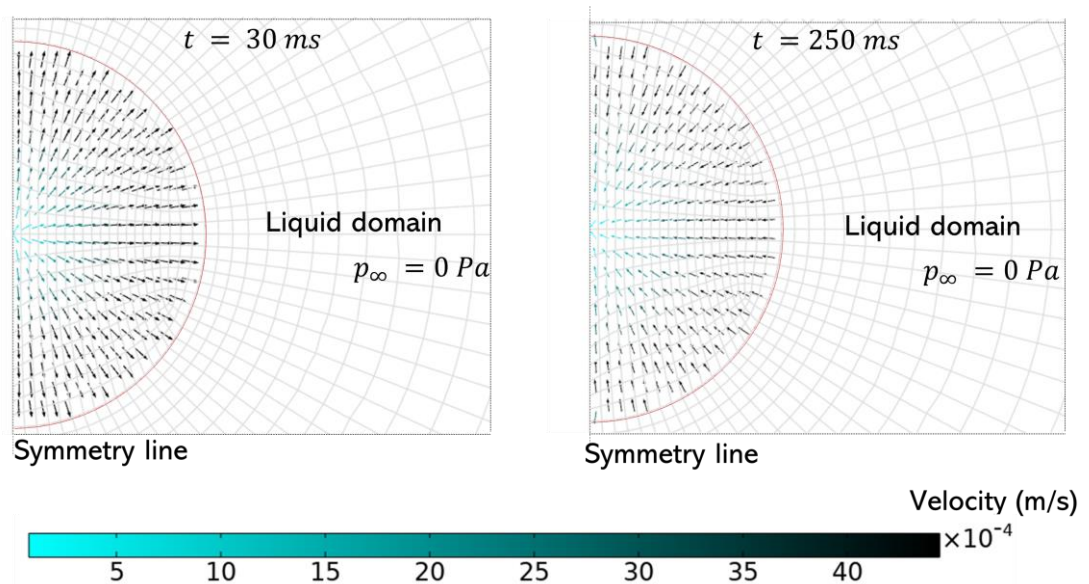


**Figure 4-9.** Mesh element and velocity field within the bubble during expansion at  $t = 30 \text{ ms}$  and  $t = 250 \text{ ms}$ . The arrow vector is plotted for the velocity field within the bubble, and is colour-coded for the magnitude of the velocity.

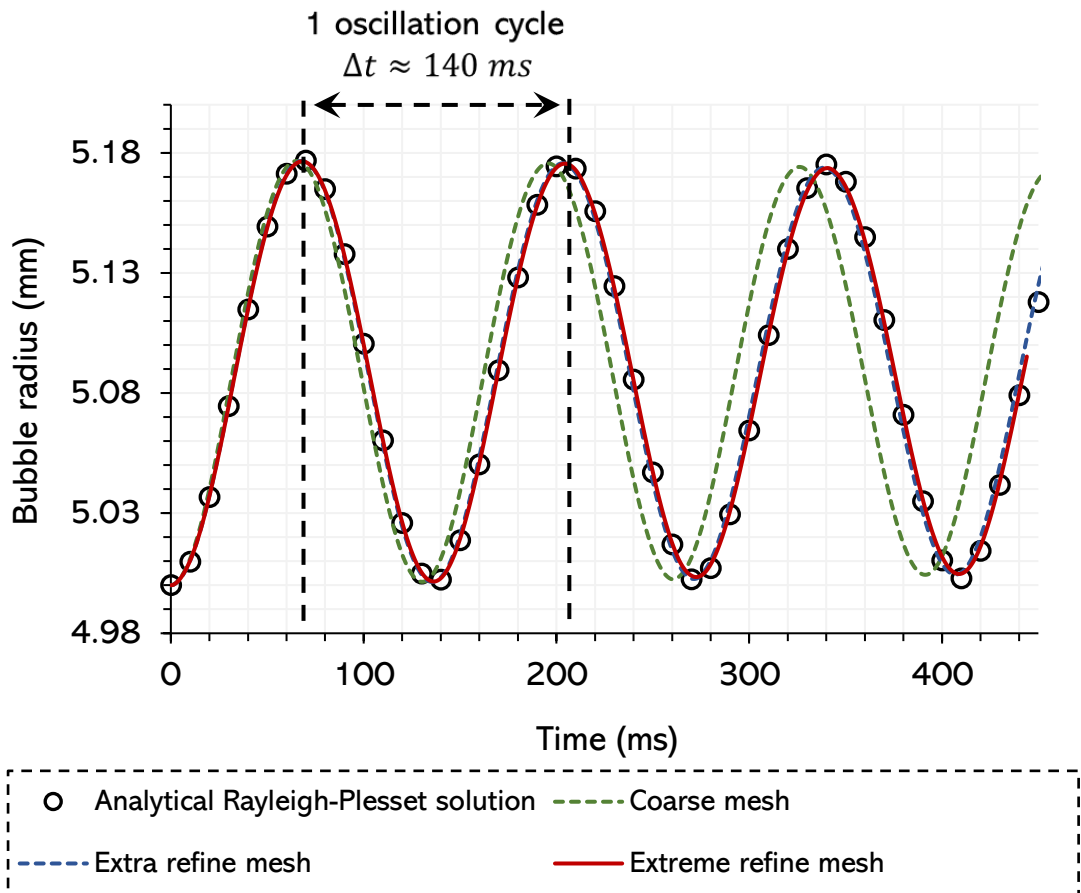


**Figure 4-10.** Bubble radius against time at different grid sizes. The bubble oscillation profile is verified against the analytical solution from Rayleigh (1917). The mesh is refined at 3 different levels: Coarse (1792 elements, 30 surface nodes), Extra refine (5152 elements, 50 surface nodes) and Extreme refine (8980 elements, 70 surface nodes).

The mesh independence was achieved and the computed bubble radius profile matches against the analytical Rayleigh-Plesset solution (seen in Figure 4-10). The Rayleigh-Plesset equation can be solved by an integrated iterative solver in COMSOL, or by the ode45 or ode23 solvers in Matlab (refer to Appendix B). The mesh smoothing technique was shown to have a slight effect on the result. The solver method is noticeably important in this case since the solution is of an oscillatory type. The time step taken by the solver needs to be smaller than the oscillation period. The tolerance in this

study is reduced to  $1e-6$  to improve the accuracy. The overpressure of only 1 Pa was chosen to eliminate unnecessary numerical instabilities. Any significant amount of overpressure requires a finer mesh, a higher-order mesh smoothing technique, and the surface tension which needs to be relaxed initially by a step function. From the verification test, the physics, boundary conditions, and type of solvers are shown to be chosen properly and can be used to develop into a more complex model. The next step is to verify the case of thermal effect which involves coupling the Navier-Stokes equation with the heat transfer equation.

#### 4.2.2. Verification of the temperature-driven growth of a bubble (thermal effect)

The analytical solution of the thermal effect on the bubble growth was derived analytically by Scriven (1959). The mass flux of the gas phase entering the bubble is determined by the amount of heat flux that keeps the interface at saturation temperature. The analytical form of the bubble radius overtime should read,

$$R_b = 2\gamma \sqrt{\frac{k_l}{\rho_l C_{pl}} t} \quad (4-9)$$

Where  $k_l$  is the thermal conductivity of the liquid,  $\rho_l$  is the liquid density,  $C_{pl}$  is the heat liquid heat capacity at constant pressure and  $\gamma$  is the growth constant which is also derived analytically.

$$\begin{aligned} & \frac{\rho_l C_{pl} (T_\infty - T_{sat})}{\rho_g \left( h_{lg} + (C_{pl} - C_{pg}) (T_\infty - T_{sat}) \right)} \\ & = 2\gamma^2 \int_0^1 e^{\left( -\gamma^2 \left( (1-\xi)^{-2} - 2 \left( 1 - \frac{\rho_g}{\rho_l} \right) \xi - 1 \right) \right)} d\xi \end{aligned} \quad (4-10)$$

The growth constant,  $\gamma$ , can be obtained using iteration or Newton-Raphson methods (refer to Appendix A.2). The analytical

temperature profile across the domain is also a function of the growth constant.

$$T = \begin{cases} T_{sat} , & r \leq R_b \\ T_{\infty} - 2\gamma^2 \left( \frac{\rho_g (h_{lg} + (C_{pl} - C_{pg})(T_{\infty} - T_{sat}))}{\rho_l C_{pl}} \right) \times \dots & \\ \dots \int_{1-\frac{R_b}{r}}^1 e^{\left( -\gamma^2 \left( (1-\xi)^{-2} - 2 \left( 1 - \frac{\rho_g}{\rho_l} \right) \xi - 1 \right) \right)} d\xi , & r > R_b \end{cases} \quad (4-11)$$

#### 4.2.2.1. Problem formulation

A bubble at saturation temperature is located within an infinite liquid medium. A similar system to Stefan's problem case is reused with the same physical parameters for both phases. The surrounding liquid water is overheated by 50°C to the saturation temperature which is 100°C. The bubble radius is 5 *um* and the liquid domain is 50 *um* x 50 *um* x 50 *um* (width x length x height). The initial temperature field is evaluated analytically from the equation (4-11) according to the bubble size at which the simulation started. The temperature at the bubble's surface and the walls are maintained at 100°C and 150 °C, respectively. As the system in this test is a full 3-dimensional, the computational domain will be reduced using symmetry planes so that only the symmetrical portion of a bubble is computed. The geometry setup is in Figure 4-11.

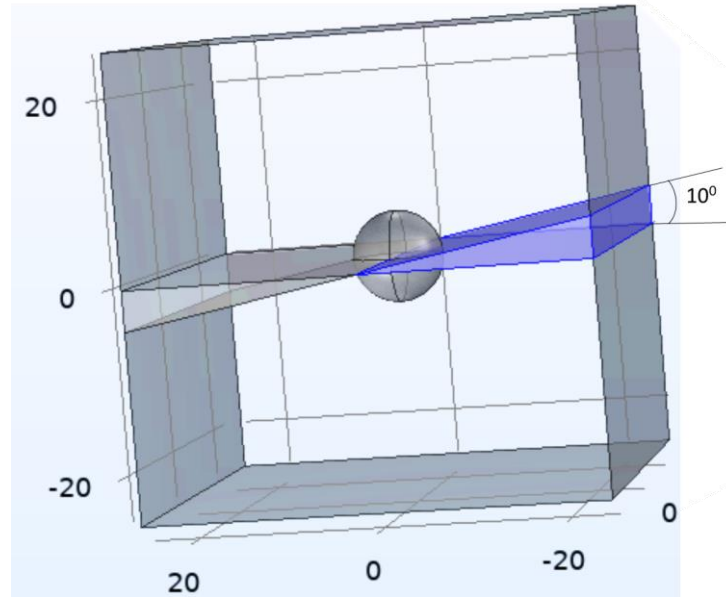


**Figure 4-11.** Representation of the full geometry setup (in grey) and a computational domain (in blue). The blue domain is a portion of the whole domain with an angle of  $10^\circ$ . The simulation will be performed in the blue segment with symmetry boundary conditions to save computational resources.

The energy balance for computing the interface velocity at the evaporating front is expressed by,

$$\rho_l \Delta H_{lg} v \cdot \mathbf{n} = (\Phi_l - \Phi_g) \cdot \mathbf{n} \quad (4-12)$$

Where  $\rho_l$  is the liquid density,  $H_{lg}$  is the latent heat of evaporation,  $v$  is the interface velocity,  $\mathbf{n}$  is the normal vector,  $\Phi_l$  and  $\Phi_g$  are the heat fluxes from liquid and gas sides (see Figure Figure 4-12).

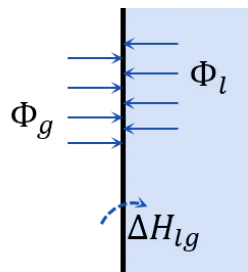


**Figure 4-12.** Schematic of phase change across the two phases interface. The  $\Phi_g$  and  $\Phi_l$  are the gas and liquid phases.  $\Delta H_{lg}$  is the latent heat of evaporation.

#### 4.2.2.2. Results

The system is simulated for 20 ns with an initial bubble radius at  $r = 5 \mu\text{m}$ . The bubble growth rate against time is seen in Figure 4-13. The computed result agrees closely with an analytical solution and the mesh independence is also achieved. There is no data in the gap between  $t = 0 \text{ ns}$  and  $t \approx 8 \text{ ns}$  as the analytical solution can predict the bubble at any point in time, while the simulation starts with a certain size of the bubble.

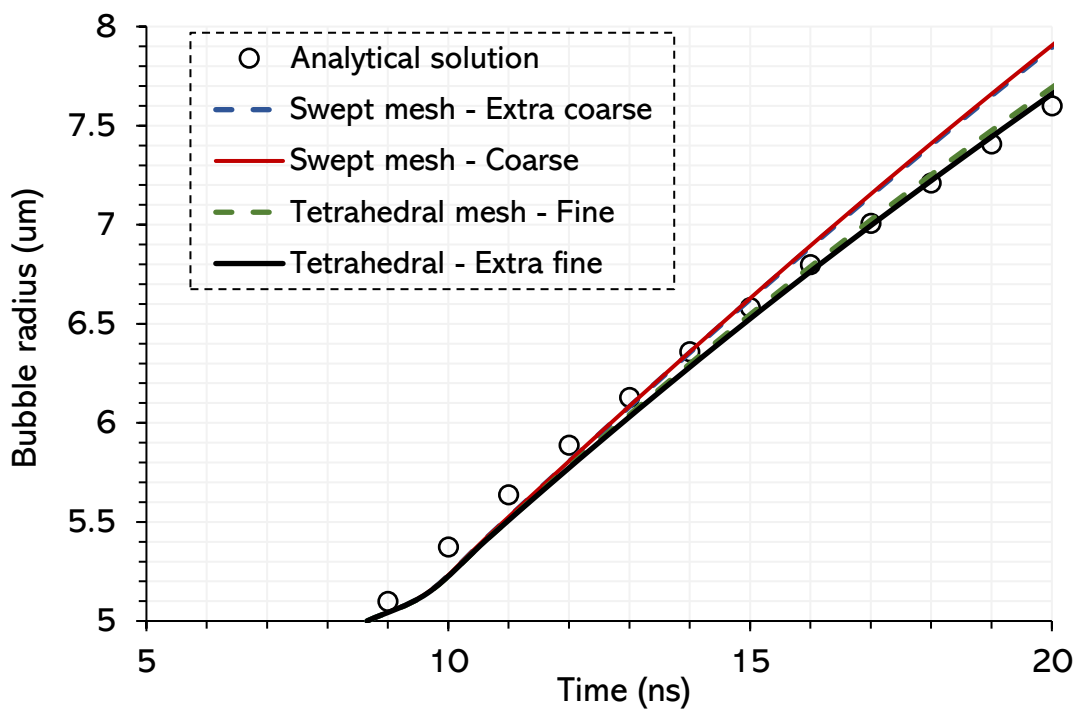


**Figure 4-13.** Bubble growth due to thermal effect (evaporation) over time at different grid sizes. The computed result is verified against the analytical solution from Scriven (1959). Four mesh configurations with two mesh structures are set up in the simulation. The grid size for swept mesh is extra coarse (3815 elements) and coarse (14350 elements). The grid size for tetrahedral mesh is fine (138768 elements) and extra fine (3971025 elements).

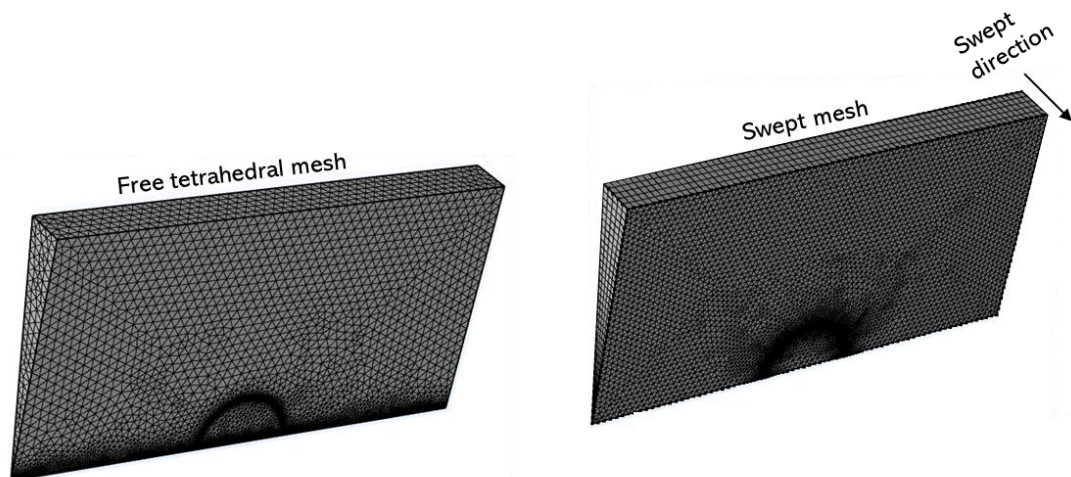


**Figure 4-14.** Two types of possible mesh types for the symmetry 3D coordinates. In the free tetrahedral mesh (left), all the faces of the domain are meshed with tetrahedral mesh. In the swept mesh (right), the front side mesh is tetrahedral and being swept towards the backside, hence the mesh on the side faces is rectangular.

There are two available mesh types to consider: the 3D free *tetrahedral elements* and free *triangular elements with swept mesh* (seen in Figure 4-14). The tetrahedral element has a better prediction over the swept mesh. The swept mesh method is analogous to the mapped mesh in 2D which is impossible to accommodate the meshing of curvature surface. Although the swept mesh has the advantage of mesh refinement with fewer elements than the 3D tetrahedral shape, it loses the resolution on the curvy bubble surface. As the bubble grows perpendicular to the sweeping direction, it cannot keep up the accuracy in cross-section planes. Having said that, one of the reasons why the two types gave a close result is due to the small angle of the chosen computational domain. The smaller the angle of the 'wedge' domain, the better the swept mesh can mesh the bubble surface as the curvature factor is not significant. The growth constant from equation (4-10) is calculated to be **66.96** by iterative methods, which gives the initial temperature profile in Figure 4-15,

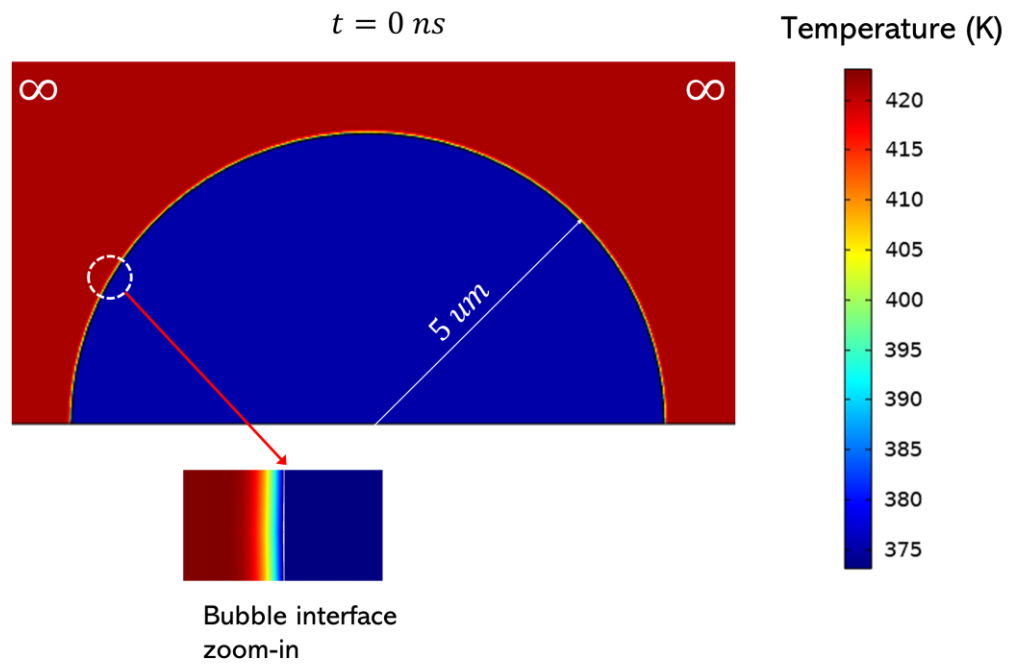


**Figure 4-15.** Temperature distribution at  $t = 0 \text{ s}$ . The bubble domain (blue) is maintained at  $100^\circ\text{C}$ , and the liquid domain (red) is at  $150^\circ\text{C}$ . The bubble radius is  $5 \mu\text{m}$  and the liquid domain is infinite.

The temperature variation is radially symmetric. The initial thermal boundary layers are expected to be thin, as the temperature difference between the bubble and the liquid is large. The thickness of the thermal boundary layers of  $0.12 \mu\text{m}$  is seen in the 1D graph in Figure 4-16. Hence, the mesh boundary layers thickness of less than  $0.12 \mu\text{m}$  were set to accurately capture and resolve the heat transfer from the surroundings to the bubble.

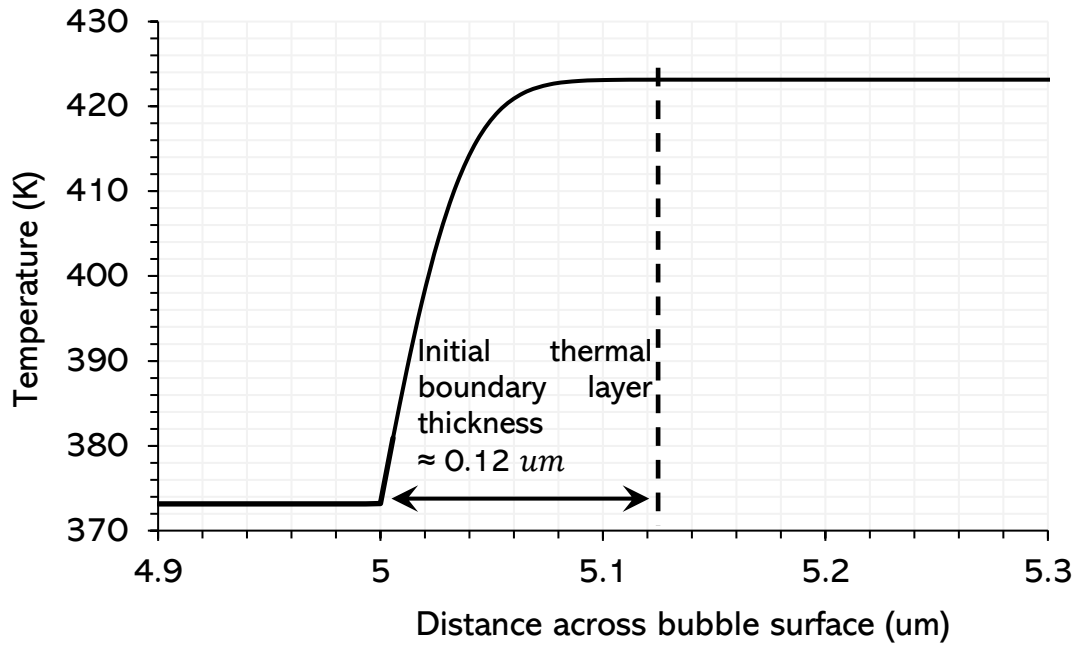


**Figure 4-16.** Thermal boundary layer thickness plot at the bubble surface. The temperature is plotted across the bubble interface for the visualisation of the thermal boundary layer. The layer thickness is  $\Delta d \approx 0.12 \mu\text{m}$ .

The mesh is not overly deformed and its quality is still high until the end of bubble expansion (seen in Figure 4-17). However, as the bubble grows many folds in size, the boundary layers at the surface will not be sufficient enough to stretch, which requires the remeshing algorithm.

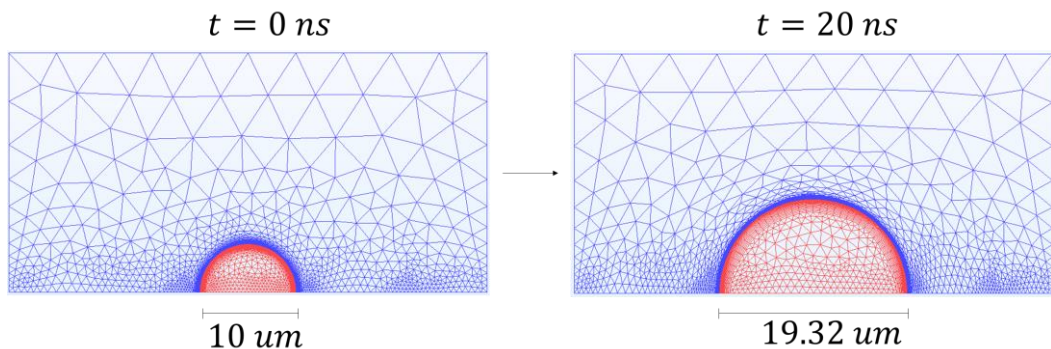


**Figure 4-17.** Mesh plot of the gas (in red) and liquid (in blue) domains at  $t = 0 \text{ ns}$  and  $t = 20 \text{ ns}$ . The colour-coded phase is plotted for the bubble (red) and the liquid (blue) domains.

The elements are extremely refined as it gets closer to the bubble interface where the important dynamics happen. Due to the nature of a circular shape, a triangular element is preferred over a rectangular shape as it tolerates the mesh deformation better.

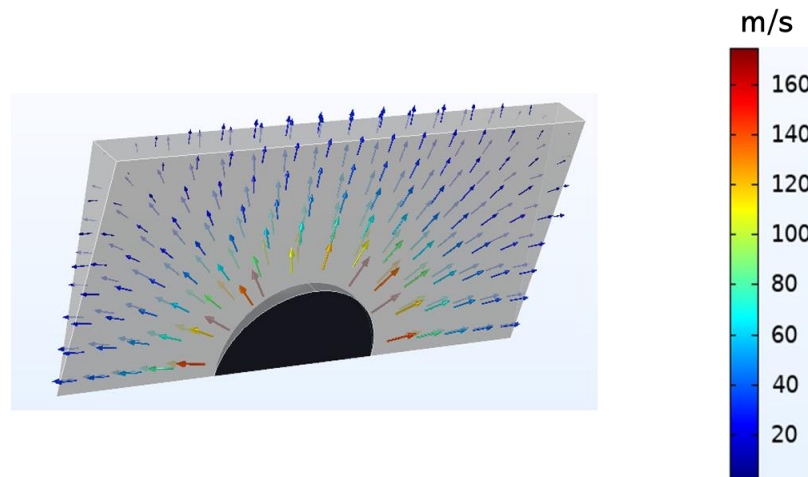


**Figure 4-18.** Flow vector field with colour-coded around the bubble.

The velocity field within the liquid and at the outer boundaries are visualised in Figure 4-18. The liquid is allowed to move out of the domain as the bubble grows and the velocity distribution is also radially symmetric. The large superheated temperature causes the bubble's surface velocity to be remarkably large for a bubble of a  $5 \mu\text{m}$  radius. The initial Young-Laplace pressure was applied to the bubble interior for numerical stability.

### **4.3. Conclusions**

The ALE interface tracking method is proven to be a sufficient and suitable interface tracking method for modelling the phase change phenomena, specifically for a bubble growth within a liquid medium. The mesh shapes and the level of refinement are shown to have a considerable effect on the result's accuracy against an analytical solution. The studies provide a degree of confidence in the coupling of the bubble growth dynamics into the droplet drying model. It should be noted that at the boiling point, the temperature gradient is already established within the droplet, which is different from the initial temperature gradient obtained from the analytical solution of bubble growth. Moreover, the drying droplet system is a multi-component solution instead of a pure liquid, in which the water activity also affects the saturation temperature at the bubble surface. Next, the 2-dimensional drying model will be developed in Chapter 5 using the FEM and ALE methods. The simulation framework for the bubble growth in Chapter 4 will then be integrated into the drying model for the study of the boiling phenomena in Chapter 6.

# Chapter 5

## **Investigation of droplet drying models using FEM**

This section reports the numerical probing of the drying model of a droplet in 1-dimension, and the progression into the 2-dimensional coordinates. The purpose of this study is to develop a numerical model that can capture drying information which is limited for current models in the literature, such as the spatial variation of heat and mass transfer along the droplet's surface, or an asymmetrical internal flow field. The drying conditions in the 1-dimensional model were set up similarly to the SDD experiment for validation. Subsequently, the model was advanced into the 2-dimensional axis-symmetrical coordinate. The PID algorithm developed in Chapter 3 was adapted to control the terminal falling velocity of the droplet. The computed results provided information on the droplet internal velocity and concentration profiles, which inherently predict the formation of the skin along with its structure and thickness. The outcome of this chapter is the mathematical framework of which the drying of a droplet can now be captured extensively, and the boiling phenomena can be integrated upon (refer to Chapter 6).

## 5.1. Considerations on the current PID feedback control scheme

Most of the numerical work related to the single droplet drying utilises the glass filament or glass knob to keep the droplet in control during drying. The results can still be practical after compensating for the heat transfer by the filament knob immersed within the droplet. Therefore, it is agreed that a good match with experimental data proves a proper choice of governing equations, boundary conditions, and methods used in a drying model. It does not, however, necessarily show that the model represents precisely what happened inside the spray dryer. One of the limits of the experimental approach lies in the limit of the droplet size that can be recreated in the lab, which is in the minimum of a millimetre range. A simulation of a falling millimetre-sized droplet is not feasible as the droplet breaks up due to a large terminal velocity and shear stress on the surface. On the other hand, a simulated *micron-sized* droplet will have no measured data to compare against. The main question is how to set a simulation of a falling droplet, of which the outcomes are comparable to the experimental data. Besides, it should be mentioned that the reason most of the simulation effort in the literature focused on the hanging droplet instead of falling, originates from the challenge of keeping the droplet within the air domain as it falls. Therefore, an innovative simulation system is specifically designed in which the modelling of the droplet drying and falling, with the velocity that matches the air velocity in the SDD experiment, is achievable without having the droplet leaving the control domain thanks to the PID scheme. This system ensures the drying outcome can be compared against the experimental data whilst maintaining numerical stability.

### 5.1.1. Gravity as a controlled variable

The current PID system (refer to Chapter 3) has the inlet velocity as a controlled variable. This is favorable since the terminal velocity is a function of a droplet size that is shrinking over time. However, in order to validate the numerical outcome with the experimental data, the droplet falling velocity must match the air velocity in the experiment, which is not always valid. In contrast to droplets within the spray dryer, the inlet velocity is fixed in the SDD experiment and the droplet size is at a millimetre range. These two differences make the current velocity-controlled PID system impractical. Moreover, the droplet also defects its sphericity when being hung under its own weight. Meanwhile, the approach of modelling a falling millimetre droplet is challenging, as its falling velocity results in a surface deformation and possible rotations.

In summary, a large droplet deforms easily when falling under the Earth's gravity of  $9.81 \text{ m/s}^2$ , and also having a constant terminal velocity while drying is impossible, as the droplet shrinks. The gravity-controlled PID algorithm is developed particularly in this chapter to solve both of the problems above.

The PID algorithm for controlling the gravity uses the same initial control parameters as the velocity-controlled PID previously. As the velocity is not a controlled variable, it is set to the air velocity in the SDD experiment. The airflow introduced to the system varied between  $0.1 \text{ m/s}$  to  $1 \text{ m/s}$ . Initially, only the proportional gain parameter,  $k_p$ , is used to review how the controlled gravity variable reacts to the displacement of the droplet (Figure 5-1).

The displacement of the droplet and the controlled gravity oscillates in the opposite direction in the early stage of falling, which is expected since the PID loop is not highly complicated and only reacts proportionally to the droplet displacement. The integral and differential parameters,  $k_d$  and  $k_I$ , would be considered if the p-only

PID cannot control the droplet. The time the PID loop takes to reach equilibrium is around  $200\text{ ms}$  and this should be regarded as relaxation time in a fully developed model.

The p-only PID has a good control profile, however, there was a small fluctuation in the equilibrium state. The differential parameter was therefore added into the control variable, so that gravity will also be adjusted to how fast the droplet is dragged down. This will reduce an early oscillation amplitude and get rid of the disturbances at equilibrium. The value of  $k_d$  is  $0.1e^6$ . The PID test is run again and plotted in Figure 5-1.

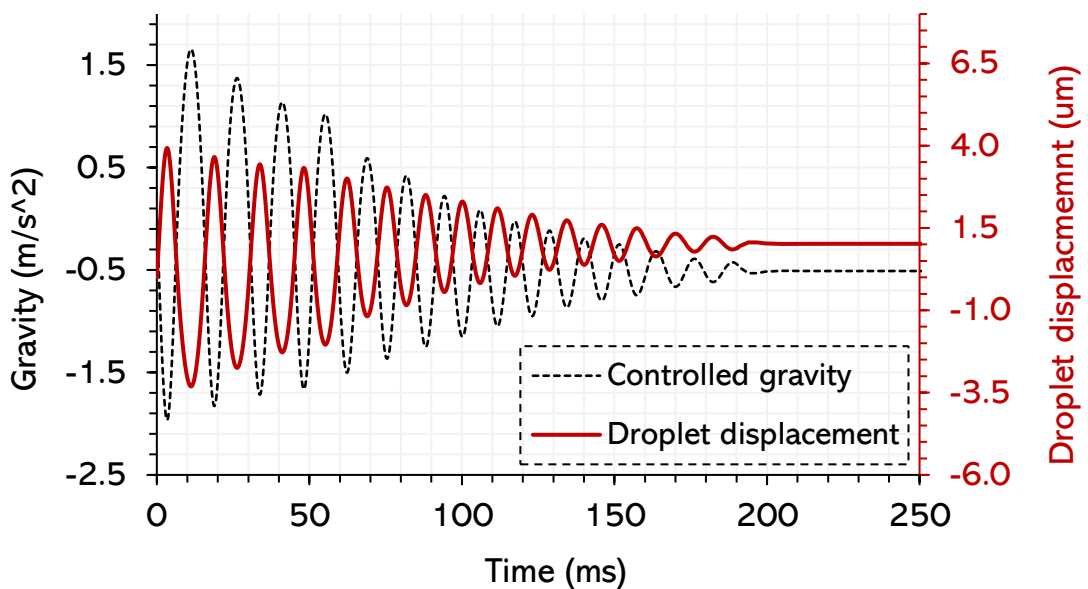


**Figure 5-1.** Gravity-controlled PID algorithm. The controlled variable is gravity (dotted black line) that is adjusted based on the droplet displacement (red line on the secondary axis). The total time interval is **250 ms**. The PID loop reached equilibrium value after around **190 ms**.

The PID parameters have a good performance in stabilizing the droplet within the domain for around  $200\text{ ms}$ . The gravity is one order-differential different from the velocity variable, hence the gravity-controlled PID has a different controlling rate on the droplet's position. Theoretically, gravity needs a longer time frame

than the velocity to reach a steady-state, as it only affects the droplet's acceleration rather than the velocity. The additional differential parameter helps by accelerating the system towards the equilibrium state within a smaller number of oscillations. The flow field around and within the droplet is plotted in Figure 5-2.

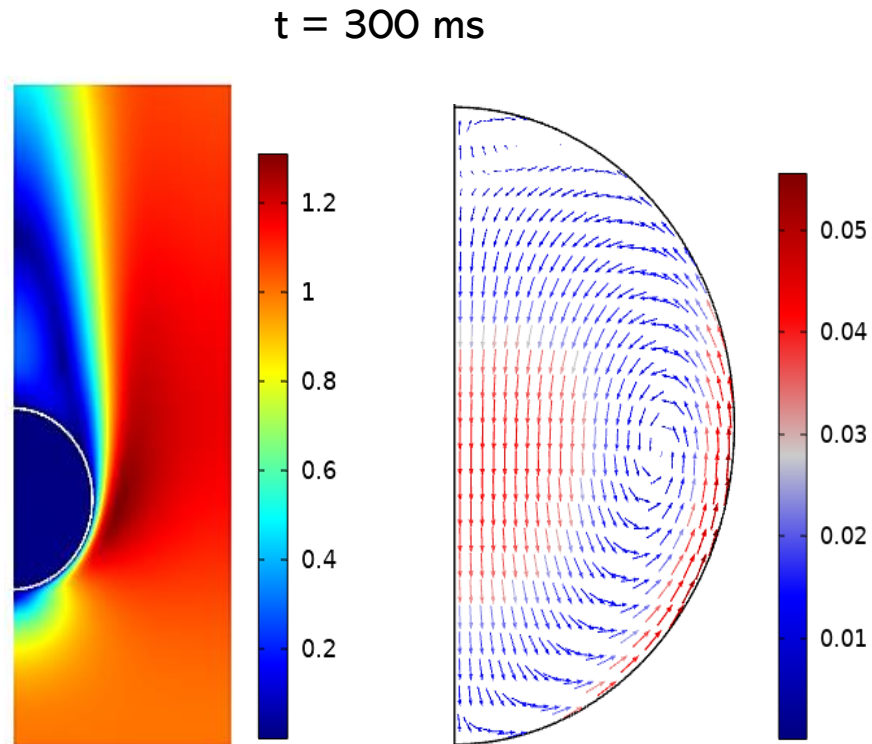


**Figure 5-2.** (Left) 2D surface plot of velocity field and (Right) internal vector flow field with droplet with colour-coded.

The vortices are formed within the droplet near the area where the flow separation occurs (refer to Figure 5-2 (right)). Figure 5-3 illustrates the internal flow evolution of the droplet.

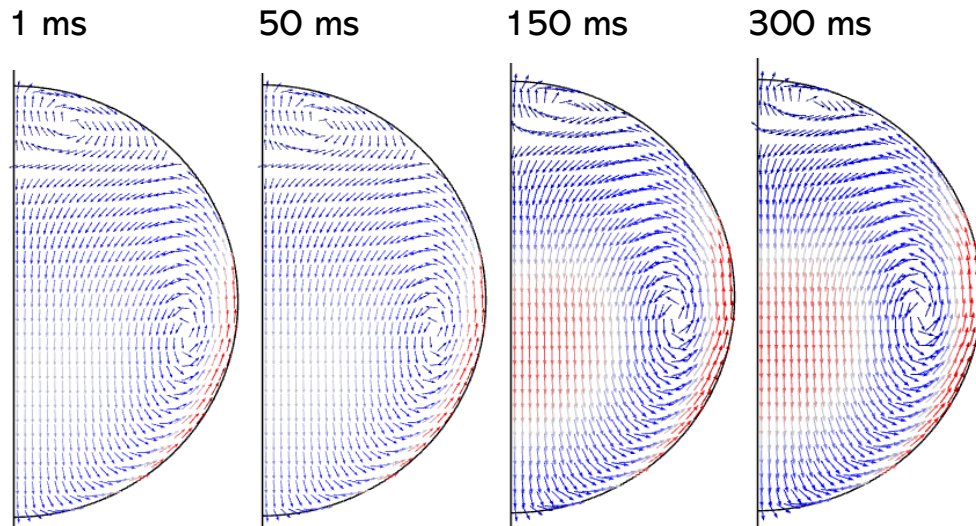


**Figure 5-3.** Flow field within the droplet during the PID control. The vortices size remains the same with the primary vortex occupying most of the droplet volume.

The flow in Figure 5-3 is formed from a constant airflow, however, this internal flow field is expected to change significantly as the droplet shrinks and gets more viscous. In applying this feedback loop to our model for sucrose droplet drying, a relaxation time of  $400\text{ ms}$  is allowed for the system to be fully steady. During this period, the inlet velocity and controlled gravity will be ramped up using the step function for numerical stabilities. It should be expected that the controlled gravity will change with time as the droplet shrinks during drying. Overall, this gravity controlled PID loop has achieved the goal of keeping a falling droplet within a domain and preserving its sphericity. This is particularly helpful in having the same simulation drying condition to the experiment for validation purposes.

## 5.2. Simulation and validation of a 1D drying model for a sucrose solution droplet

This section investigates the drying diffusion model of a sucrose droplet in a 1D coordinate. The simulation system is designed according to the experimental setup from Patel *et al.* (2008) for validation. The initial conditions, such as the droplet diameter, the initial moisture content or the air temperature, are chosen similarly to that of the experiment. All equations were solved in a radially symmetrical coordinate from the droplet centre to the surface. The computed results were compared against the data from Patel *et al.* (2008) and Woo *et al.* (2008). The outcome is the analysis of the validity of the diffusion model, including any discrepancies encountered in the drying, which is the limit of using the 1D coordinate system.

### 5.2.1. Problem formulation

The schematic of the system is presented in Figure 5-4. The model setup is designed to match the drying conditions of the experiment (Patel *et al.*, 2008). The modelling system includes a 1D sucrose droplet drying with incoming air of  $1\text{ m/s}$ . The droplet diameter is set as  $2145\text{ }\mu\text{m}$  and  $2179\text{ }\mu\text{m}$  and the initial moisture content is at  $1.5\text{ kg/kg} - \text{dry basis (db)}$  and  $1\frac{\text{kg}}{\text{kg}} - \text{dry basis (db)}$ . The air temperature is at  $95^{\circ}\text{C}$  and  $63^{\circ}\text{C}$  with relative humidity to be 2% and 2.5% respectively. The variable in the external ambient air are estimated using dimensionless numbers. The four drying conditions used in this study are summarised in Table 5-1.

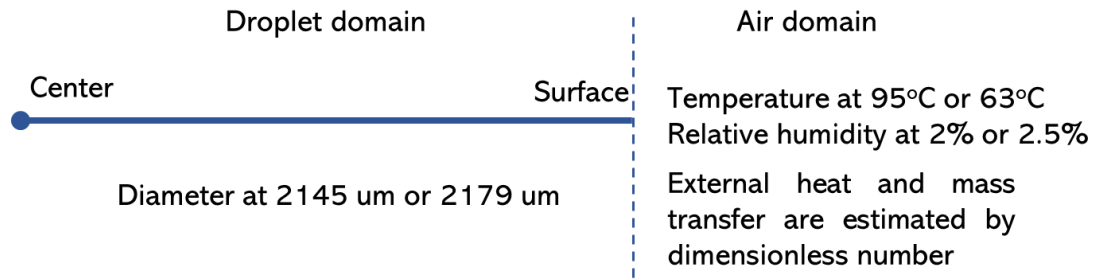


**Figure 5-4.** Schematic setup of a 1D drying model. The droplet is presented by the blue dot and the interface is at the dotted blue line. The diameter of the droplet used in this study will be at **2145  $\mu\text{m}$**  and **2179  $\mu\text{m}$** , with the air temperature at **63°C** and **95°C**, respectively. The external heat and mass transfer are estimated by dimensionless numbers.

Temperature (°C) / Relative humidity (%)	95°C / 2%		63°C / 2.5%	
Initial moisture content (kg/kg-dry basis)	1.5	1	1.5	1
Droplet diameter ( $\mu\text{m}$ )	2179 ( $\mu\text{m}$ )		2145 ( $\mu\text{m}$ )	
Initial droplet temperature (°C)	25.33°C	28°C	24.88°C	24.09°C

**Table 5-1.** Four experimental drying conditions for sucrose droplet with an initial moisture content of 60% (1.5 kg/kg) and 50% (1 kg/kg). The condition is adapted from Patel *et al.* (2008).

### 5.2.2. Governing equations

The following section presents the governing equations and boundary conditions used in the 1D model. Different diffusion models, and correlations for the diffusion coefficients and water activities of a sucrose solution will be discussed.

### 5.2.2.1. Species transport

The transport of species in a concentrated multicomponent solution is used to describe the diffusion of water and sucrose within the droplet during drying.

$$\rho \frac{\partial}{\partial t}(\omega_i) + \rho(\mathbf{u} \cdot \nabla)\omega_i = -\nabla \cdot \mathbf{j}_i \quad (5-1)$$

Where  $\rho$  is the mixture density,  $\omega_i$  is the mass fraction of  $i^{th}$  species in wet basis (water or sucrose) in the concentrated solution,  $\omega_i$  is the mass fraction of species  $i^{th}$ ,  $\mathbf{j}_i$  is the mass flux of  $i^{th}$  species relative to the mass-average velocity where,

$$\sum_{i=0}^n \mathbf{j}_i = 0 \quad (5-2)$$

And  $\mathbf{u}$  (from equation (5-1)) is the mass-average velocity of the mixture which is defined as,

$$\mathbf{u} = \frac{\sum_{i=0}^n \rho_i \mathbf{u}_i}{\sum_{i=0}^n \rho_i} \quad (5-3)$$

Where  $\rho_i$  is the density of species  $i^{th}$ . The sum of the mass fraction of all species in the solution is constrained to 1, which means that for a solution of  $n$  species, the transport equation only needs to be solved for  $(n - 1)$  species.

The formulation of the mass flux,  $\mathbf{j}_i$ , in equation (5-1) depends on the diffusion models. The popular Maxwell-Stefan model is one of the diffusion models in this study, and its mathematical expression,

$$\mathbf{j}_i = -\rho \omega_i D \sum_k \mathbf{d}_k \quad (5-4)$$

Where  $D$  is the multicomponent diffusivities and  $\mathbf{d}_k$  is the driving force acting on species,

$$\mathbf{d}_k = \frac{M}{M_k} \nabla w_k + \frac{1}{p} \left[ w_k \left( \frac{M}{M_k} - 1 \right) \nabla p \right] \quad (5-5)$$

Where  $M$  is the mixture molar mass,  $M_k$  is the molar mass of  $k^{th}$  species,  $p$  is the total pressure. In the Maxwell-Stefan diffusion model, the total diffusive flux of a species depends on the gradient of all other species' concentration and pressure, which is computationally expensive when solving for a solution with a high number of species (more than 2 or 3). The Maxwell-Stefan equation can be simplified with the *mixture-averaged approximation* or the *Fick's law approximation*, of which the diffusive flux is expressed as,

$$\mathbf{j}_i = -\rho D_i^{ma} \nabla \omega_i + \rho \omega_i D_i^{ma} \frac{\nabla M}{M_k} - \text{Mixture averaged} \quad (5-6)$$

$$\mathbf{j}_i = -\rho \omega_i D_i^F \nabla \omega_i + \rho \omega_i \sum_k D_i^F \nabla \omega_k - \text{Fick's law} \quad (5-7)$$

Where  $D_i^{ma}$  and  $D_i^F$  are the diffusion coefficient of species  $i^{th}$  in the mixture-averaged approximation and the Fick's law approximation, respectively.

Both approximations assume the diffusive flux in the mixture to be governed by Fick's law, which reduces the complexity of the full Maxwell-Stefan expression. However, the definition of the component diffusivities is different in each approximation. The  $D_i^{ma}$  term (equation (5-6)) in the mixture-averaged approximation describes the diffusion of species  $i^{th}$  relative to the remaining of the mixture. Meanwhile in the Fick's law approximation, the  $D_i^F$  (equation (5-7)) indicates the diffusion of a species into the mixture, which is convenient since any diffusivities or empirical model based on Fick's law can be used as  $D_i^F$  without any further calculation .

Apart from the advantage of a reduction in the computational effort, the net diffusive mass flux, however, does not add up to zero, when the diffusion is approximated by Fick's law. Hence, the correctional velocity is added to constraint this net diffusive flux down to zero. The second term on the right-hand side of equations (5-6) and (5-7) represents the correctional velocity term for the mixture diffusion.

Moreover, the effect of temperature on the diffusion in concentrated solution is assumed to be negligible in this specific study, considering the temperature gradient within the droplet was shown to be insignificant ( $\pm 2K$ ). The diffusion coefficient of sucrose and water in aqueous sucrose solution is adopted from Price *et al.* (2016).

$$\log D_i = a + ba_w + ca_w^2 + da_w^3 \quad (5-8)$$

Where  $D_i$  is the diffusion coefficients of species  $i^{th}$ ,  $a_w$  is the water activity and  $a, b, c, d$  are constants determined through fitting parameters (Table 5-2).

	a	b	c	d	Limit of water activity
Water	-20.89	25.92	-26.97	13.25	$a_w > 0.2$
Sucrose	-30.97	54.89	-62.34	29.12	$a_w > 0.4$

**Table 5-2.** Coefficient for water and sucrose activities in sucrose solution in equation (5-8).

#### 5.2.2.2. Heat transfer

The heat transfer equation solved within the fluid domain is expressed as,

$$\rho C_p \left( \frac{\partial T}{\partial t} + \mathbf{u} \cdot \nabla T \right) = \nabla \cdot (k \nabla T) - (\nabla p \mathbf{u}) + \mathbf{u} \nabla \tau + Q \quad (5-9)$$

Where  $T$  (K) is the temperature,  $\tau$  is the viscous stress tensor,  $C_p$  (J/(kg \* K)) is the specific heat capacity,  $\mathbf{u}$  is the velocity,  $Q$  (W/m<sup>3</sup>) is heat sources and  $k$  (W/(mK)) is the thermal conductivity of the solution.

### 5.2.3. Material properties

The thermophysical properties of air and sucrose solution are calculated using the formulation from Table 5-3.

Symbol (unit)	Parameters	Expression
$\rho_{drop} \left( \frac{kg}{m^3} \right)$	Density	$\rho_s \omega_s + \rho_w \omega_w$
$k_{drop} \left( \frac{W}{mK} \right)$	Thermal conductivity	$k_s \omega_s + k_w \omega_w$
$C_{p_{drop}} \left( \frac{J}{kg.K} \right)$	Specific heat capacity	$C_{p_s} \omega_s + C_{p_w} \omega_w$

**Table 5-3.** Physical properties of sucrose solution evaluated at the drying condition of the simulation.

#### 5.2.3.1. Boundary conditions

The correlation for water activity is estimated following the Norrish model (Patel *et al.*, 2008) (Norrish, 1966).

$$a_w = x_w e^{-K_N(1-x_w)^2} \quad (5-10)$$

Where  $K_N$  is the Norrish equation coefficient. The heat and mass transfer coefficients are estimated from dimensionless number correlations (Ranz & Marshall, 1952) (refer to Chapter 3).

$$Re = \frac{\rho_a U D}{\mu} \quad (5-11)$$

$$Pr = \frac{C_p \mu}{k} \quad (5-12)$$

$$Sc = \frac{\mu}{\rho_a D} \quad (5-13)$$

$$Nu = \frac{h_{Nu} D}{k} = 2 + 0.6 Re^{\frac{1}{2}} Pr^{\frac{1}{3}} \quad (5-14)$$

$$Sh = \frac{h_{Sh} D}{D_{va}} = 2 + 0.6 Re^{\frac{1}{2}} Sc^{\frac{1}{3}} \quad (5-15)$$

Where  $h_{Nu}$  and  $h_{Sh}$  are the heat and mass transfer coefficients calculated from the Nusselt and Sherwood numbers, respectively.  $\rho_a$  is the air density,  $U$  is the air velocity,  $D$  is the diameter of the sphere,  $C_p$  is the specific heat capacity of air,  $\mu$  is the dynamic viscosity of air and  $k$  is the thermal conductivity of air. The mass flux evaporated at the droplet's surface is,

$$m_{evap} = k_c(c_{surface} - c_\infty) = k_c(act_{wa}c_{sat} - RHc_{sat\_air}) \quad (5-16)$$

Where  $m_{evap}$  is the vapour mass flux ( $kg/m^2s$ ),  $k_c$  is the mass transfer coefficient,  $c_{surface}$  is the vapour concentration at the droplet surface,  $c_\infty$  is the vapour concentration in air,  $act_{wa}$  is the water activity,  $RH$  is the relative humidity and  $c_{sat}$  is the saturation vapour concentration.

Similarly, the heat flux at the droplet surface is a function of the temperature gradient,

$$Q = h_c(T_{surface} - T_\infty) - Q_{source} \quad (5-17)$$

Where  $Q$  is the total heat flux exchange at the interface ( $W/m^2$ ),  $h_c$  is the heat transfer coefficient,  $T_{surface}$  and  $T_\infty$  are the temperature at the surface and infinity respectively. The heat source,  $Q_{source}$ , is the evaporative cooling due to evaporation,

$$Q_{source} = m_{evap} H_{evap} \quad (5-18)$$

Where  $H_{evap}$  is the enthalpy of evaporation. The saturated pressure is calculated using the correlation from,

$$P_{sat} = 610.7 \times 10^{7.5 \left( \frac{T-273.15}{T-35.85} \right)} \quad (5-19)$$

(Monteith and Unsworth, 2013)

$$c_{sat} = \frac{P_{sat}}{RT} \quad (5-20)$$

Where constants  $A$ ,  $B$  and  $C$  equal 8.07131, 1730.63, 233.426 for  $T < 373 K$  respectively, and 8.14019, 1810.94, 244.485 for  $T > 373 K$

respectively. The saturated concentration is calculated using the ideal gas equation.

### 5.2.3.2. Study of different diffusion coefficients and water activities

This section compares different correlations for water activities and diffusion coefficients of species within the sucrose solution. The water activities correlations used in this comparison are presented as follows.

- Norrish model (Patel *et al.*, 2008):

$$a_w = \omega_w \frac{Mn_{drop}}{Mn_w} e^{-Kn \left(1 - \omega_w \frac{Mn_{drop}}{Mn_w}\right)^2} \quad (5-21)$$

- Margules equation (Starzak and Mathlouthi, 2006):

$$\ln a_w = a(\theta) \sum_{k=2}^N b_{k-2} \left(1 - \omega_w \frac{Mn_{drop}}{Mn_w}\right)^k \quad (5-22)$$

$$\text{Where } a(\theta) = \frac{a(\theta)}{\theta} + a_1 + a_2 \ln \theta + a_3 \theta + a_4 \theta^2 + a_5 \theta^3.$$

- Temperature-dependent model (Starzak and Peacock, 1997):

$$\ln a_w = \frac{Q}{RT} \left(1 - \omega_w \frac{Mn_{drop}}{Mn_w}\right)^2 \left[ 1 + a \left(1 - \omega_w \frac{Mn_{drop}}{Mn_w}\right) + \dots b \left(1 - \omega_w \frac{Mn_{drop}}{Mn_w}\right)^2 \right] \quad (5-23)$$

$$\text{Where } a = -1.0038, b = -0.24653, Q = -17638, T = 373.15$$

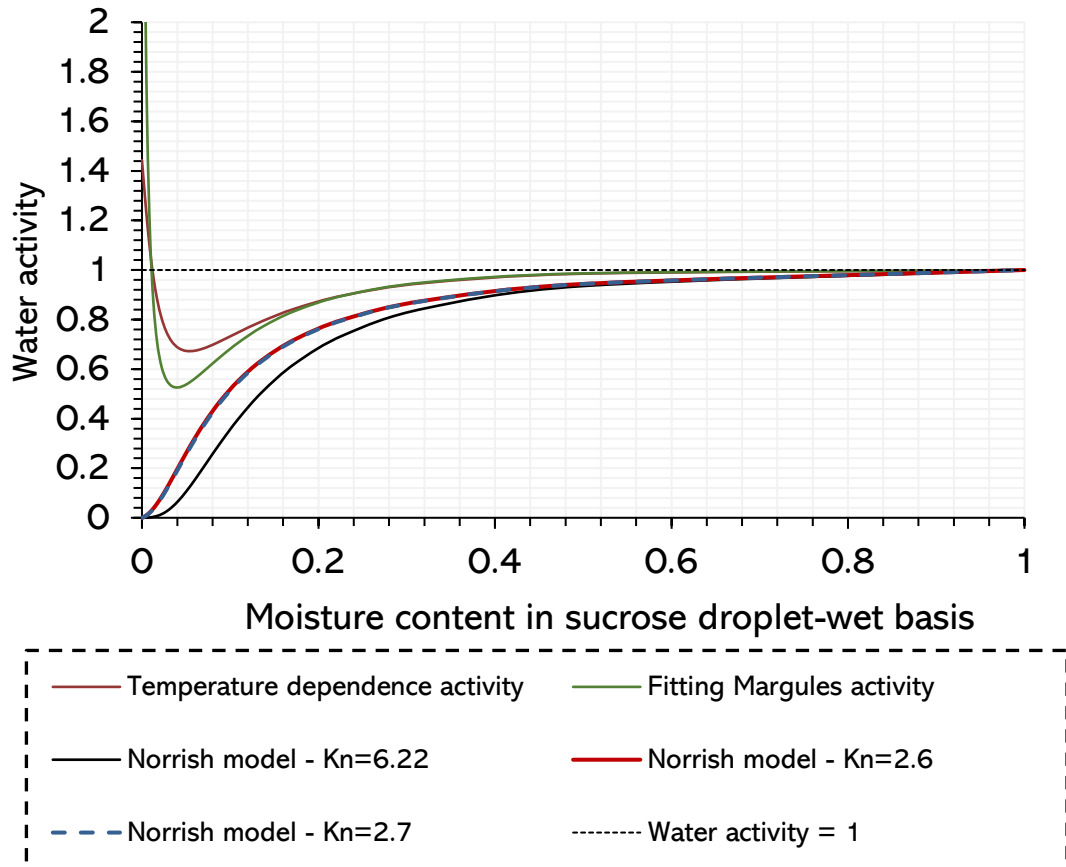


**Figure 5-5.** Comparison of water activities correlations. The x-axis is the moisture content from **0** to **1**. The line of water activity equals **1** is plotted. The water activity is from **0** to **1**. The temperature dependence and fitting Margules correlation exceed 1 at low moisture content due to the lack of experimental data.

Overall, all water activities correlations in Figure 5-5 are close to 1 at a moisture content of more than 0.5, and starts to deviate as moisture content gets below 0.5. The water activity from the Norrish model (refer to equation (5-10)) with three different Norrish coefficients decrease to zero at zero moisture content, while the water activities from the temperature-dependent and Margules equation exceeds 1 as the moisture content decreases to below 0.3. Therefore, the water activities from the Norrish model will be used in the drying model for the sucrose droplet.

The temperature-dependent water activity was also plotted at different temperature ranges (from 295K to 500K) in Figure 5-6.

The water activity was shown to be affected by the temperature especially at the low moisture content ranging from 0.02 to 0.4. The minimum point of the water activity graph increases from 295K to 350K, and decreases as the temperature increases to 500K.

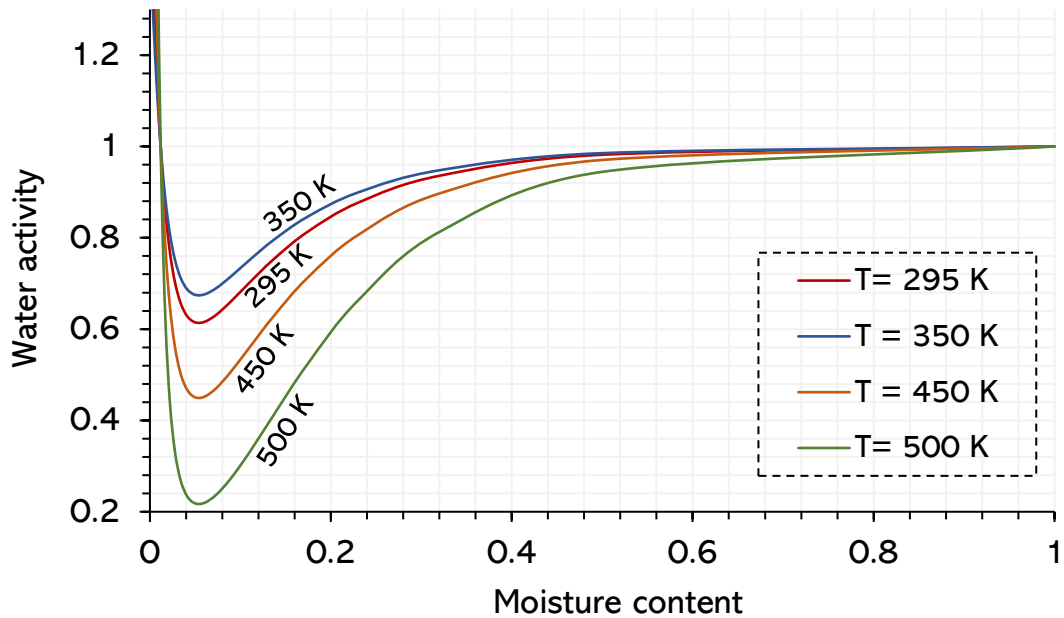


**Figure 5-6.** Temperature-dependant water activity (Starzak and Peacock, 1997) against the solution moisture content. The temperature range is from 295K to 500K. The water activity exceeds 1 as the moisture content gets below 0.01.

There are several developments on the diffusion coefficient of water in the sucrose solution such as from Price *et al.* (2014), Price *et al.* (2016), or Chenyakin *et al.* (2017). The three diffusivity coefficients for water in sucrose solution chosen in this study are from Price *et al.* (2016) (equation (5-8)) and was internally developed within the research group of Prof. Andrew Bayly at the University of Leeds.

$$D_{w_1} = 4e^{-11}\omega_{wab}^2 + 4e^{-10}\omega_{wab} - 4e^{-11} \quad (5-24)$$

(internally adopted from Dr. Muzammil Ali)

$$D_{w2} = D_{CO}(1 - \alpha\varphi_s)e^{-2060\left(\frac{1}{T_{drop}} - \frac{1}{298}\right)} \quad (5-25)$$

(Masaro and Zhu, 1999)

Where  $D_{CO}$  is  $0.5e^{-9} m^2/s$  and  $\alpha$  is 1.025,  $\varphi_s$  is the volume fraction of solids,  $T_{drop}$  is the droplet temperature. The formula is based on Masaro work (Masaro and Zhu, 1999), and the fitting parameters are internally adopted from Dr. Muzammil Ali.

$$\log D_i = a + ba_w + ca_w^2 + da_w^3 \quad (5-26)$$

(Price *et al.*, 2016)

Where  $D_i$  is the diffusion coefficients of  $i^{th}$  species,  $a_w$  is the water activity and  $a, b, c, d$  are constants determined through fitting parameters (Table 5-2 and Table 5-4).

	a	b	c	d	Limit of water activity
Water	-20.89	25.92	-26.97	13.25	$a_w > 0.2$
Sucrose	-30.97	54.89	-62.34	29.12	$a_w > 0.4$

**Table 5-4.** Coefficients for equation (5-26) including the water activity range at which the diffusion coefficients are valid.

As the diffusivities from Price *et al.* (2016) (refer to equation (5-8)) depend on the water activity, it will be calculated based on the computed water activity from the equation (5-21). Figure 5-7 represents the comparison of different diffusivities correlations for sucrose solution.

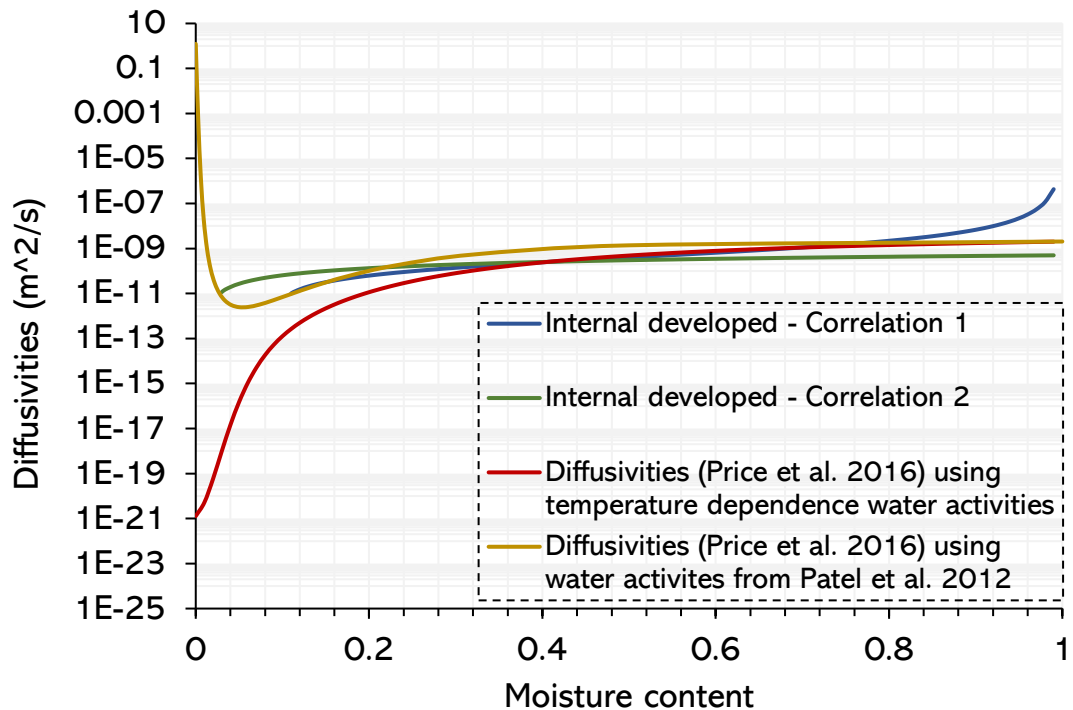


**Figure 5-7.** Comparison of different diffusivities models in log scale. The two internal developed correlations (green and blue lines) were obtained from the research group at the University of Leeds. The Price *et al.* (2016) diffusivities are calculated from the water activities ( $a_w$ ) in equation (5-21) (yellow line) and in equation (5-23) (red line).

The water diffusion coefficients in the two internal-developed correlations are negative at the low moisture content, and are not included in Figure 5-7. The reason for this negative value is the droplet temperature,  $T_{drop}$ , used to calculate the diffusion coefficient in equation (5-25) is set at a fixed value of 25°C. This means that the droplet temperature is still at 25°C when the moisture content approaches 0, which is not possible since the droplet would have reached the air temperature by that stage. As expected from the spike in water activity (refer to Figure 5-6), the diffusivities rise to an impractical value of around  $10 \text{ m}^2/\text{s}$ , which is again due to the limit in the experimental data at this moisture range. Although the diffusivities obtained from the equation (5-21) (Norrish model) can

cover the whole range of moisture content without irregular points, it is only valid within a certain range of water activity (refer to Table 5-4). The diffusion coefficient in equation (5-25) is expected to be the most suitable and accurate correlation, as it was obtained by fitting with the drying data for single droplets. Therefore, the diffusivities correlation in equation (5-25) together with the water activity (equation (5-21)) from the Norrish model (with  $K_n$  to be 2.7) will be used in the main drying model in the following section.

#### **5.2.4. Results**

##### **5.2.4.1. Validation against experimental data**

The comparison of droplet temperature and weight loss profiles between the experiment data from Patel *et al.* (2008) and the simulated data are represented in Figure 5-8, Figure 5-9, Figure 5-10 and Figure 5-11. The computed temperature is taken from the centre of the droplet in the simulation, as the thermocouple is normally situated at the droplet centre in the experiment. The moisture content is calculated by averaging the water concentration (in wet basis) over the droplet domain.

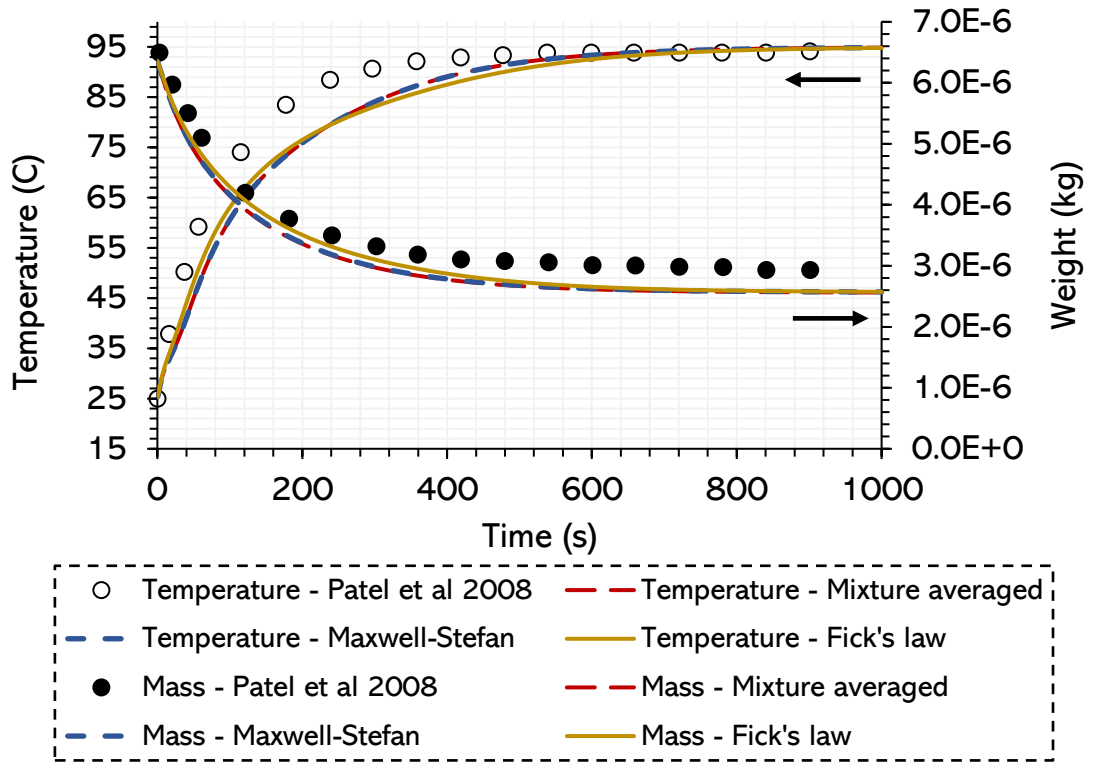


**Figure 5-8.** Droplet temperature and weight loss over time at  $T_{air} = 95^{\circ}C$  and initial moisture content of  $1.5 \text{ kg/kg} - db$ .

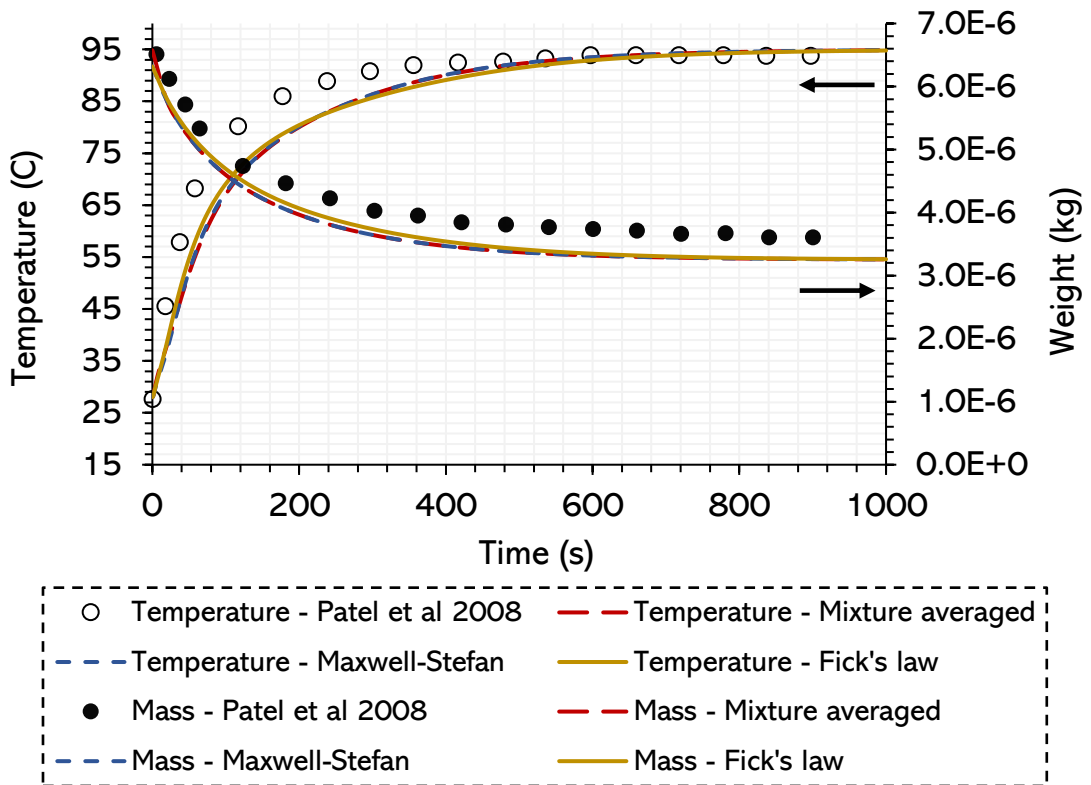


**Figure 5-9.** Droplet temperature and weight loss over time at  $T_{air} = 95^{\circ}C$  and initial moisture content of  $1 \text{ kg/kg} - db$ .

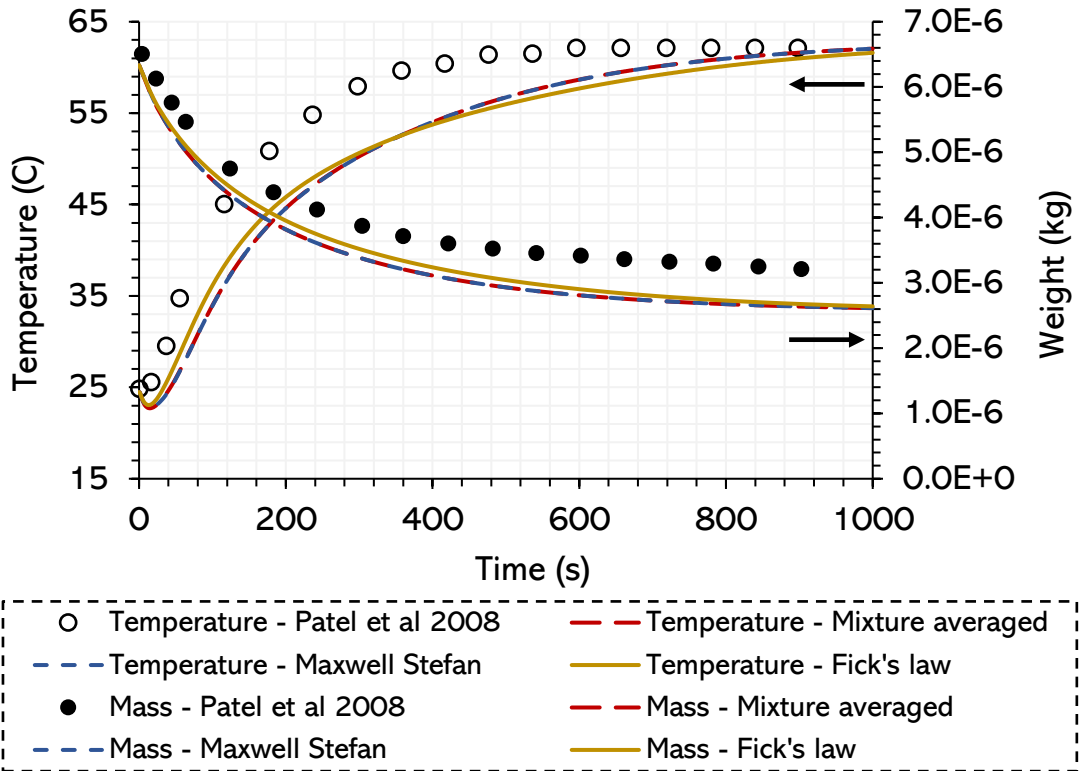


**Figure 5-10.** Droplet temperature and weight loss over time at  $T_{air} = 63^{\circ}C$  and initial moisture content of  $1.5 \text{ kg/kg} - db$ .

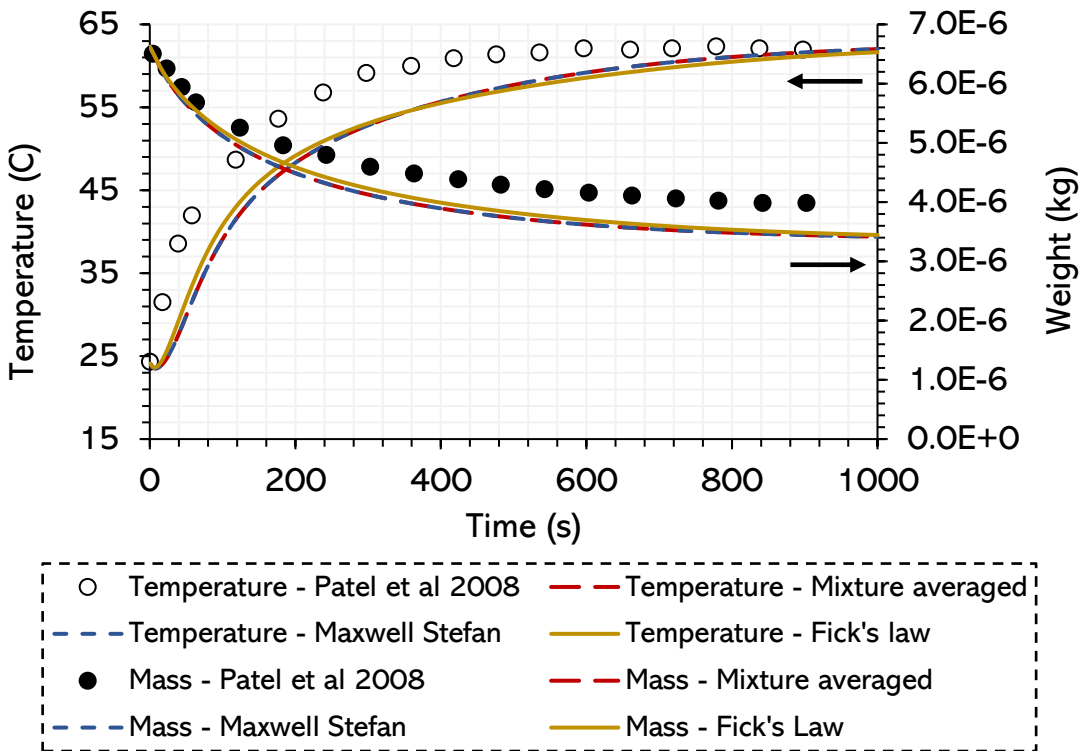


**Figure 5-11.** Droplet temperature and weight loss over time at  $T_{air} = 63^{\circ}C$  and initial moisture content of  $1 \text{ kg/kg} - db$ .

Overall, the droplet temperature and weight profiles have the same trend as the experimental data (refer to Figure 5-8, Figure 5-9, Figure 5-10 and Figure 5-11). The four computed results predict a lower droplet temperature than the measured data. Similarly, in the weight profiles, the simulated droplet loses more mass than that in the experiment, which also explained why the temperature is lower than expected due to the evaporative cooling. In a more detailed analysis, the temperature profile in Figure 5-8 and Figure 5-9 agrees with the data from Patel *et al.* (2008), meanwhile, there is a larger deviation from the experimental temperature in Figure 5-10 and Figure 5-11 with a slight cooling at the beginning of the drying. This indicates the incapability of the 1D model in predicting the droplet drying at different temperature ranges, with a better result for higher air temperature. In all four figures above, the droplet weight matches closely with experimental values at the early drying stage (at  $t < 200s$ ), before the deviation happens towards the end of drying.

The factors causing these discrepancies is thought to be the correlation of the diffusivities and water activity. Moreover, the fitting data for the diffusivities might not cover a wide range of air temperature, which is the reason why the 1D model does not predict equally well at different temperatures. We have also studied from section 5.2.3.2 that the experimental data for diffusion coefficient and water activity at this range are scarce, thus making the correlation less accurate and valid at low moisture content. Consequently, the deviation from the experiment data in all four figures for the mass profile after 200 s can be related to the validity of the water activity. The water activity at a droplet surface is plotted in Figure 5-12.

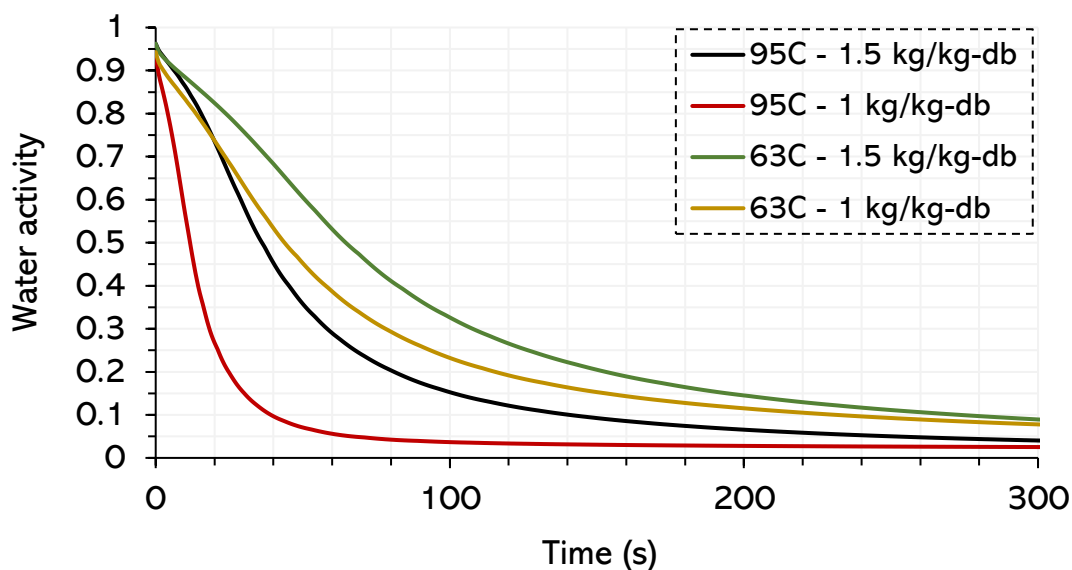


**Figure 5-12.** Water activity at the droplet surface at different drying conditions (sucrose droplet with 60% and 50% initial moisture content). The drying time is 1000 s. The air temperature is 95°C and 63°C.

According to Figure 5-12, the droplet water activity decreases sharply at  $t < 50$  s. This also explains the disagreement observed in the later drying stage (refer to Figure 5-8, Figure 5-9, Figure 5-10 and Figure 5-11). The water activity has a steeper gradient when the air temperature is at 95°C comparing to the case of 63°C. Apart from the scarcity of data for correlations, the source of error in the 1D model can also be the lack of convection effect captured within the droplet, in which the internal recirculation would affect the diffusivities. Moreover, the droplet in the experiment is hung on its own weight which affects its sphericity. This makes the estimated heat and mass transfer coefficients for a spherical droplet (equation (5-14) and (5-15)) not applicable to the experimental droplet. Additionally, the heat transfer from the filament and the thermocouple can also disturb the droplet temperature during drying.

The sucrose accumulates and forms a viscous shell at the droplet surface as drying progresses. The 'skin' thickness can be visualised

when plotting the distribution of moisture concentration along the droplet radius in the Eulerian coordinate. Figure 5-13 is the variation of moisture concentration in space and time within the droplet of  $1.5 \text{ kg/kg} - \text{db}$  at  $95^\circ\text{C}$ . Ten nodes along the line from the centre to the droplet surface are plotted as equal-distanced points to keep track of the shrinking dynamics.

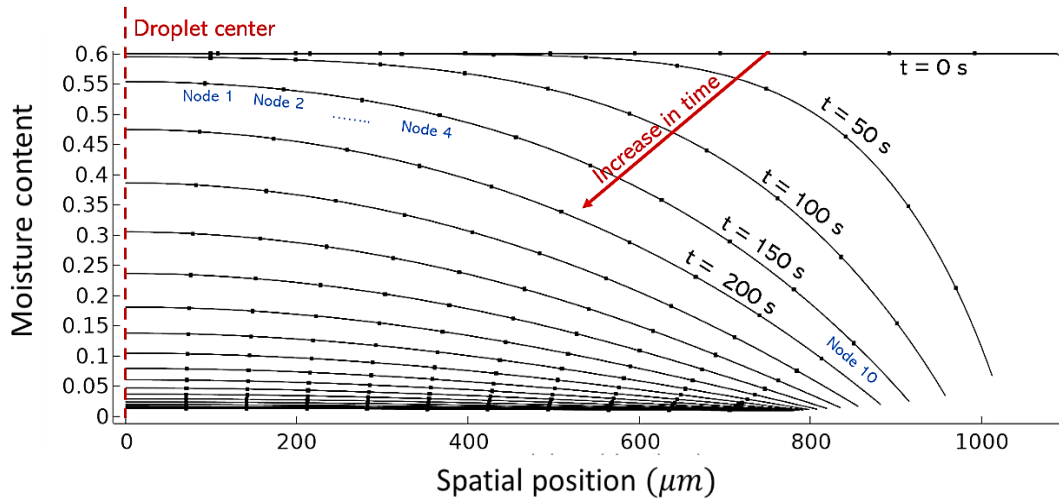


**Figure 5-13.** The moisture concentration distribution along the droplet radius over time in the Eulerian coordinate. Ten nodes (black points) are plotted from the core to the droplet surface to keep track of the shrinking. The time period is 1000 s and with the time step of 50 s. The increase in time is indicated by the red arrow.

The moisture content at the droplet surface drops significantly at  $t = 50 \text{ s}$  as seen in Figure 5-13. A large variation in water concentration within the droplet is established for the first 300 s and the skin thickness can be determined based on the criteria for the solute concentration.

The mixture-averaged and Maxwell Stefan models produce similar results and are slightly different from Fick's law. The computational time for the Maxwell Stefan, the mixture averaged and the Fick's law is 5 minutes, 3 minutes 55 seconds and 45 seconds, respectively. Therefore, Fick's law can be favourable if the diffusivity

data of all the species within the solution are known due to its fast computational time.

In conclusion, all three diffusion models produce similar results and also agree with the experimental data within an acceptable margin of error. Fick's law has the least simulation time whilst keeping a close prediction to the other two models. It is noted that the full Maxwell-Stefan and mixture-averaged model produced nearly identical predictions as the overlapping seen in all figures. Theoretically, this implies the diffusion transport within the 1D droplet can be assumed to be governed by Fick's law. The drawback of the Maxwell-Stefan model, apart from its longest simulation time, is the requirement of the bi-component diffusivities, which is scarce for both water and sucrose in sucrose solution. The only available data is provided by Price *et al.* (2016). The mixture-averaged model is an optimum choice in terms of the accuracy, the availability of diffusion coefficient data, and the computational time. Next, the 2D droplet is simulated with the flow equation fully resolved in the external air domain.

### **5.3. Simulation of a droplet drying model in a 2-dimensional coordinate**

In this section, a falling sucrose droplet at terminal velocity in an upward hot gas stream was modelled using the COMSOL Multiphysics 5.4 software. The numerical solution of the system provides insights into the true drying phenomena of a falling droplet that is inaccessible by the SDD experiment. Currently available models in the literature have the advantage to model a large droplet drying on a filament for validation with available SDD data. However, the mean size distribution of droplets within the spray dryer is much smaller and none of the SDD experiments were done with a micron size droplet. Hence, the outcome of the 2D model

developed in this chapter provides information that could be useful to improve the current SDD techniques. The current system is set up similarly to the previous 1D diffusion model. The droplet size and air temperature were set to match the experiment (Patel *et al.*, 2008).

### **5.3.1. A brief discussion on the incapability of solving the Navier-Stokes equation using 1D system**

Formerly in section 5.2, the Navier-Stokes equation was not solved for and not coupled with other physics in the 1-dimensional model. The drying was completely governed by the diffusion of species. The model still provides valuable drying details such as the drying rate, the average temperature profile, or the droplet viscosity. However, the internal distribution of moisture content and solute species were ignored due to no governing equation for the fluid flow. The problem lies technically in the flow dimension of the droplet surface and the air. While the droplet receding interface in 1D is radially symmetric  $(r, \theta)$ , the external airflow should be in the  $(x, y)$  direction which makes the full Navier-Stokes equation impossible to solve for each point at the droplet surface. Therefore, the Navier-Stokes equation was not involved in the 1D drying model.

### **5.3.2. Problem formulation**

A drying sucrose droplet falls with terminal velocity and encounters an isothermal upward hot air, in which the Multiphysics such as heat and mass transfer happen simultaneously. A schematic of the system is shown in Figure 5-14.

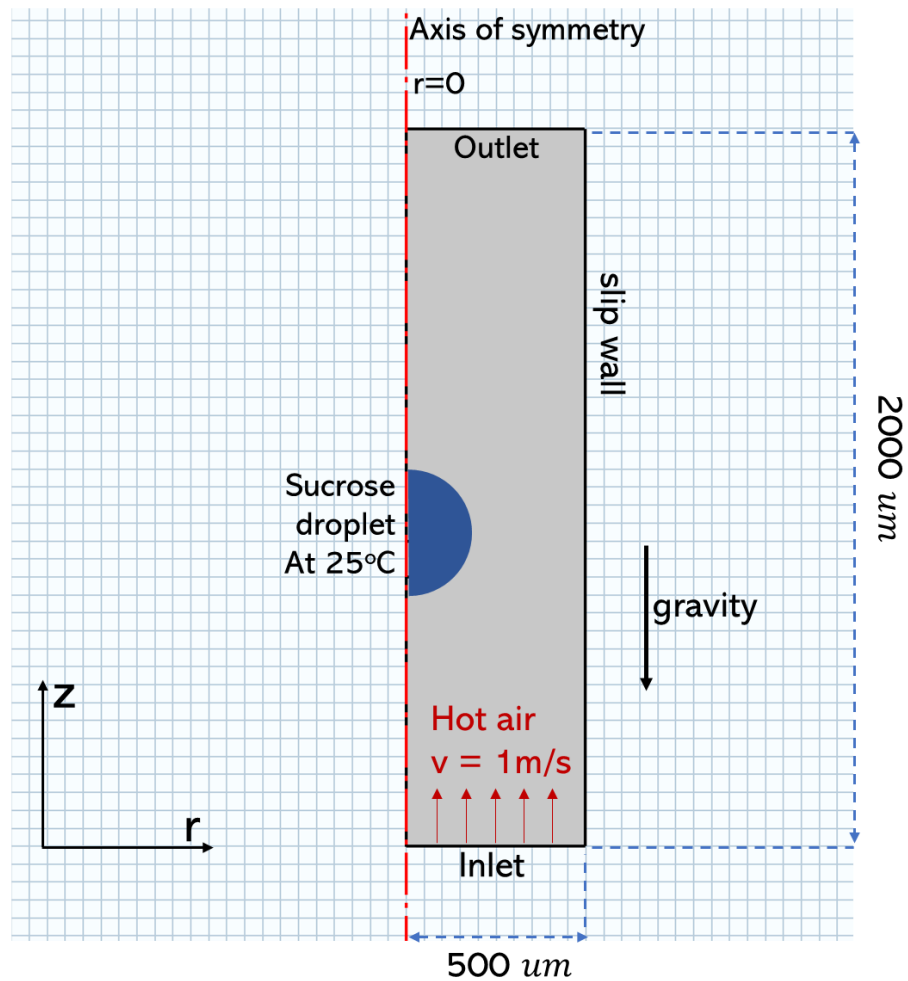


**Figure 5-14.** Schematic setup for falling sucrose droplet in 2D axis-symmetric system. The channel is  $500 \mu\text{m}$  in width and  $2000 \mu\text{m}$  in height. The inlet air is introduced at the bottom boundary at  $1 \text{ m/s}$  and exit through the outlet at the upper boundary. The air temperature is at  $95^\circ\text{C}/63^\circ\text{C}$ .

The evaporation rate depends on the temperature or the relative humidity of the air stream, and also on the initial condition of the droplet, such as moisture content or size. The downward gravity is the controlled variable and the air is introduced to the domain at a fix  $1 \text{ m/s}$  to match the experimental drying condition. The wall is set at 'slip' condition. The droplet is initially at room temperature and the surface tension is taken as the water-air surface tension,  $0.07 \text{ N/m}$ .

The inlet hot stream is set at the temperature range of 336 K to 368 K, which is the same as the experiment setup (Patel *et al.*, 2008). The droplet initial moisture content is varying between  $1 \frac{kg}{kg} - db$  to  $1.5 \frac{kg}{kg} - db$ , and its initial temperature is at 298.15 K. The vapour from the droplet evaporation will exit through the outlet set at 1 atm, and the relative humidity of incoming air is ranging from 2 % to 2.5c%. The channel height and width are  $9000 \mu m \times 10000 \mu m$ , reseptively.

### 5.3.3. Governing equations

This section introduces the governing equations solved separately in each domain with different physical parameters, and how they are coupled at the interface. All equations are solved in the 2D axis-symmetric system. The physics of drying within the droplet is very similar to the 1D case, except for the extra coupling of the Navier-Stokes equation externally and the full numerical solution of the transport of vapour in the air, instead of estimations through dimensionless numbers.

#### 5.3.3.1. Fluid flow

The fully compressible Navier-Stokes equation is solved in the liquid and air domains. The motion of fluid flow is captured by the following mass, momentum, and continuity equations.

##### 5.3.3.1.1. Liquid phase

$$\frac{\partial \rho_l}{\partial t} + \nabla \cdot (\rho_l \mathbf{u}_l) = 0 \quad (5-27)$$

$$\rho_l \frac{\partial \mathbf{u}_l}{\partial t} + \rho_l (\mathbf{u}_l \cdot \nabla) \mathbf{u}_l = \nabla \cdot [-p_l \mathbf{I} + \boldsymbol{\tau}_l] + \mathbf{F}_l \quad (5-28)$$

$$\boldsymbol{\tau}_l = \mu_l (\nabla \mathbf{u}_l + (\nabla \mathbf{u}_l)^T) - \frac{2}{3} \mu_l (\nabla \cdot \mathbf{u}_l) \mathbf{I} \quad (5-29)$$

## 5.3.3.1.2. Gas phase

$$\frac{\partial \rho_g}{\partial t} + \nabla \cdot (\rho_g \mathbf{u}_g) = 0 \quad (5-30)$$

$$\rho_g \frac{\partial \mathbf{u}_g}{\partial t} + \rho_g (\mathbf{u}_g \cdot \nabla) \mathbf{u}_g = \nabla \cdot [-p_g \mathbf{I} + \boldsymbol{\tau}_g] + \mathbf{F}_g \quad (5-31)$$

$$\boldsymbol{\tau}_l = \mu_g (\nabla \mathbf{u}_g + (\nabla \mathbf{u}_g)^T) - \frac{2}{3} \mu_g (\nabla \cdot \mathbf{u}_g) \mathbf{I} \quad (5-32)$$

Where  $\rho_i$  is the density of the fluid ( $kg/m^3$ ),  $u_i$  is the velocity of the fluid ( $m/s$ ),  $p_i$  is the pressure,  $F_i$  is the gravitational force ( $N/m^3$ ),  $\tau_i$  is the viscous stress tensor,  $i^{th}$  is the phase number such as liquid or gas.

**5.3.3.2. Heat transfer**

## 5.3.3.2.1. Liquid phase

$$\rho_l C_{pl} \left( \frac{\partial T_l}{\partial t} + \mathbf{u}_l \cdot \nabla T_l \right) = \nabla \cdot (k \nabla T) - (\nabla p_l \mathbf{u}_l) + \mathbf{u}_l \nabla \tau_l + Q \quad (5-33)$$

## 5.3.3.2.2. Gas phase

$$\rho_g C_{pg} \left( \frac{\partial T_g}{\partial t} + \mathbf{u}_g \cdot \nabla T_g \right) = \nabla \cdot (k \nabla T) - (\nabla p_g \mathbf{u}_g) + \mathbf{u}_g \nabla \tau_g + Q \quad (5-34)$$

Where  $T$  is the temperature ( $K$ ),  $p$  is the pressure ( $Pa$ ),  $C_{pi}$  is the specific heat capacity  $J/(kg * K)$  of  $i^{th}$  phase,  $u$  is the velocity ( $m/s$ ),  $q$  is the conduction heat flux ( $W/m^2$ ),  $\tau_i$  is the viscous stress tensor ( $Pa$ ),  $Q$  is the source term ( $W/m^3$ ),  $i^{th}$  is the phase such as liquid or gas.

**5.3.3.3. Species transport**

The transport in gas and liquid phase are considered as the species transport in dilute and concentrated solution, respectively.

## 5.3.3.3.1. Liquid phase

$$\rho_d \frac{\partial}{\partial t} (\omega_{il}) + \rho_d (\mathbf{u}_l \cdot \nabla) \omega_{il} = -\nabla \cdot \mathbf{j}_{il} \quad (5-35)$$

### 5.3.3.3.2. Gas phase

$$\frac{\partial c_{ig}}{\partial t} + \nabla \cdot (-D_{va} \nabla c_i) + \mathbf{u}_g \cdot \nabla c_i = 0 \quad (5-36)$$

Where  $c_{ig}$  is the concentration of  $i^{th}$  species in the gas phase,  $\omega_{il}$  is the mass fraction of  $i^{th}$  species in liquid,  $c_{il}$  is the concentration of  $i^{th}$  species in the liquid phase,  $\mathbf{u}_g$  is the velocity field in the gas phase,  $\mathbf{u}_l$  is the velocity field in the droplet,  $D_{va}$  is the diffusion of vapour in air,  $D_{ws}$  is the relative diffusivity of water to sucrose in the bi-component system. The flow is solved in a fully compressible form. The diffusion model used within the droplet is the mixture-averaged model (discussed in section 5.2) with the internal-developed diffusivities correlation from the equation (5-8).

### 5.3.4. Boundary and initial conditions

The moving interface is handled by a set of equations mentioned in equation (3-21) and (3-22). The inlet velocity is 1 m/s and the outlet is set at atmospheric pressure. The 'slip' condition is applied to the side-walls. Initially, the droplet and air are at the conditions specified in Patel *et al.* (2008) paper. The hot air is introduced at the inlet which takes a few milli-second to fully established the whole domain. This ensures numerical stability as there is no sudden jump in temperature across the droplet's surface. The stress balance condition at the interface, which can be referred to in equations (3-69), (3-70), (3-71) and (3-72), is revised as follows,

$$\mathbf{u}_1 = \mathbf{u}_2 + \left( \frac{1}{\rho_1} - \frac{1}{\rho_2} \right) M_f \mathbf{n}_i \quad (5-37)$$

$$\mathbf{n}_i \cdot \boldsymbol{\tau}_2 = \mathbf{n}_i \cdot \boldsymbol{\tau}_1 + \mathbf{f}_{st} \quad (5-38)$$

$$\mathbf{f}_{st} = \sigma (\nabla_s \cdot \mathbf{n}_i) \mathbf{n}_i - \nabla_s \sigma \quad (5-39)$$

$$\mathbf{u}_{mesh} = \left( \mathbf{u}_1 \cdot \mathbf{n}_i - \frac{M_f}{\rho_1} \right) \mathbf{n}_i \quad (5-40)$$

Variables in equations (5-37), (5-38), (5-39) and (5-40) can be found on page 123.

The activity water correlation was taken from Patel *et al.* (2008),

$$a_w = n_w e^{(-K_N(1-n_w)^2)} \quad (5-41)$$

The local surface concentration is determined by,

$$c = a_w c_{sat} \quad (5-42)$$

Where  $a_w$  is the water activity,  $c_{sat}$  is the saturated vapour concentration and  $c$  is the vapour concentration at the droplet surface. The saturated pressure is,

$$P_{sat} = 10^{\left(\frac{A-B}{(T-273)+C}\right)} \quad (5-43)$$

$$c_{sat} = \frac{P_{sat}}{RT} \quad (5-44)$$

The evaporative cooling at the droplet's interface due to evaporation flux is accounted for by the heat sources condition,

$$Q = m_{evap} H_{evap} \quad (5-45)$$

### 5.3.5. Material properties

The droplet physical properties were taken from correlation or mixture averaged formula.

Symbols (Units)	Parameters	Expressions
$\rho_{drop}$ $\left(\frac{kg}{m^3}\right)$	Density of droplet	$\rho_s\omega_s + \rho_l\omega_l$
$k_{drop}$ $\left(\frac{W}{mK}\right)$	Droplet thermal conductivity	$k_s\omega_s + k_l\omega_l$
$Cp_{drop}$ $\left(\frac{J}{kg*K}\right)$	Specific heat capacity	$Cp_s\omega_s + Cp_l\omega_l$
$\mu_{drop}$ (Pa.s)	Sucrose solution dynamic viscosity (Simion et al., 2011)	$\log \mu = \log \mu_0 - \frac{E_a}{2.303RT}$ $\frac{E_a}{T} = \frac{a + bX + cX^2 + dX^3 + e\ln T + f(\ln T)}{1 + gX + hX^2 + i\ln T}$

**Table 5-5.** Sucrose solution physical properties used in the simulation of the 2D droplet drying model.

### 5.3.6. Numerical method

The method used in this research is the FEM, and the ALE method as discussed previously (refer to Chapter 3) in which a motion that happened at an interface will be propagated throughout all other mesh nodes. Hence the whole mesh deforms at the same time to conform with the moving interface. The detailed theory of this method was discussed in Chapter 3. The mesh motion due to the mass exchange across the droplet's surface is obtained through the mass and momentum balance equation evaluated at the interface. The mass flux variable from the liquid domain needs to be coupled with the vapour flux generated at the droplet's surface.

### 5.3.7. Results and discussions

The developed model was computed numerically to aid the exploration of the drying of the multi-component droplet, which is the sucrose solution, falling with terminal velocity in an upcoming hot air. During the simulation course, the initial droplet size and air temperature were varied from 2145  $\mu\text{m}$  to 2179  $\mu\text{m}$  and from 63°C to 95°C, respectively. The first section reports a qualitative analysis of the validation of the computational results against the experimental data (Patel *et al.*, 2008). The next section focuses on analysing the critical variables such as local velocity and pressure fields, temperature gradient along the droplet surface, local evaporation rate, or internal water activity as a function of time both in the liquid domain. This type of information is impossible to retrieve from the SDD experiment and is not yet addressed by any other drying models.

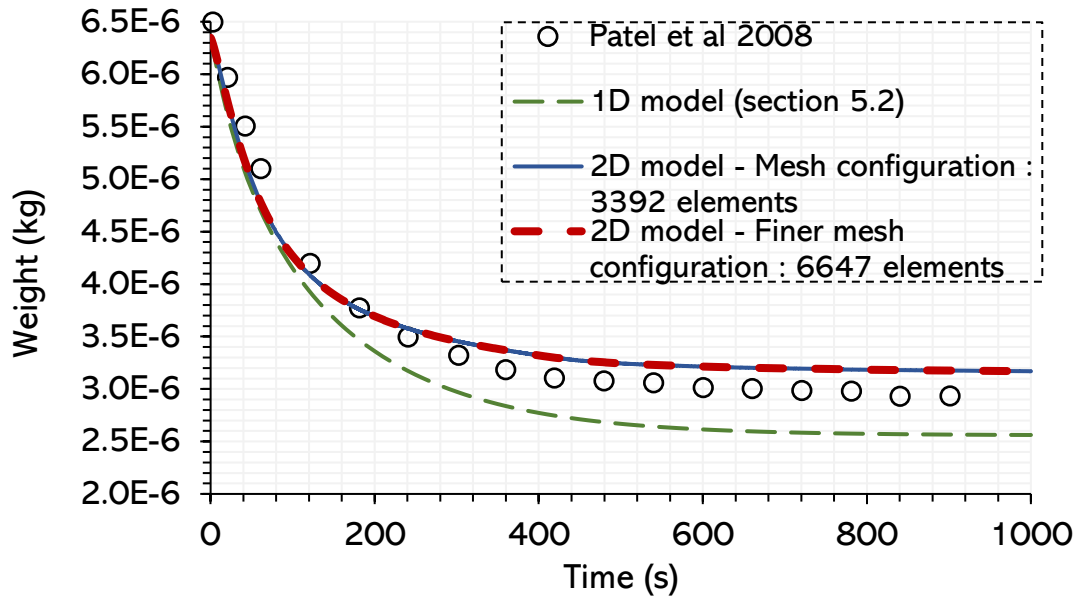
First, the droplet's total mass is computed to show the accuracy and reliability of the 2D model in capturing the global drying information comparing to the 1D model. Since the droplet mass varies based solely on evaporation, the conservation of mass within the droplet domain can be easily determined,

$$\frac{d}{dt}m_{drop} = \frac{d}{dt}(V_{drop}\rho_{drop}) = \frac{d}{dt}(-JA_{drop}) \quad (5-46)$$

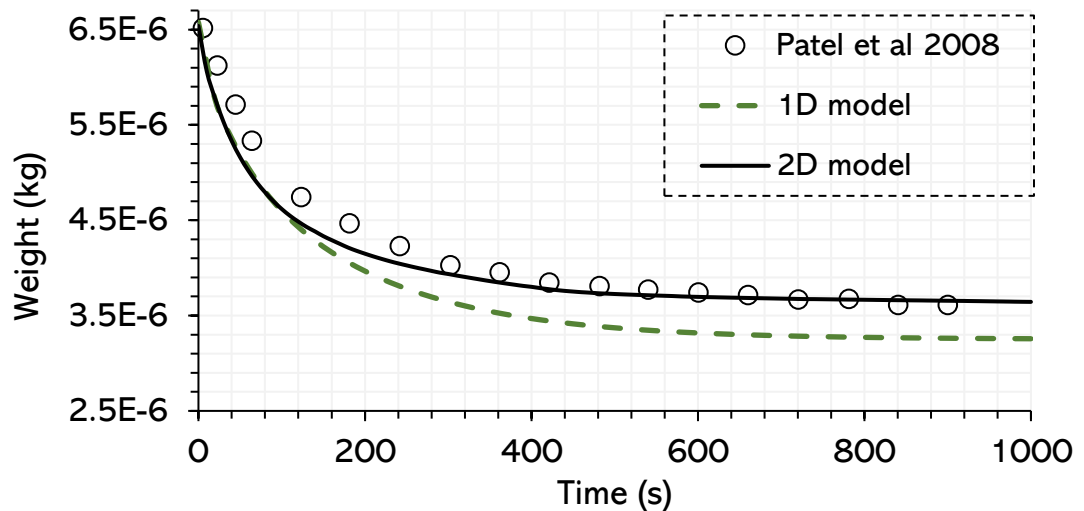
Or in terms of global mass,

$$\int dm_{drop} = \int \rho_{drop}dV_{drop} = - \int JdA_{drop} \quad (5-47)$$

The total computed evaporation rate can be integrated along the droplet surface from the simulated results and the total mass of the droplet over time is obtained by integrating over the droplet domain following equation (5-47).

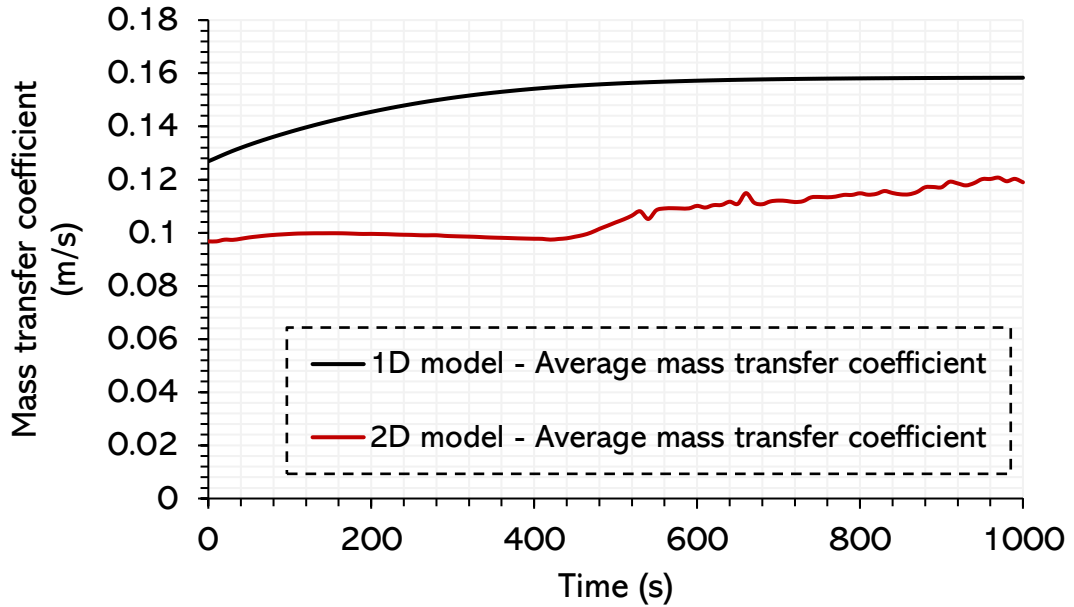


**Figure 5-15.** Droplet mass profile of a **2179  $\mu\text{m}$  – 1.5 kg/kg – db** droplet. The computed results are compared against the 1D drying model developed in section 5.2. The drying interval is **1000 s** and the air temperature is at 95°C. 2D model was repeated with two mesh configurations for a mesh independence test.



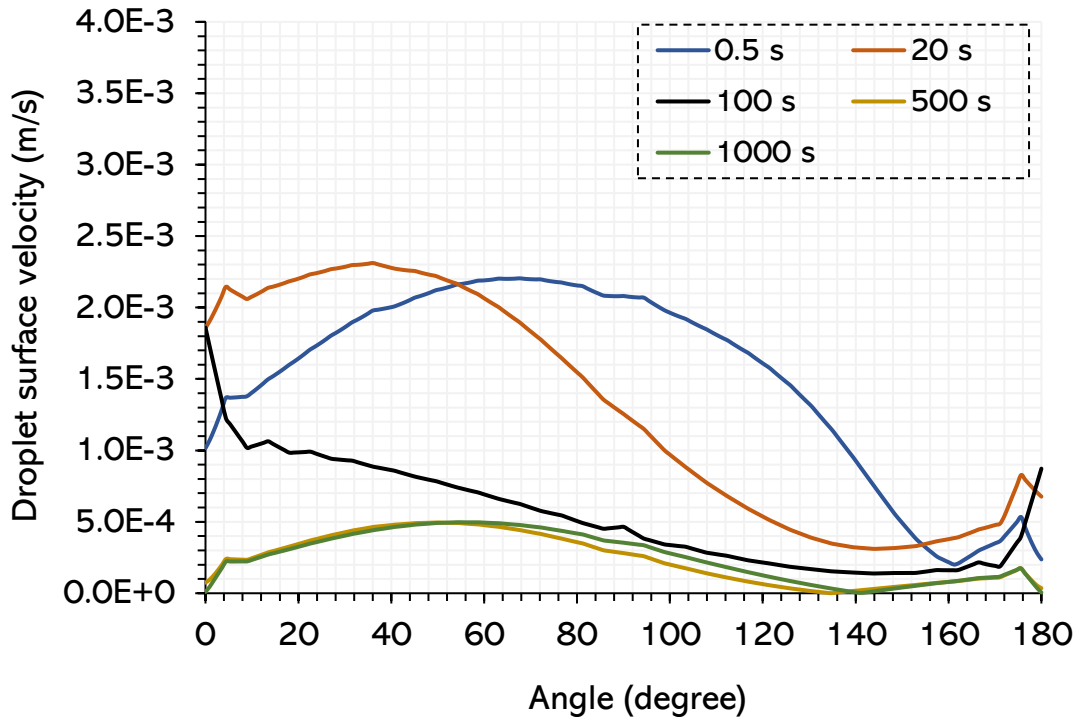
**Figure 5-16.** The temperature profile of a **2145  $\mu\text{m}$  – 1 kg/kg – db** droplet against the Patel *et al.* (2008) data. The 'normal mesh' configuration (3392 elements) was used as the mesh independence is reached in Figure 5-15. Drying time is **1000 s** and the air temperature is at 95°C.

Figure 5-15 and Figure 5-16 show the prediction of the 2D drying model to the experimental data (Patel *et al.*, 2008). The model predicted a steep gradient of mass loss for the first 100 s period followed by a falling rate period. As mentioned in section 5.2.3.2, the correlation data for water activity and diffusion coefficient of sucrose solution are not fully explored with many assumptions at the low moisture content region. The droplet mass starts to leveling out sooner than the experimental data, which is about 50% of the initial value, as sucrose is accumulated at the surface. The limit in the solubility model used in the viscosity correlation might also be a source of error causing a difference between computed and measured results. The 1D model (section 5.2) and 2D model predict the same droplet weight profile in the constant rate period for both setups (droplet with 60% and 50% initial moisture content). The 1D model however has a higher mass transfer coefficient in the falling rate period (after  $t = 200$  s). This can be illustrated by comparing the average heat and mass transfer coefficient on the droplet surface in the 1D and 2D model in Figure 5-17.



**Figure 5-17.** Comparison of the averaged mass transfer coefficient in the 1D and 2D drying model. The mass transfer coefficient is computed from the Sherwood number in the 1D model, and from the averaged flux along the droplet surface in the 2D model. The air temperature is at 95°C and the droplet initial moisture content is 1.5 kg/kg-db.

The difference in the mass transfer is shown in Figure 5-17. The 1D model predicts a higher mass transfer coefficient than that of the 2D model throughout the drying period. This explains the smaller droplet mass towards the end of the drying period (Figure 5-15). Several factors can cause a disagreement between the two models including the internal recirculation which affects the diffusivity or the droplet surface motion due to the shear stress from the external air flow. The droplet interface velocity will be examined in the following section. The magnitude of the velocity at the droplet interface is plotted in Figure 5-18.



**Figure 5-18.** Droplet surface velocity magnitude at  $t = 0.5s, 20s, 100s, 500s$  and  $1000s$ . The plotting angle starts from the front of the droplet ( $0^\circ$ ) towards the back of the droplet ( $180^\circ$ ).

The droplet interface velocity decreases over time with a peak value of around  $0.002\text{ m/s}$  at  $t = 0.5s$  (as the droplet starts falling) and around  $5e^{-3}\text{ m/s}$  at  $t = 1000s$  as the viscosity increases. The velocity at the interface can have an effect on the overall as well as local heat and mass transfer coefficient, as it will affect the internal velocity field within the droplet and the accumulation of the sucrose.

Next, the sphericity of the droplet is examined. This aspect can be used to justify the current PID system for maintaining the droplet surface. Three radii, as shown in Figure 5-19, were used to visualise the sphericity of the droplet during drying and falling.

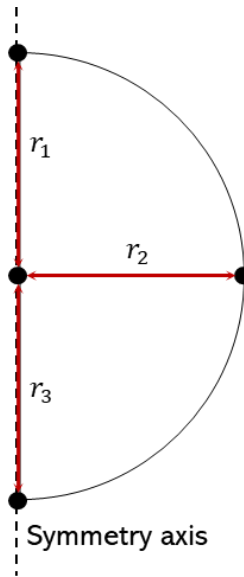


**Figure 5-19.** Three reference radii for calculating droplet sphericity.

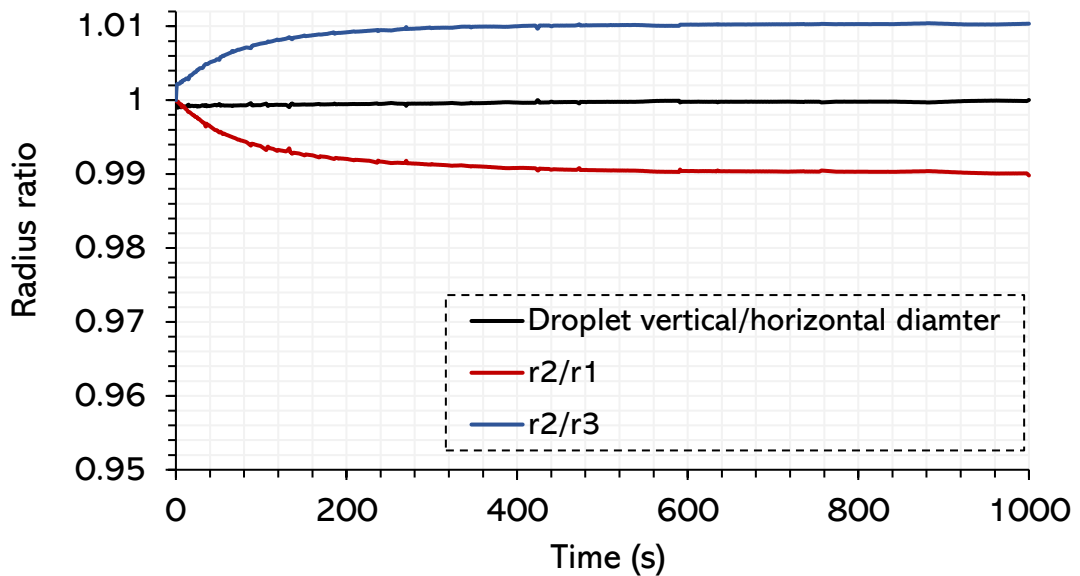


**Figure 5-20.** Droplet sphericity plots. The definition of the three radii  $r_1$ ,  $r_2$  and  $r_3$  can be found in Figure 5-19. The ratio between the three radii represents the shrinking rate at three different points on the droplet surface. The sphericity of the droplet will be based on how close the three ratios are to 1.

The surface tension is defined generally as,

$$\Delta P = \gamma \left( \frac{1}{R_1} + \frac{1}{R_2} \right) \quad (5-48)$$

Where  $\Delta P$  is the pressure difference between the gas and liquid domains,  $\gamma$  is the surface tension,  $R_1$  and  $R_2$  are the two principal radii of curvature which are the same in the case of a perfect spherical droplet. The droplet is said to be spherical when the two ratios are equal to 1 and any elongated effect will make the  $\frac{r_1+r_3}{r_2} = \frac{R_{horizontal}}{R_{vertical}} \neq 1$ . The vertical and horizontal diameters ratio is indeed very close to 1 in Figure 5-20.

Apart from the external forces, the asymmetrical drying also contributes to the droplet's sphericity, as the droplet shrinks from different directions. The evaporative flux is expected to be strongest at the droplet front and decreases proportionally to the middle and towards the backside, which causes the  $r_3$  to shrink faster than the  $r_2$  and  $r_2$  to shrink faster than the  $r_1$  radius. This explains why the  $\frac{r_2}{r_3} < 1$  and  $\frac{r_2}{r_3} > 1$  throughout the drying process. Overall, the droplet maintains its shape well as the two ratios are very close to unity. Figure 5-21 and Figure 5-22 are the temperature profiles (1D and 2D models) of the sucrose droplet at 95°C with 1.5 kg/kg and 1 kg/kg initial moisture content.

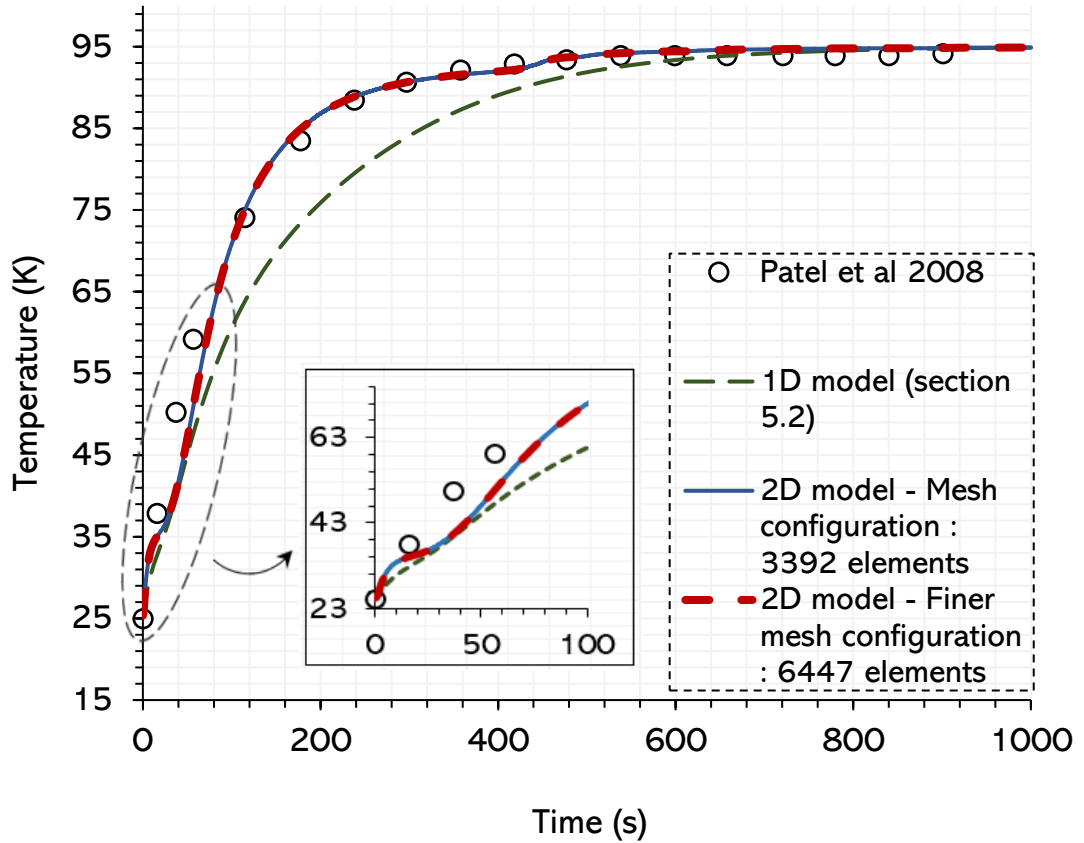


**Figure 5-21.** Temperature profile of a **2179  $\mu\text{m}$  – 1.5 kg/kg – db** sucrose droplet in 1D (dotted green line) and 2D models (blue and dotted red lines). The 2D model was repeated with 2 mesh configurations for the mesh independence test. The subplot is the zoom-in of the wet-bulb section of the droplet temperature. The air temperature is set at **95°C**.

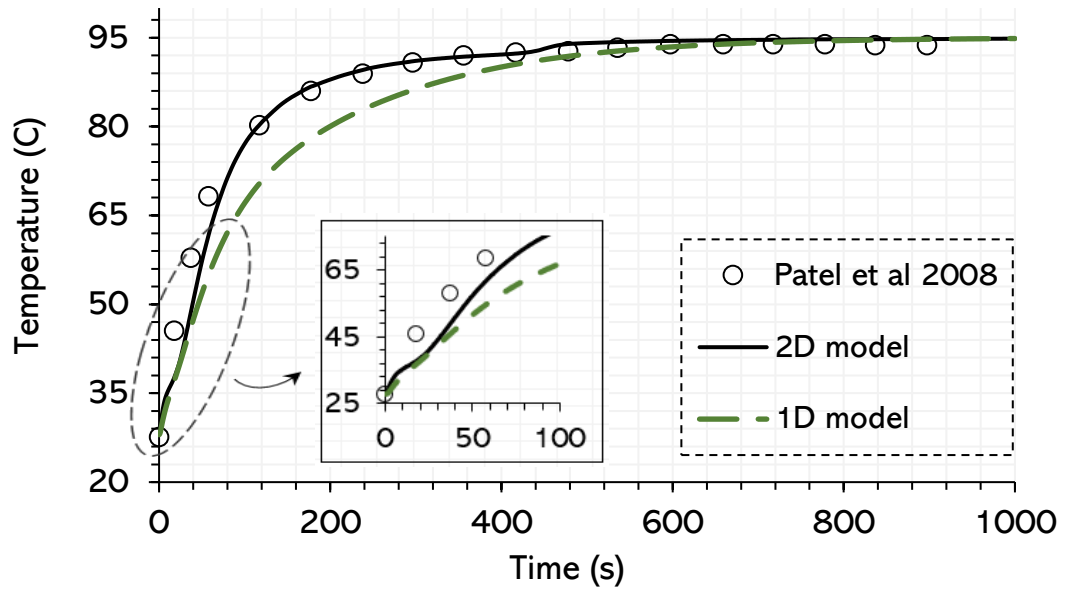


**Figure 5-22.** Temperature profile of a **2145  $\mu\text{m}$  – 1 kg/kg – db** sucrose droplet in 1D (dotted green line) and 2D models (black line). One mesh configuration was used as the mesh independence is reached in Figure 5-21. The subplot is the zoom-in of the wet-bulb section of the droplet temperature. The air temperature is set at **95°C**.

The computed temperature is evaluated at the centre of the droplet which is the same as how the thermocouple is positioned in the SDD experiment. The 2D simulation results agree with the droplet temperature measured in the experiment. A clear region of the wet-bulb temperature is not observed, but rather a brief slowing down of temperature gradient at around  $t = 18\text{ s}$  (Figure 5-21) and  $t = 8\text{ s}$  (Figure 5-22). With an agreement of the 2D droplet mass profile to the experimental data in Figure 5-15 and Figure 5-16, the 2D droplet temperature is predicted to also fit the measured temperature (refer to Figure 5-21 and Figure 5-22). The mesh refinement does not improve the result noticeably throughout the drying, hence the mesh configuration of 3392 elements will be used for all other simulation runs. For the case of lower initial moisture content droplet (**2145  $\mu\text{m}$  – 1 kg/kg – db**), the discrepancy

between the 1D and 2D models is similar to that of the  $1.5 \text{ kg/kg} - db$  sucrose droplet. The difference between the 1D and 2D models in the later drying stages, where the sucrose has already accumulated at the droplet surface, indicates that the internal flow field of the droplet can have a considerable impact on the formation of the sucrose viscous layer, hence resulting in different heat and mass transfer coefficient compared to the 1D model.

### 5.3.7.1. Local variables analysis

The surface water activity is plotted in Figure 5-23 and Figure 5-24.

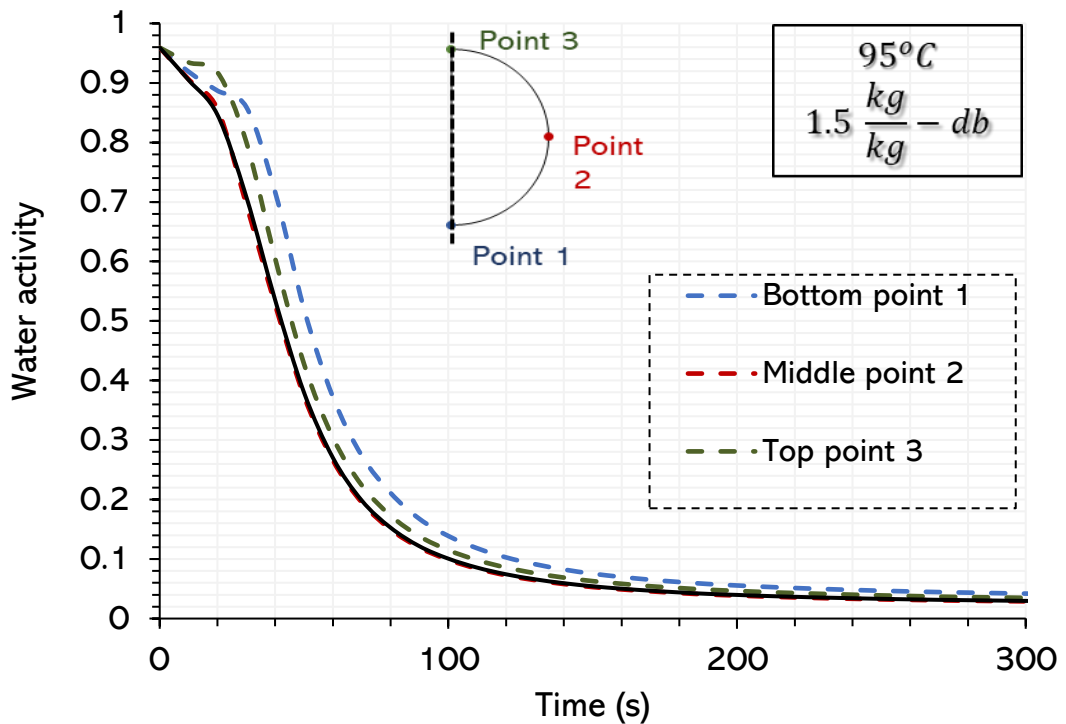


**Figure 5-23.** Water activity on the droplet interface at  $95^{\circ}\text{C} - 1.5 \frac{\text{kg}}{\text{kg}} - db$ . The water activity is plotted at three different locations along the droplet surface: bottom (blue), middle (red) and top (green) points. The averaged water activity is plotted in black line.

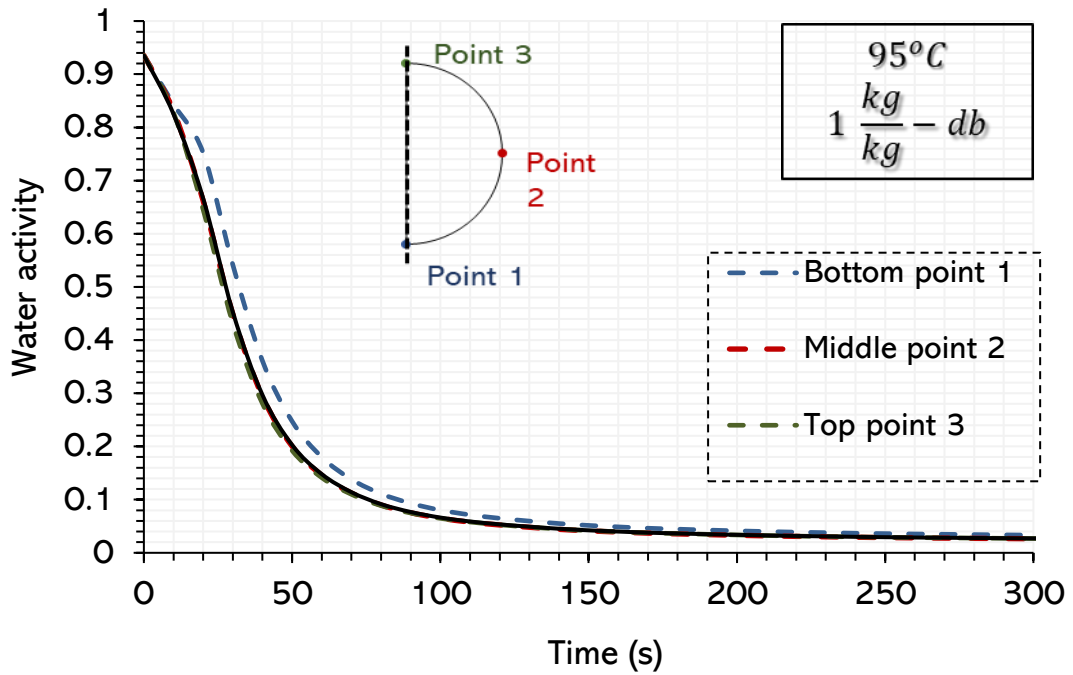
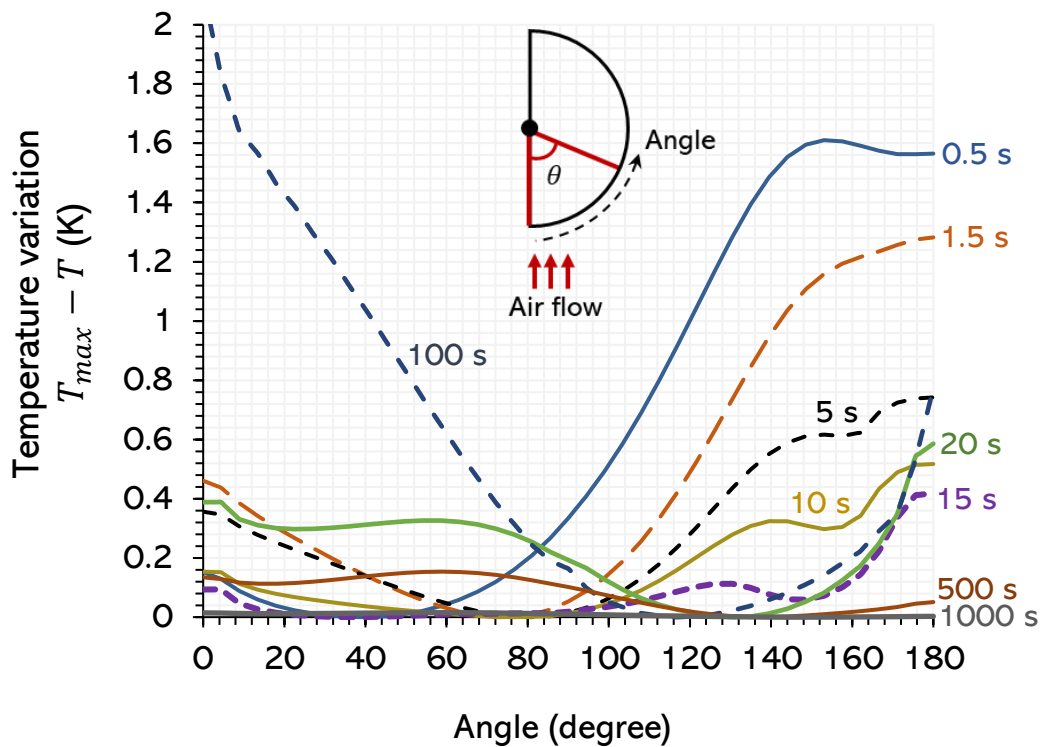


**Figure 5-24.** Water activity on the droplet interface at  $95^{\circ}\text{C} - 1 \frac{\text{kg}}{\text{kg}} - db$ . The water activity is plotted at three different locations along the droplet surface: bottom (blue), middle (red) and top (green) points. The averaged water activity is plotted in black line.

Figure 5-23 and Figure 5-24 present the water activity at three separate points and averaging across the droplet interface. The plot emphasises how water activity is locally controlled by the local evaporation rate and convection effect. The activity is tracked at 3 points: bottom, middle and top points (as shown in Figure 5-23). A similar pattern is observed in both cases ( $95^{\circ}\text{C} - 1.5 \frac{\text{kg}}{\text{kg}} - db$  and  $95^{\circ}\text{C} - 1 \frac{\text{kg}}{\text{kg}} - db$ ). At the first stage where the local water concentration is slowly removed, the middle point has the largest gradient followed by the bottom and top points. After 20 s (Figure 5-23) and 10 s (Figure 5-24), the water activity experienced a sharp drop down to 0.02 where the skin formation initiated. Interestingly, the water removal is strongest at the top and middle points, as the water activity at the bottom point is always the highest during

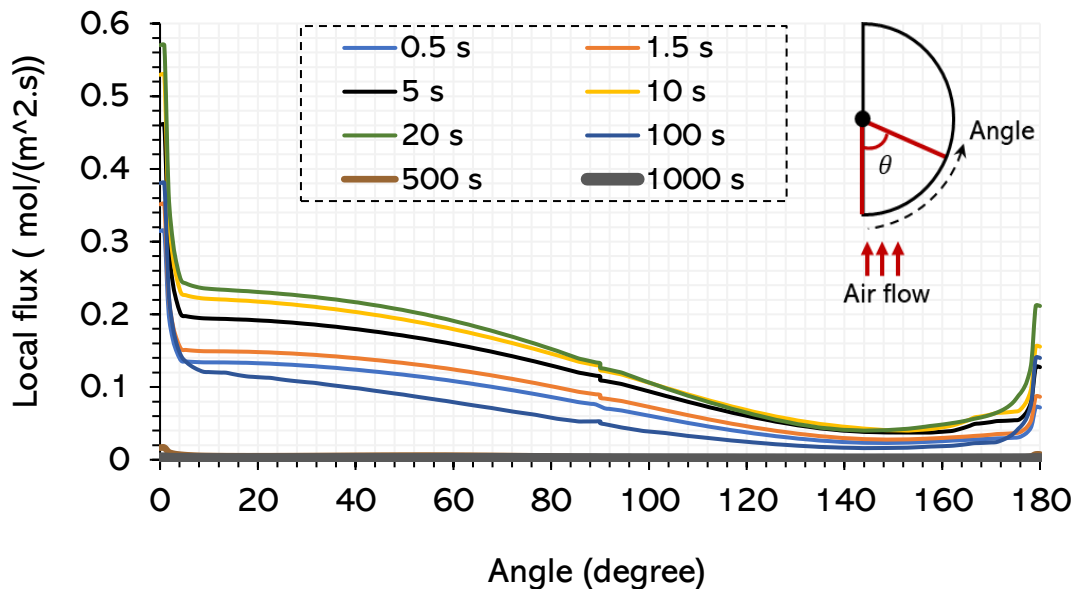
drying. This implies the water mainly flows towards the droplet's front leaving the solute to accumulate at the top point first. This phenomenon underlines the weakness of using the 1D model to predict particle morphologies as it neglects the asymmetry aspect of the concentration field. The average line (black line) pattern is very similar to point 2. This makes the middle point the representative position for the parameters on the droplet surface at the later drying stage.

From here onwards, the analysis focuses on the droplet of **2179  $\mu\text{m}$  – 1.5 kg/kg – db** as the other case exhibited similar behaviour. The local temperature variation along the droplet's surface is plotted across the total time range (seen in Figure 5-25).



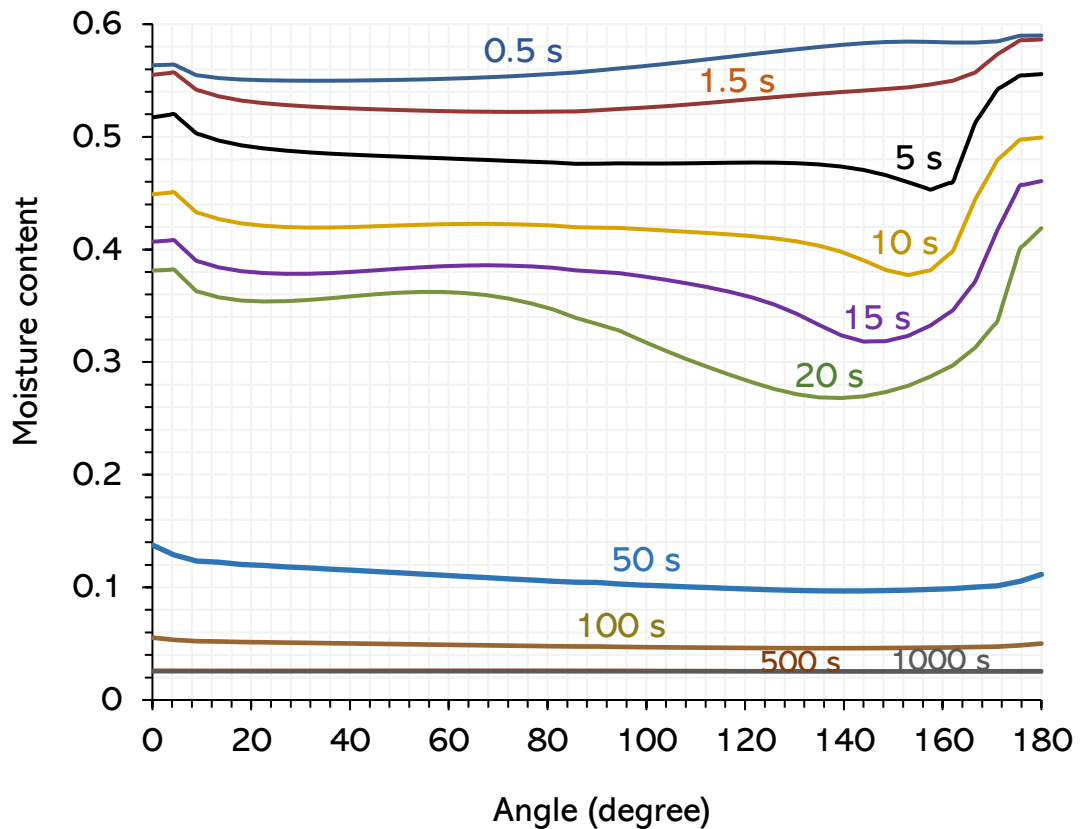
**Figure 5-25.** Surface temperature difference to the maximum temperature along the droplet surface  $T_{max} - T_{surface}$ . The time interval is from  $t = 0.5 \text{ s}$  to  $1000 \text{ s}$ . The temperature is plotted against the phase angle, from the droplet front ( $0^\circ$ ) to the back ( $180^\circ$ ).

Figure 5-25 is constructed by subtracting the surface temperature at every node,  $T_{surface}$ , from the maximum temperature,  $T_{max}$ , along the droplet surface. Hence, all curves must touch the x-axis only once since the  $T_{max}$  is also on the surface. The interpretation is that the higher the  $y$ -value in Figure 5-25, the lower the temperature at that point. The temperature appears to vary everywhere along the surface due to a low initial moisture content leading to no actual constant wet-bulb period. The distribution is uneven with a range up to  $\pm 1.5 K$  seen at the early drying stage ( $t < 10 s$ ) at the top point, and increases to  $\pm 2.0 K$  at later stage. The droplet stagnation point starts to heat up from initial temperature until  $t = 10 s$ , before the peak temperature is at the back of the droplet. The moisture content of the dried particle, as shown in Figure 5-27, is an important criterion of the particulate product. The integration of the local vapour flux can be used to check the consistency of the global droplet mass loss. Figure 5-26 is an illustration of an uneven local mass flux distributed at the droplet's surface.



**Figure 5-26.** Local flux along with the droplet interface versus time. The plotted timesteps are from  $t = 0.5 s$  to  $t = 1000 s$ . The flux is plot based on the angle to the droplet centre starting from the front of the droplet. Plots for all timesteps are colour-coded in the legend.

At the early drying stage, the variation is maximum due to an uneven moisture removal between the top and bottom points of the droplet (Figure 5-26). The flux is always higher at the droplet front which is expected since the air is greatest at this location. The maximum flux difference along the droplet surface is  $\pm 0.2 \frac{\text{mol}}{\text{m}^2\text{s}}$ , and the variation vanishes after 100 s.



**Figure 5-27.** Moisture content along with the interface versus time. The time interval is from  $t = 0.5 \text{ s}$  to  $1000 \text{ s}$ . The moisture is plotted against the phase angle of the droplet, starting from the front ( $0^\circ$ ) to the back side ( $180^\circ$ ). The schematic for the phase angle can be found in Figure 5-26.

The local moisture content is also plotted in Figure 5-27. The graph suggests that the location that loses the most moisture is at the separation point near the back of the droplet. This is an interesting result as the point with the strongest evaporation flux is not the point with the highest moisture removal. This can be explained by

looking into the diffusion and convection effects within the droplet. The internal flow field might be significant enough to supply enough moisture towards the droplet front, whilst leaving the sucrose to accumulate at the backside. This also predicts that the shell will start to form near the droplet back and develop onwards. This hypothesis will be confirmed once the internal flow and concentration fields are examined in the next section. The significant drop in mass flux is also shown by the drop of more than 96% in moisture content in Figure 5-27.

#### **5.3.7.2. Internal flow dynamic of the droplet**

In this section, the internal flow field and the species transport leading to the formation of the final dried-particle morphology are analysed. The external air flow induces the internal flow through the force balance at the droplet surface. The uneven distribution of stress on the interface results in the internal velocity gradient leading to vortices. The surface stress is linked to the liquid viscosity which is indirectly involved in the force balance. The formation of the vortices within the droplet follows the same principle as discussed in Chapter 3. The effects of the non-uniform viscosity distribution and changing shear stress on the receding droplet interface combine to form complicated flow dynamics. The next section is dedicated to this phenomenon and how sensitive the final particle morphology is to the initial conditions. Figure 5-28 shows an example of the vortices within the droplet at  $t = 2 \text{ s}$ . This figure combines 3 types of plots: streamlines, vectors and line plots. The three plot types describe the most relevant factors to the formation of vortices.

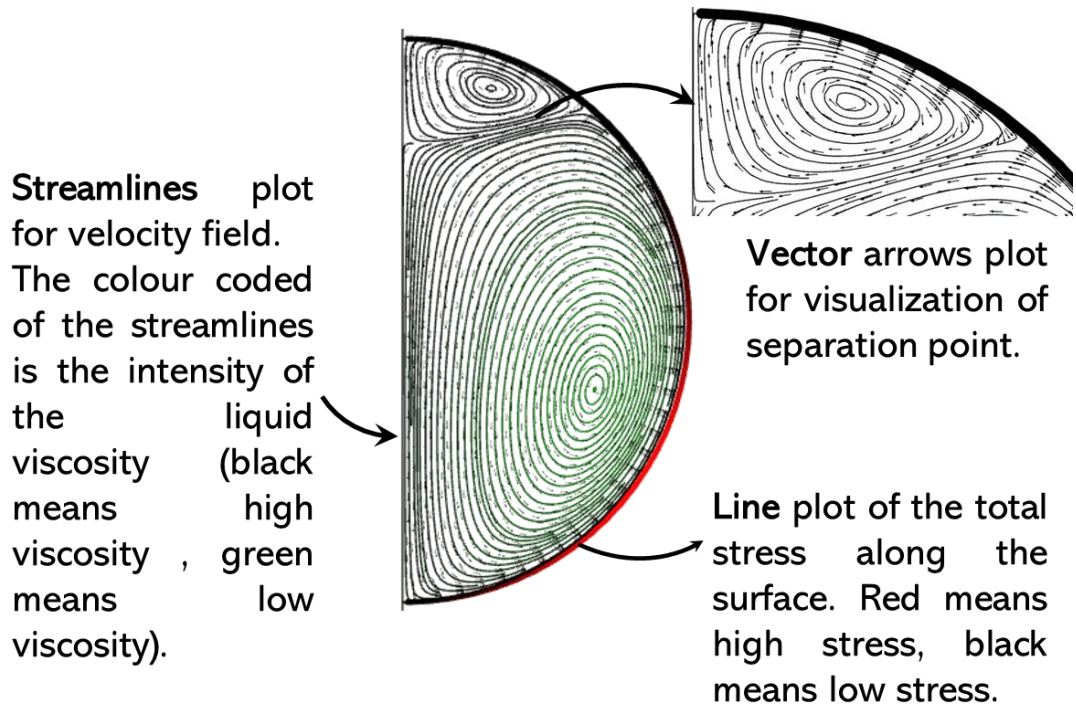


**Figure 5-28.** Illustration of plot types for visualisation of the droplet internal flow field. The streamlines and vector arrows are plotted for the velocity field, and colour-coded with the magnitude of the liquid viscosity. The stress on the surface is shown in the Line plot (red means high and black means low stress).

The shear stress plot on the interface helps to visualise and locate both the separation point and vortices. The 'Vortex Reynolds number' is defined as the number of circulations around the vortex structure to the liquid viscosity (Bandyopadhyay and Balasubramanian, 1995). The velocity is plotted using streamlines but the colour-coding for the streamlines is purposely chosen for the viscosity so that the vortex Reynolds number can be qualitatively estimated. Figure 5-29 is a series of droplet internal flow fields at chosen times.

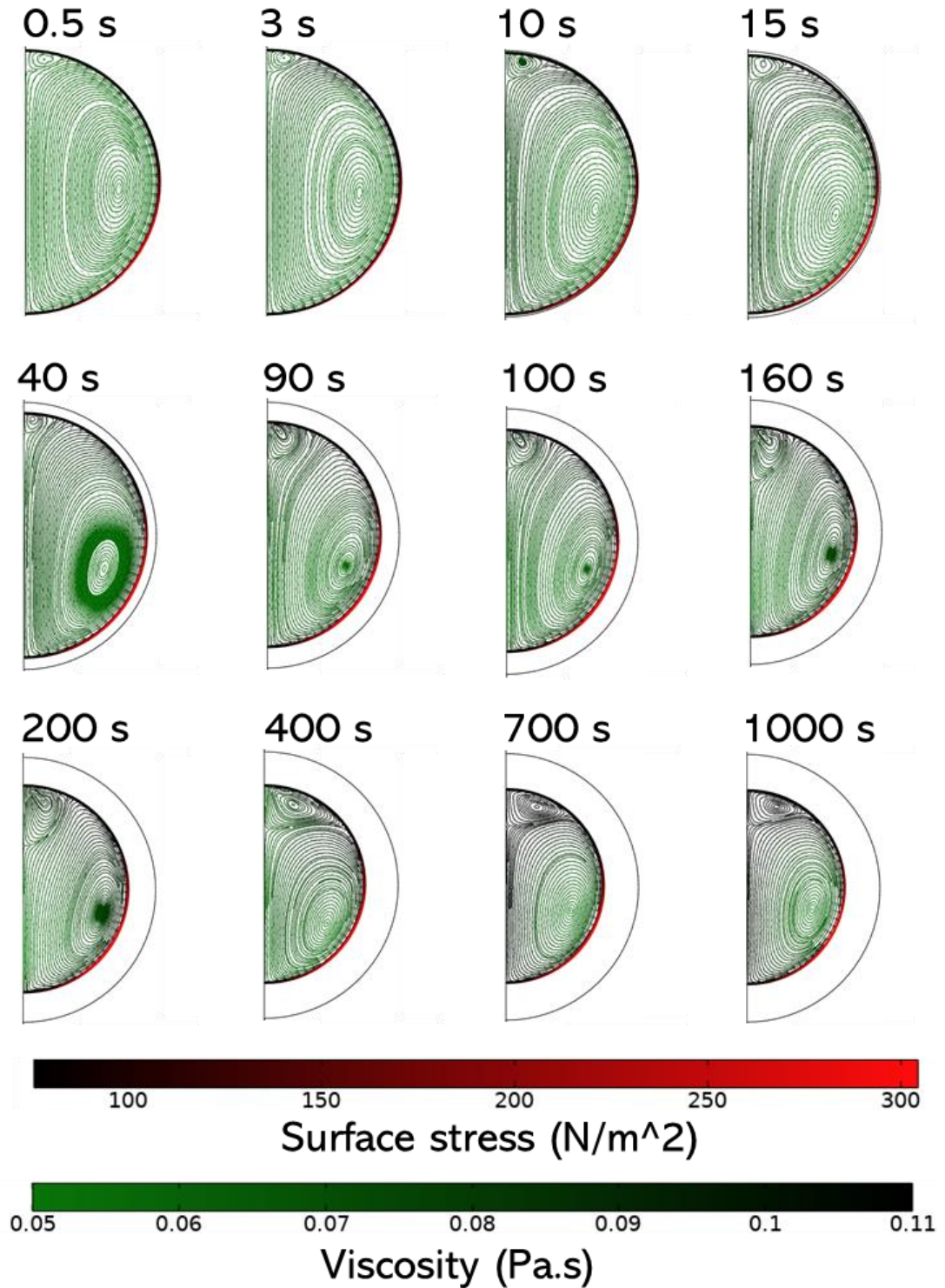


**Figure 5-29.** Droplet internal flow field with stress plot at the surface. The internal velocity field is plotted using streamlines and vector arrows, the surface stress is plotted using a line plot. The flow field is plotted from  $t = 0.5 \text{ s}$  to  $1000 \text{ s}$ .

At  $t = 0.5 s$ , the stress is highest at the droplet front, the upward flow is curving along with the interface from the stagnation point to the 'separation point' where the friction is maximum, the flow detaches and forms a big lower vortex as shown in Figure 5-29 ( $t = 0.5 s$ ). This inherently creates another clockwise vortex to compensate for the momentum direction, which is a secondary small vortex. The two adjacent vortex problem has been discussed clearly in the work of Tesař (2015). The induced vortex received the momentum from the other vortex through shear stress. The experiment by Tesař (2015) illustrated how the fluid rotation-motion is induced by a wall shear stress.

The vortex dynamics should follow the most viscous point since it determines the maximum stress on the surface. At  $t = 3s$  and  $10s$ , the viscosity starts to increase near the separation point as indicated by the colour change to black (compared to the green colour area at  $t = 0.5 s$ ). The main pattern always consists of two vortices: the primary (large) and the secondary (small) vortex. The small vortex size is constant until  $t = 40 s$  before being distorted, increased in size and then developed into the secondary vortex towards the end of the drying period. The main vortex occupied most of the droplet volume, locates at the bottom and adjacent to the largest shear stress area on the surface. As drying progresses, the droplet viscosity increases which lowers the velocity field and causes resistance to the heat and mass transfer. It is in fact the main influence on the flow pattern. There is a slight change in the internal dynamics seen from  $t = 90 s$  to  $t = 200s$  (Figure 5-29), and the main patterns re-established and remain towards the end. The high viscosity region within the droplet can be visualised by the black streamlines for example at  $t = 1000 s$ .

A number of theories have been developed to explain the pattern and the position of the vortex within the droplet and its size

evolution over time. The most relevant theories are *Helmholtz's vortex theorem* (Helmholtz, 1867) and *Kelvin's circulation theorem* (McDonald and Witting, 1984). Helmholtz's second theorem, in particular, states that the vortex cannot be destroyed within the fluid, but extends to end at the solid boundary or form a closed-loop instead. This explains why the vortex is always adjacent to the droplet interface, which also suggests that the water-rich region will always be neighboring the droplet's surface. The Kelvin's circulation theorem states that *for a flow with the conservative body forces (such as gravity in this case), the circulation around a close curve stays constant with time*. In detail, the vortices will remain constant unless there is a change in net viscous force, body forces or density-pressure relationship (Kundu 1990). In this drying droplet case, the net viscous force is obviously changing with time due to the changing moisture content, hence explaining the size dynamics of the small vortex region.

The same system is set up for a pure water droplet with the same parameters including the radius to compare and emphasise how drying affects the size and location of vortices. The simulation of a water droplet with the size of  $2179 \mu\text{m}$  falling at  $1 \text{ m/s}$  using the gravity controlled PID loop is set up. The viscosity, the droplet size and the flow pattern are constant in this case, hence the pure water droplet is compared with the sucrose droplet at  $t = 1 \text{ s}$  when the sucrose droplet has not shrunk much.

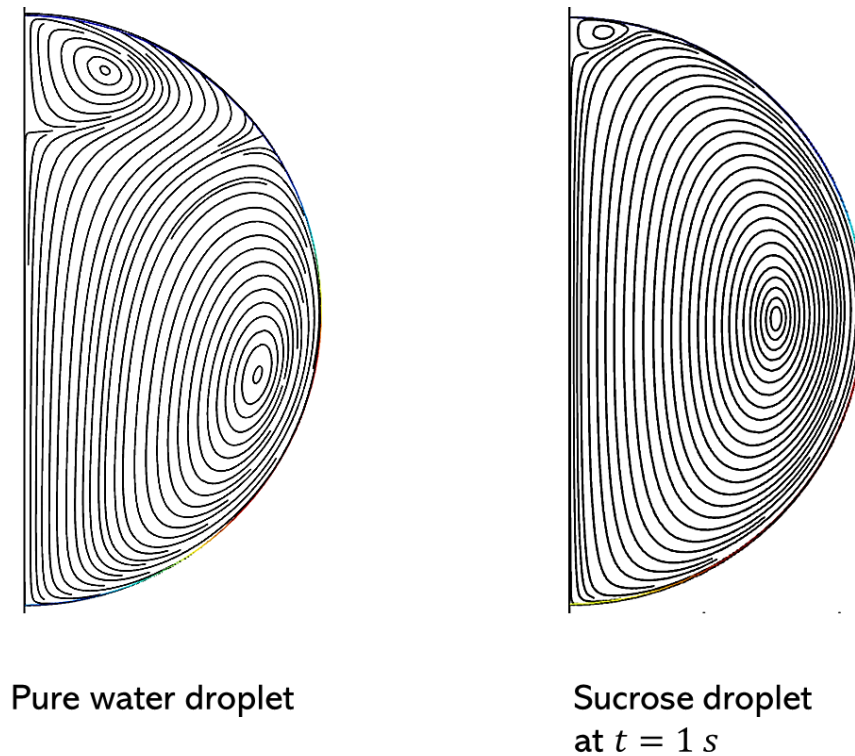


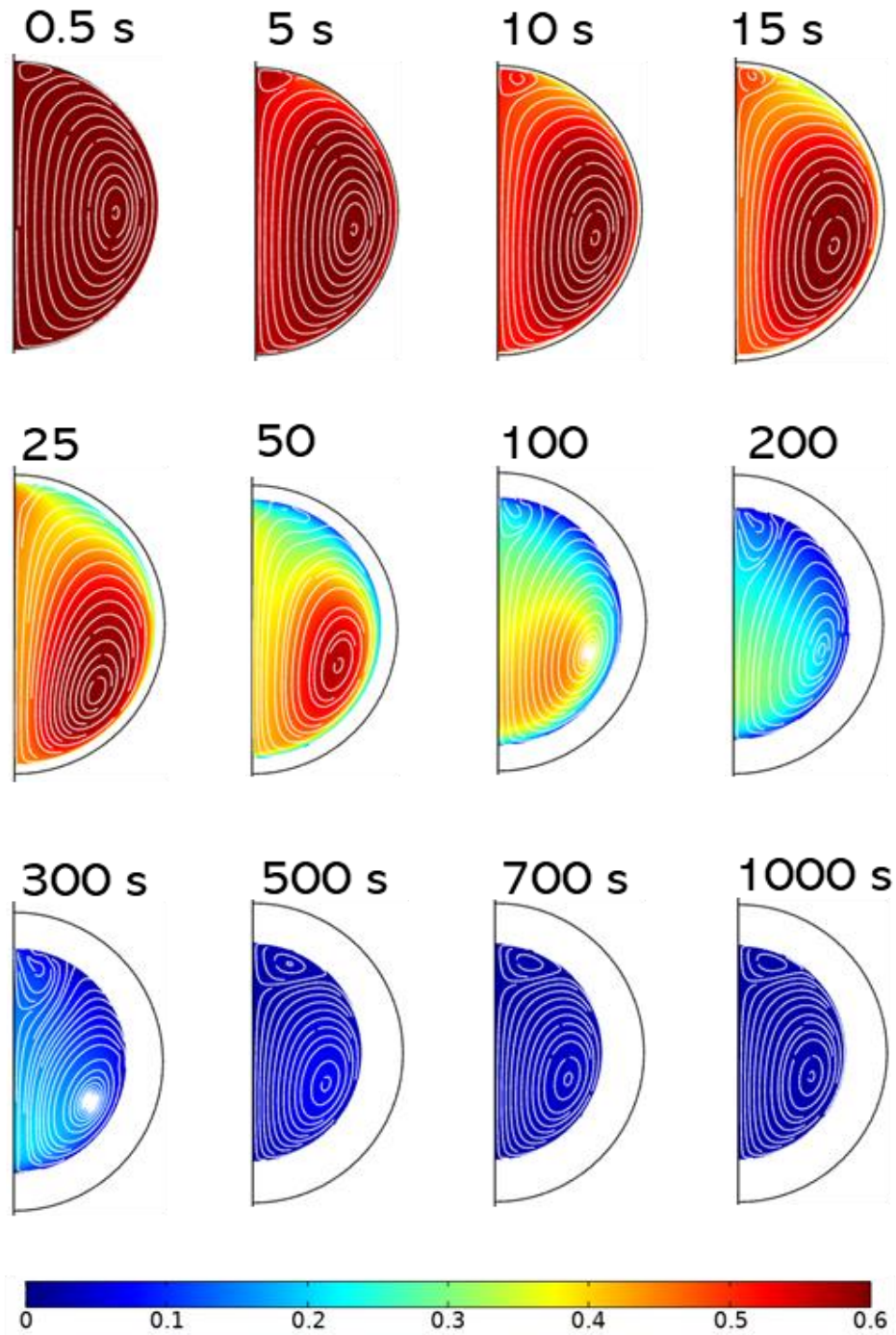
**Figure 5-30.** Internal velocity field comparison between the pure water droplet to the drying sucrose droplet.

The flow pattern of the water droplet on the left of Figure 5-30 has two vortices with the separation point on the top of the primary vortex. This separation point is also expected to also be the separation point of the external air flow. The vortex within the water droplet can also be explained using the previous discussion. In the sucrose droplet case (Figure 5-30-right), the increase in the viscosity at the separation point affects the stress directly at the surface. It should be noticed the velocity magnitude within the two droplets is not the same due to density difference. The velocity field within the water droplet is faster with one order of magnitude higher than that of the sucrose droplet. The local concentration field discusses in the next section is critical to the understanding of the morphology outcomes of the drying droplet. Figure 5-31 is a 2D surface plot of water concentration on a mass basis. Overall, Figure 5-31 exhibits a highly asymmetrical distribution of water within a droplet which cannot be predicted by previous 1D drying

models or observed during the SDD experiment. This concentration profile is critical to, for example, determine the strength of the structure formed so the possible deformed area under droplet collisions can be anticipated.

The sucrose solute forms a very thin concentrated layer initially at the interface due to evaporation. As the velocity field is established, the sucrose-rich region accumulates at the separation point ( $t = 5 s$ ), where the velocity is lowest, and circling around the primary vortex. This is contrary to the expectation of the sucrose forming at the front where the evaporative flux is strongest. As drying progresses, a high moisture content area is surrounded by a circular ring-shaped of high viscosity sucrose (refer to Figure 5-31 at  $t = 15 s, 25s$  or  $50 s$ ).

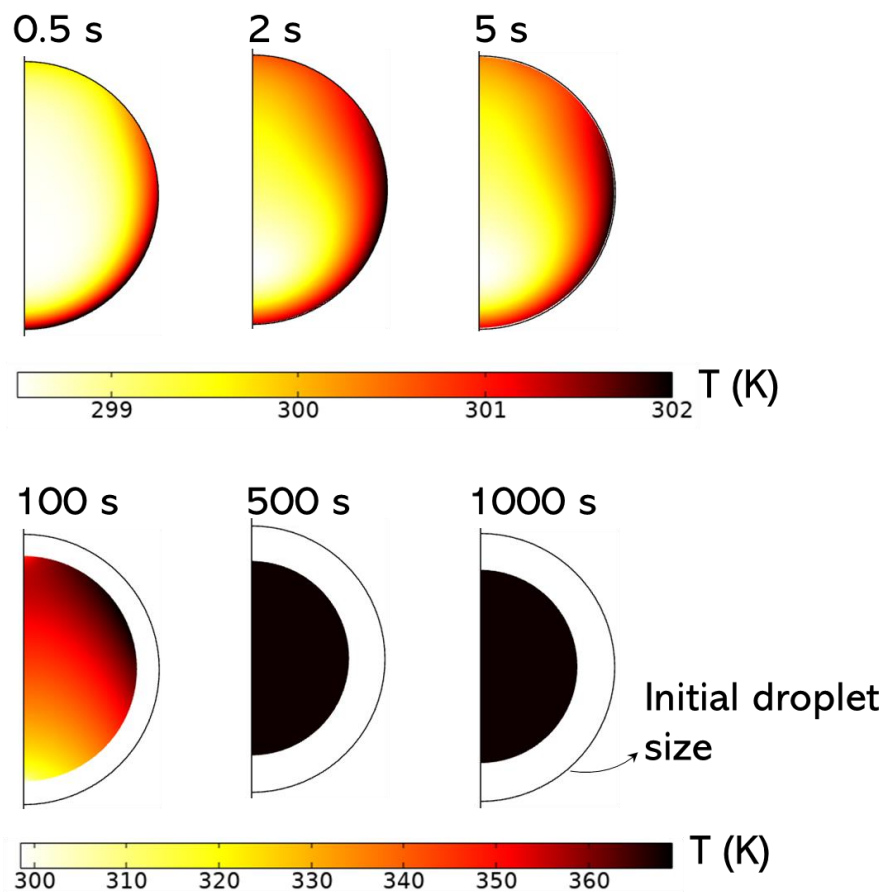
The local sucrose concentration will determine the skin's thickness. The convection effect has most of the water localised near the interface on the lower portion of the droplet. The droplet shell structure is 'hardened' and thickened from the pattern discussed above, and the surface layer is not radially-symmetric thickened as expected. Therefore, a bubble is likely to form at the centre of the primary vortex, at which the collapsing process would probably cause a strong deformation on the thin shell leading to a hollow dried-particle.



$$m_{\text{water}} \left( \frac{\text{kg}}{\text{total kg}} \right)$$

**Figure 5-31.** Moisture content of the sucrose droplet during drying. The air temperature is at 95°C and the initial moisture content is 1.5 kg/kg. The surface plot of the water concentration is colour-coded and the streamline of the velocity field is plotted in white lines. The drying time is 1000 s.

The main aim of this study is to provide information that is inaccessible by the current SDD experiment. The non-uniform concentration field emphasises the applicability of the 2D/3D model to predict the final morphologies. It should be noted that the outcome of the internal concentration field relies totally on the validity of the diffusivity model used, which is often poor-behaved at the extremes of sucrose concentration. This leaves a degree of improvement by having a more reliable diffusivity correlation, such as the correlation that fitted with more data points at two extreme regions. Next, the droplet internal temperature field is studied.



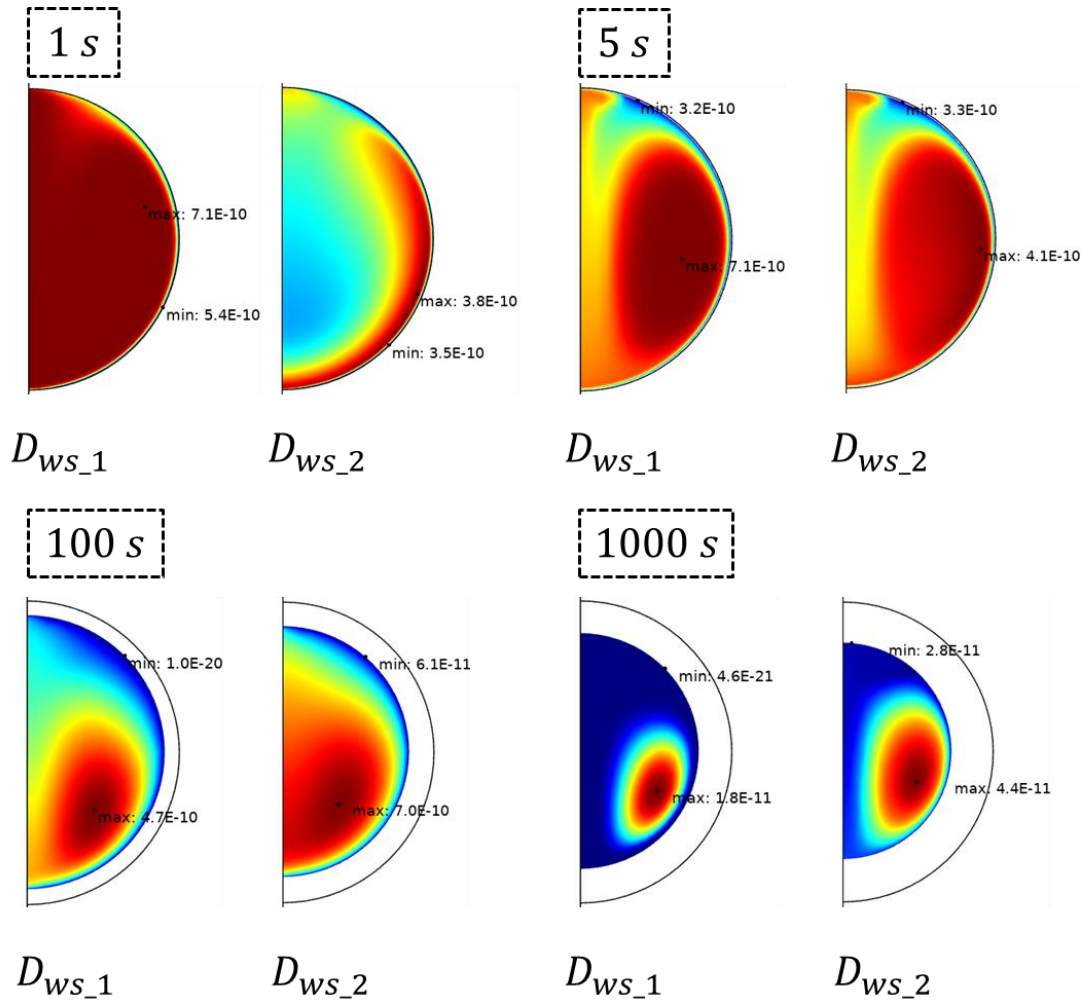
**Figure 5-32.** Temperature distribution within the sucrose droplet during drying. The droplet and air temperature are at 25°C and 95°C, and the initial moisture content is 1.5 kg/kg. The colour-coded temperature scale for the first 5 s (upper 3 plots) is provided separately for better visualisation of the temperature field in the early drying stage. The temperature scale is provided.

Figure 5-32 illustrates an even temperature distribution within the droplet throughout the drying process. The temperature scale is separated into two periods from  $t = 0.5\text{ s}$  to  $5\text{ s}$  and from  $t = 100\text{ s}$  to  $500\text{ s}$ . This provides a better visualisation of the temperature gradient within the droplet in the early drying stage. Overall, the droplet front is heated up first as the hot air is flowing upwards, and the internal temperature field becomes uniform in the later drying stage as the droplet size is smaller. The temperature difference is around  $\pm 3\text{ K}$  (based on the temperature scale). The temperature distribution within the droplet is not radially symmetrical due to the convection effect of the internal flow field shown in Figure 5-29. The lowest temperature region is not at the droplet core, which is expected to be the region with the highest moisture content, and it should be located in the middle of the primary vortex. The variation decreases quickly after  $t = 5\text{ s}$  and is uniform within the droplet towards the end of the drying stage. Another observation is how stable the droplet shrinks compared to its original position, represented by a solid black line, thanks to the innovative gravity-controlled PID algorithm so the droplet always falls at  $1\text{ m/s}$ .

### 5.3.8. Different diffusivity correlation models

A different study was carried out where the whole simulation was performed again with a different diffusivity correlation. The correlation used in this comparison is from Price *et al.* (2016) (equation (5-26)) in section 5.2.3.2 on page 164. The difference in the internal concentration gradient driven by the new diffusion coefficients is observed and presented in Figure 5-33. The maximum and minimum diffusivities values are plotted on each domain at each time step. The correlation  $D_{ws_1}$ , from Price *et al.* (2016), is used to compare with the new correlation  $D_{ws_2}$ , adopted from Dr Muzammil Ali at the University of Leeds. The maximum diffusion coefficient in both cases are close to each other and the minimum is highly

distinct. Figure 5-34 and Figure 5-35 plots the temperature and mass profiles of a droplet drying using the two diffusion coefficients. The diffusivities in both cases are not much different in the early drying stage. At  $t = 100\text{ s}$ , the difference in diffusivities is of 9 order of magnitude, which suggests the early skin formation in the case of  $D_{ws\_1}$  (Price *et al.*, 2016) model (Figure 5-33). The size of the primary vortex is smaller using the diffusivities from Price *et al.* (2016). Moreover, the diffusion coefficient has shown to be a critical variable as it also depicts the time when the sucrose starts to accumulate at the separation point. This can be seen in Figure 5-33 at  $t = 1\text{ s}$ . However, this does not reflect how much water is evaporated through the droplet surface. In Figure 5-34, the droplet with  $D_{ws\_1}$  model continues to lose mass gradually (Figure 5-34-dotted red lines), while the  $D_{ws\_2}$  model has a similar trend but levels out after 200 seconds. The  $D_{ws\_2}$  correlation produces a much better temperature profile against experimental data. The slight wet-bulb period is also anticipated (black line in Figure 5-35) followed by an accurate computed temperature including the transition period where the slope slows down and the droplet reaches the air temperature. In conclusion, the diffusivity correlation is crucial to the success of the drying model as it affects heavily the internal flow field and the local evaporation rate. It also drives the drying rate of the droplet which has been proved by a significant difference in the temperature and mass profiles of the discussed two case scenarios.



**Figure 5-33.** Comparison plot between two diffusion coefficients.

$D_{ws\_1}$ : Price *et al.* (2016) diffusivities

$D_{ws\_2}$ : internally-developed diffusivities

Max and Min points: diffusion coefficients ( $m^2/s$ ).

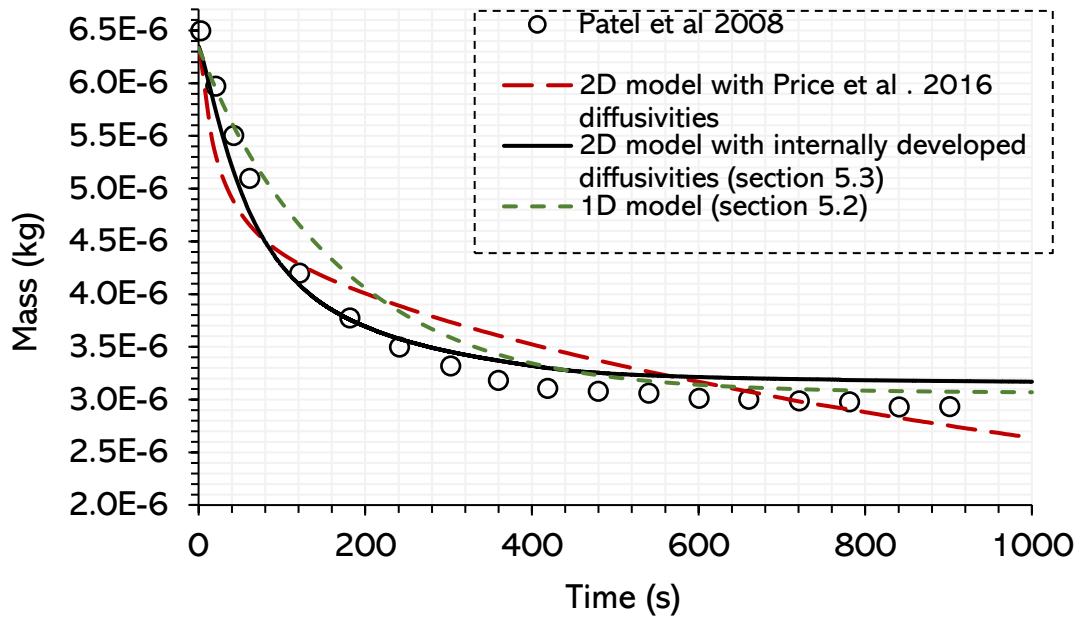


**Figure 5-34.** Mass profile of a  $2179 \text{ um} - 1.5 \text{ kg/kg} - db$  droplet with different diffusivity models. The air temperature is set at  $95^\circ\text{C}$  and the drying time is 1000 s. The mass of the droplet from using the Price *et al.* (2016) diffusivity is compared with the results in section 5.3.2.

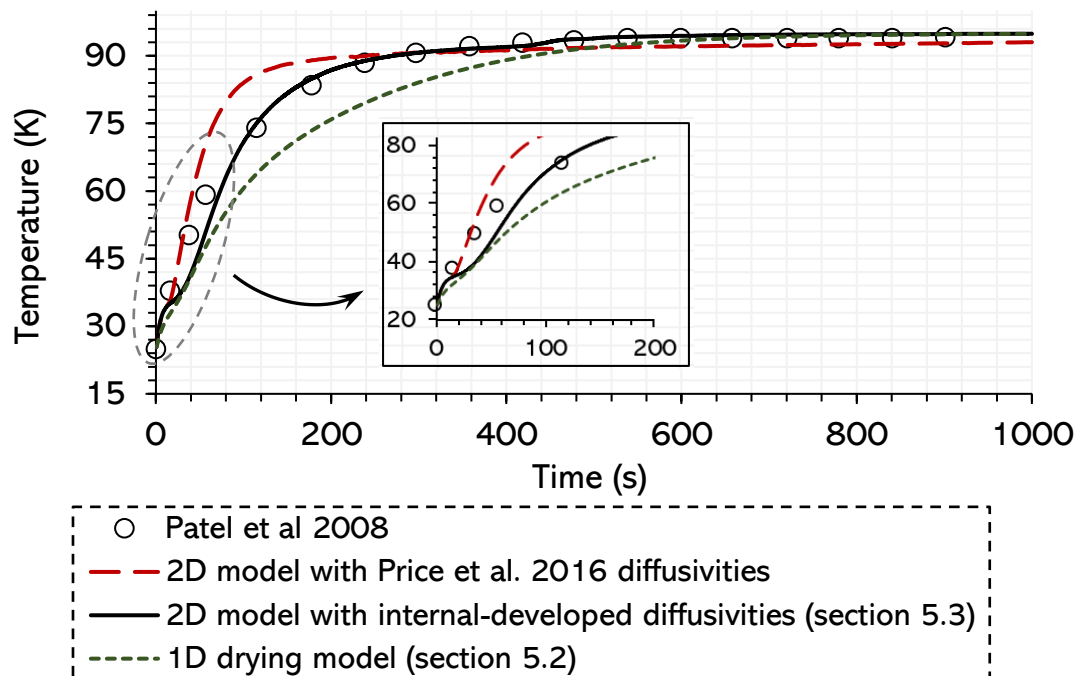


**Figure 5-35.** Mass profile of a  $2179 \text{ um} - 1.5 \text{ kg/kg} - db$  droplet with different diffusivity models. The air temperature is set  $95^\circ\text{C}$  and the drying time is 1000 s. The droplet temperature from using the Price *et al.* (2016) diffusivity is compared with the results in section 5.3.2.

## **5.4. Simulation of a true-sized droplet drying within a spray dryer**

The numerical probing into the modelling of sucrose droplet drying in a 2D axis-symmetrical system has proven the applicability of the chosen method in coupling and solving a set of governing equations of different physics. Therefore, the developed model can provide critical information on the drying of a micron-sized droplet within a spray dryer, which is inaccessible with the current SDD technique. The simulation environment is kept identical to the previous cases with the droplet scaled down to microns size. The control variable for the PID algorithm is now the inlet velocity to represent the real falling terminal velocity, hence the gravity is set back to a constant of  $9.81 \text{ m/s}^2$ .

### **5.4.1. Problem formulation**

A droplet of  $50 \mu\text{m}$  in radius is drying and falling against the upcoming hot air in this simulation system. The coordinate is 2-dimensional axis-symmetrical and the schematic of the simulation is shown in Figure 5-36.

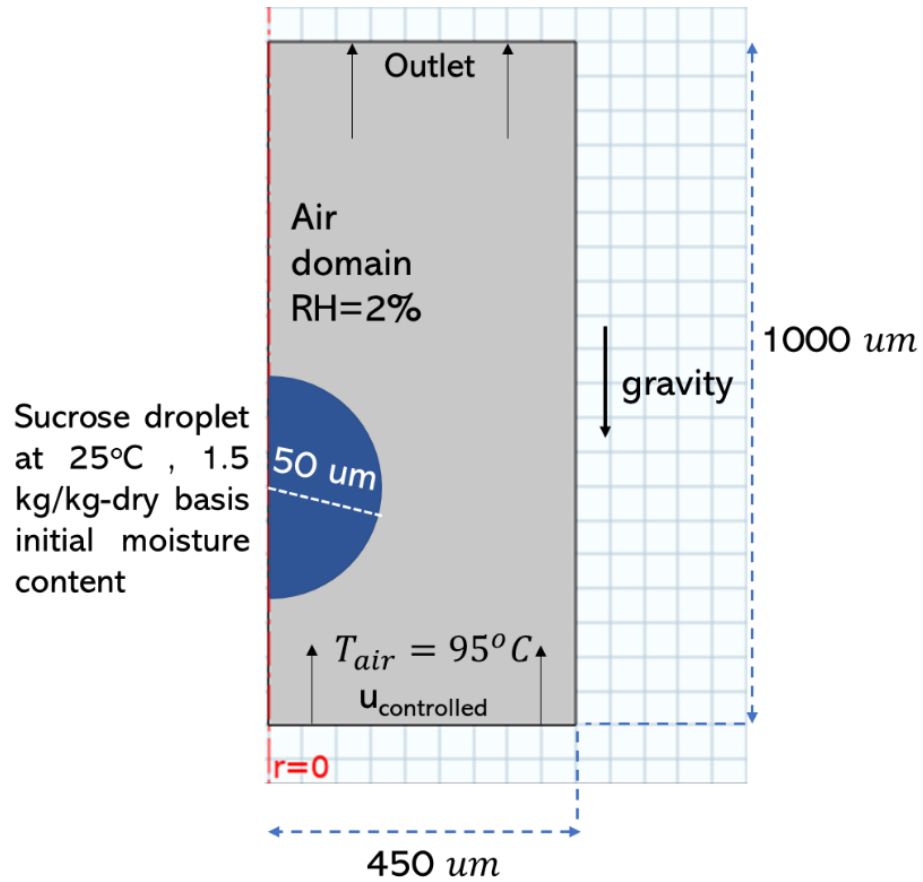


**Figure 5-36.** Schematic of a falling 50  $\mu\text{m}$  droplet at  $25^\circ\text{C}$ , 1.5 kg/kg initial moisture content. The air temperature is at  $95^\circ\text{C}$  and the relative humidity is 2.5%. The terminal falling velocity of the droplet is controlled by the PID algorithm developed in Chapter 3. The domain is 450  $\mu\text{m}$  in width and 1000  $\mu\text{m}$  in height. 'Slip' condition at the side wall.

#### 5.4.2. Results and discussions

Figure 5-37 is a combined plot of the temperature and mass profiles of the droplet over time. The droplet reaches air temperature after 5 seconds. The wet-bulb temperature period is, in this case, at  $35^\circ\text{C}$ . Figure 5-38 is a surface plot of a moisture content during drying. The velocity field settles quickly within a 50  $\mu\text{m}$  droplet. The two vortex appeared early and stay constant until the end of drying. The primary vortex size is more than 4 times the secondary vortex. The droplet shrinks 33% from 50  $\mu\text{m}$  down to 38.5  $\mu\text{m}$ . The shell forms

at the lower half of the interface is markedly thin which is around  $1 \mu\text{m}$  (Figure 5-39). A similar pattern of shell formation to the previous case was observed. The sucrose shell also grows from the separation and surrounds the water-rich region.

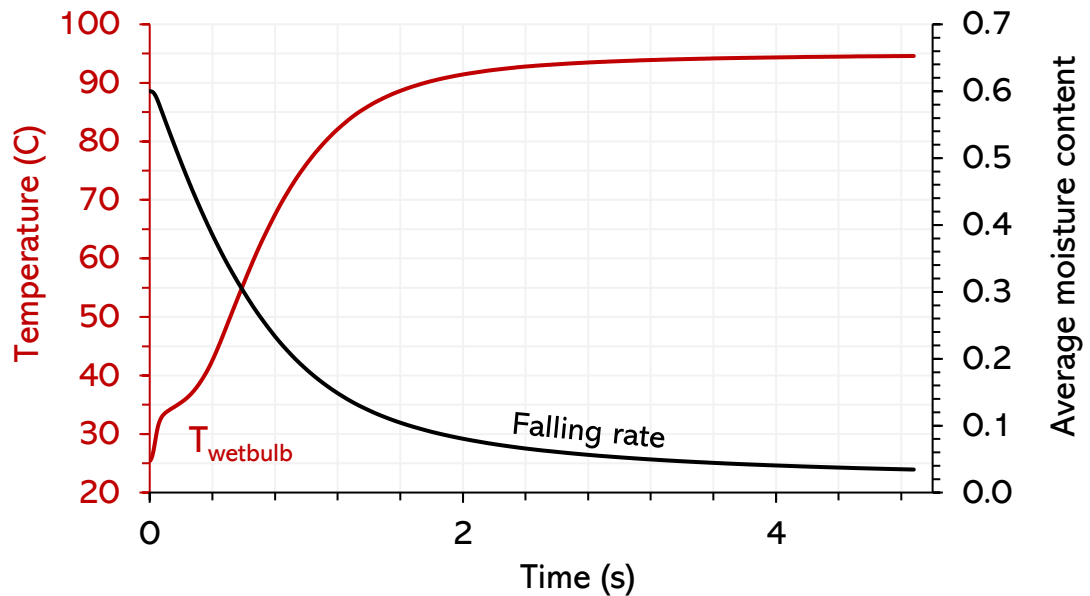


**Figure 5-37.** Droplet temperature (in black) and mass (in red) against time. The drying time is around 5s. The computed temperature is taken at the centre of the droplet and the moisture content is averaged over the droplet domain.

Overall, the droplet temperature reaches the air temperature in 3 seconds and the moisture content decreases from 0.6 to 0.03. The constant rate drying period is shown to be from  $t = 0 \text{ s}$  to  $t = 1.2 \text{ s}$ , followed by the falling rate period until the end of drying. The droplet temperature shows a wet-bulb at around  $35^\circ\text{C}$  which was less clear to observed in the case of  $2179 \mu\text{m}$  droplet (refer to section 5.3). This can be explained by the significantly smaller size of the droplet ( $50 \mu\text{m}$  compared to  $2179 \mu\text{m}$ ). The evaporative cooling by evaporation equals the heat transfer from the air stream to the droplet leading to the wet-bulb temperature in Figure 5-37. As shown in Figure 5-38, the sucrose content starts to accumulate at the droplet surface at  $t = 0.3\text{s}$  with most of the moisture content

concentrated at the droplet core. As the moisture content decreases further until 1s, the variation in sucrose concentration disappears which indicates the start of the falling rate period. The internal flow pattern (shown in Figure 5-38) also consists of two vortices: primary (lower) and secondary (upper) vortex, which is similar to the result in section 5.3. The two vortices start to develop and are fully established at  $t = 2$  s. The size of the secondary vortex nearly equals the primary vortex. This is due to the separation point is located near the middle point on the droplet surface. Besides, the vortices are still formed with a similar pattern observed in Figure 5-29, and situated adjacent to the droplet interface. The fact that the relative size between the two vortices changes with the droplet size can be highly useful to predict the distribution of mass within the dried-particle. Following the analysis in this Chapter 5, the large sucrose droplet with low initial moisture content is predicted to have an uneven distribution of sucrose at the end of the drying stage, whereas the small sucrose droplet at the same initial condition would produce an even spherical dried-particle. Additionally, as the moisture-rich region is predicted to be located near the interface, the size of the hollow region inside the dried-particle will, theoretically, have the same size as the primary vortex.

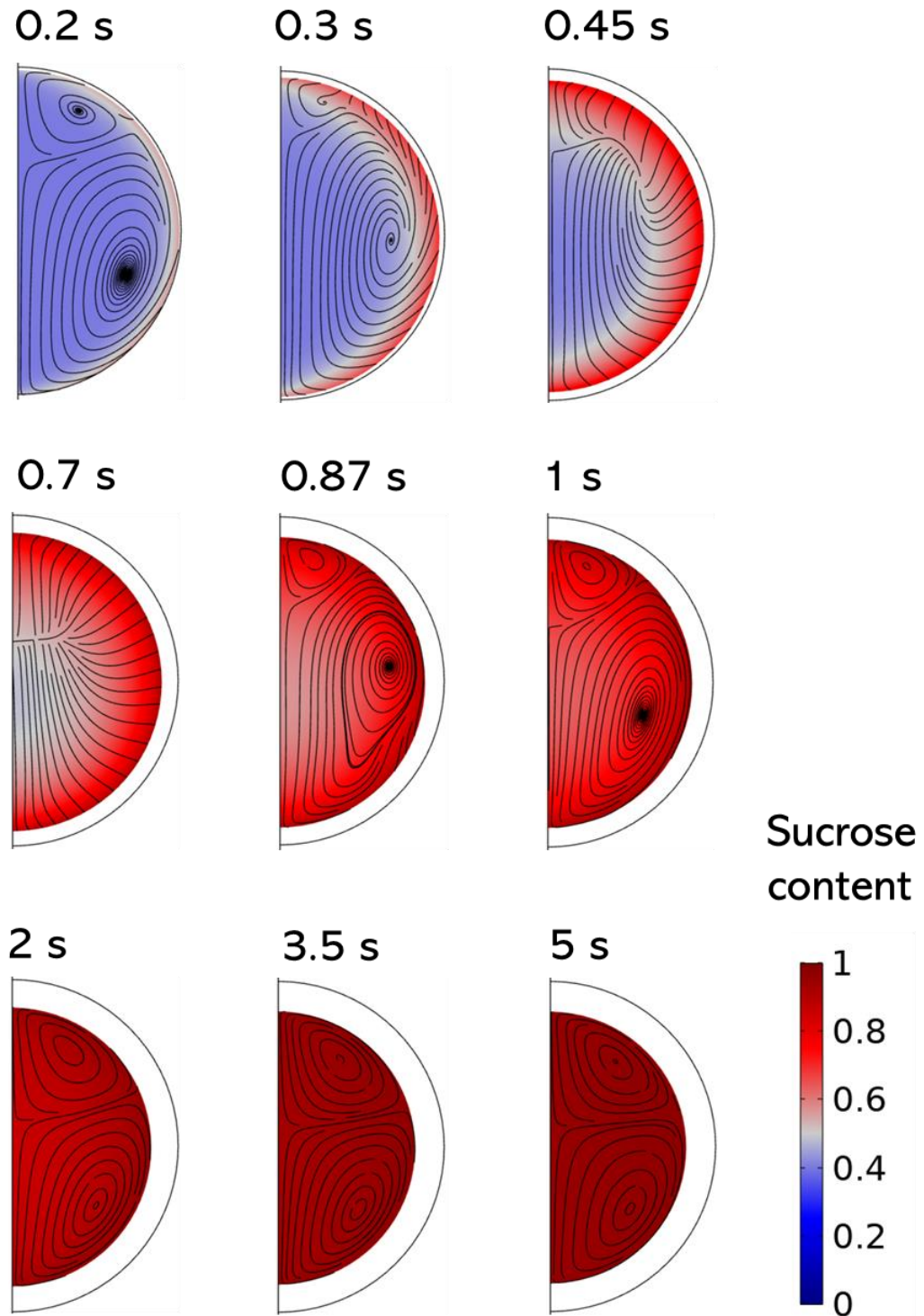


**Figure 5-38.** Surface plot of sucrose content within a 50  $\mu\text{m}$  droplet falling in air with initial temperature and moisture content to be 25.33°C and 1.5 kg/kg. The air temperature is 95°C. The sucrose content plot is colour-coded and the streamline (black lines) is plotted for the velocity field within the droplet.

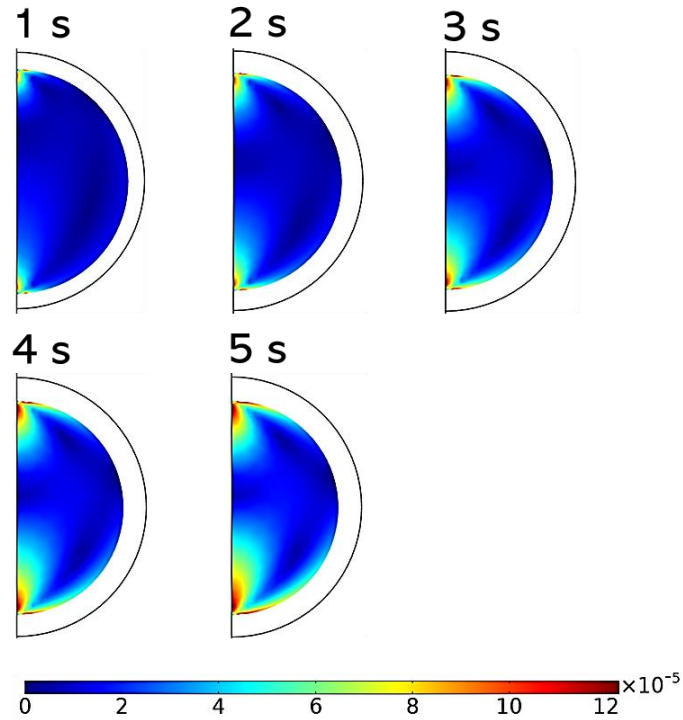


**Figure 5-39.** Velocity profile within 50  $\mu\text{m}$  droplet falling in air with initial temperature and moisture content to be 25.33°C and 1.5 kg/kg. The air temperature is 95°C. The velocity plot is colour-coded. The maximum velocity is  $1.2e^{-4}\text{m/s}$ .

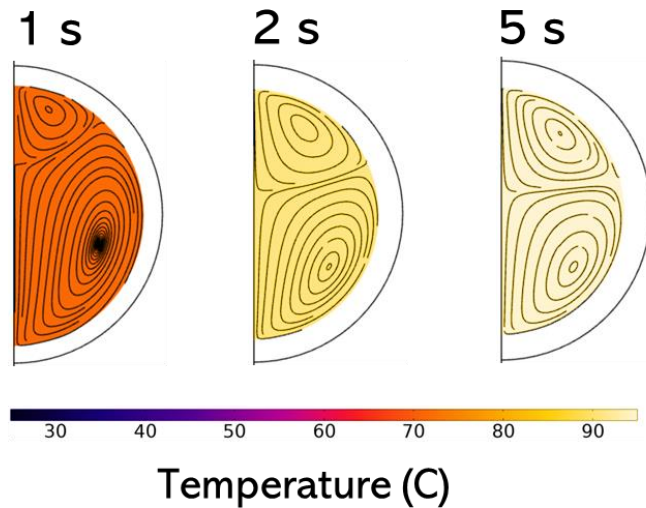


**Figure 5-40.** Temperature distribution within a 50  $\mu\text{m}$  droplet falling in air with initial temperature and moisture content to be 25.33°C and 1.5 kg/kg. The air temperature is 95°C. The temperature surface plot is colour-coded and the streamline (black lines) is plotted for the velocity field within the droplet.

The temperature field is uniform within the droplet, as shown in Figure 5-40. The even temperature distribution can be explained by the small size ( $50 \mu\text{m}$  in radius) and a low initial moisture content droplet ( $1.5 \text{ kg/kg}$ ). Therefore, the assumption of uniform temperature within the droplet in the 1D model is valid in this case as the internal flow and different heat and mass transfer on the droplet surface do not have any effect on the global drying. The terminal falling velocity of the droplet is shown in Figure 5-41. The PID has a good adjustment against the shrinkage of a droplet. As the shell is formed, the boundary condition at the interface might shift to the no-slip condition instead of the normal surface tension. The internal flow field hence will be affected. The surface velocity of a  $50 \mu\text{m}$  is at the same order of magnitude comparing to the previous case of  $2179 \mu\text{m}$  droplet.

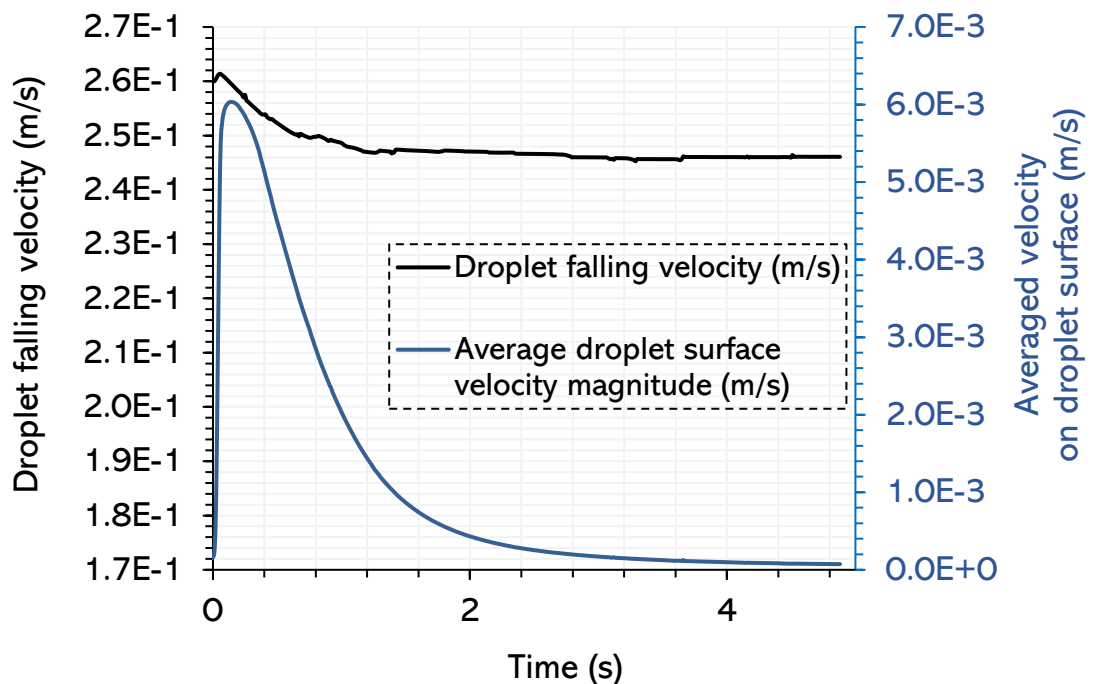


**Figure 5-41.** Terminal falling velocity (black line) and averaged surface velocity (blue line) of a  $50 \mu\text{m}$  droplet falling in air with initial temperature and moisture content of  $25.33^\circ\text{C}$  and  $1.5 \text{ kg/kg}$ . The air temperature is at  $95^\circ\text{C}$ . The droplet falling velocity is controlled by the PID algorithm developed in Chapter 3.

As the system involves Multiphysics which is highly coupled during the simulation, the initial condition, the mesh configurations and the solver settings are important in achieving the solution convergence. The next section will discuss these features in detail and suggestions for a more efficient simulation, in terms of computational efforts and accuracy.

## **5.5. Important simulation aspects to achieve solution convergence and optimise efficiency**

### **5.5.1. Mesh structure**

During the simulation work in this chapter, it has been noticed that the solution convergence/divergence is extremely sensitive to the mesh structure. A slight change in the number of nodes on the droplet surface, from 30 nodes to 20 nodes, for example, will completely diverge the simulation. It is also very hard for the quadrilateral structure to run smoothly without tolerance error comparing to a triangular structure. However, the quad mesh can produce a high-resolution concentration field within the droplet with the same coarseness as the triangular mesh. The boundary layers are normally added in all the fluid dynamics problem with moving interface, to save unnecessary computational effort in the tangential direction and resolve more details in a normal direction. It might be true if the system involved a well-structured geometry with defined corners and edges, but it is not the case for the droplet with curved geometry. The droplet has a circular shape interface and together with complex dynamics of the flow, the solution in the tangential direction is as important as the normal direction at the interface. Therefore, the purpose of adding the boundary layers is to have a structured Jacobian matrix to avoid skewness. The schematic is shown in Figure 5-42.

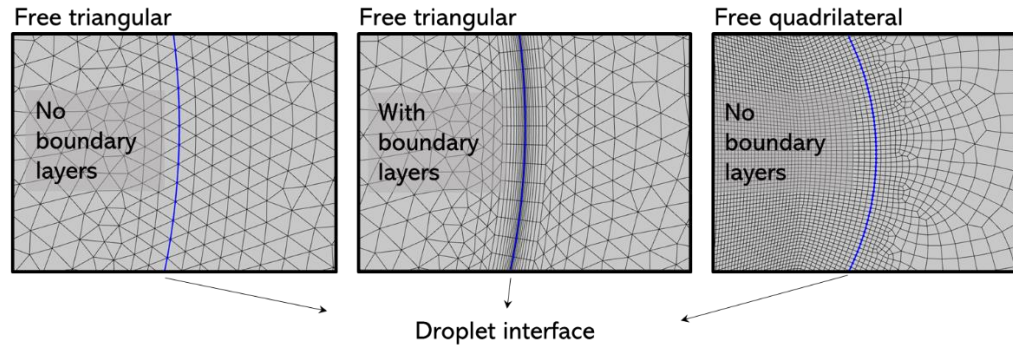


**Figure 5-42.** Different mesh structure with/without boundary layers.

The quad mesh is able to obtain the same effect as the triangular mesh with boundary layers since the boundary layer mesh is indeed a quadrilateral structure. However, in order to achieve such refinement, the number of elements required in the quad-mesh is a lot higher. The free-triangular mesh with boundary layers is suggested as it is much more computationally efficient.

### 5.5.2. Element Peclet and Reynolds numbers

For convection-dominant physics, the discretisation process becomes a problem. A steep gradient anywhere in the control domain can introduce numerical instabilities, for example, a Dirichlet boundary condition that is initially too far-off from equilibrium or changing over time, or an initial condition that is a function of position. This instability is seen as an oscillation in computed solutions which can lead to divergence. The cell *Peclet* and *Reynolds* number are defined as the ratios, within the mesh cell, of the *convective flux* to the *diffusive flux*, and the *inertia* to the *viscosity* effects respectively,

$$Pe_{element} = \frac{h|v|}{D} \quad (5-49)$$

$$Re_{element} = \frac{h\rho|v|}{\mu} \quad (5-50)$$

Where  $v$  is the convective velocity in the cell,  $\rho$  is the liquid density,  $\mu$  is the dynamic viscosity and  $h$  is the element size. According to

Huyakorn (1977) and Quarteroni and Alberto Valli (1988), the numerical instability has resulted as the cell Peclet number exceeds 2. This is likely to happen in the current drying system as the convection effect dominates the droplet interior.

If we consider briefly the previous droplet drying problem in which the convective velocity within the droplet is around  $10e^{-4} m/s$  and the diffusivity of water in sucrose solution is assumed to be around  $1e^{-10} m^2/s$ . This requires the mesh size to be less than  $2e^{-7} m$  at most, or in other words, a droplet interface length of  $3500 \mu m$  would ask for at least 17,500 surface nodes to reach numerical stabilities. The current simulation system used 40 nodes on the droplet surface as a 'fine mesh' option and the computational time takes 44 hours on the 8-core 5Ghz Xeon-chip computer. The infeasible number of mesh elements (17,500 nodes) can be resolved by several stabilisation techniques invented within the computational fluid dynamics community. In order to maintain the numerical stability within each element, a pseudo diffusivity is added to increase the denominator value in equation (5-49). This artificial diffusion coefficient,  $D_{artificial}$ , reads,

$$D_{artificial} = \delta h|v|$$

$$D_{total} = D + D_{artificial} \quad (5-51)$$

Where  $\delta$  is the tuning parameter that can be adjusted accordingly. It is obvious that adding an extra diffusivity without compensating any other variables will affect the accuracy of the result, as it is not a 'true' diffusivity. Equation (5-51) conveniently set the artificial diffusivity as a function of mesh size, hence the refined mesh will have a very small  $D_{artificial}$ . An optimal tuning parameter is used so the solution is still accurate while demanding a sensible computational effort. The weakness of the artificial diffusion was improved by adding it to a certain direction of flow only, for

example, streamline or crosswind directions. Generally, *streamline stabilisation* helps to 'damp' out the oscillation and the *crosswind stabilisation* reduces the under and overshoots in solution. The constraint of the Peclet number, however, gives us an idea and a condition to initiate a guess on the initial mesh size. The utilisation of this stabilisation technique was evident in the simulation in Chapter 5, section 5.3. The solution convergence was impossible to achieve without the stabilisation turned on.

### **5.5.3. Variables scaling**

The variable scaling is a necessary process in the finite element method, especially in coupling multi-physics. The Jacobian matrix, which is the final matrix that the code collects all the coefficients and variables into, is well behaved if the matrix value is standardised or close to 1. Different physics will have different value scale, for example at normal condition, a room temperature of 298 K, a pressure of  $1e^5 Pa$  and a droplet of  $50e^{-6} \mu m$  will be later put into one matrix which will create numerical underflow or overflow (too many digits). Therefore, scaling is the process of tuning all the values within the matrix down to unity. In many commercial or open-source software, this scaling is often automatically done by algorithms, but sometimes it does not always anticipate the physics properly. The droplet might shrink significantly or the number of moles of vapour within the droplet might increase by a thousand-fold. We need to inspect the physics carefully and manually scale all the variables. The scaling value is normally the value we expect that variable to reach. If the scaling value is chosen properly, the solution divergence is eliminated and even achieves a faster convergence rate. The idea is very similar to the non-dimensional equation. Sometimes, instead of calculating the values with tens of digits, an equation with an equivalent dimensionless variable can be easier to deal with and to code. The scaling variable was also crucial in the model in Chapter 5, section 5.3. The automatic algorithm predicted

a wrong scaling of the temperature leading to divergence. The solution convergence was reached by using the air temperature value in the scaling option. In addition, the bubble growth modelling also requires a manual scaling of the interface displacement as this will vary rapidly during a simulation.

#### **5.5.4. Time step of the solver**

The time step is the final important factor to consider. As the system is highly dynamic, the solution gradients, such as temperature, concentration, velocity field,..etc, are possibly very steep across the interfaces in the simulation domain. This can diverge easily if the time step is too large, especially in the early time when all the fluxes and flows are introduced into the domain. A step function is a powerful tool to 'relax' this steep gradient to below the relative tolerance so the error is not signified.

#### **5.5.5. 'Smooth function' for numerical stability**

Initially, at  $t = 0 \text{ ms}$ , the large difference between the droplet and air temperature will cause a large heat transfer across the droplet's interface, which will cause the solution to diverge. This is because the temperature gradient has not developed yet in the domain when the significant heat exchanges at the interface happen at  $t = 0 \text{ ms}$ . In order to reduce this numerical instability, the initial domain temperature is set to the initial droplet's temperature, and hot air is gradually introduced into the domain as the droplet falls. Moreover, other parameters, such as gravitational constant, inlet airflow, evaporation rate and evaporative cooling rate, were also ramped up steadily over time using the 'Smooth', or the 'Step' function (refer to Figure 5-43) to remove the abrupt changes across the boundaries within the system. The relaxation time allowing all variables to reach their true value is set to be  $150 \text{ ms}$ . The example equation of integrating the 'Smooth' function into the simulation is shown in equation (5-52).

$$T_{air}|_{t=0} = T_{droplet}|_{t=0} * f_{smooth} \left( \frac{t}{150[ms]} \right) \quad (5-52)$$

Where  $T_{air}|_{t=0}$  is the air temperature set at  $t = 0 \text{ ms}$ ,  $T_{droplet}|_{t=0}$  is the droplet initial temperature and  $f_{smooth} \left( \frac{t}{150[ms]} \right)$  is the 'smooth' function (as shown in Figure 5-43). As the simulation time,  $t$ , approaching  $150 \text{ ms}$ , the value of  $\left( \frac{t}{150[ms]} \right)$  will increase smoothly from 0 to 1 which means the  $T_{air}$  will also increase from the droplet temperature to the air temperature in  $150 \text{ ms}$ . It should be noted that in the relaxation period of  $150 \text{ ms}$ , there is evaporation, or heat and transfer happened within the domain.

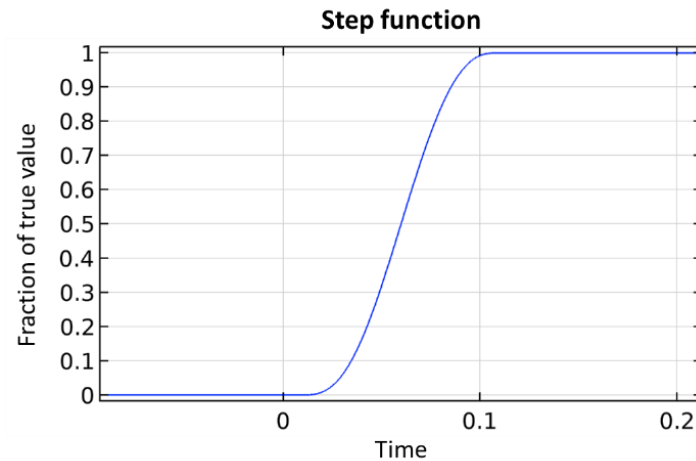


**Figure 5-43.** Plot of the 'Smooth' function used to decrease the high gradient changes across the interface in the simulation initially. All the initially variables are ramped up smoothly using this function in a period of **150 ms**, instead of setting the initial value at  $t = 0 \text{ ms}$ .

## 5.6. Conclusions

The study in Chapter 5 confirms the necessity of a 2-dimensional/3-dimensional model for predicting the final morphologies outcomes of a dried-particle. It emphasises the lack of information on the local variables, which is important, in the 1-dimensional model. The shape of the shell layer depends heavily on the asymmetrical flow field within the droplet. The diffusivity model also affects the global drying rate and the size of the internal vortices. Now the region where the bubble nucleates and the shell thickness can be defined computationally with the developed 2-dimensional drying model. Currently, the simulation of drying within the spray dryer relies on the kinetic data from the SDD experiment. The current SDD technique cannot produce a droplet at microns size hence limits the type of kinetic data available. The 2-dimensional axis-symmetrical drying model was extended, after validation, to a small droplet that is similar in size to the droplets in the spray dryer. This will contribute to the advanced analysis on a smaller scaled droplet drying system. The current CFD model can be developed further to include a more complex multiphysics and a more variety of solution types. The developed PID algorithm describes accurately the falling of a drying droplet which removed the defect of sphericity if hung on a filament, and the terminal velocity problems in the conventional method of SDD technique. Finally, the aim of improving and advancing the models in the literature to closely match the real physics that happen in the spray dryer was accomplished reasonably. The boiling phenomenon will be considered in the next chapter with the focus being on the dynamics of the bubble expansion.

# Chapter 6

## Numerical probing of boiling droplet

This chapter investigates the boiling phenomena within the drying droplet. A single bubble will be integrated into the droplet domain and coupled with the 2-dimensional droplet drying model developed in Chapter 5. The bubble is located at the droplet centre in the initial study (section 6.2), and then off-set from the centre in the following section (section 6.3). The goal is to develop a boiling model, in which the growth and collapse of the bubble are governed by both the inertia (fluid flow) and the thermal (heat transfer) effects within the droplet. The outcome of this numerical probing is the insight into the influence of the bubble dynamics on the global drying rate, the internal droplet velocity, moisture content, and temperature fields. The bubble *nucleation* phenomenon is not considered in this model, hence the model is separated into two stages. In the **1<sup>st</sup> stage - Drying** (the droplet temperature is below the boiling point), the droplet dries without the presence of the bubble from the room temperature. In the **2<sup>nd</sup> stage - Boiling** (the droplet temperature reaches the boiling point), the droplet reaches the boiling point and continues to dry with the bubble domain being added internally. The bubble is sensitive to the conditions at boiling, such as the droplet temperature field or the internal moisture content.

## 6.1. Discussion on the numerical stability and the time-stepping scheme for a bubble-droplet system

Before the boiling model is described, critical features of the simulation and its solvers, such as the solver time step, tolerance error or surface mesh nodes in the bubble-droplet system, need to be reviewed. This is due to the difference in the simulation configurations used in Chapter 4 and Chapter 5. The simulation for the phase change problem in Chapter 4 has a tighter relative tolerance and requires more mesh elements, meanwhile, the configuration in Chapter 5 has a coarser mesh and larger time step. This section discusses the suitable time step for the solver to take when the bubble is integrated into the droplet drying model. The maximum time step required for the bubble simulation (refer to Chapter 4) is noticeably smaller than that of the droplet drying case (refer to Chapter 5), which raises the question of what is the most suitable initial time step, and how to guess it when the bubble is introduced into the system. First, we need to visit the theory behind the time-stepping scheme for the numerical solvers. In general, the algorithm for choosing a suited timestep, when solving a PDEs, to achieve a solution convergence can be referred to as the well known *Courant-Friedrichs-Lewy*, (*CFL*) *convergence condition*,

$$\left( CFL = \frac{u\Delta t}{h} \right) \leq (C_{\max} = 1) \quad (6-1)$$

Where  $u$  is the advection velocity of the information 'parcel',  $h$  is the element size and  $\Delta t$  is the timestep chosen.

The formal definition from Laney (1998) in the 'Computational Gas dynamics' book states '*the full numerical domain of dependence must contain the physical domain of dependence*'. The idea behind this is to have a time step so that the information 'parcel' will only

travel to the neighboring element. Considering a 1D domain which is discretised as in Figure 6-1.

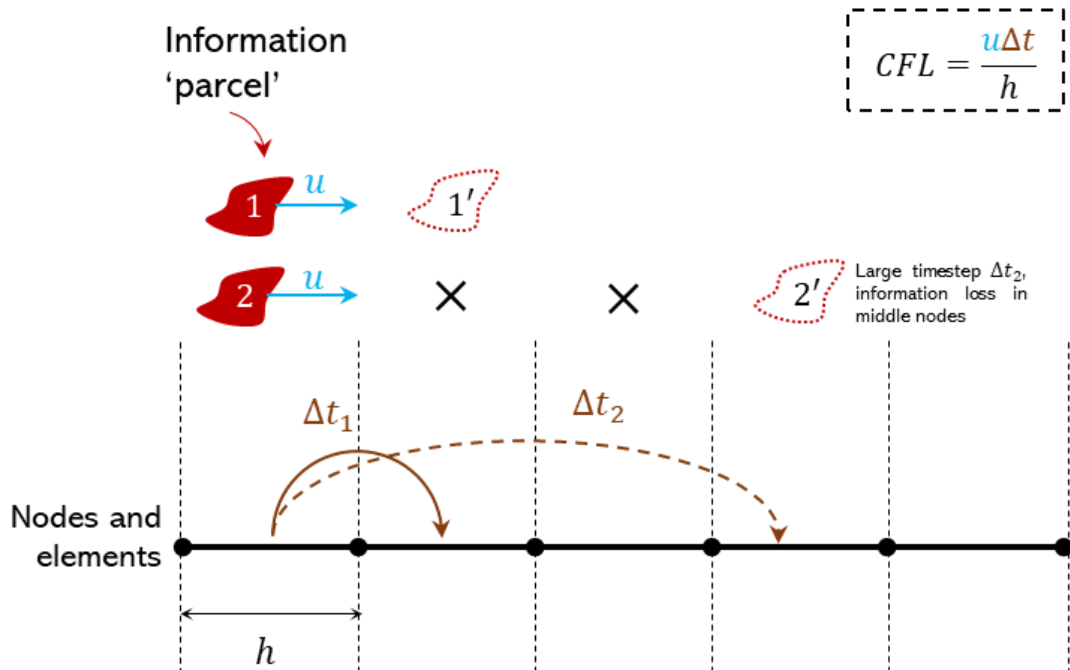


**Figure 6-1.** CFL condition visualisation. The cases of comparison are  $CFL < 1$  and  $CFL > 1$ .

In the bubble-droplet system, the 'bottleneck' area for the timestep should be the phase interface and the droplet interior, which carries critical information affecting the drying rate. In the case of a single droplet drying, the timestep can be adaptive to the shrinking rate of the droplet and also to the changing internal advection/diffusion velocities. In Chapter 3 and Chapter 5, the timestep was relatively large of around 3 ms to 5 ms as the drying starts, and reduced down to the smallest of  $1e^{-3}$  ms. As the bubble is integrated into the liquid domain such as the droplet, the time-stepping scheme should be constrained by how fast the bubble grows. The time step decreases to the smallest of  $1e^{-9}$  ms and the largest timestep was around  $1e^{-4}$  ms depending on the initial bubble size. If we force the solver to choose a fixed timestep that is too large, the solution diverges immediately at the initial step. Besides, the bubble size determines the number of nodes needed to represent the surface curvature, in

which the CFL number is also influenced. If the ratio between the bubble and the droplet radii is too small, the timestep can be constrained to be extremely small to resolve the bubble interface, that it becomes impractical to solve for the physics in the droplet and the air. For example, a  $100\ \mu\text{m}$  droplet requires around 40 nodes on the surface while a  $5\ \mu\text{m}$  bubble requires 80 nodes to have an acceptable level of mesh refinement (Figure 6-2). This results in an element size at the droplet and the bubble surfaces equal  $2\ \mu\text{m}$  and  $0.1\ \mu\text{m}$ , respectively.

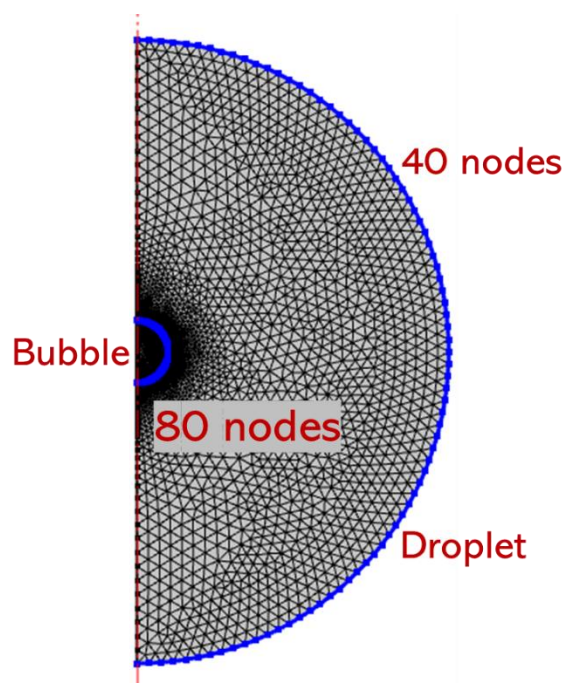


**Figure 6-2.** Number of nodes required at the interface to have a good representation of the surface curvature.

If the bubble grows 5 times faster than the droplet shrinkage rate, the largest timestep in the case of the bubble-droplet is 100 times smaller than that of the droplet only case. These examples had not taken into account the convective velocity induced to the bubble from the droplet which also increases the variable  $u$  in equation (6-1). It is possible to relate the number of mesh nodes on the bubble interface to the element size, and given an analytical solution of the velocity of the interface, we can guess the initial bubble size

according to the droplet size so that the convergence is achieved without using devoting large computational effort at first.

## **6.2. Drying droplet with a centred-bubble at boiling point in a 2D axis-symmetrical coordinate**

There are plenty of literature studies on the bubble growth within a confined-layer of liquid (Araia and Doi, 2012) (Navon, Chekhmir and Lyakhovsky, 1998) (Gaudron, Warnez and Johnsen, 2015) (Yang and Church, 2005) (Solano-Altamirano, Malcolm and Goldman, 2015). The most relative work to this study comes from Hecht and King (2000a), who looked at the bubble growth within a drying droplet system. However, no currently published models can couple the Navier-Stokes equation with the heat transfer equation to describe the bubble kinetics. Therefore, the investigation in this section aims to resolve the discussed problem using FEM, hence achieving the full implementation of the bubble dynamics onto the drying droplet. Firstly, a system of the centralised-bubble within a droplet is considered. The heat and mass transfer coefficients at the droplet surface are estimated and evaluated using dimensionless numbers. Hence, the heat and mass transfer coefficients on the droplet surface do not vary spatially, and the bubble expansion is expected to be radially symmetrical. This starting system reduced the need of resolving the fluid flow equation in the air, since the bubble is the main focus. The outcome of this study provides a preliminary simulation framework of the bubble-droplet system and how droplet drying is affected by bubble growth.

### **6.2.1. Governing equations**

The governing equations in this section are similar to Chapter 5 and will be summarised in the following.

### 6.2.1.1. Fluid flow

All the governing equations are presented here. Please refer to Chapter 5 for further detailed descriptions of each equation.

#### 6.2.1.1.1. Liquid phase

$$\frac{\partial \rho_l}{\partial t} + \nabla \cdot (\rho_l \mathbf{u}_l) = 0 \quad (6-2)$$

$$\rho_l \frac{\partial \mathbf{u}_l}{\partial t} + \rho_l (\mathbf{u}_l \cdot \nabla) \mathbf{u}_l = \nabla \cdot [-p_l \mathbf{I} + \boldsymbol{\tau}_l] + \mathbf{F}_l \quad (6-3)$$

$$\boldsymbol{\tau}_l = \mu_l (\nabla \mathbf{u}_l + (\nabla \mathbf{u}_l)^T) - \frac{2}{3} \mu_l (\nabla \cdot \mathbf{u}_l) \mathbf{I} \quad (6-4)$$

#### 6.2.1.1.2. Gas phase

$$\frac{\partial \rho_g}{\partial t} + \nabla \cdot (\rho_g \mathbf{u}_g) = 0 \quad (6-5)$$

$$\rho_g \frac{\partial \mathbf{u}_g}{\partial t} + \rho_g (\mathbf{u}_g \cdot \nabla) \mathbf{u}_g = \nabla \cdot [-p_g \mathbf{I} + \boldsymbol{\tau}_g] + \mathbf{F}_g \quad (6-6)$$

$$\boldsymbol{\tau}_g = \mu_g (\nabla \mathbf{u}_g + (\nabla \mathbf{u}_g)^T) - \frac{2}{3} \mu_g (\nabla \cdot \mathbf{u}_g) \mathbf{I} \quad (6-7)$$

#### 6.2.1.1.3. Species transport

$$\rho \frac{\partial}{\partial t} (\omega_{wa}) + \rho (\mathbf{u} \cdot \nabla) \omega_{wa} = -\nabla \cdot \mathbf{j}_{wa} \quad (6-8)$$

$$\rho \frac{\partial}{\partial t} (\omega_{su}) + \rho (\mathbf{u} \cdot \nabla) \omega_{su} = -\nabla \cdot \mathbf{j}_{su} \quad (6-9)$$

The diffusion model used in this study is the mixture-averaged model (refer to Chapter 5). The diffusion coefficient of sucrose and water in an aqueous sucrose solution is the internal-developed correlation from Dr. Muzammil.

$$D_{ws} = D_{co} (1 - \alpha \phi_s) e^{-2060 \left( \frac{1}{T_{drop}} - \frac{1}{298} \right)} \quad (6-10)$$

### 6.2.1.2. Heat transfer

The heat transfer within the droplet and bubble is as follows,

$$\begin{aligned} \rho C_p \left( \frac{\partial T}{\partial t} + \mathbf{u} \cdot \nabla T \right) + \nabla \cdot (\mathbf{q}) \\ = \alpha_p T \left( \frac{\partial p}{\partial t} + \mathbf{u} \cdot \nabla p \right) + \boldsymbol{\tau} : \nabla \mathbf{u} + Q \end{aligned} \quad (6-11)$$

### 6.2.2. Problem formulation

The system consisting of a 100  $\mu\text{m}$  droplet with a 5  $\mu\text{m}$  bubble is studied. The simulation aims to model the full drying process, starting from a droplet at room temperature, 25°C heating up to a boiling point, 100°C and finally reaches the air temperature of 140°C. However as discussed in Chapter 3, the ALE method only tracks the interface motion of an already defined-volume, so the bubble cannot be modelled to nucleate out of zero volume during drying. Hence, the bubble domain has to be added either initially or manually at the boiling point. Moreover, the bubble-droplet system also poses the problem of conditions set at boiling point. The analytical solution (refer to Chapter 3) for the temperature field surrounding the bubble might not match the actual temperature field within the droplet as it reaches 100°C, which might cause the simulation to diverge. This challenge will be reconsidered if the bubble-droplet system poorly behaves at the boiling point.

The process is divided into two stages: **stage 1** (drying) and **stage 2** (boiling). This can help to tackle the zero-volume problem. The idea is to have a droplet dries without the presence of a bubble in stage 1 until the droplet temperature reaches boiling point, and a bubble of 5  $\mu\text{m}$  is then added manually (stage 2) into the interior of the droplet as shown in Figure 6-3. The bubble will grow taking the already developed droplet temperature profile as an initial condition. Further details of the two stages are discussed in the following section.

In **stage 1**, the droplet will dry from  $25^{\circ}\text{C}$  with the same governing equations and boundary conditions used in Chapter 5- section 5.2. The timestep at which the bubble domain is added depends on the droplet temperature. Therefore, the temperature at the droplet centre is tracked, and as soon as it reaches the boiling point,  $100^{\circ}\text{C}$ , the bubble is added. The average droplet temperature at this point is shown to be higher than a boiling point by approximately  $4^{\circ}\text{C}$ , so the heat flux to the bubble interior is not zero at the beginning of stage 2.

In **stage 2**, the bubble will grow as a function of the heat flux at the interface. The vapour and heat entering the bubble are assumed to be uniformly distributed, hence no temperature or vapour concentration gradient is established within the bubble.

The external air velocity is set at  $1\text{ m/s}$ , the initial droplet moisture content is  $1.5\text{ kg/kg} - \text{db}$ . The initial droplet temperature is at  $25^{\circ}\text{C}$ , the air temperature is at  $140^{\circ}\text{C}$  with 2% relative humidity. The overall simulation schematic is illustrated in Figure 6-3.

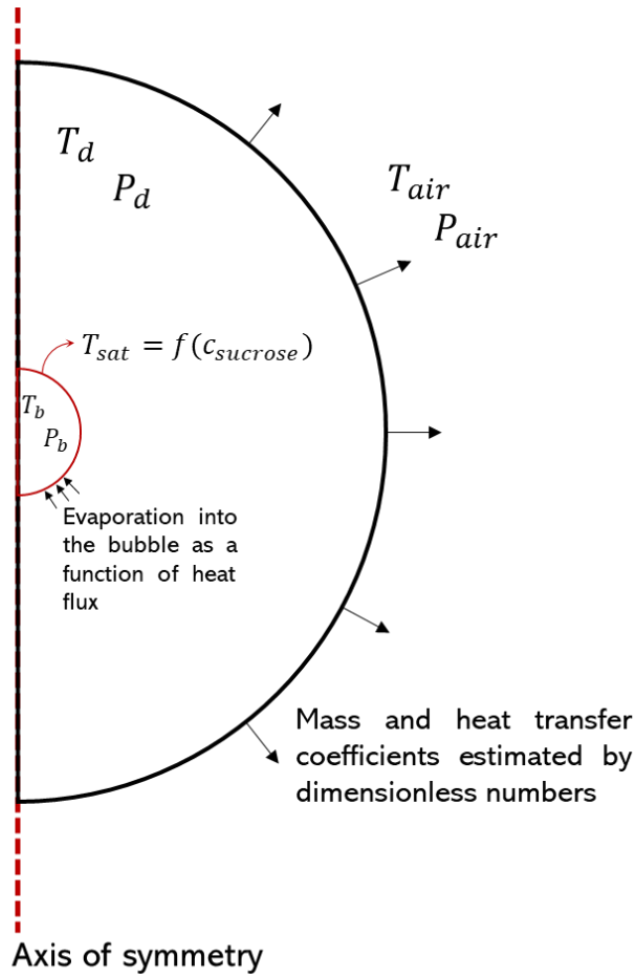


**Figure 6-3.** Schematic setup of the bubble-droplet system. The droplet and the bubble are **50  $\mu\text{m}$**  and **5  $\mu\text{m}$**  in radius, respectively. The droplet initial temperature and moisture content are 25°C and 1.5 kg/kg-db, respectively. The bubble contains air only at the boiling point ( **$t = 70 \text{ ms}$** ).

### 6.2.2.1. Boundary conditions

#### 6.2.2.1.1. Droplet

The same set of equations are solved at the droplet surface as in Chapter 5, Section 5.2.3.1 and is revisited in this section. The water activity is estimated based on the Norrish model (Patel *et al.*, 2008), and the vapour concentration at the droplet surface is,

$$a_w = x_{\text{water}} e^{-K_N(1-x_{\text{water}})^2} \quad (6-12)$$

$$K_N = 2.7$$

$$c = a_w c_{sat} \quad (6-13)$$

The saturated pressure is taken as,

$$P_{sat} = 610.7 \times 10^{7.5 \left( \frac{T-273.15}{T-35.85} \right)} \quad (6-14)$$

(Monteith and Unsworth, 2013)

$$c_{sat} = \frac{P_{sat}}{RT} \quad (6-15)$$

The gas is assumed to be ideal. The heat and mass transfer coefficients are estimated (Ranz & Marshall, 1952). The evaporation flux is a function of concentration gradient,

$$m_{evap} = k_c (c_{surface} - c_{\infty}) = k_c (act_{wa} c_{sat} - RH c_{sat}) \quad (6-16)$$

Similarly, the heat flux at the droplet surface is proportional to the temperature gradient,

$$Q = h_c (T_{surface} - T_{\infty}) - Q_{source} \quad (6-17)$$

The heat source,  $Q_{source}$ , is the evaporative cooling due to evaporation,

$$Q_{source} = m_{evap} H_{evap} \quad (6-18)$$

#### 6.2.2.1.2. Bubble

The bubble is assumed to be thermally driven. As the sucrose droplet is a multicomponent solution, the boiling point needs modification to take into account the changing solute concentration during drying. The saturation temperature,  $T_{sat}$ , constrained at the bubble surface can be calculated from the theory boiling-point elevation (Starzak and Peacock, 1998),  $\Delta T$ , which is the solution of the Clausius-Clapeyron equation with Raoul's law (Joffe, 1945) (Atkins and De Paula, 2006)

$$T_{sat} = T_{boiling} + \Delta T = 100^{\circ}C + iK_B molal_{sucrose} \quad (6-19)$$

Where  $T_{boiling}$  is the boiling temperature of pure water,  $i$  is the van 't Hoff factor which is 1 for sugar solution. The ebullioscopic constant of the solvent,  $K_B$ , can be expressed as,

$$K_B = \frac{RT_b^2 M_w}{\Delta H_{evap}} = 0.512 \text{ (for water)} \quad (6-20)$$

Where  $R$  is the gas constant,  $T_b$  is the boiling point of pure solvent (which is assumed to be 100°C for water in this study),  $M_w$  is the molar mass of water and  $\Delta H_{evap}$  is the latent heat of vapourisation. The molality of the sucrose content,  $molal_{sucrose}$ , is shown as,

$$molal_{sucrose} = \frac{n_{sucrose}}{m_{water}} \quad (6-21)$$

Where  $n_{sucrose}$  is the mol of sucrose and  $m_{water}$  is the mass of solvent which is water in this case.

#### 6.2.2.2. Material properties and initial conditions

The same material properties correlation as the droplet drying model in Chapter 5 was used. The vapour properties are not needed as no equations are solved for in the bubble and air domains. The bubble expansion is governed directly by the Dirichlet condition which is the saturation temperature, as shown in (6-19). The bubble, which is formed from the dissolved air within the droplet exiting the atomiser in the spray dryer, is assumed to initially contain air only.

#### 6.2.3. Results and discussions

In **stage 1**, the droplet dries without the presence of the bubble until it reaches the air temperature, which is at 140°C. The droplet temperature and weight profiles in **stage 1** are plotted in Figure 6-4, in order to obtain the time step at which the droplet temperature exceeds the boiling point (assumed to be 104°C in this study).

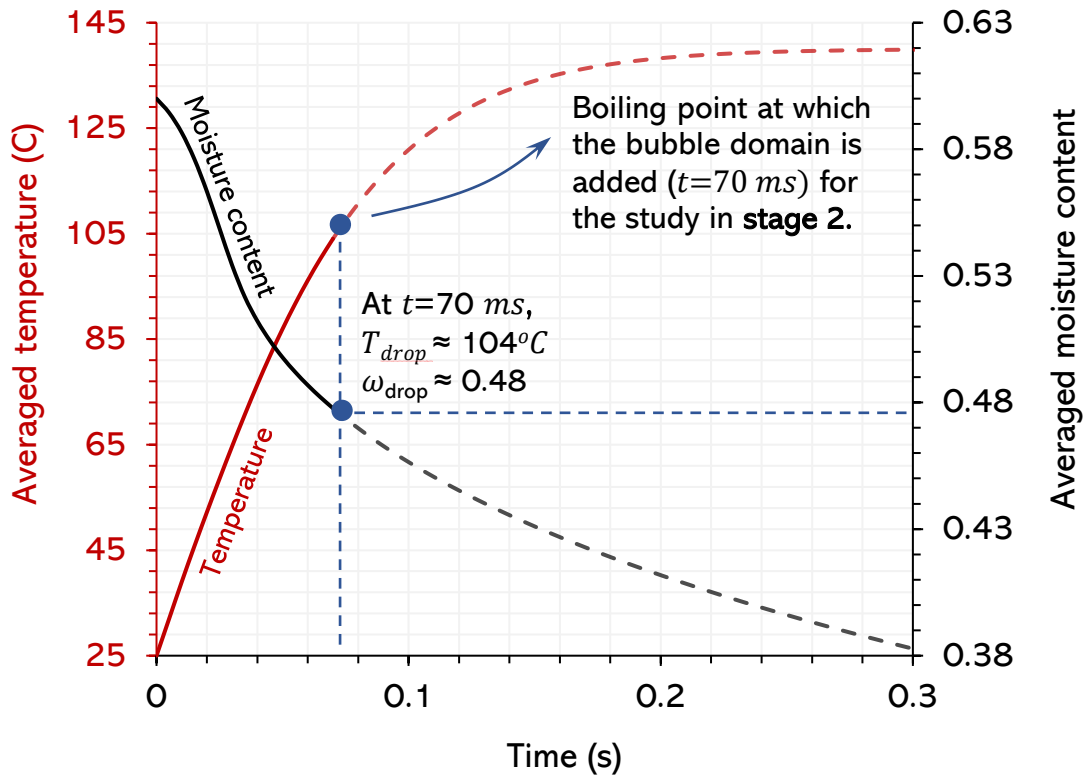


**Figure 6-4.** Droplet temperature and weight profiles over time in **stage 1**. No bubble is included, and the droplet dries until its averaged temperature reaches the air temperature. The ‘boiling point’ (blue dot) is marked at  $t = 70 \text{ ms}$ , from which the bubble domain is added to continue the droplet drying in stage 2. At boiling point (70 ms), the droplet temperature is at **104°C** and its averaged moisture content is at **0.48**. The bubble will take these values as an initial condition in the **stage 2** study.

According to Figure 6-4, the droplet reaches  $104^\circ\text{C}$  at  $t \approx 70 \text{ ms}$  which is the chosen time step for the bubble to be added. The total drying time in the second stage is  $150 \text{ ms}$ . The distribution of temperature and moisture content at the boiling point is illustrated in Figure 6-5.

Stage 2 - Initial conditions

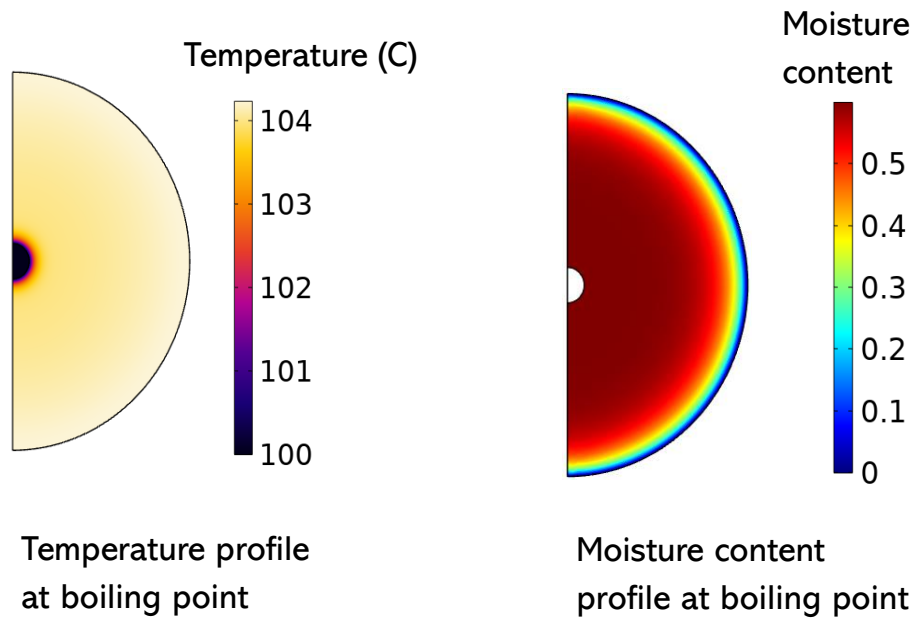


**Figure 6-5.** The initial condition of **stage 2 (boiling)**. The average droplet temperature is at 104°C and the moisture content is at 0.48 (refer to **Figure 6-4**).

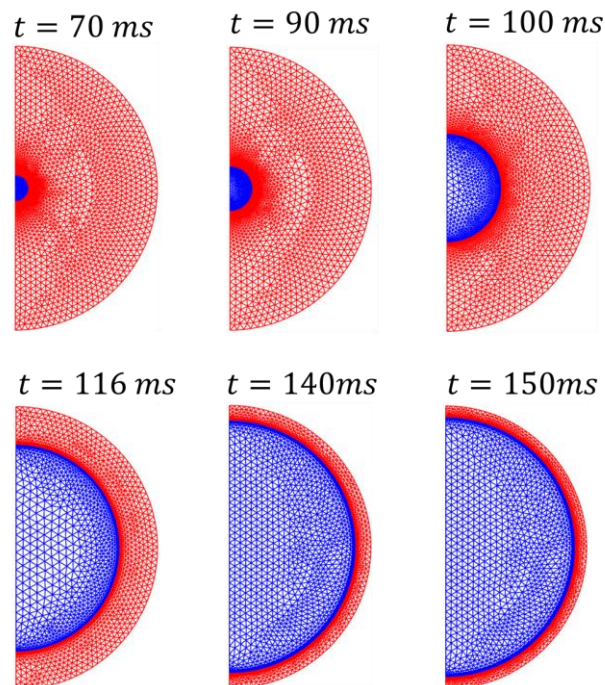


**Figure 6-6.** Mesh plot of the bubble-droplet system over time. The phase is colour-coded (blue for gas phase and red for liquid phase).

The thermal and concentration boundary layer can be seen at the bubble surface (Figure 6-5). The established temperature and concentration gradients at the boiling point do not cause the divergence problem as discussed previously. The simulation stops when the bubble radius is close to the droplet size, which causes an extreme mesh deformation (shown in Figure 6-6 at  $t = 150 \text{ ms}$ ). The bubble expands to five times its original size, hence the simulation stops at  $t = 173 \text{ ms}$ . The remeshing technique was employed to keep a high mesh quality throughout the simulation.

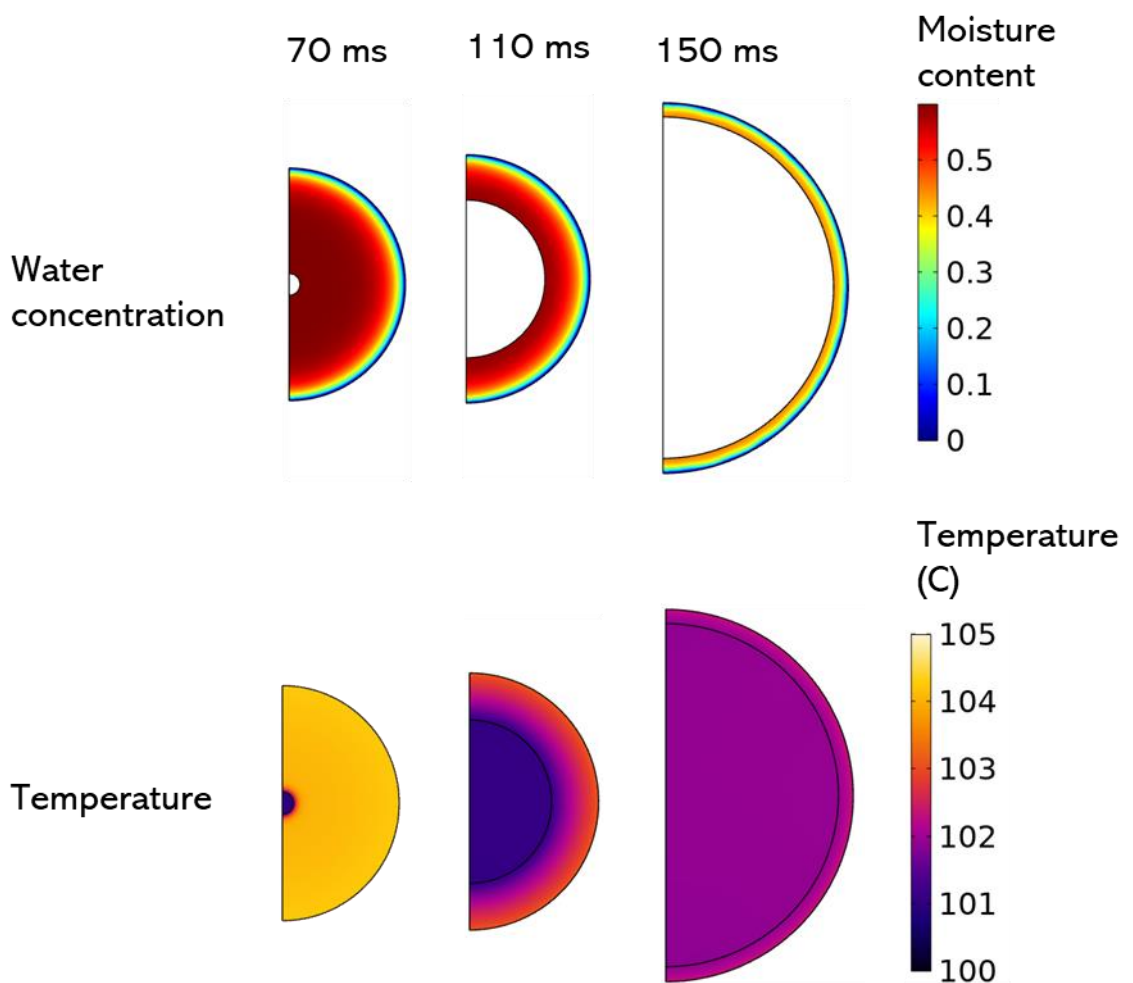


**Figure 6-7.** Concentration and temperature 2D plot in **stage 2 (boiling)**.

The concentration profile (upper plot) and the temperature profile (lower plot) are plotted at  $t = 70 \text{ ms}$ ,  $110 \text{ ms}$  and  $150 \text{ ms}$ . The scale for the surface are provided for concentration and temperature surface plots.

As the droplet temperature is higher than the bubble temperature at the boiling point, the direction of the vapour mass flux is towards the bubble interior (Figure 6-7). Therefore, the mass flux at the bubble-droplet surface now competes with the drying flux at the droplet-air interface since the two fluxes are in the opposite direction. The bubble dynamic significantly affects the droplet radius, and hence the evaporative flux compared to the case of no bubble. The droplet averaged temperature and moisture content in **stage 2** are plotted in Figure 6-8.

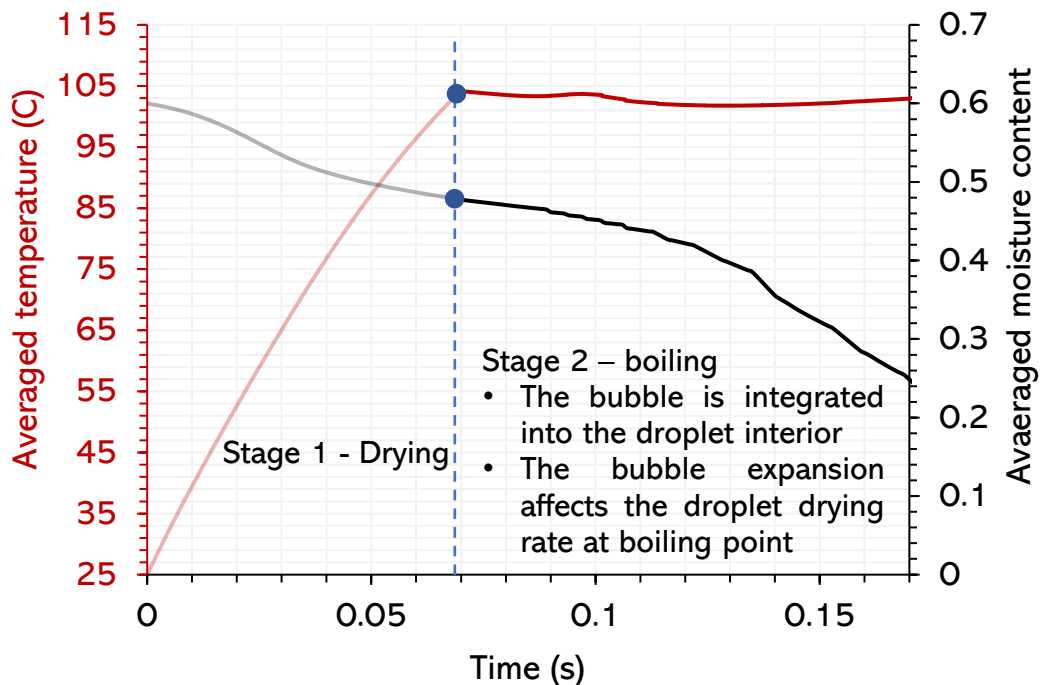


**Figure 6-8.** Droplet temperature (red line) and moisture content (black line) in stage 2 (boiling) of the drying. The stage 2 study starts at  $t = 0.07 \text{ s}$  (from the dotted blue line). The simulation stops at  $t = 173 \text{ ms}$ .

From  $t = 70 \text{ ms}$  to  $t = 173 \text{ ms}$ , the droplet moisture content decreases by 48% (from 0.48 to 0.25), while the temperature remains around  $105^\circ\text{C}$ , as shown in Figure 6-8. According to the temperature and moisture plots in Figure 6-4, the droplet temperature would have reached  $136^\circ\text{C}$  and the moisture content

only drops to 0.42 if the droplet continues to dry until  $t = 173 \text{ ms}$  without the presence of the bubble. This indicates the considerable influence of the bubble growth on the internal droplet temperature and moisture content. The next section is an interpretation of how the droplet affects bubble dynamics and vice versa.

Initially, at the beginning of stage 2, the droplet average temperature ( $104^\circ\text{C}$ ) is higher than that of the bubble (at  $100^\circ\text{C}$ ), which causes evaporation at the bubble surface. The bubble grows in size due to the mass flux of vapour. Consequently, the sucrose concentration increases at the bubble surface which elevates the boiling point (saturation temperature) according to the equation (6-19). In case the bubble saturation temperature exceeds the temperature of the surrounding liquid, the bubble will start to shrink due to the negative heat flux (refer to equation (6-17)). Otherwise, if the droplet is heated up at a faster rate than the increase of the bubble saturation temperature, the bubble will keep expanding. In summary, the bubble growth and collapse rate depend strongly on numerous factors such as the sucrose content at its surface, the degree of droplet overheat temperature at boiling point, the air temperature, the droplet internal moisture content at the boiling point, or the bubble size. Next, the heat and mass transfer coefficients at the droplet surface, which were estimated by the dimensionless number, are plotted in Figure 6-9.

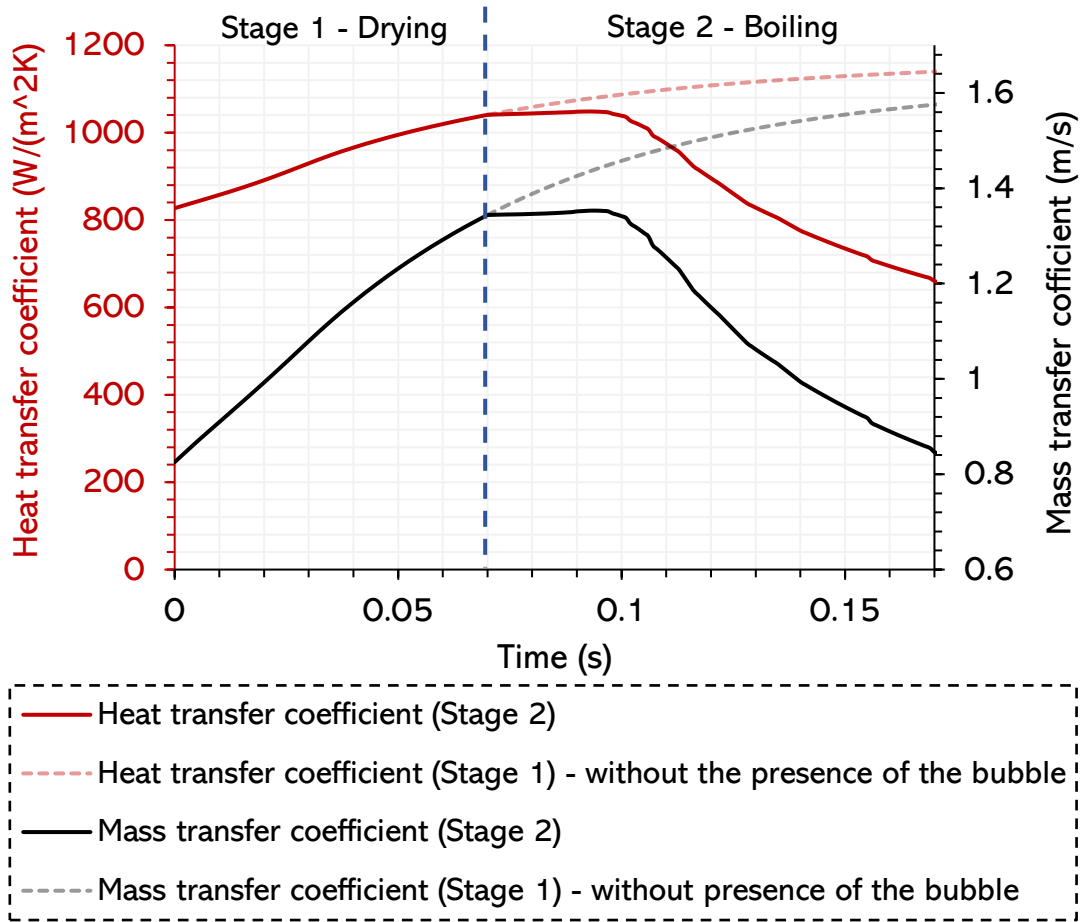


**Figure 6-9.** The averaged heat (red line) and mass transfer (black line) coefficients at the droplet interface in Stage 2. The bubble domain is added at  $t = 70 \text{ ms}$ . The heat and mass transfer coefficients for Stage 1 (no bubble) were included (dotted red and black lines) to see the effect of the bubble on the droplet drying.

The heat transfer coefficient ( $htc$ ) and the mass transfer coefficient ( $kc$ ) were estimated using the Sherwood and Nusselt numbers as shown in the following (refer to Chapter 5 for further details).

$$Re = \frac{\rho_a U D}{\mu} \quad (6-22)$$

$$Pr = \frac{C_p \mu}{k} \quad (6-23)$$

$$Sc = \frac{\mu}{\rho_a D} \quad (6-24)$$

$$Nu = \frac{htcD}{k} = 2 + 0.6 Re^{\frac{1}{2}} Pr^{\frac{1}{3}} \quad (6-25)$$

$$Sh = \frac{k_c D}{D_{va}} = 2 + 0.6 Re^{\frac{1}{2}} Sc^{\frac{1}{3}} \quad (6-26)$$

From equation (6-25) and (6-26), the heat and mass transfer coefficients can be evaluated as,

$$htc = \frac{k \left( 2 + 0.6 Re^{\frac{1}{2}} Pr^{\frac{1}{3}} \right)}{D} \quad (6-27)$$

$$k_c = \frac{k_c D}{D_{va}} = \frac{\left( 2 + 0.6 Re^{\frac{1}{2}} Sc^{\frac{1}{3}} \right)}{D} \quad (6-28)$$

Where  $D$  is the droplet radius ( $\mu m$ ). As Reynolds number is also a linear function of the droplet radius, the  $htc$  and  $k_c$  can be derived as a general function of the droplet radius,

$$htc = f(D^{-1}, D^{-\frac{1}{2}}) \quad (6-29)$$

$$k_c = f(D^{-1}, D^{-\frac{1}{2}}) \quad (6-30)$$

This equation reveals the direct relationship between the heat and mass transfer coefficients and the droplet radius. The  $htc$  and  $k_c$  would decrease if the droplet radius increases and vice versa. Hence, the radius of the droplet and bubble over time are plotted together in Figure 6-10.

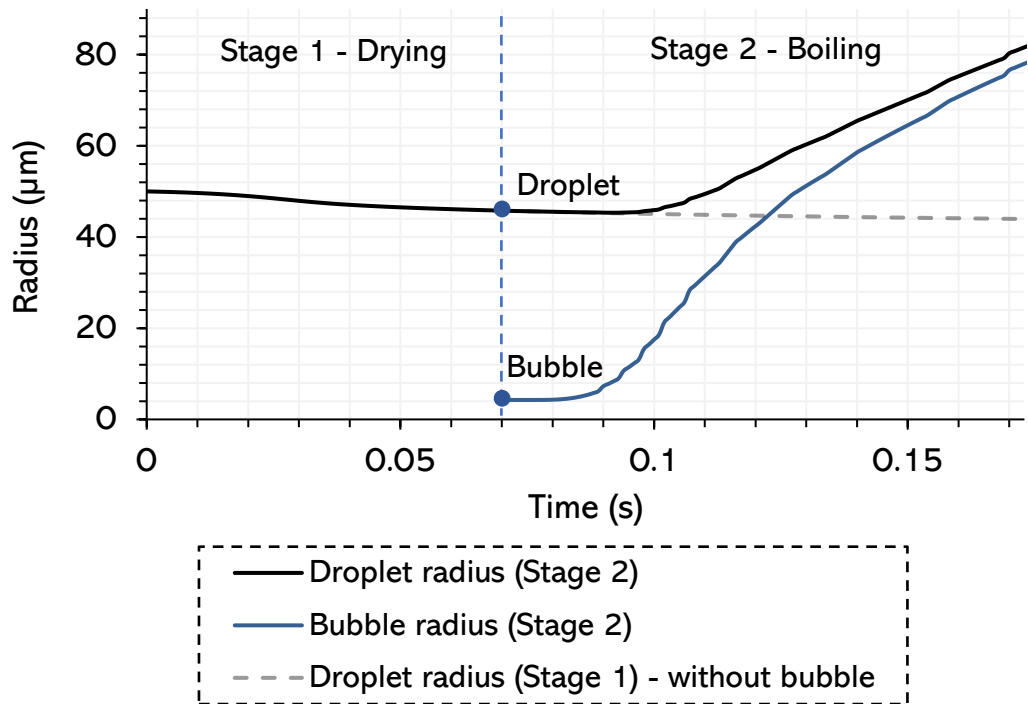


**Figure 6-10.** Droplet (black line) and bubble (blue line) radii over time in Stage 2 (boiling) study. The droplet radius is plotted for the whole drying period and the bubble radius is plotted from  $t = 70 \text{ ms}$ .

Around 15  $\text{ms}$  after the boiling point, both the droplet and the bubble radii stay relatively constant. The droplet radius then increases sharply by the bubble expansion at around  $t = 0.1 \text{ s}$ , which explains the sudden declines in the heat and mass transfer at  $t = 0.1 \text{ s}$  in Figure 6-9. The bubble expansion effect on the droplet size can be visualised clearly in Figure 6-6 and Figure 6-7.

In conclusion, the bubble-droplet system is highly dynamic, and the bubble growth effect on the drying rate is not negligible. The bubble kinetics depends on the bubble initial size, the degree of liquid overheat and the amount of solute present in the droplet at the boiling point. Having investigated the complex physics of the bubble expansion, it is concluded that the analytical solution for the bubble within a confined liquid that contains multi-species is challenging to obtain, which stresses the importance of the numerical model in dealing with this Multiphysics problem. Moreover, asymmetrical droplet drying (refer to Chapter 5), which is believed to play

important role in driving the droplet drying, was not included in this study as it focused on the evaporation phenomena. The next section looks at the offset-bubble at the boiling point to examine how the bubble initial position affects the droplet internal flow.

### **6.3. Drying droplet with an offset-bubble at boiling point in a 2D axis-symmetrical coordinate**

This section investigates the case where the bubble is offset from the droplet centre at the boiling point. The simulation framework from the previous case (section 6.1) is adopted in this study. The governing equations and boundary conditions at the bubble and droplet surfaces are the same in section 6.1. The drying period is also divided into two stages: stage 1 (drying) from  $t = 0 \text{ ms}$  to  $t = 70 \text{ ms}$ , and stage 2 (boiling) from  $t = 70 \text{ ms}$  onwards. The schematic of the offset-bubble case is shown in Figure 6-11.

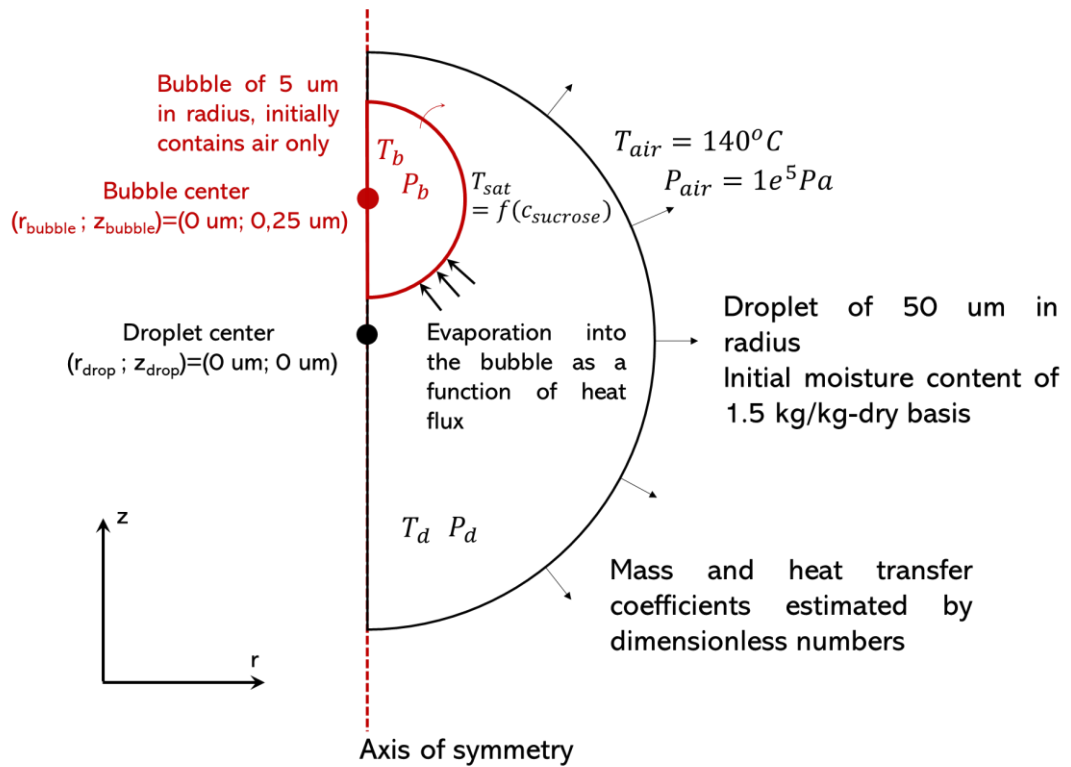


**Figure 6-11.** Schematic of the offset-bubble at the boiling point of the drying droplet. The bubble centre is **0.25  $\mu\text{m}$**  vertically above the droplet centre at the boiling point ( $t = 70 \text{ ms}$ ,  $T \approx 104^{\circ}\text{C}$ ). The droplet initial radius and moisture content are **50  $\mu\text{m}$**  and 1.5 kg/kg-db. The initial bubble radius is **5  $\mu\text{m}$** .

The overall simulation time is around 120  $\text{ms}$ , which is less than that of the centred-bubble case by 43  $\text{ms}$ . This is due to the fact that the offset-bubble is nearer to the top side of the droplet surface, which takes less time to cause extreme mesh deformation within the droplet that forces the simulation to stop. The droplet averaged temperature and moisture content are shown in Figure 6-12. The temperature increases from  $25^{\circ}\text{C}$  and maintained at around  $104^{\circ}\text{C}$  at the boiling point. The moisture content drops by 33% (from 0.6 to 0.4) at  $t = 120 \text{ ms}$ . The averaged temperature and moisture contents from the centred-bubble case are also shown in Figure 6-12 for comparison. The offset-bubble has shown to have a slight

effect on the moisture content and no effect on the droplet temperature compared to the case of centred-bubble.

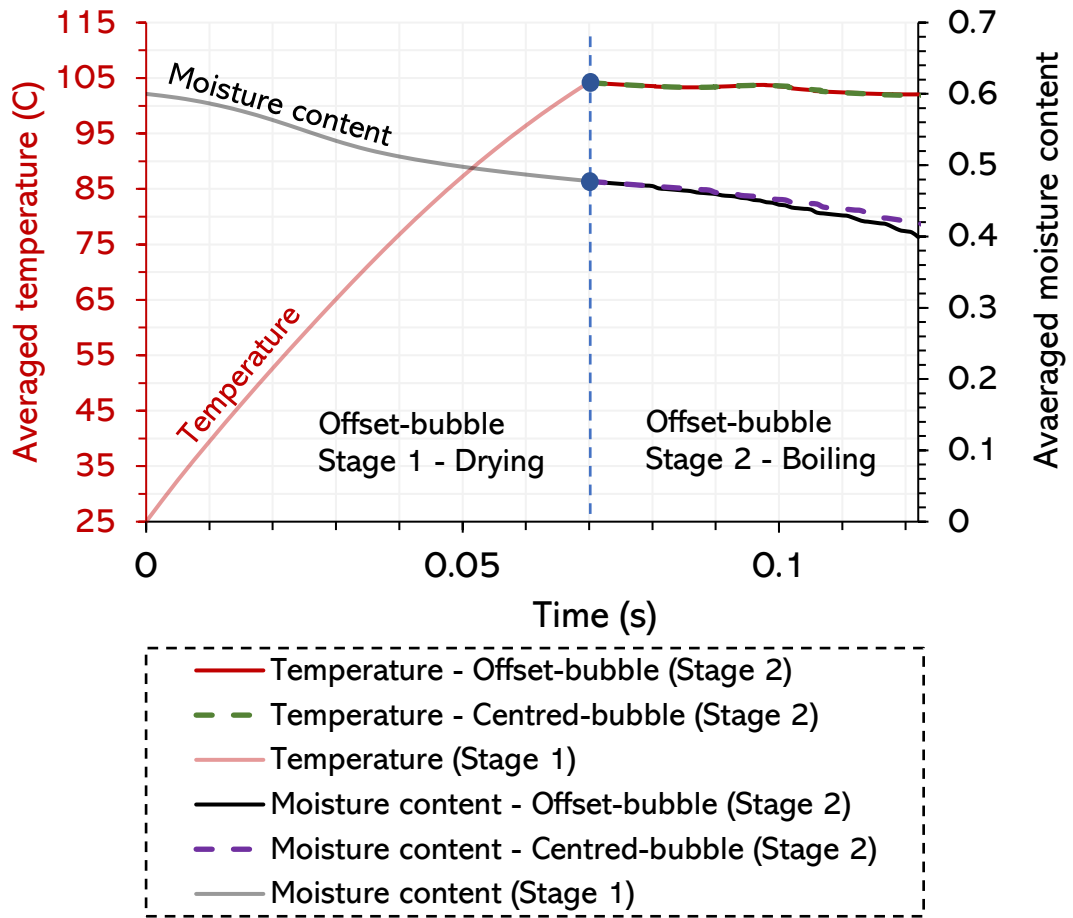


**Figure 6-12.** Droplet averaged temperature and moisture content in the offset-bubble case. The time interval is 112 ms. The offset-bubble starts to grow at the boiling point (blue circle). The droplet temperature and moisture content from the centred-bubble case are also plotted (dotted green lines).

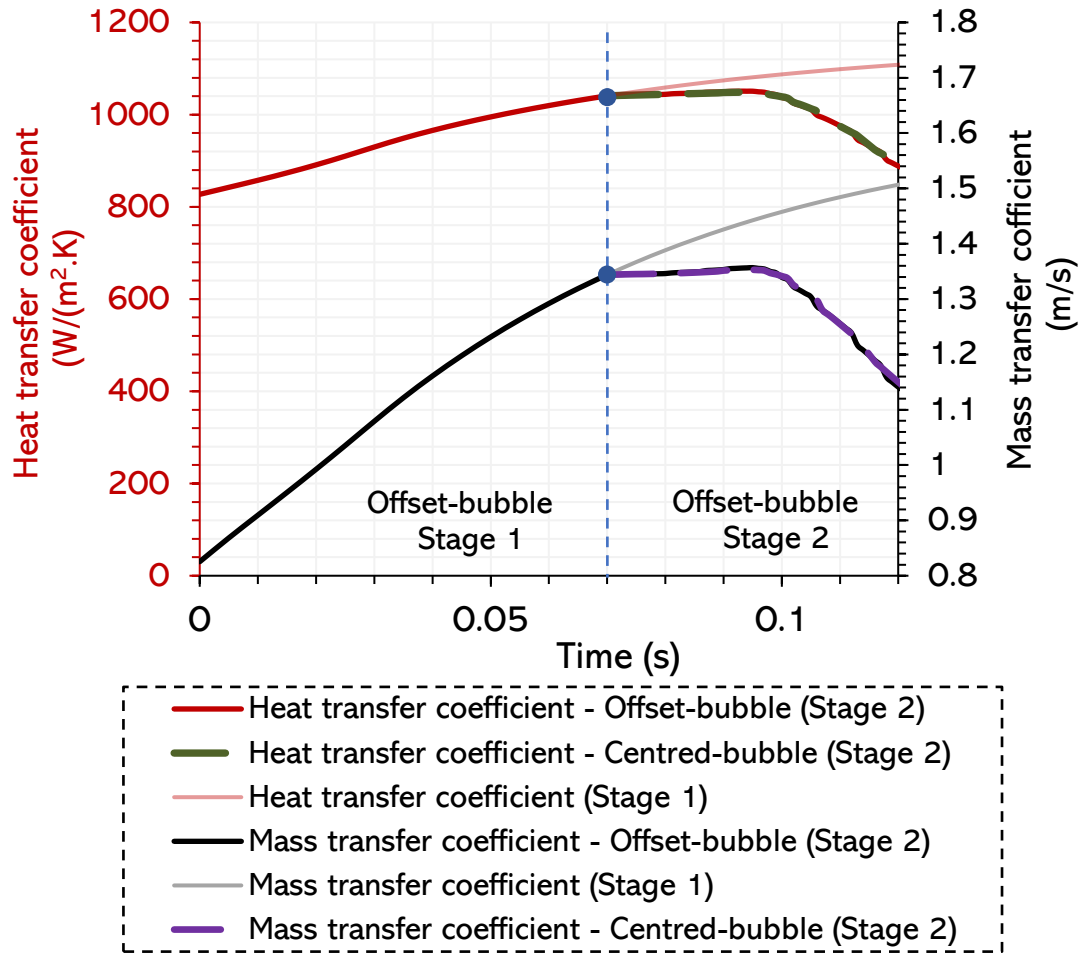


**Figure 6-13.** Averaged heat and mass transfer coefficients at the droplet surface in the offset-bubble case. The two stages are divided at  $t = 70 \text{ ms}$  (boiling point). The heat and mass transfer coefficients in the centred-bubble case are plotted in the dotted green lines. The heat and mass transfer coefficients profile without the presence of the bubble are plotted (faded colour lines).

Next, the heat and mass transfer coefficients at the droplet surface are compared to the previous case (centred-bubble) in Figure 6-13. No change in  $htc$  and  $k_c$  are observed, which is expected as offsetting the bubble should only affect the internal flow of the droplet rather than the variables at the surface. Furthermore, the  $htc$  and the  $k_c$  are a function of the droplet radius which is the same for both cases in Figure 6-15. Hence the position of the bubble at the boiling point does not have any considerable effect on the droplet drying rate.

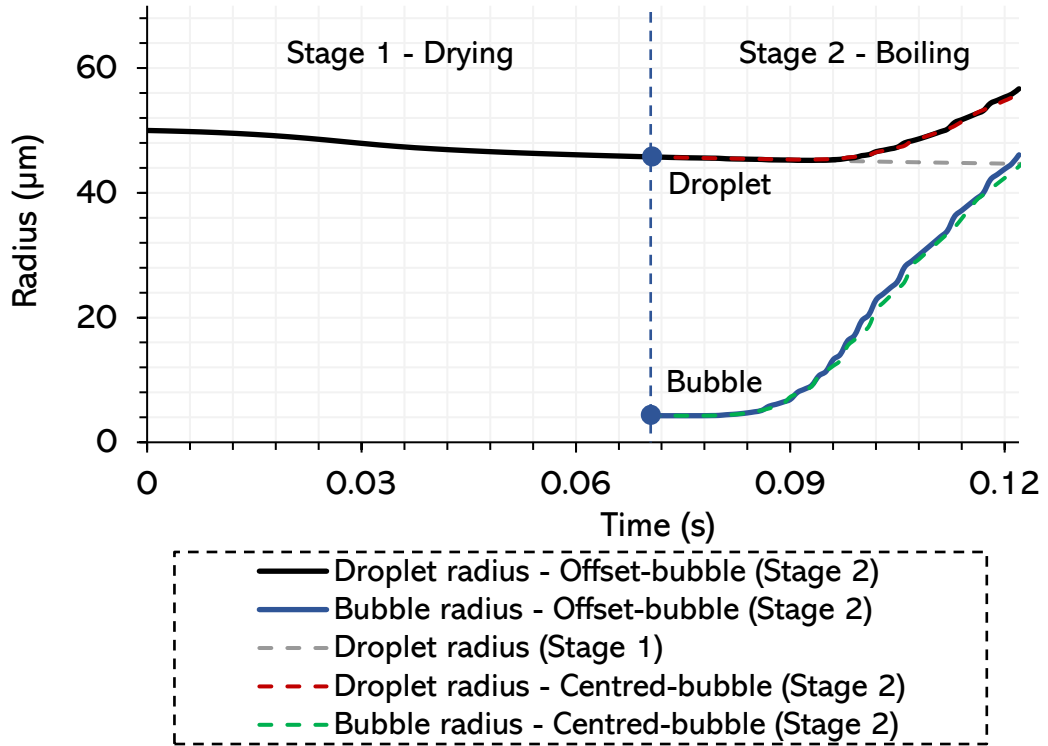


**Figure 6-14.** The droplet and bubble radius over time of the offset-bubble case. The droplet radius is plotted for the whole time interval (112 ms) and the bubble radius is plotted from  $t = 70 \text{ ms}$ . The droplet and centred-bubble radius profiles are in dotted green lines.

Figure 6-14 is the bubble and droplet radii plot over time, for the two cases of centred-bubble and offset-bubble. It shows a negligible difference in the radius profiles, implying that the initial position of the bubble does not have a significant effect on the growth of both the bubble and the droplet. The local temperature on the droplet surface is plotted in Figure 6-15. The effect of offsetting the bubble makes the temperature distribution on the droplet surface not symmetrical compared to the case of centred-bubble. The temperature of the top side of the bubble surface (dotted lines) increases at a faster rate compared to the bottom side, meanwhile the temperature of the droplet top side ( $angle > 90^\circ$ ) drops faster than that at the bottom point. The temperature variation along both the droplet and bubble surfaces are around  $1.5^\circ\text{C}$  which is negligible.

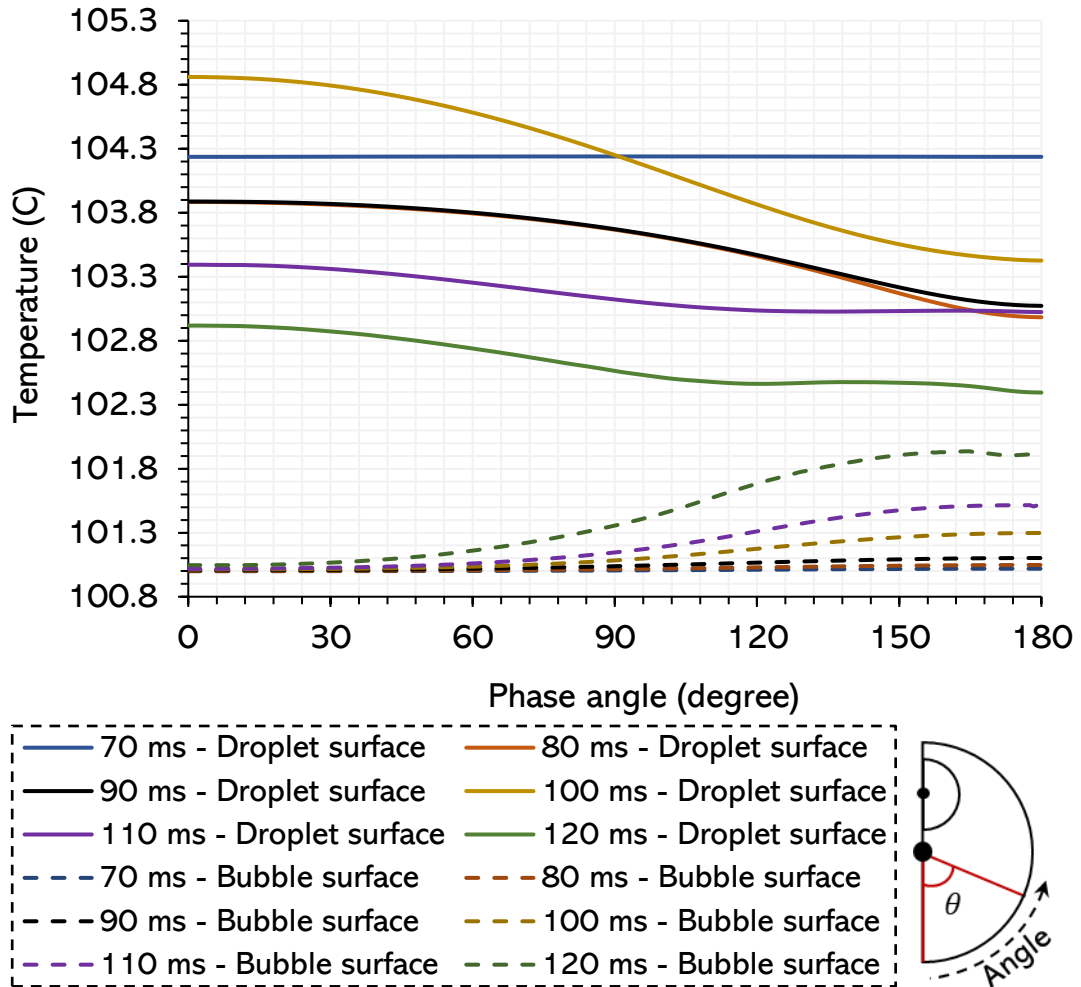


**Figure 6-15.** The temperature variation along the droplet and the bubble surfaces. The angle (measured in degree) starts from the bottom point ( $0^\circ$ ) and ends at the top of the surface ( $180^\circ$ ). The temperature of the droplet surface (colour lines) and the bubble surface (dotted lines) are plotted at the same time step.

The bubble expansion can be visualised in the temperature surface plot in Figure 6-16. The bubble expands slowly from  $5 \mu\text{m}$  to around  $6.8 \mu\text{m}$  for the first  $20 \text{ ms}$ , and starts to accelerate to reach the size of  $46 \mu\text{m}$  at  $t = 112 \text{ ms}$ . According to the colour-coded plot in Figure 6-16, the temperature field is cooler on the top part of the droplet, which can be seen at  $t = 80 \text{ ms}$  or  $90 \text{ ms}$ . This was also indicated in the surface temperature variation graph in Figure 6-15. Moreover, the bubble moves towards the droplet centre as soon as the boiling starts ( $t = 70 \text{ ms}$ ). The coordinate of the bubble centre changes from

$(0, 25 \mu\text{m})$  to  $(0, 15 \mu\text{m})$  at  $t = 90 \text{ ms}$ . The initial motion of the bubble can be thought to be related to the non-symmetrical pressure field within the droplet. This can be addressed by considering the force balance equation at the droplet interface (refer to Rayleigh-Plesset equation derivation in Appendix A, section A.3). The droplet surface pressure is a function of the distance from the bubble surface to the droplet surface. Hence, the pressure on the top of the droplet is expected to be larger than that of the bottom region. The surface pressure of the droplet in both the offset and the centred-bubble cases is therefore plotted in Figure 6-17 in order to justify this hypothesis. The pressure distribution along the droplet with the centred-bubble case is as expected. This non-symmetrical pressure profile in the offset-bubble case explains the motion of the bubble as seen in Figure 6-16.

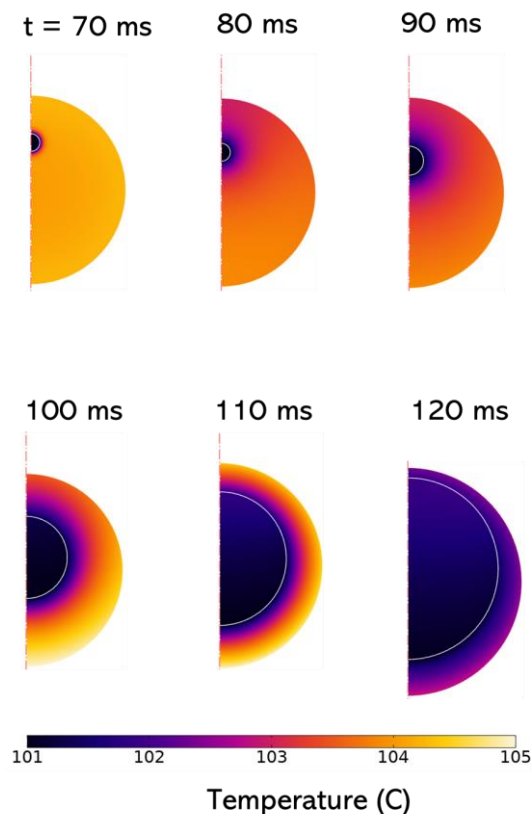


**Figure 6-16.** Temperature surface plot of the droplet and bubble domains. The bubble surface is represented by the half-white circle. The droplet and bubble temperatures at the boiling point are  $104^\circ\text{C}$  and  $100^\circ\text{C}$  respectively.

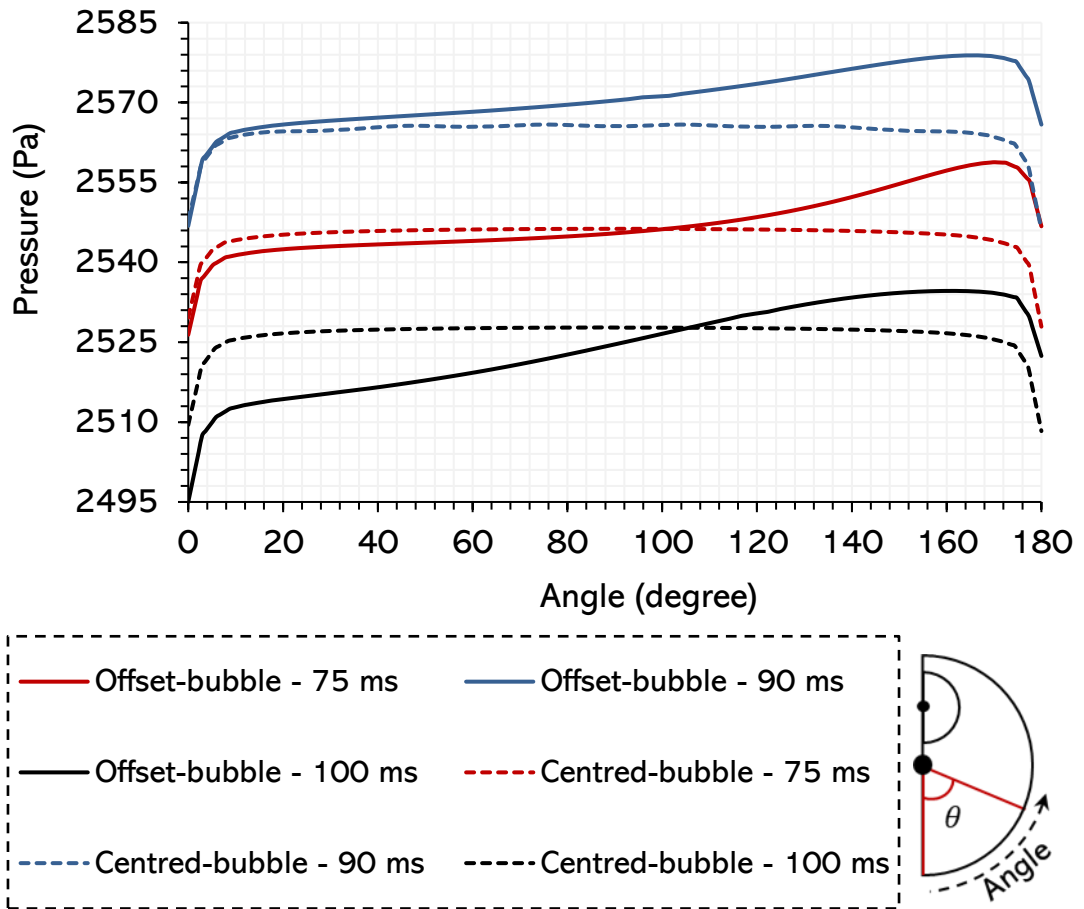


**Figure 6-17.** Pressure variation plot along the droplet surface for the timesteps at  $t = 75 \text{ ms}$ ,  $90 \text{ ms}$  and  $100 \text{ ms}$ . The pressure is plotted against the angle (as represented above the plot) starting from the bottom to the top of the droplet surface. The offset-bubble (solid colour lines) and the centred-bubble (dotted colour lines) cases are compared.

## 6.4. Conclusions

The investigation of the bubble-droplet system has revealed new drying behaviours of the droplet above the boiling point. The bubble has been shown to have a considerable effect on the drying rate of the droplet. The bubble presence causes the droplet averaged temperature to level out in the boiling period compared to the case of no bubble. The droplet heat and mass transfer coefficients decrease in the boiling period due to the increases in the droplet radius as the bubble expands. The second study focuses on the offset-bubble at the boiling point, in which the initial position of the bubble is set to be above the droplet centre, and the computed result was compared with the case of centred-bubble. The aim was to analyse the relationship between the initial bubble location and the drying system. The offset-bubble recentralises itself by moving towards the droplet centre and expands at the same time. This is thought to be related to the uneven distribution of the pressure along the droplet surface. Similarly, slight surface temperature variations are also observed in the offset compared to the centred-bubble case. According to the study observations, the bubble is predicted to be sensitive to the condition at the boiling point, such as the initial bubble radius, the bubble position, or the droplet temperature and moisture content at 100°C.

Overall, the bubble was set to grow in a stable environment without being affected much by the internal flow within the droplet domain. This is because the study does not consider the external air flow, which can cause the asymmetrical flow field within the droplet (refer to Chapter 5). Moreover, the bubble shrinkage is also possible if its saturation temperature exceeds the droplet temperature due to the increases in the sucrose concentration at the bubble surface, and this should be considered in future work.

# Chapter 7

## Conclusions and future plan

Chapter 7 summarises the key findings of the research and presents conclusions from the thesis. The considerations for a better and improved drying model together with alternative methods are discussed. Suggestions on a more complex simulation setup for future work are provided.

## **7.1. Conclusions and considerations to improve the current model**

The thesis broadened the understanding by providing further insights into the droplet drying within the spray dryer, and explored new drying behaviours at the boiling regime. The Finite Element Method (FEM) coupled with the Arbitrary Lagrangian-Eulerian (ALE) interface tracking algorithm has proven to be a robust method for simulating the Multiphysics system with a moving interface. The developed drying model is capable of describing the internal velocity, moisture content and temperature fields within the droplet, which is inaccessible by other drying models and experimental methods. The consequences of the bubble expansion on the droplet drying rate are evaluated which is critical in predicting the morphology of the dried-particle. The theoretical framework developed in this thesis can be extended further to accurately capture the physics of boiling within the droplet. After the research introduction in Chapter 1 and the literature review in Chapter 2, the main conclusions drawn from the key findings of this thesis are summarised in the following sections.

The initial work in Chapter 3 focuses on the analogous setup to the droplet drying system, such as the fixed or the falling sphere in the air. The aim is to ensure that the fundamental physics are properly implemented in the simulation, to check for the errors in the code and to justify whether the simulation represents real-world physics. For example, the drag and lift coefficients are validated against experimental data from the literature, or the computed heat and mass transfer coefficients are verified against the averaged heat and mass transfer coefficient calculated from dimensionless numbers. The outcome is the validated simulation setup and an approved numerical method that can be used to build the next 1-dimensional drying model. Next, the benchmarks for the phase change problem

are performed in Chapter 4. This provides a degree of confidence for integrating a bubble into a droplet domain later in Chapter 6.

The second part is the modelling of the droplet drying in the 1-dimensional coordinate in Chapter 5. The droplet heat and mass transfer coefficients are estimated from the dimensionless numbers. As the model is conducted on a 1-dimensional coordinate, the timeframe for the results reproducibility is short. This allowed a convenient sensitivity analysis to be performed on the diffusion models, water activity and diffusion coefficients correlations. The analysis provides an optimal choice of parameters that can be utilised to progress into a 2-dimensional model. In practice, the water activity and the diffusivities of a solute would be virtually impossible to calculate at two extreme points (0% and 100% moisture content). Overall, the computed results agreed with the experimental data with some disagreements as the droplet moisture content decreases to a low value. The disagreement is mainly driven by the validity of the diffusivity correlation. In other words, the diffusivity correlation is derived from the experimental data which is not feasible to collect at the very low range of moisture content (near-solid phase). Therefore, the accuracy and validity of the correlation are not guaranteed at the end of the drying period. Moreover, the 1D model does not take into account the fluid flow within the droplet domain in which the convection might have an effect on the drying rate. All other sources of errors are also discussed in Chapter 5.

The third key achievement is the adaption of the simulation framework from the 1D model and redesigned into a 2-dimensional axis-symmetrical system in the second half of Chapter 5. The system consists of a spherical droplet falling and drying in hot air. The fluid flow is now resolved both within the air and the droplet domains, hence the heat and mass transfer coefficients are not estimated but computed. In order to model the terminal velocity of

the droplet, the proportional-integral-derivative (PID) feedback algorithm is developed. This is a powerful method to ensure the droplet always fall with terminal velocity as it shrinks in size, and to preserve the droplet sphericity. The PID loop also prevents the mesh from being heavily deformed due to the moving interface of the droplet falling through the air (refer to the ALE interface tracking method in Chapter 3). The success in developing the PID loop is a critical accomplishment that made computed results being comparable to the experimental data. The main outcome of this 2-dimensional drying model is the new detailed insights into the droplet internal flow while drying. The local information within the droplet is now obtainable thanks to the 2-dimensional coordinates system. The asymmetrical moisture and temperature distribution within the liquid domain are evaluated. The moisture-rich region is now located which is useful for the study of the boiling in Chapter 6. The fluid flow is also resolved from which the vortex formation pattern can be visualised. The position and size of the vortex are vital to the prediction of the shell thickness and morphological development. As a result, the weakest and strongest point of the shell can now be located.

The final work is the simulation of the bubble-droplet system. The physics is strongly coupled between the expanding bubble and the drying droplet. The benchmarks for the bubble growth simulation were carried out independently (refer to Chapter 4) before being integrated into the droplet. Together with the verification of the bubble dynamics within the liquid medium and the robust diffusion drying model (developed in Chapter 5), the bubble is coupled into the droplet domain with the boundary conditions derived from Chapter 4. The bubble expansion is driven by the heat flux that arises from the difference between the bubble and the droplet temperature. The Navier-Stokes equation is solved to examine the effect of the expanding bubble on the droplet size and sphericity.

Two simulation cases are considered: the centred-bubble and the offset-bubble cases. The first setup is the droplet having a bubble at its centre at the boiling point. The bubble has been shown to significantly affect the heat and mass transfer at the droplet surface, which in turn affects the droplet temperature and moisture content at the boiling point.

## **7.2. Suggestions for a more advanced simulation system and alternative methodology**

A more advanced drying system can be developed upon the current drying model from this thesis. As the 2-dimensional axis-symmetrical coordinate was used in the drying model in Chapter 5, it did not take into account the physics such as the rotational motion of the droplet, or the Karmen vortex shedding in the wake at a high Reynolds number. In order to consider these asymmetrical factors in future work, a full 3-dimensional simulation is needed. A 3-dimensional coordinate will ensure the vortex shedding in the droplet wake and the moving separation point on the droplet surface are included, hence the drying of a high Reynolds number droplet drying system is captured accurately. Moreover, the developed model considers a single droplet drying, which is a simplified system of billion of droplets drying within the spray dryer. The drying of one droplet can influence other droplets by the vapour concentration it releases into the air. Hence, another droplet domain can be added to the current simulation setup in which the evaporation from one droplet can affect the air relative humidity of the air surrounding another droplet. The droplets alignment to the airflow is also another potential factor to study. The relative position of droplets to each other can determine the falling velocity of each droplet over time. For example, in the case in which one droplet completely obstructs another droplet to the airflow direction, the droplet behind experiences a different pressure field hence having a different falling

velocity to the droplet upfront to the airflow. Additionally, as the drying progress, the shell can form at the droplet surface in which the theory of the Fluid-Structure interaction (FSI) can be employed. The interaction between the internal flow within the droplet and the shell formed can be simulated with the increasing shell's thickness during the simulation. The initiation of the shell formation can be described by having a mathematical condition on the solute concentration, over which the viscous liquid is treated as the solid layer. Together with the stress and strain coupled with the 2D drying mode, the morphological evolution of the droplet can be predicted more robustly. However, it should be kept in mind that the main challenge is the adoption of a suitable solid theory for different types of solution, as the drying of the polymeric solution will result in the plastic shell comparing to the solid shell from drying the colloidal solution. There are numerous areas that can be explored for the case of droplet drying at the boiling point.

Next, the study in this thesis considered a single bubble within the droplet. The centre and offset cases are simulated with outcomes highlighted in Chapter 6. However, the bubble was placed on the axis of symmetry due to the nature of the 2-dimensional axis-symmetrical coordinate, which means that the bubble can only move vertically inside the droplet. This problem can be solved in future work by setting up the model in a full 3-dimensional coordinate. The bubble initial position can, therefore, be anywhere within the droplet and it can move with more degree of freedom comparing to the 2-dimensional case. Moreover, there should be more than one bubble at boiling which has been observed experimentally. The current bubble-droplet simulation can be progressed to include multiple bubbles, with the bubble forming randomly within the droplet domains. A further step can be taken by coupling the bubble dynamics with the shell through the use of FSI. It should be noted that the bubble is highly chaotic in nature,

so it is challenging to determine the initial conditions for the bubbles at the boiling point.

Finally, an alternative method to solve the PDEs is recommended to replace the current FEM method. The integration of machine learning into Computational Fluid Dynamics has drawn much attention over the past years, and the published work is increasing rapidly (Brunton, Noack and Koumoutsakos, 2020) (Sadrehaghighi, 2020) (Koumoutsakos, 1999). The concept of machine learning can be applied to decrease the computing time of solving the mathematical drying model. Overall, the common factor between machine learning and the FEM method is the optimisation of the loss function. As explained in detail in Chapter 3, the backbone of the FEM is based on the theory that the system will seek to maximise its entropy. Therefore, the FEM aims to minimise the error function which is the difference between the computed results to its equilibrium state. Machine learning also operates according to this idea. In order to understand how machine learning can be implemented, we need to know the basics of machine learning. Machine learning is a concept of predicting the output based on a large set of inputs and a middle algorithm which is referred to as the neural network. The accuracy of the prediction of the neural network can be increased significantly with a larger set of input, as the network can adjust itself according to the loss function. The loss function, in this case, is how far off the prediction is from the true or analytical solution, which is normally obtained from the experiments or mathematical models. There has been a debate as to whether machine learning can replace the mechanistic model, because machine learning is the predictive method without providing insights into the physics.

The following example should clarify this point. There is a success in the implementation of the convolutional neural network into the CFD done by Oliver Hennigh (Hennigh, 2017). The code is available

on <https://github.com/loliverhennigh>. The work uses the convolutional neural network (CNN) to predict the drag and lift of the flow past the cylinder case. The computational method used is the Lattice-Boltzmann method and the code is written in Python using Tensorflow. A set of training data is generated from CFD simulation by varying positions and sizes of the cylinder within the domain. The outcome is an extremely fast prediction of the drag and lift by the CNN with the averaged mean square error of 0.72 (Hennigh, 2017). Although the CNN approach is convenient in providing the prediction of the results, it does not describe the physics of the flow past the cylinder. Therefore, the information about the Karmen vortex shedding or turbulence flow is not feasible to obtain using the machine learning method. Having said that, the current method of running the CFD is not optimised, as the whole simulation has to re-run again whenever there is a small change in the operating or initial conditions. Therefore, the idea of coupling the machine learning to the CFD would be a more favourable approach since the machine learning can provide accurate output with much less computational effort, and the training inputs of the neural network can be supplied by the CFD simulation which is only required to perform once. The drying model of the droplet can utilise this idea to run the CFD simulation of a specific range of temperature as an input to the neural network, which can then be used to provide the drying information at other temperature ranges. The simulation setup certainly still needs all the verification and validation benchmarks to ensure it agrees with the experimental observation.

## References

- Abramzon, B. and Sirignano, W. A. (1989) 'Droplet vaporization model for spray combustion calculations', *International Journal of Heat and Mass Transfer*, 32(9), pp. 1605–1618. doi: 10.1016/0017-9310(89)90043-4.
- Adhikari, B. *et al.* (2009) 'Experimental studies and kinetics of single drop drying and their relevance in drying of sugar - rich foods : A review', *International Journal of Food Properties*, 2912. doi: 10.1080/10942910009524639.
- Akhavan Mahdavi, S. *et al.* (2016) 'Microencapsulation optimization of natural anthocyanins with maltodextrin, gum Arabic and gelatin', *International Journal of Biological Macromolecules*, 85, pp. 379–385. doi: 10.1016/j.ijbiomac.2016.01.011.
- Al-Khattawi, A. *et al.* (2018) 'The design and scale-up of spray dried particle delivery systems', *Expert Opinion on Drug Delivery*. Taylor & Francis, 15(1), pp. 47–63. doi: 10.1080/17425247.2017.1321634.
- Alamilla-Beltrán, L. *et al.* (2005) 'Description of morphological changes of particles along spray drying', *Journal of Food Engineering*, 67(1–2), pp. 179–184. doi: 10.1016/j.jfoodeng.2004.05.063.
- Alharbi, A. N. (2019) 'Modelling of Droplet Drying Mechanisms', p. 168. doi: 10.25392/leicester.data.10303769.v1.
- Amador, L. Martin de Juan (2016) 'Chapter 19 - Strategies for Structured Particulate Systems Design', *Computer Aided Chemical Engineering*, 39, pp. 509-579. doi:10.1016/B978-0-444-63683-6.00019-8.
- Anderson Jr, J. D. (2010) *Fundamentals of aerodynamics*. Tata McGraw-Hill Education.

- Araia, S. and Doi, M. (2012) 'Skin formation and bubble growth during drying process of polymer solution', *European Physical Journal E*, 35(7), pp. 1–9. doi: 10.1140/epje/i2012-12057-2.
- Atkins, P. and De Paula, J. (2006) 'Atkins' physical chemistry'. Oxford press.
- Baldelli, A. *et al.* (2016) 'Effect of crystallization kinetics on the properties of spray dried microparticles', *Aerosol Science and Technology*. Taylor & Francis, 50(7), pp. 693–704. doi: 10.1080/02786826.2016.1177163.
- Baldwin, K. A. *et al.* (2011) 'Drying and deposition of poly(ethylene oxide) droplets determined by Péclet number', *Soft Matter*, 7(17), p. 7819. doi: 10.1039/c1sm05220a.
- Bandyopadhyay, P. R. and Balasubramanian, R. (1995) 'Vortex reynolds number in turbulent boundary layers', *Theoretical and Computational Fluid Dynamics*, 7(2), pp. 101–117. doi: 10.1007/BF00311808.
- Baracu, T. and Boşneagu, R. (2019) 'Numerical analysis of the flow around a cylinder for the perspective of correlations of the drag coefficient of the ship's hulls', *Scientific Bulletin" Mircea cel Batran" Naval Academy*. Naval Academy Publishing House, 22(2), pp. 256A--267. doi: 10.21279/1454-864X-19-I2-031.
- Bayly, A. E. (2015) 'Structure development during drying - a review of the state of the art', *Ifpri*, pp. 1–48.
- Beard, K. V. and Pruppacher, H. R. (1971) 'A Wind Tunnel Investigation of the Rate of Evaporation of Small Water Drops Falling at Terminal Velocity in Air', *Journal of Atmospheric Sciences*, pp. 1455–1464. doi: 10.1175/1520-0469(1979)036<1255:AWTIOT>2.0.CO;2.
- Boel, E. *et al.* (2020) 'Unraveling particle formation: From single droplet drying to spray drying and electrospraying',

*Pharmaceutics*, 12(7), pp. 1–58. doi: 10.3390/pharmaceutics12070625.

Boraey, M. A. and Vehring, R. (2014) 'Diffusion controlled formation of microparticles', *Journal of Aerosol Science*. Elsevier, 67, pp. 131–143. doi: 10.1016/j.jaerosci.2013.10.002.

Brunton, S. L., Noack, B. R. and Koumoutsakos, P. (2020) 'Machine Learning for Fluid Mechanics', *Annual Review of Fluid Mechanics*, 52, pp. 477–508. doi: 10.1146/annurev-fluid-010719-060214.

Charlesworth, D. H. and Marshall, W. R. (1960) 'Evaporation from drops containing dissolved solids', *AIChE Journal*, 6(1), pp. 9–23. doi: 10.1002/aic.690060104.

Chenyakin, Y. *et al.* (2017) 'Diffusion coefficients of organic molecules in sucrose-water solutions and comparison with Stokes-Einstein predictions', *Atmospheric Chemistry and Physics*, 17(3), pp. 2423–2435. doi: 10.5194/acp-17-2423-2017.

Cheong, H. W., Jeffreys, G. V., & Mumford, C. J. (1986) 'A receding interface model for the drying of slurry droplets', *AIChE journal*, 32(8), pp. 1334-1346. doi: 10.1002/aic.690320811

Chequer, F. M. D. *et al.* (2013) 'Spray drying-overview', *Intech*, p. 13. doi: 10.1016/j.colsurfa.2011.12.014.

Chinè, B. and Monno, M. (2011) 'Multiphysics Modeling of a Gas Bubble Expansion', *Proceedings of 2011 European Comsol Conference*, pp. 2–7.

Chou, K. Sen *et al.* (2014) 'A quick and simple method to test silica colloids' ability to resist aggregation', *Colloids and Surfaces A: Physicochemical and Engineering Aspects*, 448(1), pp. 115–118. doi: 10.1016/j.colsurfa.2014.02.020.

Clift, R., Grace, J. R. and Weber, M. E. (1978) 'Wall effects, Bubbles,

Drops and Particles', Academic Press, New York.

- Dalmaz, N. *et al.* (2007) 'Heat and Mass Transfer Mechanisms in Drying of a Suspension Droplet: A New Computational Model', *Drying Technology*, 25(2), pp. 391–400. doi: 10.1080/07373930601184569.
- Davies, J. F., Haddrell, A. E. and Reid, J. P. (2012) 'Time-Resolved Measurements of the Evaporation of Volatile Components from Single Aerosol Droplets', *Aerosol Science and Technology*, 46(6), pp. 666–677. doi: 10.1080/02786826.2011.652750.
- van Dyke, M. and White, F. M. (1982) 'An Album of Fluid Motion', *Journal of Fluids Engineering*, pp. 542–543. doi: 10.1115/1.3241909.
- Epstein, P. S. and Plesset, M. S. (1951) 'Erratum: On the Stability of Gas Bubbles in Liquid and Gas Solutions', *Journal of Chemical Physics*, 19(2), p. 256. doi: 10.1063/1.1748182.
- Farid, M. (2003) 'A new approach to modelling of single droplet drying', *Chemical Engineering Science*, 58(13), pp. 2985–2993. doi: 10.1016/S0009-2509(03)00161-1.
- Feng, Z. C. and Leal, L. G. (1997) 'Nonlinear Bubble Dynamics', *Annual Review of Fluid Mechanics*, 29(1), pp. 201–243. doi: 10.1146/annurev.fluid.29.1.201.
- Frost, D. L. (1988) 'Dynamics of Explosive Boiling of a Droplet.', *The Physics of fluids*, 31(9), pp. 2554–2561. doi: 10.1063/1.866608.
- Fu, N., Woo, M. W. and Chen, X. D. (2012) 'Single Droplet Drying Technique to Study Drying Kinetics Measurement and Particle Functionality: A Review', *Drying Technology*, 30(15), pp. 1771–1785. doi: 10.1080/07373937.2012.708002.
- Fyhr, C. and Kemp, I. C. (2007) 'Comparison of Different Drying Kinetics Models for Single Particles', *Drying Technology*, 16(7),

pp. 37–41. doi: 10.1080/07373939808917465.

- Gabitto, J. and Tsouris, C. (2008) 'Drag coefficient and settling velocity for particles of cylindrical shape', *Powder Technology*, 183(2), pp. 314–322. doi: 10.1016/j.powtec.2007.07.031.
- Gaudron, R., Warnez, M. T. and Johnsen, E. (2015) 'Bubble dynamics in a viscoelastic medium with nonlinear elasticity', *Journal of Fluid Mechanics*, 766(1), pp. 54–75. doi: 10.1017/jfm.2015.7.
- Godsave, G. A. E. (1953) 'Studies of the combustion of drops in a fuel spray-the burning of single drops of fuel', *Symposium (International) on Combustion*, 4(1), pp. 818–830. doi: 10.1016/S0082-0784(53)80107-4.
- Goossens, W. R. A. (2019) 'Review of the empirical correlations for the drag coefficient of rigid spheres', *Powder Technology*. Elsevier B.V., 352, pp. 350–359. doi: 10.1016/j.powtec.2019.04.075.
- Gopireddy, S. R. and Gutheil, E. (2012) 'Modeling and Simulation of Water Evaporation from a Droplet of Polyvinylpyrrolidone (PVP) Aqueous Solution', *Iclass*, 12, pp. 1–8.
- Gopireddy, S. R. and Gutheil, E. (2013) 'Numerical simulation of evaporation and drying of a bi-component droplet', *International Journal of Heat and Mass Transfer*, 66, pp. 404–411. doi: 10.1016/j.ijheatmasstransfer.2013.07.010.
- Grosshans, H. *et al.* (2016) 'A new model for the drying of mannitol-water droplets in hot air above the boiling temperature', *Powder Technology*. Elsevier B.V., 297, pp. 259–265. doi: 10.1016/j.powtec.2016.04.023.
- Guo, X., Lin, J. and Nie, D. (2011) 'New formula for drag coefficient of cylindrical particles', *Particuology*. Chinese Society of Particuology, 9(2), pp. 114–120. doi:

10.1016/j.partic.2010.07.027.

- Hadamard, J. S. (1911) 'Mouvement permanent lent d'une sphère liquid et visqueuse dans un liquide visqueux', *CR Hebd. Seances Acad. Sci. Paris*, 152, pp. 1735–1738.
- Handscomb, C. S., Kraft, M. and Bayly, A. E. (2009) 'A new model for the drying of droplets containing suspended solids', *Chemical Engineering Science*, 64(4), pp. 628–637. doi: 10.1016/j.ces.2008.04.051.
- Haque, M. A., Adhikari, B. and Putranto, A. (2016) 'Predictions of drying kinetics of aqueous droplets containing WPI-lactose and WPI-trehalose by application of composite reaction engineering approach (REA)', *Journal of Food Engineering*. Elsevier Ltd, 189, pp. 29–36. doi: 10.1016/j.jfoodeng.2016.05.019.
- Harpole, G. M. (1981). 'Droplet evaporation in high temperature environments', *J. Heat Transfer.*, 103(1), pp. 86–91. doi: 10.1115/1.3244437
- Hecht, J. P. and King, C. J. (2000a) 'Spray drying: Influence of developing drop morphology on drying rates and retention of volatile substances. 1. Single-drop experiments', *Industrial and Engineering Chemistry Research*, 39(6), pp. 1756–1765. doi: 10.1021/ie9904652.
- Hecht, J. P. and King, C. J. (2000b) 'Spray Drying: Influence of Developing Drop Morphology on Drying Rates and Retention of Volatile Substances. 2. Modelling', *Industrial & Engineering Chemistry Research*, 39(6), pp. 1756–1765. doi: 10.1021/ie9904652.
- Helmholtz, H. von (1867) 'LXIII. On Integrals of the hydrodynamical equations, which express vortex-motion', *The London, Edinburgh, and Dublin Philosophical Magazine and Journal of Science*. Taylor & Francis, 33(226), pp. 485–512.

- Hennigh, O. (2017) 'Lat-Net: Compressing Lattice Boltzmann Flow Simulations using Deep Neural Networks'. Available at: <http://arxiv.org/abs/1705.09036>.
- Van Hooijdonk, E. *et al.* (2013) 'Functionalization of vertically aligned carbon nanotubes', *Beilstein Journal of Nanotechnology*, 4(1), pp. 129–152. doi: 10.3762/bjnano.4.14.
- Huang, D. (2011) 'Modeling of Particle Formation during Spray Drying', *European Drying Conference - EuroDrying'2011*, pp. 26–28.
- Huyakorn, P. S. (1977) 'Solution of steady-state, convective transport equation using an upwind finite element scheme', *Applied Mathematical Modelling*, 1(4), pp. 187–195. doi: 10.1016/0307-904X(77)90004-X.
- Imron, C. *et al.* (2018) 'Mathematical Modeling of Drag Coefficient Reduction in Circular Cylinder Using Two Passive Controls at  $Re = 1000$ ', *Mathematical and Computational Applications*, 23(1), p. 2. doi: 10.3390/mca23010002.
- Irfan, M. and Muradoglu, M. (2017) 'A front tracking method for direct numerical simulation of evaporation process in a multiphase system', *Journal of Computational Physics*. Elsevier Inc., 337, pp. 132–153. doi: 10.1016/j.jcp.2017.02.036.
- Joffe, J. (1945) 'Boiling-point elevation', *Journal of Chemical Education*, 22(6), pp. 270–272. doi: 10.1021/ed022p270.
- Kaneda, M. *et al.* (2008) 'Internal flow in polymer solution droplets deposited on a lyophobic surface during a receding process', *Langmuir*, 24(16), pp. 9102–9109. doi: 10.1021/la801176y.
- Kaneko, S. *et al.* (eds) (2014) 'Chapter 2 - Vibration Induced by Cross-Flow', *Flow-induced Vibrations (Second Edition)* Academic Press, pp. 29–115. doi: 10.1016/B978-0-08-

098347-9.00002-3.

- Kieviet, F. G., Van Raaij, J., De Moor, P. P. E. A., & Kerkhof, P. J. A. M. (1997) 'Measurement and modelling of the air flow pattern in a pilot-plant spray dryer', *Chemical Engineering Research and Design*, 75(3), pp. 321-328. doi: 10.1205/026387697523778.
- Kim, E. H. J., Chen, X. D. and Pearce, D. (2009) 'Surface composition of industrial spray-dried milk powders. 2. Effects of spray drying conditions on the surface composition', *Journal of Food Engineering*. Elsevier Ltd, 94(2), pp. 169-181. doi: 10.1016/j.jfoodeng.2008.10.020.
- Kotake, S. and Okazaki, T. (1969) 'Evaporation and combustion of a fuel droplet', *International Journal of Heat and Mass Transfer*, 12(5), pp. 595-609. doi: 10.1016/0017-9310(69)90041-6.
- Koumoutsakos, P. (1999) 'Application of machine learning algorithms to flow modeling and optimization', *Annual Research Briefs*, pp. 169-178.
- Kulmala, M. *et al.* (1995) 'Mass transfer from a drop-II. Theoretical analysis of temperature dependent mass flux correlation', *International Journal of Heat and Mass Transfer*, 38(9), pp. 1705-1708. doi: 10.1016/0017-9310(94)00302-C.
- Kulmala, Schwarz, J. and Smolík, J. (1994) 'Mass transfer from a drop-I. Experimental study and comparison with existing correlations', *International Journal of Heat and Mass Transfer*, 37(14), pp. 2139-2143. doi: 10.1016/0017-9310(94)90315-8.
- Kuznetsov, G. V., Piskunov, M. V. and Strizhak, P. A. (2016) 'Evaporation, boiling and explosive breakup of heterogeneous droplet in a high-temperature gas', *International Journal of Heat and Mass Transfer*. Elsevier Ltd, 92, pp. 360-369. doi: 10.1016/j.ijheatmasstransfer.2015.08.061.

- Laney, C. B. (1998) 'Computational Gasdynamics', Cambridge University Press. doi: 10.1017/CBO9780511605604.
- Langrish, T. A. G. (2009) 'Multi-scale mathematical modelling of spray dryers', *Journal of Food Engineering*. Elsevier Ltd, 93(2), pp. 218–228. doi: 10.1016/j.jfoodeng.2009.01.019.
- Langrish, T. a. G. and Fletcher, D. F. (2003) 'Prospects for the Modelling and Design of Spray Dryers in the 21st Century', *Drying Technology*, 21(2), pp. 197–215. doi: 10.1081/DRT-120017743.
- Legros, J. C., Piskunov, M. V., & Strizhak, P. A. (2015) 'Difference of evaporation and boiling for heterogeneous water droplets in a high-temperature gas', *MATEC Web of Conferences*, 37, p. 01027. doi:10.1051/matecconf/20153701027.
- Lin, S. X. Q., & Chen, X. D. (2002) 'Improving the glass-filament method for accurate measurement of drying kinetics of liquid droplets', *Chemical Engineering Research and Design*, 80(4), pp. 401-410. doi: 10.1205/026387602317446443.
- Lubetkin, S. D. (2003) 'Why is it much easier to nucleate gas bubbles than theory predicts?', *Langmuir*, 19(7), pp. 2575–2587. doi: 10.1021/la0266381.
- M. Horowitz, C. H. K. W. (1989) 'Phenomenology of Kármán vortex streets in oscillatory flow', *Experiments in Fluids*, 7(4), pp. 217–227. doi: 10.1007/BF00198001.
- Mezhericher, M., Levy, A., & Borde, I. J. D. T. (2010) 'Theoretical models of single droplet drying kinetics: a review', *Drying Technology*, 28(2), pp. 278-293. doi: 10.1080/07373930903530337.
- Masaro, L. and Zhu, X. X. (1999) *Physical models of diffusion for polymer solutions, gels and solids*, *Progress in Polymer Science (Oxford)*. doi: 10.1016/S0079-6700(99)00016-7.

- McDonald, B. E. and Witting, J. M. (1984) 'A conservation law related to Kelvin's circulation theorem', *Journal of Computational Physics*. Elsevier, 56(2), pp. 237–243.
- Meneghini, J. R., Saltara, F., Siqueira, C. L. R., & Ferrari Jr, J. A. (2001) 'Numerical simulation of flow interference between two circular cylinders in tandem and side-by-side arrangements', *Journal of fluids and structures*, 15(2), pp. 327-350. doi: 10.1006/jfls.2000.0343
- Mezhericher, M., Levy, A. and Borde, I. (2008) 'Heat and mass transfer of single droplet/wet particle drying', *Chemical Engineering Science*, 63(1), pp. 12–23. doi: 10.1016/j.ces.2007.08.052.
- Miglani, A. and Basu, S. (2015) 'Sphere to ring morphological transformation in drying nanofluid droplets in a contact-free environment', *Soft Matter. Royal Society of Chemistry*, 11(11), pp. 2268–2278. doi: 10.1039/C4SM02553A.
- Miyatake, O., Tanaka, I., & Lior, N. (1997) 'A simple universal equation for bubble growth in pure liquids and binary solutions with a nonvolatile solute', *International journal of heat and mass transfer*, 40(7), pp. 1577-1584. doi: 10.1016/S0017-9310(96)00224-4
- Monteith, J. and Unsworth, M. (2013) '*Principles of environmental physics: plants, animals, and the atmosphere*', *Principles of Environmental Physics (Fourth Edition) Academic Press*, doi: 10.1016/B978-0-12-386910-4.00018-4.
- Mujumdar, A. S. (Ed.). (1995). 'Handbook of industrial drying, revised and expanded', *CRC Press*, 2.
- Munson, B. R., Young, D. F., & Okiishi, T. H. (1990) 'Elementary fluid dynamics-The Bernoulli equation', *Fundamentals of Fluid Mechanics*, pp. 129-135.

- Nandiyanto, A. B. D. and Okuyama, K. (2011a) 'Progress in developing spray-drying methods for the production of controlled morphology particles: From the nanometer to submicrometer size ranges', *Advanced Powder Technology. The Society of Powder Technology Japan*, 22(1), pp. 1–19. doi: 10.1016/j.appt.2010.09.011.
- Nandiyanto, A. B. D. and Okuyama, K. (2011b) 'Progress in developing spray-drying methods for the production of controlled morphology particles: From the nanometer to submicrometer size ranges', *Advanced Powder Technology. The Society of Powder Technology Japan*, 22(1), pp. 1–19. doi: 10.1016/j.appt.2010.09.011.
- Navon, O., Chekhir, A. and Lyakhovskiy, V. (1998) 'Bubble growth in highly viscous melts: Theory, experiments, and autoexplosivity of dome lavas', *Earth and Planetary Science Letters*, 160(3–4), pp. 763–776. doi: 10.1016/S0012-821X(98)00126-5.
- Nešić, S. and Vodnik, J. (1991) 'Kinetics of droplet evaporation', *Chemical Engineering Science*, 46(2), pp. 527–537. doi: 10.1016/0009-2509(91)80013-O.
- Newbold, F. R. and Amundson, N. R. (1973) 'A model for evaporation of a multicomponent droplet', *AIChE Journal*, 19(1), pp. 22–30. doi: 10.1002/aic.690190105.
- Norrish, R. (1966) 'Equation for the activity coefficients and equilibrium relative humidities', *International Journal of Food Science & Technology*, 1, pp. 25–39.
- Ozawa, K., Nishitani, E. and Doi, M. (2005) 'Modeling of the drying process of liquid droplet to form thin film', *Japanese Journal of Applied Physics*, 44(6A), pp. 4229–4234. doi: 10.1143/JJAP.44.4229.

- Pai, V. and Favelukis, M. (2002) 'Dynamics of spherical bubble growth', *Journal of Cellular Plastics*, 38(5), pp. 403–419. doi: 10.1177/0021955X02038005164.
- Pandey, K., & Basu, S. (2018). 'How boiling happens in nanofuel droplets', *Physics of Fluids*, 30(10), p. 107103. doi: 10.1063/1.5048564
- Park, J. and Choi, H. (1998) 'Numerical solutions of flow past a circular cylinder at reynolds numbers up to 160', *KSME International Journal*, 12(6), pp. 1200–1205. doi: 10.1007/BF02942594.
- Patel, K. C., Chen, X. D., Lin, S. X., & Adhikari, B. (2008) 'A Composite Reaction Engineering Approach to Drying of Aqueous Droplets Containing Sucrose, Maltodextrin (DE6) and Their Mixtures', *AIChE Journal*, 55(1), pp. 217–231. doi: 10.1002/aic.11642.
- Payvar, P. (1987) 'Mass transfer-controlled bubble growth during rapid decompression of a liquid', *International Journal of Heat and Mass Transfer*, 30(4), pp. 699–706. doi: 10.1016/0017-9310(87)90200-6.
- Perdana, J. *et al.* (2013) 'Mimicking Spray Drying by Drying of Single Droplets Deposited on a Flat Surface', *Food and Bioprocess Technology*, 6(4), pp. 964–977. doi: 10.1007/s11947-011-0767-4.
- Pijush K. Kundu (1990) 'Chapter 5 - Vorticity Dynamics', *Fluid Mechanics Academic Press*, pp. 119–140. doi: 10.1016/B978-0-12-428770-9.50011-2.
- Ploumhans, P. *et al.* (2002) 'Vortex methods for direct numerical simulation of three-dimensional bluff body flows: Application to the sphere at  $Re = 300, 500, \text{ and } 1000$ ', *Journal of Computational Physics*, 178(2), pp. 427–463. doi:

10.1006/jcph.2002.7035.

- Poozesh, S. and Bilgili, E. (2019) 'Scale-up of pharmaceutical spray drying using scale-up rules: A review', *International Journal of Pharmaceutics*. Elsevier B.V., 562(March), pp. 271–292. doi: 10.1016/j.ijpharm.2019.03.047.
- Prakash, S. and Sirignano, W. A. (1980) 'Theory of convective droplet vaporization with unsteady heat transfer in the circulating liquid phase', *International Journal of Heat and Mass Transfer*, 23(3), pp. 253–268. doi: 10.1016/0017-9310(80)90113-1.
- Preston, A. T., Colonius, T. and Brennen, C. E. (2007) 'A reduced-order model of diffusive effects on the dynamics of bubbles', *Physics of Fluids*, 19(12), pp. 1–12. doi: 10.1063/1.2825018.
- Price, H. C. *et al.* (2014) 'Quantifying water diffusion in high-viscosity and glassy aqueous solutions using a Raman isotope tracer method', *Atmospheric Chemistry and Physics*, 14(8), pp. 3817–3830. doi: 10.5194/acp-14-3817-2014.
- Price, H. C., Mattsson, J. and Murray, B. J. (2016) 'Sucrose diffusion in aqueous solution', *Phys. Chem. Royal Society of Chemistry*, 18(28), pp. 19207–19216. doi: 10.1039/C6CP03238A.
- Prosperetti, A. (1982a) 'A generalization of the Rayleigh--Plesset equation of bubble dynamics', *The Physics of Fluids*. American Institute of Physics, 25(3), pp. 409–410.
- Prosperetti, A. (1982b) 'A generalization of the Rayleigh-Plesset equation of bubble dynamics', *Physics of Fluids*, 25(3), pp. 409–410. doi: 10.1063/1.863775.
- Quarteroni, A. and Alberto Valli (1988) 'Numerical Approximation of Partial Differential Equations.', *Mathematics of Computation*, 50(181), p. 355. doi: 10.2307/2007945.
- Raffin, R. P. *et al.* (2006) 'Powder characteristics of pantoprazole

delivery systems produced in different spray-dryer scales', *Drying Technology*, 24(3), pp. 339–348. doi: 10.1080/07373930600564381.

- Rajagopalan, V. N. (2014) 'Generation of multicopmponent polymer blend microparticles using droplet evaporation technique and modeling evaporation of binary droplet containing non-volatile solute'. (Doctoral Dissertation). Retrieved from [https://uknowledge.uky.edu/cme\\_etds/39/](https://uknowledge.uky.edu/cme_etds/39/)
- Rajani, B. N., Kandasamy, A. and Majumdar, S. (2009) 'Numerical simulation of laminar flow past a circular cylinder', *Applied Mathematical Modelling*. Elsevier Inc., 33(3), pp. 1228–1247. doi: 10.1016/j.apm.2008.01.017.
- Ranz, W. E. and Marshall, W. R. (1952) 'Evaporation from drops, Parts I & II', *Chem Eng Prog.*, 48, pp. 141-146.
- Ranz, W. E., Marshall, W. R. and others (1952) 'Evaporation from drops', *Chemical Engineering Progress*, 48(3), pp. 141–146.
- Rasmussen, R. *et al.* (1985) 'A Wind Tunnel Investigation of the Effect of an External, Vertical Electric Field on the Shape of Electrically Uncharged Rain Drops', *Journal of the Atmospheric Sciences*, pp. 1647–1652. doi: 10.1175/1520-0469(1985)042<1647:awtiot>2.0.co;2.
- Rayleigh, Lord (1917) 'VIII. *On the pressure developed in a liquid during the collapse of a spherical cavity*', *Philosophical Magazine Series 6*, 34(200), pp. 94–98. doi: 10.1080/14786440808635681.
- Renksizbulut, M. and Yuen, M. C. (1983) 'Experimental Study of Droplet Evaporation in a High-Temperature Air Stream', *Journal of Heat Transfer*, 105(2), pp. 384–388. doi: 10.1115/1.3245590.
- Renksizbulut, M. and Yuen, M C (1983) 'Numerical Study of Droplet

Evaporation in a High-Temperature Stream', *Journal of Heat Transfer*, 105(2), pp. 389–397. doi: 10.1115/1.3245591.

Robinson, A. J. and Judd, R. L. (2004) 'The dynamics of spherical bubble growth', *International Journal of Heat and Mass Transfer*, 47(23), pp. 5101–5113. doi: 10.1016/j.ijheatmasstransfer.2004.05.023.

Roesle, M. L. and Kulacki, F. A. (2010) 'International Journal of Heat and Mass Transfer Boiling of small droplets', *International Journal of Heat and Mass Transfer*. Elsevier Ltd, 53(23–24), pp. 5587–5595. doi: 10.1016/j.ijheatmasstransfer.2010.06.039.

Rogers, S. *et al.* (2012) 'Particle shrinkage and morphology of milk powder made with a monodisperse spray dryer', *Biochemical Engineering Journal*. Elsevier B.V., 62, pp. 92–100. doi: 10.1016/j.bej.2011.11.002.

Ruckenstein, E. and Davis, E. J. (1971) 'The effects of bubble translation on vapor bubble growth in a superheated liquid', *International Journal of Heat and Mass Transfer*, 14(7), pp. 939–952. doi: 10.1016/0017-9310(71)90120-7.

Rybczynski, W. (1911) 'Über die fortschreitende Bewegung einer flüssigen Kugel in einem zähen Medium', *Bull. Acad. Sci. Cracovie A*, 1, pp. 40–46.

Sadek, C. *et al.* (2015) 'Drying of a single droplet to investigate process–structure–function relationships: a review', *Dairy Science and Technology*, 95(6), pp. 771–794. doi: 10.1007/s13594-014-0186-1.

Sadrehaghighi, Ideen. (2020) 'Artificial Intelligence (AI) and Deep Learning For CFD', doi: 10.13140/RG.2.2.22298.59847.

Sato, Y. and Ničeno, B. (2013) 'A sharp-interface phase change model for a mass-conservative interface tracking method', *Journal of Computational Physics*, 249, pp. 127–161. doi:

10.1016/j.jcp.2013.04.035.

- Sazhin, S. S. (2006) 'Advanced models of fuel droplet heating and evaporation', *Progress in Energy and Combustion Science*, 32(2), pp. 162–214. doi: 10.1016/j.pecs.2005.11.001.
- Schutyser, M. A. I., Perdana, J. and Boom, R. M. (2012) 'Single droplet drying for optimal spray drying of enzymes and probiotics', *Trends in Food Science and Technology*. Elsevier Ltd, 27(2), pp. 73–82. doi: 10.1016/j.tifs.2012.05.006.
- Scriven, L. E. (1959) 'On the dynamics of phase growth', *Chemical engineering science*. Elsevier, 10(1–2), pp. 1–13.
- Simion, A. I., Dobrovici, P. E., Grigoras, C. G., & Rusu, L. (2011), 'Modeling of the thermo-physical Properties of aqueous sucrose solutions I. Density and dynamic and kinematic viscosity.', *Annals of Food Science and Technology*, 12, pp. 225-232.
- Singh, V. *et al.* (2012) 'A facile synthesis of PLGA encapsulated cerium oxide nanoparticles: release kinetics and biological activity', *Nanoscale*, 4(8), p. 2597. doi: 10.1039/c2nr12131j.
- Solano-Altamirano, J. M., Malcolm, J. D. and Goldman, S. (2015) 'Gas bubble dynamics in soft materials', *Soft Matter*. Royal Society of Chemistry, 11(1), pp. 202–210. doi: 10.1039/c4sm02037e.
- Starzak, M. and Mathlouthi, M. (2006) 'Temperature dependence of water activity in aqueous solutions of sucrose', *Food Chemistry*, 96(3), pp. 346–370. doi: 10.1016/j.foodchem.2005.02.052.
- Starzak, M. and Peacock, S. (1998) 'Boiling point elevation for aqueous solutions of sucrose: A comparison of different prediction methods', *Zuckerindustrie*, 123(6), pp. 433–441.
- Starzak, M. and Peacock, S. D. (1997) 'Water activity coefficient in aqueous solutions of sucrose -a comprehensive data analysis', *Zuckerindustrie*, 122(5), pp. 380–387.

- Strotos, G. *et al.* (2011) 'Numerical investigation of the evaporation of two-component droplets', *Fuel*. Elsevier Ltd, 90(4), pp. 1492–1507. doi: 10.1016/j.fuel.2011.01.017.
- Sugiyama, Y. *et al.* (2006) 'Buckling and crumpling of drying droplets of colloid-polymer suspensions', *Langmuir*, 22(14), pp. 6024–6030. doi: 10.1021/la053419h.
- Taqieddin, A., Allshouse, M. R. and Alshawabkeh, A. N. (2018) 'Editors' Choice—Critical Review—Mathematical Formulations of Electrochemically Gas-Evolving Systems', *Journal of The Electrochemical Society*, 165(13), pp. E694–E711. doi: 10.1149/2.0791813jes.
- Tesař, V. (2015) 'Induced fluid rotation and bistable fluidic turn-down valves (a survey)', *EPJ Web of Conferences*, doi: 10.1051/epjconf/20159202096.
- Thybo, P. *et al.* (2008) 'Droplet size measurements for spray dryer scale-up', *Pharmaceutical Development and Technology*, 13(2), pp. 93–104. doi: 10.1080/10837450701830957.
- Tran, T. T. H. *et al.* (2017) 'Model parameters for single-droplet drying of skim milk and its constituents at moderate and elevated temperatures', *Drying Technology*. Taylor & Francis, 35(4), pp. 444–464. doi: 10.1080/07373937.2016.1182548.
- Tran, T. T. H., Jaskulski, M., Peglow, M., Avila-Acevedo, J. G., & Tsotsas, E. (2015), 'A new validated model for single droplet drying process', *1st Nordic Baltic Drying Conference- Gdańsk, Poland*.
- Trueman, R. E. *et al.* (2012) 'Auto-stratification in drying colloidal dispersions: A diffusive model', *Journal of Colloid and Interface Science*. Elsevier Inc., 377(1), pp. 207–212. doi: 10.1016/j.jcis.2012.03.045.
- Tsapis, N. *et al.* (2005) 'Onset of Buckling in Drying Droplets of

Colloidal Suspensions', *Phys. Rev. Lett.* American Physical Society, 94(1), p. 18302. doi: 10.1103/PhysRevLett.94.018302.

Turner, M. J. (1956) 'Stiffness and Deflection Analysis of Complex Structures', 'Journal of the Aeronautical Sciences', *Journal Of The Aeronautical Sciences*, 23(9), pp. 145–160.

Vachaparambil, K. J. and Einarsrud, K. E. (2020) 'Numerical simulation of bubble growth in a supersaturated solution', *Applied Mathematical Modelling*. Elsevier Inc., 81, pp. 690–710. doi: 10.1016/j.apm.2020.01.017.

Vehring, R. (2008) 'Pharmaceutical particle engineering via spray drying', *Pharmaceutical Research*, 25(5), pp. 999–1022. doi: 10.1007/s11095-007-9475-1.

Werner, S. R. L. *et al.* (2008) 'Single droplet drying: Transition from the effective diffusion model to a modified receding interface model', *Powder Technology*, 179(3), pp. 184–189. doi: 10.1016/j.powtec.2007.06.009.

Wieselberg, C. (1922) 'New data on the laws of fluid resistance', *National Advisory Committee For Aeronautics*.

Williamson, C. H. K. (1996) 'Vortex dynamics in the cylinder wake', *Annual Review of Fluid Mechanics*, 28, pp. 477–539. doi: 10.1146/annurev.fl.28.010196.002401.

Woo, M. ., Mujumdar, a. . and Daud, W. R. . (2010) 'Spray Drying Technology', accessed 25<sup>th</sup> January 2021, <<https://www.yumpu.com/en/document/view/32880341/spray-drying-technologypdf-national-university-of-singapore>>.

Woo, M. W. *et al.* (2008) 'Comparative study of droplet drying models for CFD modelling', *Chemical Engineering Research and Design*, 86(9), pp. 1038–1048. doi: 10.1016/j.cherd.2008.04.003.

- Wu, Y., Zhang, Xiaosong and Zhang, Xuelai (2016) 'Simplified analysis of heat and mass transfer model in droplet evaporation process', *Applied Thermal Engineering*. Elsevier Ltd, 99, pp. 938–943. doi: 10.1016/j.applthermaleng.2016.01.020.
- Xi, X. *et al.* (2017) 'A new flash boiling model for single droplet', *International Journal of Heat and Mass Transfer*, 107, pp. 1129–1137. doi: 10.1016/j.ijheatmasstransfer.2016.11.027.
- Yang, X. and Church, C. C. (2005) 'A model for the dynamics of gas bubbles in soft tissue', *The Journal of the Acoustical Society of America*, 118(6), pp. 3595–3606. doi: 10.1121/1.2118307.
- Zapryanov, Z. and Tabakova, S. (2013) 'Dynamics of bubbles, drops and rigid particles', *Springer Science & Business Media*, 50, doi: 10.1007/978-94-015-9255-0.
- Zbicinski, I. (2017) 'Modeling and scaling up of industrial spray dryers: A review', *Journal of Chemical Engineering of Japan*, 50(10), pp. 757–767. doi: 10.1252/jcej.16we350.

# Appendix A

**Drag coefficient, Newton-Raphson method and bubble-droplet system**

## A.1. Iteration procedure for determining the drag coefficient of a flow past a cylinder

This section presents the iteration process to find the converged value of the drag coefficient for the flow past the cylinder simulation. The drag coefficient correlations used are from Clift *et al.* (1978) and Munson *et al.* (1990).

Length [m]	$\rho_{cylinder}$ [kg/m <sup>3</sup> ]	radius [m]	$\rho_{air}$ [kg/m <sup>3</sup> ]	$\mu_{air}$ [kg/(m.s)]	Cd	Re	Terminal velocity [m/s]
5	1000	3.00E-04	1.225	1.81E-05	1.00	249.43	6.142
5	1000	3.00E-04	1.225	1.81E-05	1.55	200.64	4.941
5	1000	3.00E-04	1.225	1.81E-05	1.59	197.90	4.873
5	1000	3.00E-04	1.225	1.81E-05	1.59	197.72	4.869
5	1000	3.00E-04	1.225	1.81E-05	1.59	197.70	4.869
5	1000	3.00E-04	1.225	1.81E-05	1.59	197.70	4.869
5	1000	3.00E-04	1.225	1.81E-05	1.59	197.70	4.869

**Figure A.1-1.** Iteration for determining the drag coefficient on the circular cylinder using Munson (1990) empirical equation

Length [m]	$\rho_{cylinder}$ [kg/m <sup>3</sup> ]	radius [m]	$\rho_{air}$ [kg/m <sup>3</sup> ]	$\mu_{air}$ [kg/(m.s)]	Cd	Re	Terminal velocity [m/s]
5	1000	3.00E-04	1.225	1.81E-05	1.00	249.43	6.142
5	1000	3.00E-04	1.225	1.81E-05	1.14	233.27	5.745
5	1000	3.00E-04	1.225	1.81E-05	1.15	232.84	5.734
5	1000	3.00E-04	1.225	1.81E-05	1.15	232.82	5.733
5	1000	3.00E-04	1.225	1.81E-05	1.15	232.82	5.733
5	1000	3.00E-04	1.225	1.81E-05	1.15	232.82	5.733
5	1000	3.00E-04	1.225	1.81E-05	1.15	232.82	5.733

**Figure A.1-2.** Iteration for determining the drag coefficient on the circular cylinder using Clift *et al.* (1978) empirical equation.

## A.2. Newton-Raphson method for solving the moving interface equations (transcendental equations) in Chapter 4

The Newton-Raphson technique is highly effective for solving equations with no specific formula for the exact solution. Generally, assuming that  $x$  is the solution of a function  $f(x)$ , we can guess the value of  $x$  to be  $x_i$  and solve the following equation for the next value of  $x_{i+1}$ ,

$$x_{i+1} = x_i - \frac{f(x_i)}{f'(x_i)} \quad (\text{A.1-1})$$

The guessing procedure is repeated until there is no the difference between  $x_i$  and  $x_{i+1}$ , or in other words,  $x_{i+1}$  is converged.

In Chapter 4, the growth constant variable in the Stefan problem was obtained using this Newton-Raphson method. In order to solve the equation (4-3), it was first rearranged as follows,

$$f(\gamma) = \gamma e^\gamma \operatorname{erf}(\gamma) - \frac{C_{pg}(T_w - T_{sat})}{h_{lg}\sqrt{\pi}} = 0 \quad (\text{A.1-2})$$

$$f\gamma_{i+1} = \gamma_i - \frac{f(\gamma_i)}{f'(\gamma_i)} \quad (\text{A.1-3})$$

For the specific system defined in section 4.1, the term  $\left(\frac{C_{pg}(T_w - T_{sat})}{h_{lg}\sqrt{\pi}}\right)$  is a constant value of 0.113. Following the Newton-Raphson technique, the initial random guess of  $\gamma$  was 1, which can be used to calculate the value of  $e^\gamma$  and  $\operatorname{erf}(\gamma)$  subsequently. Equation (A.1-4) was then used to guess the next value of  $\gamma$ . The iteration process can be seen in the table below.

$\gamma$	$e^\gamma$	$\operatorname{erf}(\gamma)$	$f(\gamma)$	$\frac{f(\gamma_i)}{f'(\gamma_i)}$	$\gamma_i - \frac{f(\gamma_i)}{f'(\gamma_i)}$
1.00000	2.71828	0.84270	2.17786	12.91905	0.83142
0.83142	1.99624	0.76033	1.14909	6.51826	0.65513
0.65513	1.53603	0.64581	0.53705	3.38603	0.49653
0.49653	1.27959	0.51744	0.21592	1.90823	0.38338
0.38338	1.15833	0.41230	0.07025	1.24109	0.32677
0.32677	1.11269	0.35600	0.01660	0.98206	0.30986
0.30986	1.10078	0.33877	0.00271	0.91212	0.30689
0.30689	1.09876	0.33572	0.00036	0.90014	0.30648
0.30648	1.09849	0.33530	0.00005	0.89851	0.30643
0.30643	1.09845	0.33525	0.00001	0.89830	0.30642
0.30642	1.09845	0.33524	7.7404E-07	0.89827	0.30642
0.30642	1.09845	0.33524	9.9195E-08	0.89827	0.30642

### A.3. Bubble growth within a confined liquid with mass fluxes at the bubble-droplet and the droplet-air interfaces

The system consists of a centred-bubble oscillating within a droplet with no drying on the outside. Initially, the system is in equilibrium and the bubble will grow due to the mass flux from the surrounding liquid above the boiling point. The bubble dynamics derivation procedure also starts with the general Navier-Stoke equation as shown below,

$$\rho_l \left( \frac{\partial u}{\partial t} + u \frac{\partial u}{\partial r} \right) = - \frac{\partial p}{\partial r} + \frac{1}{r^2} \frac{\partial}{\partial r} (r^2 \tau_{rr}) - \frac{\tau_{\theta\theta} + \tau_{\varphi\varphi}}{r} \quad (\text{A.1-5})$$

Where  $\rho_l$  is the liquid density,  $u$  is the velocity,  $p$  is the pressure,  $r$  is the radial coordinates of a given point in liquid,  $\tau_{\theta\theta}$  and  $\tau_{\varphi\varphi}$  are the two stress tensors in spherical coordinates. The continuity equation requires the velocity and radial location of any point within the droplet to satisfy,

$$u(r, t) = \frac{R^2}{r^2} U(t) \quad (\text{A.1-6})$$

Where  $U$  is the bubble surface velocity and  $R$  is the bubble radius. Equation (A.1-6) can be differentiated with respect to radial location,  $r$ , and time,  $t$ ,

$$\frac{du}{dt} = - \frac{R^2}{r^2} \dot{U} + \frac{2R}{r^2} U \dot{R} \quad (\text{A.1-7})$$

$$\frac{du}{dr} = \frac{-2R^2 U}{r^2} \quad (\text{A.1-8})$$

The stress tensor components in spherical coordinates can be simplified through expression,

$$\tau_{\theta\theta} + \tau_{\varphi\varphi} = -\tau_{rr} \quad (\text{A.1-9})$$

Integrating the left-hand-side of equation (A.1-5) from the bubble surface to the droplet surface gives,

$$\int_{R_b}^{R_d} \rho_l \left( \frac{\partial u}{\partial t} + u \frac{\partial u}{\partial r} \right) dr = \rho_l \left[ \left( \frac{1}{R_d} - \frac{1}{R_b} \right) (-R^2 \dot{U} - 2RU\dot{R}) + \frac{R^4 U^2}{2} \left( \frac{1}{R_d^4} - \frac{1}{R_b^4} \right) \right] \quad (\text{A.1-10})$$

Here, the fluid is assumed to be Newtonian fluid which indicates,

$$\tau_{rr} = 2\mu \frac{\partial u}{\partial r} \quad (\text{A.1-11})$$

The right-hand side of the equation (A.1-5) is also integrated from  $R_b$  to  $R_d$  using the above assumptions and integration by parts technique,

$$\begin{aligned} \int_{R_d}^{R_b} \left( -\frac{\partial p}{\partial r} + \frac{1}{r^2} \frac{\partial}{\partial r} (r^2 \tau_{rr}) - \frac{\tau_{\theta\theta} + \tau_{\varphi\varphi}}{r} \right) dr & \quad (\text{A.1-12}) \\ & = P_{R_b} - P_{R_d} + 4\mu R^2 U \left( \frac{1}{R_d^3} - \frac{1}{R_b^3} \right) + \tau_{rrR_d} \\ & \quad - \tau_{rrR_b} \end{aligned}$$

Equating the two equations (A.1-10) and (A.1-12) gives the velocity profile of the bubble surface within the liquid droplet,

$$\begin{aligned} -R^2 \dot{U} \left( \frac{1}{R_d} - \frac{1}{R_b} \right) - 2RU\dot{R} \left( \frac{1}{R_d} - \frac{1}{R_b} \right) + \frac{R^4 U^2}{2} \left( \frac{1}{R_d^4} - \frac{1}{R_b^4} \right) & \quad (\text{A.1-13}) \\ & = \frac{P_{R_b} - P_{R_d}}{\rho_l} + \frac{4\mu R^2 U}{\rho_l} \left( \frac{1}{R_d^3} - \frac{1}{R_b^3} \right) \\ & \quad + \frac{\tau_{rrR_d} - \tau_{rrR_b}}{\rho_l} \end{aligned}$$

The momentum balance is evaluated at the bubble and droplet surface,

$$J_b^2 \left( \frac{1}{\rho_b} - \frac{1}{\rho_l} \right) + P_b - P_{R_b} + \tau_{rrR_b} = \frac{2\sigma}{R_b} \quad (\text{A.1-14})$$

And

$$J_d^2 \left( \frac{1}{\rho_l} - \frac{1}{\rho_a} \right) + P_d - P_{R_d} + \tau_{rrR_d} = \frac{2\sigma}{R_d} \quad (\text{A.1-15})$$

Equations (A.1-14) and (A.1-15) are rearranged to find the expressions for the stress tensor at the two interfaces,

$$\tau_{rrR_b} = \frac{2\sigma}{R_b} - J_b^2 \left( \frac{1}{\rho_b} - \frac{1}{\rho_l} \right) - P_b + P_{R_b} \quad (\text{A.1-16})$$

And

$$\tau_{rrR_d} = \frac{2\sigma}{R_d} - J_d^2 \left( \frac{1}{\rho_l} - \frac{1}{\rho_a} \right) - P_d + P_{R_d} \quad (\text{A.1-17})$$

Substituting equation (A.1-16) and (A.1-17) into equation (A.1-13) gives the velocity profile of the bubble surface,

$$\begin{aligned} -R^2 \dot{U} \left( \frac{1}{R_d} - \frac{1}{R_b} \right) - 2RU \dot{R} \left( \frac{1}{R_d} - \frac{1}{R_b} \right) + \frac{R^4 U^2}{2} \left( \frac{1}{R_d^4} - \frac{1}{R_b^4} \right) \\ = \frac{1}{\rho_l} \left[ \frac{2\sigma}{R_d} - \frac{2\sigma}{R_b} + P_b - P_d + J_b^2 \left( \frac{1}{\rho_b} - \frac{1}{\rho_l} \right) \right. \\ \left. - J_d^2 \left( \frac{1}{\rho_l} - \frac{1}{\rho_a} \right) + \frac{4\mu R^2 U}{\rho_l} \left( \frac{1}{R_d^3} - \frac{1}{R_b^3} \right) \right] \end{aligned} \quad (\text{A.1-18})$$

and the velocity of the bubble interface,  $U$ , must satisfy,

$$U = \frac{J_b}{\rho_l} + \dot{R}_b \quad (\text{A.1-19})$$

Where  $R$  is the bubble radius,  $\dot{U}$  are the bubble interface velocity over time,  $\sigma$  is the surface tension at the interface between two fluids,  $\rho_b$ ,  $\rho_l$  and  $\rho_a$  are the bubble, liquid and air densities,  $\mu$  is the dynamic viscosity of the liquid,  $J_b$  and  $J_b$  are the mass flux at the bubble and droplet interfaces. This set of equations can be solved using any common PDEs solver. The recommended solvers are ode23 or ode45 in Matlab. The code for implementing the equation (A.1-18) into Matlab is shown in appendix B. Matlab code for the bubble growth within the droplet drying using the solute-fixed coordinate.

# Appendix B

## **1D model for a boiling droplet using the solute-fixed coordinate**

The code for describing the droplet drying using the solute-fixed coordinate is adopted from Dr. Muzammil Ali from the research group at the University of Leeds. The code shows how the bubble governing equation and the ode23/ode45 solvers are integrated into the code for droplet drying.

## B.1. Matlab code for a 1D boiling droplet

```

clc
clear all
clear function
close all

global deltaR deltaR3 deltaR4 mr1value mrdiffvalue liqisvalue Pbvalue
nnewvalue Pb_pressure S Rnb Rnd Ini_Pequil Jd Pddropvalue rhoBvalue;
Pa=101325; Rnd=1.734e-3; Pb_pressure=(101325+2*S/Rnd)+2*S/Rnb;
nnewvalue=0; Pbvalue=(101325+2*S/Rnd)+2*S/Rnb;
mr1value=0; mrdiffvalue=0; liqisvalue=0; S=0.0725; Rnb=300e-6;
Ini_Pequil=(101325+2*S/Rnd)+2*S/Rnb;
Pddropvalue=101325+2*S/Rnd; rhoBvalue=29*Ini_Pequil/(8.314*392);
%Initial temperature of the droplet (K)
Ti=23+273; rhoBvalue=29*Ini_Pequil/(8.314*392);
%Temperature of Air (K) Tair=140+273;
%Diameter of the droplet (micron) dp=1734;
%Relative Humidity of Air (%) RH=0.022;
%Size of the droplet (m) dp=dp/1000000;
%Radius of droplet (m) r=dp/2;
%Initial moisture content in droplet (wt/wt) wi=0.95;
%density of solids (kg/m3) rhesolid=1520;
%density of solvent (kg/m3) rhesolvent=1000;
%density of the slurry droplet (kg/m3) rhodrop=rhesolid*(1-wi)+rhesolvent*wi;
%Heat capacity of air [J/kg-K] CPair=1006.43;
%Density of air (kg/m3) roair=1.068;
%Viscosity of Air (kg/ms) muair = 0.000189;
%Air Velocity (m/s) vair=0.0;
%Latent heat of vaporization of water [J/Kg] hfg=2450000;
%Thermal conductivity of air (W/mK) kair=0.0285;
%Thermal Conductivity of Droplet (Assumed equal to water) (W/mk)
%lam=0.52;
%volume of Droplet Vdrop=4/3*pi()*r^3;
%droplet total mass (kg) mdrop=Vdrop*rhodrop; mwater=mdrop*wi;
%Surface area of the droplet Adrop=4*pi()*r^2;
%Initial concentration of moisture in the droplet (kg/m3) Ci=wi/(1-wi);
CPsolid=1063.57;
% Cp of water (J/kg-K) CPwater=4185;
%Mass of solids (kg) msolid=(1-wi)*rhodrop*Vdrop;
%Diffusion coefficient of vapour into the air (m2/s) Daw=3.564e-
10*(Ti+Tair)^1.75;

```

```

%Schmidt number [a dimensional] Sc=muair/(roair*Daw);
%Velocity of droplet(m/s) vr=0.75;
%Calculation of Reynolds number Re=roair*dp*abs(vair-vr)/muair;
%Calculation of sherwood number Sh=2+0.6*Re^0.5*Sc^(1/3);
%Calculation of mass transfer coefficient (m/s) kc=Sh*Daw/dp;
%Calculation of Prandtl Number Pr=(muair*CPair)/kair;
%Calculation of Nusselt Number Nu=2+0.6*Re^0.5*Pr^(1/3);
%Calculation of Heat transfer coefficient (W/m2K) htc=Nu*kair/dp;
%Spacial increments space=50; n=space; n1=n-1;
%Space descritization dr (m)
dr=r/space; %Radius of droplet is divided into equal increments.
%Time descritization dt (sec) size=30000; tfinal=(size); %seconds
avgu=mwater/msolid;
%display(r/dr+1); C=Ci*ones(1,space);
u=zeros(1,space);
Ct=u; rd=u; v=u; w=u; R=u; Q=u; x=u; Rd=r; avgmoist=u; r=zeros(1,space);
s=zeros(1,n);
solid=zeros(1,n); liquid=zeros(1,n); Tn(1)=Ti; mliq=zeros(1,n);
betas=u;gams=u;
t=zeros(1,space); mr=0; mremv=0; D303=6e-10; avegm=wi; wfraction=0;
mremoved=0;
Tp=Ti*ones(1,space); radial=zeros(1,space); act1=1.0; Z=msolid/(4*3.14);
dz=Z/(space);
F=0; G=1; gmi=zeros(1,n); k=1; dlim=16.5e-11; rad_nw=100e-6; %initial
bubble size
Pair=101325; %Air Pressure in Pascal
nw=0; mass_of_vapour=0; init_bubble_rad=100e-6; rbubble(1)=rad_nw;
% RP_R=zeros(10001,2);]
mr1=zeros(size,1); mr(1,1)=0; mr2=zeros(size,1); mr2(1,1)=0;
mrdiff=zeros(size,1);
mrdiff(1,1)=0; nnew=zeros(size,1); Rmatrix=zeros(size,2);
Rmatrix(:,1)=Rnb; Rmatrix(:,2)=0;Rmatrixo=zeros(size,2);Rmatrixo(1,1)=Rnb;
Rmatrixo(1,2)=0; Pbmatrix=zeros(size,1); Pbmatrix(1,1)=101325+2*S/Rnb;
liqvis=zeros(size,1); liqvis(1,1)=0.001/998;
D=zeros(size,1); nnewtotal=0;
o=1; deltaR=(1/Rnd-1/Rnb); deltaR3=(1/Rnd^3-1/Rnb^3); deltaR4=(1/Rnd^4-
1/Rnb^4);
for k=1 : tfinal
    if Tp(k)>=372
        dt=(1e-2)*10^-6;
options=odeset('Reltol',1e-2,'Abstol',1e-2);

```

```

nnewtotal=0;
[RP_t,RP_R]=ode45(@f1,[(o-1)*dt]:dt:(o+2)*dt],[Rmatrixo(o,1)
Rmatrixo(o,2)];
Rmatrixo(o+1,1)=RP_R(2,1);
Rmatrixo(o+1,2)=RP_R(2,2);
%
Rmatrix(k+1,1)=Rmatrixo(o+1,1);
Rmatrix(k+1,2)=Rmatrixo(o+1,2);
Rvalue=Rmatrix(k+1,1);
o=o+1;
    else
        dt=0.01;
    end
k
for i=1:n
    if(Tp(k)<372)
AA=8.07131; AB=1730.63; AC=233.426;
    else
AA=8.14019; AB=1810.94; AC=244.485;
    end
Psat=10^(AA-AB/(Tp(k)-273.15+AC));
Psatairb=10^(AA-AB/(Tp(k)-273.15+AC));
%Conversion of pressure from MMHG into Pascal
Psat=Psat*101325/760;
Psatairb=Psatairb*101325/760;
act_bubble=(C(1)*342/18/(1+C(1)*342/18))*10^(-4.43*(1-
(C(1)*342/18/(1+C(1)*342/18))^2);
mair_bubble=initial_n*29;
if Tp(k)>=372
bubble_rh=(Pbvalue*(abs(mass_of_vapour)/18)/((abs(mass_of_vapour)/18+m
air_bubble/28.97)))/Psatairb;
%pause(5);
kc_bubble=Sh*Daw/(2*Rmatrix(k,1));
kc=Sh*Daw/(2*r(n));
if bubble_rh==act_bubble
    mr1(k,1)=0;
else
mr1(k,1)=(alpha*kc_bubble*(18/8314)*101325/(Tp(k))*log((1-
bubble_rh*Psatairb/101325)/(1-act_bubble*Psat/101325))); %kg/m^2s
end

```

```

mr2(k+1,1)=mr1(k,1);
mrdiff(k,1)=(mr2(k+1,1)-mr2(k,1))/(dt);
mr1value=mr1(k,1);
mrdiffvalue=mrdiff(k,1);
nnew(k,1)=mr1(k,1)*4*pi*Rmatrix(k,1)^2*dt*1000/18;
nnewvalue=nnew(k,1);
for p=1:k
    nnewtotal=nnewtotal+nnew(p,1);
end
ntotal=nnewtotal+initial_n;
Pbmatrix(k+1,1)=((ntotal)*Rg*Tp(k))/((4/3)*pi*Rmatrix(k,1)^3);
Pbvalue=Pbmatrix(k,1);
rhoBvalue=((initial_n*29e-3)+(nnewtotal*18e-3))/(4/3*pi*Rmatrix(k,1)^3);%%% NEED CHECK
else
    Rmatrix(k,1)=Rnb;
    Rmatrix(k,2)=0;
end
mass_of_vapour=mass_of_vapour+(mr1(k,1)*dt)*4*3.14*Rmatrix(k,1)^2;
nw=nw+(mr1(k,1)*dt*4*3.14*Rmatrix(k,1)^2)/18.015;
if i==1
    rhodropA=rhosolid*(1-(C(i+1)/(1+C(i+1))))+rhosolvent*(C(i+1)/(1+C(i+1)));
    rhodropB=rhosolid*(1-(C(i)/(1+C(i))))+rhosolvent*(C(i)/(1+C(i)));
    CsA=rhosolid/(1+(0.5*(C(i+1)+C(i))*rhosolid/rhosolvent));
    CsB=rhosolid/(1+(C(i)*rhosolid/rhosolvent));
    if(Tp(k)<373.15)
        AA=8.07131; AB=1730.63; AC=233.426;
    else
        AA=8.14019; AB=1810.94; AC=244.485;
    end
    Psat=10^(AA-AB/(Tp(k)-273.15+AC));
    Psatairb=10^(AA-AB/(Tp(k)-273.15+AC));
    %Conversion of pressure from MMHG into Pascal
    Psat=Psat*101325/760;
    Psatairb=Psatairb*101325/760;
    act1=(C(i)*342/18/(1+C(i)*342/18))*10^(-4.43*(1-(C(i)*342/18/(1+C(i)*342/18)))^2);
    alpha=1.0;
    if(r(n)<=0)
        r(n)=dp/2;

```

```

end
mass_of_vapour=mass_of_vapour+(mr1(k,1)*dt)*4*3.14*Rmatrix(k,1)^2;
nw=nw+(mr1(k,1)*dt*4*3.14*Rmatrix(k,1)^2)/18.015;
if(nw<0)
nw=0;
end
if Tp(k)>=372
r(i)=Rmatrix(k,1)+(3*dz/CsA)^(1/3);
else
    r(i)=(3*dz/CsA)^(1/3);
end
r(i+1)=(((r(i))^3)+3*dz/CsA)^(1/3);
%diffusivity of sucrose
DwsA=4e-11*(0.5*(C(i+1)+C(i)))^2+4e-10*(0.5*(C(i+1)+C(i)))-4e-11;
DwsB=4e-11*(0.5*(C(i)+C(i)))^2+4e-10*(0.5*(C(i)+C(i)))-4e-11;
D(k,1)=4e-11*(0.5*(C(1,1)+C(1,1)))^2+4e-10*(0.5*(C(1,1)+C(1,1)))-4e-11;
liqvis(k,1)=1.38e-23*Tp(1,k)/(6*pi*5e-8*D(k,1));
liqvisvalue=liqvis(k,1);
if(DwsA<dlim)
DwsA=dlim;
end
if(DwsB<dlim)
DwsB=dlim;
end
A=DwsA*CsA*CsA*(0.5*(r(i+1)+r(i)))^4*dt/dz^2;
B=DwsB*CsB*CsB*(0.5*r(i))^4*dt/dz^2;
u(i)=0;
v(i)=1+A;
w(i)=-(A);
elseif i>=2 && i<n
j=i-1/2;
rhodropA=rhosolid*(1-(C(i+1)/(1+C(i+1))))+rhosolvent*(C(i+1)/(1+C(i+1)));
rhodropB=rhosolid*(1-(C(i)/(1+C(i))))+rhosolvent*(C(i)/(1+C(i)));
preA=(C(i+1)+C(i))/2;
preB=(C(i)+C(i-1))/2;
CsA=rhosolid/(1+(0.5*(C(i+1)+C(i))*rhosolid/rhosolvent));
CsB=rhosolid/(1+(0.5*(C(i)+C(i-1))*rhosolid/rhosolvent));
DwsA=4e-11*(0.5*(C(i+1)+C(i)))^2+4e-10*(0.5*(C(i+1)+C(i)))-4e-11;
DwsB=4e-11*(0.5*(C(i-1)+C(i)))^2+4e-10*(0.5*(C(i-1)+C(i)))-4e-11;

```

```

if(DwsA<dlim)
DwsA=dlim;
end
if(DwsB<dlim)
DwsB=dlim;
end
r(i+1)=(((r(i))^3)+3*dz/CsA)^(1/3);
B=(DwsB*CsB*CsB*(0.5*(r(i-1)+r(i)))^4)*dt/dz^2;
A=(DwsA*CsA*CsA*(0.5*(r(i+1)+r(i)))^4)*dt/dz^2;
u(i)=-B;
v(i)=1+A+B;
w(i)=-A;
elseif i==n
j=n-1/2;
preA=(C(i)+C(i))/2;
preB=(C(i)+C(i-1))/2;
rhodropA=rhosolid*(1-(C(i)/(1+C(i))))+rhosolvent*(C(i)/(1+C(i)));
rhodropB=rhosolid*(1-(C(i)/(1+C(i))))+rhosolvent*(C(i)/(1+C(i)));
CsA=rhosolid/(1+(0.5*(C(i)+C(i))*rhosolid/rhosolvent));
CsB=rhosolid/(1+(0.5*(C(i)+C(i-1))*rhosolid/rhosolvent));
DwsA=4e-11*(0.5*(C(i)+C(i-1)))^2+4e-10*(0.5*(C(i)+C(i-1)))-4e-11;
DwsB=4e-11*(0.5*(C(i)+C(i-1)))^2+4e-10*(0.5*(C(i)+C(i-1)))-4e-11;
if(DwsA<dlim)
DwsA=dlim;
end
if(DwsB<dlim)
DwsB=dlim;
end
end
r(i+1)=(((r(i))^3)+3*dz/CsA)^(1/3);
A=(DwsA*CsA*CsA*(0.5*(r(n)+r(n)))^4)*dt/dz^2;
B=(DwsB*CsB*CsB*(0.5*(r(n)+r(n-1)))^4)*dt/dz^2;
u(i)=-(B);
v(i)=1+B;
w(i)=0;
betaval=DwsB*dt/(dz*dz);
end
end
if (rem(k,1/dt)==1)
for j=1:n

```

```

if (i==n)
end
end
end
for i=1
s(1)=C(i);
end
for i=2:n-1
s(i)=C(i);
end
for i=n
j=n-1/2;
if(Tp(k)<373.15)
AA=8.07131; AB=1730.63; AC=233.426;
else
AA=8.14019; AB=1810.94; AC=244.485;
end
Rd=r(n);
DRvalue=r(n);
Psat=10^(AA-AB/(Tp(k)-273.15+AC));
Psatair=10^(AA-AB/(Tair-273.15+AC));
deltaR=(1/DRvalue-1/Rmatrix(k+1,1));
deltaR3=(1/DRvalue^3-1/Rmatrix(k+1,1)^3);
deltaR4=(1/DRvalue^4-1/Rmatrix(k+1,1)^4);
Pddropvalue=Pbvalue-2*S/(Rmatrix(k+1,1));
%Conversion of pressure from MMHG into Pascal
Psat=Psat*101325/760;
Psatair=Psatair*101325/760;
Xwater=RH*Psatair/101325;
Wwater=Xwater*(18/(18+28.8));
kair=(1-Wwater)*(7e-5*((Tair+Tp(k))/2)+0.0047)+Wwater*0.015; %thermal
conductivity as a function of air and water vapor temperature in the bulk
Daw=1.963e-7*((Tair+Tp(k))/2)-3.33307e-5;
%Phy Chem. Ref. Data, vol. 1 3-11, 1972.
muair=4e-8*((Tair+Tp(k))/2)+6e-6;
%Heat capacity of air [J/kg-K]
CPair=(1-RH)*1010.23+RH*1880;
%Calculation of Prandtl Number
Pr=(muair*CPair)/kair;

```

```

%Schmidt number [a dimensional]
Sc=muair/(roair*Daw);
%Calculation of Reynolds number
Re=roair*(2*Rd)*abs(vair-vr)/muair;
%Calculation of sherwood number
Sh=2+0.6*Re^0.5*Sc^(1/3);
%Calculation of Nusselt Number
Nu=2+0.6*Re^0.5*Pr^(1/3);
%Calculation of Heat transfer coefficient (W/m2K)
htc=Nu*kair/(2*Rd);
%Calculation of mass transfer coefficient (m/s)
kc=Sh*Daw/(2*Rd);
Adrop=4*pi()*Rd^2;
act1=(C(n)*342/18/(1+C(n)*342/18))*10^(-4.43*(1-
(C(n)*342/18/(1+C(n)*342/18)))^2);
alpha=log((act1*Psat/101325-RH*Psatair/101325)/(1-
act1*Psat/101325)+1)/((act1*Psat/101325-RH*Psatair/101325)/(1-
act1*Psat/101325));
if(alpha>1)
alpha=1.0;
end
if((act1*Psat-RH*Psatair)<0)
mr=0;
else
mr=(alpha*kc*(18/8314)*101325/((Tp(k)+Tair)/2)*log((1-
RH*Psatair/101325)/(1-act1*Psat/101325)));
end
%mr=0.001;
Jd=mr;
% mr=0.0;
mremoved=mremoved+(kc*Adrop*(18/8314)*101325/((Tp(k)+Tair)/2)*log((1-
-RH*Psatair/101325)/(1-act1*Psat/101325)));
F=(alpha*(kc*(18/8314)*101325/((Tp(k)+Tair)/2)*log((1-
RH*Psatair/101325)/(1-act1*Psat/101325))));
end
DwsA=4e-11*(0.5*(C(n-1)+C(n)))^2+4e-10*(0.5*(C(n-1)+C(n)))-4e-11;
if(DwsA<dlim)
DwsA=dlim;
end
A=(DwsA*Cs*Cs*r(n)^4)*dt/dz^2;
G=DwsA*Cs*Cs*r(n)^2;

```

```

s(i)=C(i)-(A*F*dz/G);
mfract=mwater/(msolid+mwater);
end
R(n+1) = 0; Q(n+1) = 0;
for i=1:n
ii = n-i+1;
R(ii) = -u(ii)/(w(ii)*R(ii+1)+v(ii));
Q(ii) = -(s(ii)+w(ii)*Q(ii+1))/(w(ii)*R(ii+1)+v(ii));
end
%%%%%%%%%
% Compute solution
%%%%%%%%%
x(1) = Q(1);
for i=1:n-1
x(i+1) = R(i+1)*x(i) + Q(i+1);
end
lhs=u(n)*C(n-1)+v(n)*C(n);
rhs=s(n);
C=x;
%end
t(k+1)=t(k)+dt;
%%%%%%%%%Calculation of Mass
%%%%%%%%%Removed%%%%%%%%%
mremv=mremv+F*Adrop*dt;
mwater=mwater-F*Adrop*dt;
CPwater=0.00876*(Tp(k)-273)^2-0.6042*(Tp(k)-273)+4190;
CPsolid=3.5242*(Tp(k)+273)+1319.7;
betame=1.0;
Tp(k+1)=Tp(k)+betame*(htc*Adrop*(Tair-Tp(k))-
hfg*mr*Adrop+0.5*3.14*500e-6*sqrt(htc*500e-6*0.035)*(Tair-
Tp(k)))*dt/(msolid*(CPsolid+sum(C(1:n))/n*CPwater));
Vliq=mwater/rhosolvent;
Vsol=msolid/rhosolid;
Vfrac=Vliq/(Vsol+Vliq);
avgu=mwater/msolid;
avegm=sum(C(1:n))/n;
fprintf('%8.13f,', mr*dt);  fprintf('%8.5f',t(k));
fprintf('%8.3f',Tn(1)); fprintf('%8.3f',Tn(n));
fprintf('\n'); fprintf('%8.3f',C(1));

```

```

fprintf('%8.3f',C(n)); fprintf('Mfraction = %8.3f',avegm);
fprintf('Mass Removed (kg) = %8.12f',mremv);
fprintf('Mass Fraction = %8.12f',sum(mliq(1:n-1))/(sum(mliq(1:n-1))+msolid));
fprintf(' %8.6f',C(1)); % centre concentration
fprintf(' %8.6f',C(n)); % surface concentration
fprintf(' %8.6f',avgmoist(k)); % surface concentration
fprintf(' %8.6f',gmi(k)); % surface concentration
fprintf(' %8.6f',mwater/msolid); % volume averaged concentration/fraction
function RP=f1(RP_t,RP_R)
global deltaR deltaR3 deltaR4 mr1value mrdiffvalue liqisvalue Pbvalue
nnewvalue Pb_pressure S Rnb Rnd Ini_Pequil Jd Pddropvalue rhoBvalue;
Pb_pressure=101325+2*S/Rnb;
nnewvalue=0;
Pbvalue=101325+2*S/Rnb;
mr1value=0; mrdiffvalue=0; liqisvalue=0; S=0.0725; Rnb=100e-6;
Ini_Pequil=101325+2*S/Rnb;
vA=1.48e-5;
Pstat=102755; Pv=2.33*10^3;
%k=1.47; Rg=8.314; %gas constant
T= 300; %K
Rn=100e-6;
Vn=4/3*pi*Rn^3;
RP_n=Pstat*Vn/(Rg*T);
rhoA=1.2043845867; %%as in COMSOL at 293.15
vA=0.00001813968; %%as in COMSOL at 293.15
rhoL=999.615085156; %%as in COMSOL at 293.15
vL=0.00100934733/rhoL; %%as in COMSOL at 293.15
S=0.0725; %surface tension
Pa=101325;
theta=0;
% end
rhoB=RP_n*29e-3/(4/3*pi*RP_R(1)^3);
Pdrop=101325;
RP(1)=RP_R(2);
%%%%%%%%%%%%%% WITH MASS FLUX- -- BUBBLE ONLY
%%%%%%%%%%%%%%
% term1=(RP_R(2)/RP_R(1))*(-mr1value/rhoL-4*vL/RP_R(1));
% term2=3/2*(RP_R(2)^2/RP_R(1));
% term3=mrdiffvalue/rhoL;
% term4=1/(2*RP_R(1))*(mr1value/rhoL)^2;

```

